



**HAL**  
open science

# Semiconducteurs organiques à base de triazastarphène : vers un transport tridimensionnel en phase cristalline

Qian Li

► **To cite this version:**

Qian Li. Semiconducteurs organiques à base de triazastarphène : vers un transport tridimensionnel en phase cristalline. Material chemistry. Université de Bordeaux, 2019. English. NNT : 2019BORD0144 . tel-03275311

**HAL Id: tel-03275311**

**<https://theses.hal.science/tel-03275311>**

Submitted on 1 Jul 2021

**HAL** is a multi-disciplinary open access archive for the deposit and dissemination of scientific research documents, whether they are published or not. The documents may come from teaching and research institutions in France or abroad, or from public or private research centers.

L'archive ouverte pluridisciplinaire **HAL**, est destinée au dépôt et à la diffusion de documents scientifiques de niveau recherche, publiés ou non, émanant des établissements d'enseignement et de recherche français ou étrangers, des laboratoires publics ou privés.

THÈSE PRÉSENTÉE  
POUR OBTENIR LE GRADE DE  
**DOCTEUR DE**  
**L'UNIVERSITÉ DE BORDEAUX**

ÉCOLE DOCTORALE DES SCIENCES CHIMIQUES  
SPÉCIALITÉ: CHIMIE ORGANIQUE

Par Qian LI

**Organic Semiconductors Based on Triazastarphene Towards 3D  
Charge Transport in Crystalline Phase**

Sous la direction de : Prof. Thierry TOUPANCE  
(co-encadrant :Dr. Yohann NICOLAS)

Devant être soutenue le jeudi 19 septembre 2019 à 14h

Membres du jury :

M. BLANCHARD, Philippe	DR CNRS, Université d'Angers	Rapporteur
M. PORIEL, Cyril	DR CNRS, Université de Rennes 1	Rapporteur
M. FAGES, Frédéric	Professeur, Aix-Marseille Université	Examineur
M. CASTET, Frédéric	Professeur, Université de Bordeaux	Examineur
M. TOUPANCE, Thierry	Professeur, Université de Bordeaux	Directeur de Thèse
M. NICOLAS, Yohann	Maitre de Conférences, Bordeaux INP	Co-encadrant de Thèse

Membres invités:

M. ABBAS, Mamatimin      CR CNRS, Bordeaux INP



# Acknowledgements

This work was performed in Molecular chemistry and Materials group (C2M), Institute of Molecular Science (ISM), University of Bordeaux. During my four years study in France I have got a lot of help and support from many people and organizations.

Firstly, I would like express my thanks to “China Scholarship Council” who has provided me financial support for four years. I can only have the opportunity to study abroad with the help of my country. I will keep in mind the support that my country gave to me and to serve my motherland as return.

My deepest gratitude goes to Professor Thierry TOUPANCE and Yohann NICOLAS, my supervisors, for their generous support, constant encouragement and helpful guidance from the first to the last day of my study in France. They walked me through all the stages of my research and the writing of my thesis. Without their help I can never complete such an interesting and complicated academic project. I will never forget their unconditional support in and out of the lab to facilitate my study and life in France.

This work is the result of a teamwork and collaboration of many people. I would like to thank Professor Mamatimin ABBAS from IMS for helping me to fabricate different kinds of devices to characterize the charge carrier transport properties of the materials. I would like to thank Professor Frédéric CASTET for helping me with the simulation and theoretical calculation with Gaussian software. I would like to thank all the members from CESAMO who helped me with the characterization of the compounds, especially Aline LACOUDRE who did all the analysis of molecular packing in crystalline phase.

I am very happy that I met many perfect colleagues in the group during the last four years. I would like to express my gratitude to Luc VELLUTINI, Céline OLIVIER, Emilie GENIN, Karine HEUZE, Anne THIENPONT, Marie-Anne DOURGES, Svitlana POIX-SHINKARUK, Laurent THOMAS, Imane BARBARA, Camille BERTRAND, Szu-Hsuan LEE, Juan Angel Moreno BALDERRAMA, Antoine Tiya DJOWE, Hongtao JI, Nisreen YOUSEFALHAJ and Lisa ROUVIERE. I will always remember their friendly help in the laboratory.

Lastly, I really appreciate my family members who have offered me countless love and support during my study abroad.



## Résumé en Français

Au cours des dernières décennies, des efforts considérables ont été dédiés au développement de semiconducteurs organiques (OSCs) et de nombreux semiconducteurs de type p ou n originaux ont été décrits présentant des conductivités plus élevées que celles obtenues avec le silicium amorphe.

Néanmoins, la plupart des mobilités élevées rapportées jusqu'à présent pour les OSCs ont été mesurées sur des monocristaux ou des films minces bien cristallisés selon une direction. Par conséquent, un des inconvénients qui limite encore les applications des OSCs est la forte anisotropie de leurs propriétés de transport de charge en phase cristalline. De manière à vaincre l'unidimensionnalité du transport de charge dans la plupart des OSCs, l'objectif de cette thèse a été de concevoir et de synthétiser des molécules qui pouvaient fournir des chemins de transport de charge tridimensionnel équilibré à l'état solide.

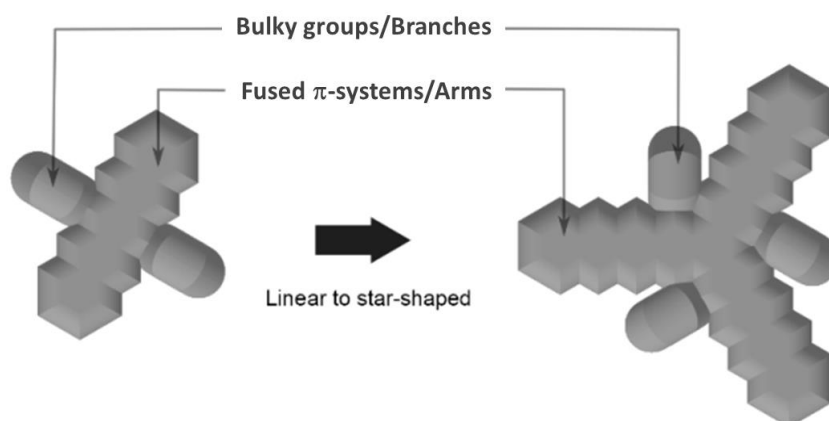


Figure 1. Stratégie de conception de molécules en étoile.

Dans ce but, notre stratégie repose sur l'extension des molécules linéaires usuelles en électronique organique en molécules en étoile de symétrie  $C_{3h}$  (Figure 1). Les molécules cible sont donc composées d'un coeur plan constitué de cycles aromatiques fusionnés (nommés ensuite "bras") et de groupements encombrés placés proches du centre de l'étoile (nommés dans la suite "branches"). Dans de telles structures moléculaires, les bras pi-conjugués sont supposés conduire efficacement à des empilement pi-pi avec les molécules voisines tandis que des branches doivent générer un fort encombrement stérique afin d'augmenter la solubilité des matériaux, d'empêcher l'empilement colonnaire 1D des molécules et d'ajuster le recouvrement orbitalaire pi.

A partir de ces structures moléculaires modèle, deux arrangements supra-moléculaires pouvant conduire à un transport de charge 3D peuvent être envisagés (Figure 2). Dans

le premier cas, deux premières molécules peuvent s'empiler à partir d'une interaction pi-pi entre l'un de leur bras ("empilement par les bras" ou "arm packing"). Dans la seconde hypothèse, ces deux premières molécules se superposent l'une au-dessus de l'autre ("empilement en colonne entrelacée" ou "intertwined column packing"). Ainsi, deux dimères initiaux sont formés. Lorsque les empilements selon les bras et en colonne sont étendus à grande échelle, les deux modes d'empilement mettent en jeu des empilements face-à-face entre la molécule initiale et six molécules voisines dans différentes directions, de manière à ce que le transport de charge tridimensionnel puisse devenir possible.

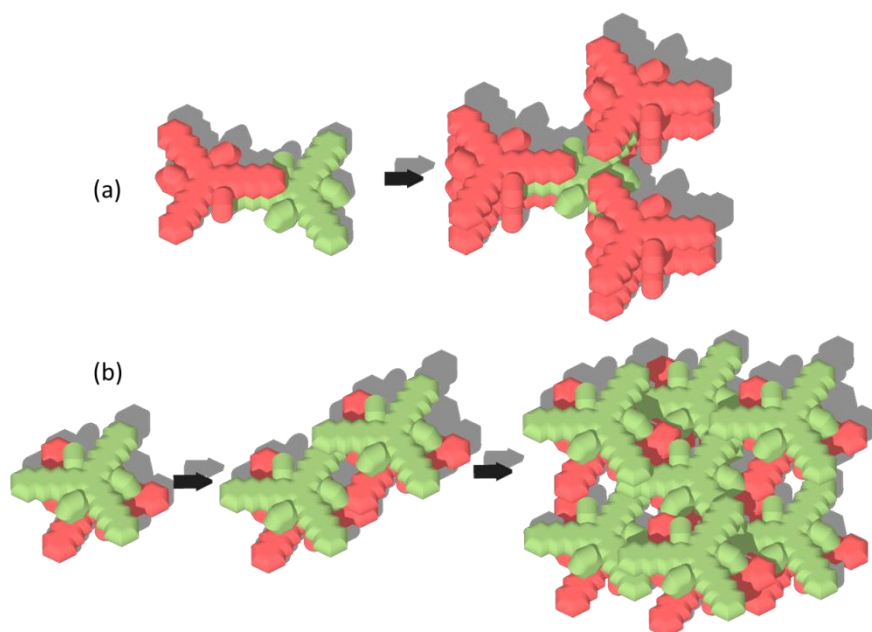


Figure 2. Représentation schématique des deux arrangements supramoléculaires envisagés. Les deux modes d'empilement différents sont générés à partir d'un premier dimère obtenu soit par un empilement pi selon les bras ("empilement par les bras" ou "arm packing") (a) soit par empilement des molécules les unes sur les autres ("empilement en colonne entrelacée" ou "intertwined column packing") (b).

Dans le second chapitre, huit nouvelles molécules en forme d'étoile ont été tout d'abord synthétisées à partir des systèmes pi-conjugués 5,11,17-triazatrinaphthylène (TAN) et 6,14,22-triazatriantrylène (TAA) en suivant les règles de conception préédictées. Parmi ces huit molécules, sept dérivés TAN ont été obtenus par réaction de substitution nucléophile aromatique entre le composé 6,12,18-trichloro-TAN (TAN-3Cl) et l'amine désirée (Méthode A, Figure 3). Du fait de la faible solubilité du TAN-3Cl, une autre voie synthétique a été développée mettant en jeu une réaction de cyclisation ("one pot") lors de la dernière étape (Méthode B) ce qui a permis d'obtenir avec un bon rendement le dérivé TAN-N-Pent. La méthode B qui ne met en jeu que

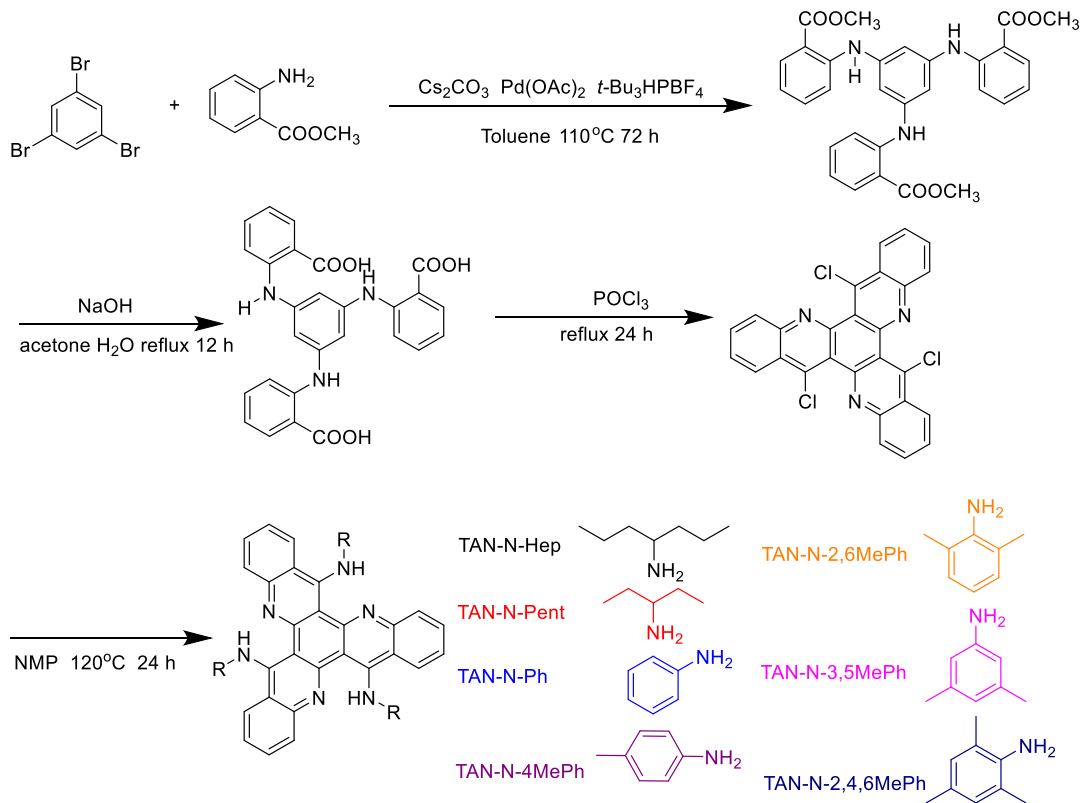


Figure 3. Voie de synth èse utilis ée pour obtenir les d ériv és TANs (M éthode A).

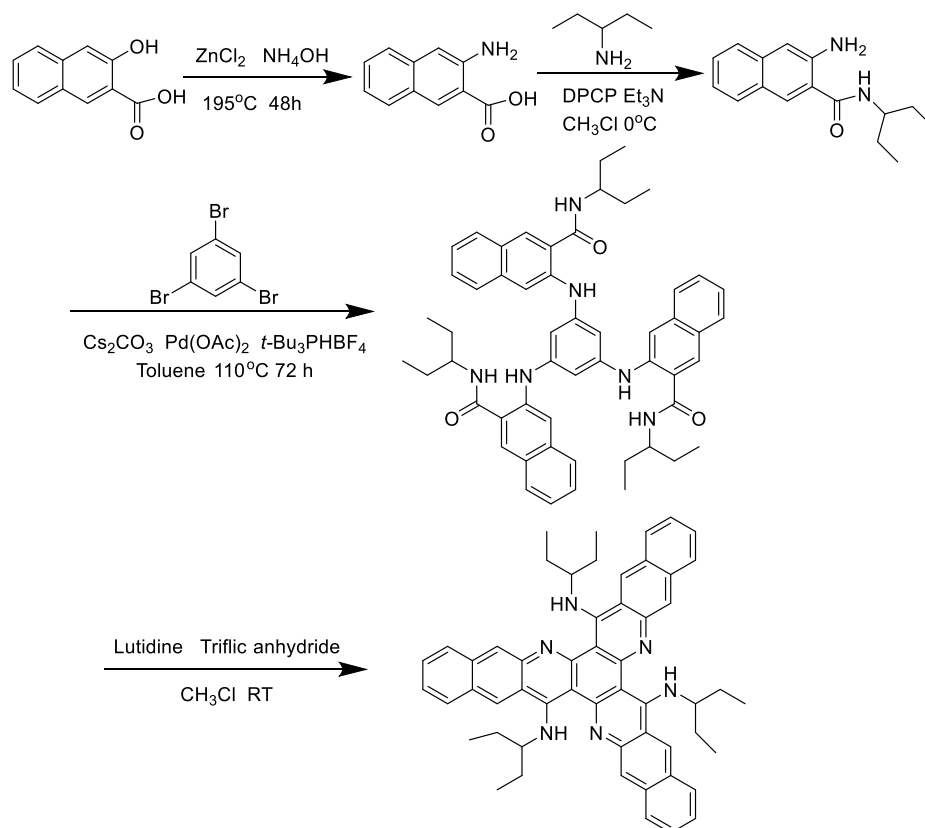


Figure 4. Voie de synth èse mettant en jeu des interm édiaires solubles pour obtenir le TAA-N-Pent (M éthode B).



des intermédiaires solubles durant le processus a permis de concevoir des systèmes aux bras pi-conjugués plus étendus. Ainsi, le dérivé TAA-N-Pent a été aussi synthétisé selon la méthode B (Figure 4).

Pour chaque composé la structure moléculaire a été confirmée par spectroscopie RMN et spectroscopie de masse haute résolution. Ainsi, un seul système de résonances pour les protons et les carbones des unités «bras-branché» a été détecté par spectroscopie de RMN  $^1\text{H}$  et  $^{13}\text{C}$  confirmant la structure de symétrie  $\text{C}_3$  en solution de chaque composé en étoile (Figure 5). Par ailleurs, les propriétés électroniques et l'organisation moléculaire à l'état solide de ces molécules organiques originales ont été déterminées par spectroscopie d'absorption UV-visible, par voltampérométrie cyclique, par diffraction des rayons X sur monocristaux, par calculs théoriques de type DFT et par microscopie optique. Enfin, les propriétés de transport de charge de ces nouveaux matériaux ont été étudiées en transistors à effet de champ organique (OFET) élaborés par voie liquide, et leur capacité à être utilisés comme matériaux transporteurs de trous dans des dispositifs photovoltaïques a été évaluée en cellules solaires à perovskite hybride organique-inorganique (PSCs).

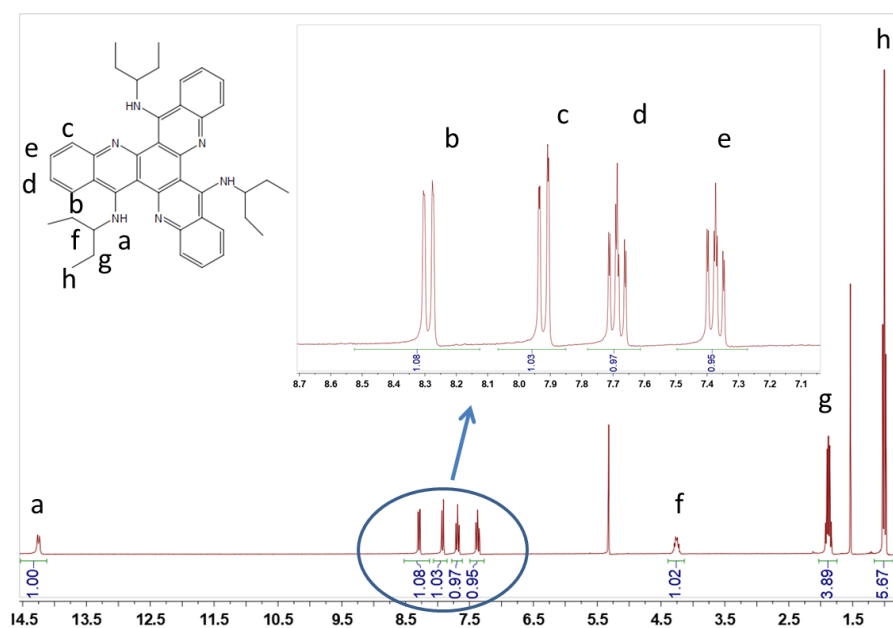


Figure 5. Spectre RMN  $^1\text{H}$  du TAN-N-Pent.

Issus des données de spectroscopie d'absorption UV-visible absorption et de voltampérométrie cyclique (Figure 6), les niveaux HOMO des dérivés TAN (TAN-N-Pent, TAN-N-Ph, TAN-N-2,4,6MePh, TAN-N-4MePh, TAN-N-3,5MePh et TAN-N-2,6MePh) et du composé TAA-N-Pent ont été estimés être compris entre -5.08 et -5.27 eV ce qui se situe dans la gamme attendue pour les matériaux transporteurs de trous conduisant à des transistors à effet de champ organiques

(OFETs) ou à des cellules photovoltaïques organiques (OPVs) stables.

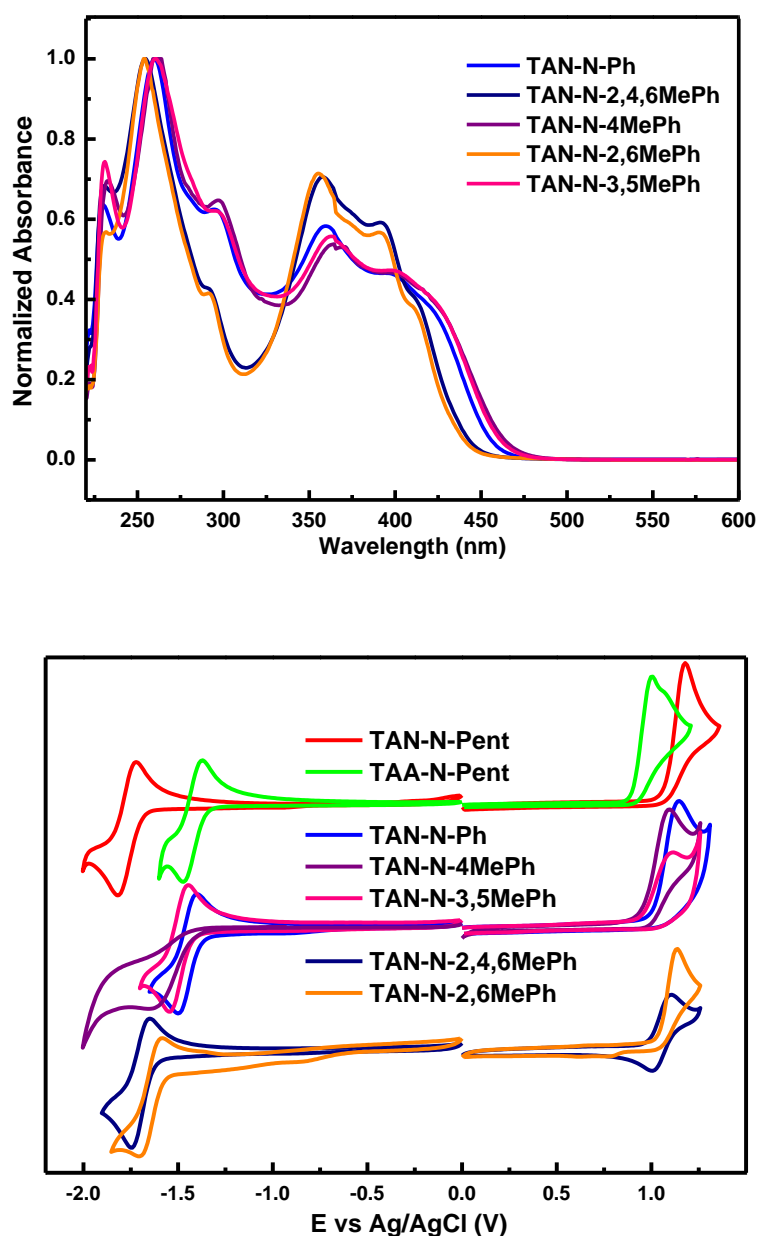


Figure 6. Spectres d'absorption UV-visible dans CH<sub>2</sub>Cl<sub>2</sub> et cyclovoltammogrammes enregistrés dans le THF des dérivés TAN et TAA.

D'autre part, l'empilement moléculaire déduit des structures aux rayons X de ces composés (Figure 7) a révélé qu'un transport de charge de haute dimensionnalité peut être obtenu pour certaines de ces molécules. Pour les molécules substituées par des groupements alkylamine, le composé TAN-N-Pent présente un arrangement 1D cofacial en épî tandis que le dérivé TAA-N-Pent conduit à un arrangement 2D en mur de briques du fait de ses bras plus longs. Pour les molécules substituées par des groupements arylamine, les molécules TAN-N-Ph, TAN-N-4MePh et

TAN-N-2,6MePh présentent une distribution de la densité électronique des orbitales frontières répartie sur les bras et les branches. De plus, d'abondantes interactions de type branche-bras et branche-branche ont été observées en phase cristalline. Ainsi, ces composés sont prometteurs pour donner un transport de charge de haute dimensionnalité. Seule la molécule TAN-N-3,5MePh présente un motif d'empilement où les molécules sont décalées avec de longues distances entre les molécules voisines et peu d'interactions. De façon plus intéressante, le dérivé TAN-N-2,4,6MePh a conduit à un empilement original couche par couche bidimensionnel.

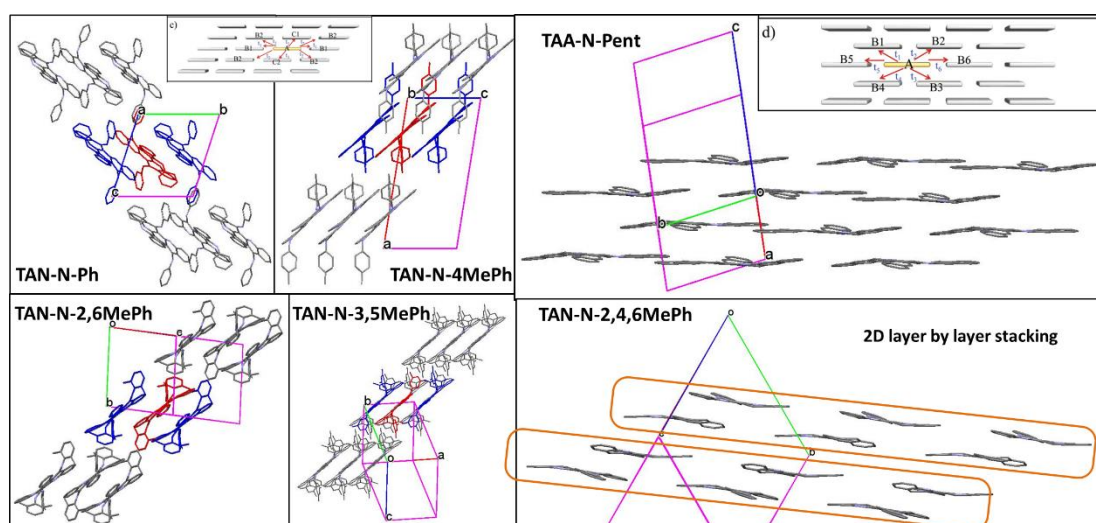


Figure 7. Empilement moléculaire des dérivés TAA-N-Pent, TAN-N-Ph, TAN-N-2,4,6MePh, TAN-N-4MePh, TAN-N-2,6MePh et TAN-N-3,5MePh.

Des transistors à effet de champ organiques de type p et d'architecture "Bottom-gate/ top-contact" ont été fabriqués à partir de films minces de TAN-N-Pent and TAA-N-Pent élaborés par enduction centrifuge. Les dispositifs fabriqués à température ambiante n'ont conduit à aucun effet de champ. Puis un recuit thermique a été introduit après le dépôt par enduction centrifuge de la couche active et le composé TAA-N-Pent a montré une cristallisation visible après 20 min de recuit à 140 °C. Les dispositifs mettant en jeu ces films minces cristallisés ont conduit à une mobilité de trous de  $1.2 \times 10^{-4} \text{ cm}^2 \text{ V}^{-1} \text{ s}^{-1}$  (Figure 8). Bien que les mobilités obtenues avec ces dispositifs n'atteignent par l'état de l'art, ce résultat met clairement en évidence que la morphologie du film affecte fortement les performances des dispositifs.

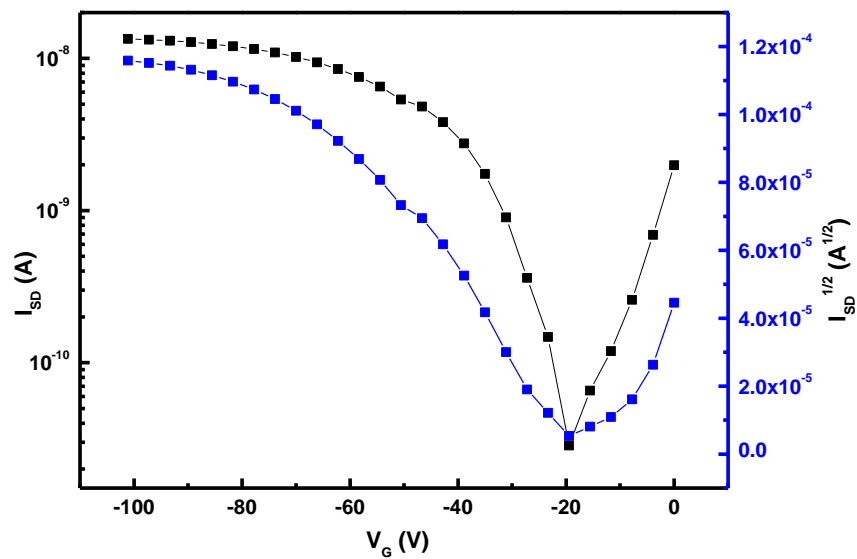


Figure 8. Courbe de transfert d'OFETs mettant en jeu un film mince de TAA-N-Pent élaboré par enduction centrifuge puis recuit à 140 °C.

Par ailleurs, cinq dérivés dotés de substituants arylamine, les composés TAN-N-Ph, TAN-N-2,4,6MePh, TAN-N-4MePh, TAN-N-2,6MePh et TAN-N-3,5MePh qui présentent un niveau d'énergie de la HOMO proche de celui du spiro-OMeTAD ont été employés comme matériau transporteur de trous (HTM) dans des cellules solaires hybrides mésoscopiques à perovskite de type  $\text{TiO}_2/(\text{FAPbI}_3)_{0.85}(\text{MAPbBr}_3)_{0.15}$  (Table 1). Quel que soit le dérivé considéré un effet photovoltaïque a été observé avec des efficacités de conversion énergétique (PCEs) comprises entre 6 to 10%. Les meilleures performances ont été obtenues en employant le composé TAN-N-2,6MePh comme transporteur de trous ce qui a conduit à des PCEs atteignant 10,4% avec une densité de courant de court-circuit ( $J_{sc}$ ) de  $18,58 \text{ mA cm}^{-2}$ , une phototension en circuit ouvert ( $V_{oc}$ ) de 0,92 V et un facteur de forme (FF) de 0,61. Même si le nombre de composé est restreint et les relations entre structures et performances difficiles à établir, les meilleures performances sont obtenues lorsque les positions 3, 4 et 5 des phényles sont non-substitués.

Table 1. Paramètres photovoltaïques des cellules solaires à perovskite hybride mettant en jeu TAN-N-Ph, TAN-N-2,4,6MePh, TAN-N-4MePh, TAN-N-2,6MePh ou TAN-N-3,5MePh comme conducteurs de trous.

<b>Material</b>	<b>J<sub>sc</sub> (mA/cm<sup>2</sup>)</b>	<b>V<sub>oc</sub> (V)</b>	<b>FF</b>	<b>PCE (%)</b>
<b>TAN-N-Ph</b>	16,1	0,89	0,61	8,8
<b>TAN-N-2,4,6MePh</b>	12,5	0,89	0,53	5,9
<b>TAN-N-4MePh</b>	11,3	0,89	0,64	6,4
<b>TAN-N-2,6MePh</b>	18,6	0,92	0,61	10,4
<b>TAN-N-3,5MePh</b>	12,3	0,92	0,55	6,3
<b>Spiro-OMeTAD</b>	22,1	1,07	0,75	17,7

En outre, de nouvelles molécules fluorescentes ont été préparées en utilisant comme réactif certaines des molécules précédentes pour former des dérivés organoborés (Figure 9). Ainsi, les dérivés TAN-N-Pent et TAA-N-Pent ont réagi avec le trifluorure diéthylétherate de bore pour conduire à deux molécules (TAN-Pent-BF<sub>2</sub> et TAA-Pent-BF<sub>2</sub>) avec trois nouveaux cycles fusionnés incluant les atomes de bore comme dans le cas des dérivés de type BODIPY. Des bandes d'émission dans le visible ont été observées dans les régions du bleu et du vert pour TAN-Pent-BF<sub>2</sub> et TAA-Pent-BF<sub>2</sub>, respectivement, avec de grands décalages de Stokes (100 nm pour TAN-Pent-BF<sub>2</sub> et 142 nm pour TAA-Pent-BF<sub>2</sub>). Par conséquent, deux applications potentielles prometteuses peuvent être proposées pour ces composés. Tout d'abord, comme ils présentent de grands décalages de Stokes shifts, ils peuvent être utilisés pour des applications en luminescence comme les dérivés de type BODIPY. D'autre part, du fait de l'introduction d'unités BF<sub>2</sub>, les niveaux d'énergie LUMO sont plus faibles (environ -3.2 eV) ce qui confère potentiellement à ces composés des propriétés de semiconducteurs de type n.

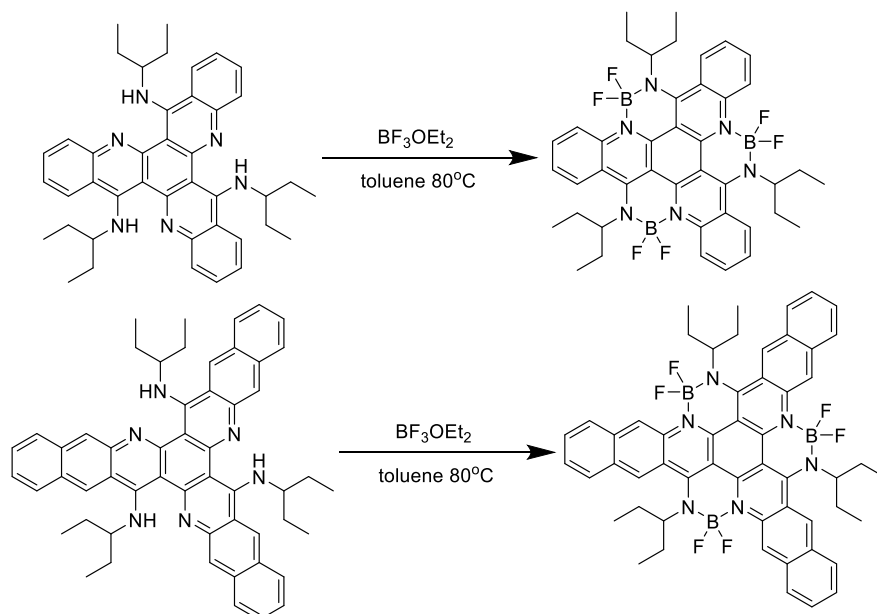


Figure 9. Voie de synthèse des composés TAN-Pent-BF<sub>2</sub> et TAA-Pent-BF<sub>2</sub>.

Une autre molécule intéressante a été introduite dans le chapitre de ce travail. Il s'agit du 6,12,18-trihydroxy-5,11,17-triazatrinaphthylène (TAN-3OH). Dans la littérature scientifique, ce composé a été intégré avec succès dans des OLEDs. Il possède la particularité de conduire à l'état solide à une fluorescence retardée activée thermiquement (TADF) ainsi qu'à un phénomène de transfert de protons à l'état excité (ESIPT) (Figure 10). La faible solubilité de TAN-3OH empêche sa mise en forme directe en solution. En revanche, la décomposition d'un dérivé TAN substitué par une amine secondaire permet d'obtenir des films minces de TAN-3OH par voie liquide ce qui ouvre de nouvelles voies vers l'élaboration de diodes électroluminescentes organiques (OLEDs) par voie liquide.

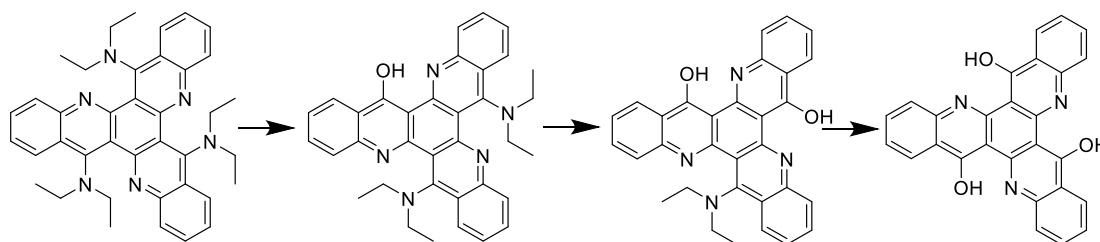


Figure 10. Processus de décomposition du dérivé TAN-N-2Et.

A partir des résultats décrits dans le second chapitre, les atomes d'azote sur les branches ont été éliminés et une série de triazastarphènes substitués directement par des carbones C<sub>sp2</sub> ou C<sub>sp</sub> ont été conçus puis synthétisés comme matériaux de type n dans le troisième chapitre. Une voie de synthèse originale et efficace a été développée pour former les unités acridine des molécules cible de type TAN (TAN-Ph et TAN-MePh) et TAA (TAA-Ph, TAA-OMePh, TAA-tBuPh et TAA-CF<sub>3</sub>Ph) (Figure 11).

Ces travaux constituent le premier exemple d'une synthèse directe de dérivés acridine de symétrie  $C_{3h}$  et permettent l'élaboration de systèmes pi plus étendus.

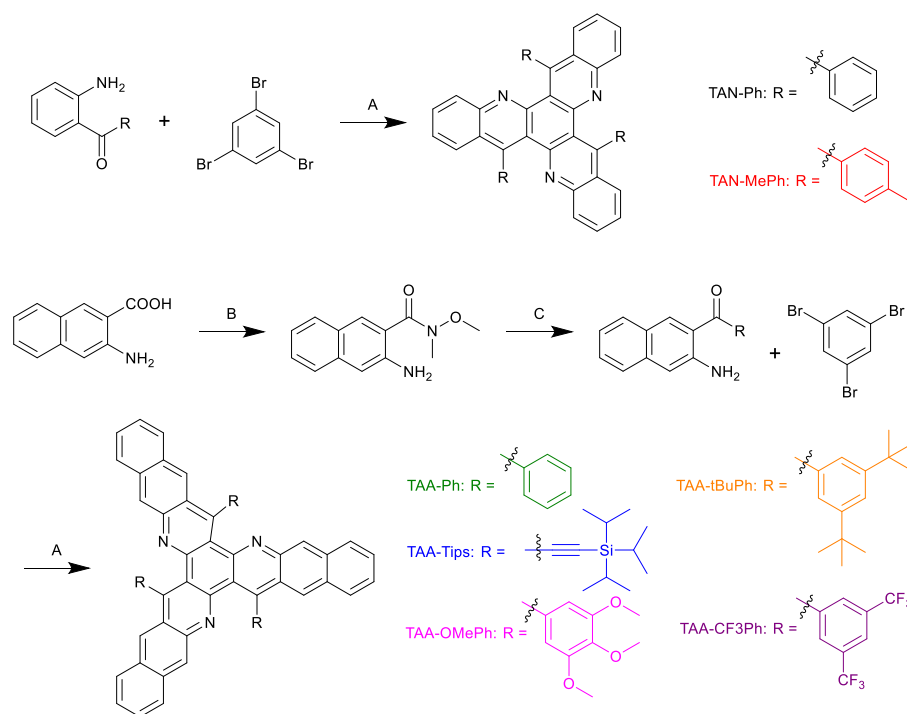


Figure 11. Voie de synthèse des dérivés TAN et TAA. A:  $Pd_2(dba)_3$ , Brettphos,  $K_2CO_3$ , *t*-BuOH,  $100^\circ C$ , 24 h. B: MeNHOMe•HCl, DPCP,  $Et_3N$ , DCM,  $0^\circ C$ ., une nuit. C: Br-R / H-R, *n*-BuLi, THF,  $-78^\circ C$ . / PhMgCl, THF,  $0^\circ C$ .

Leurs propriétés moléculaires ont été étudiées soigneusement par voltampérométrie cyclique, spectroscopie d'absorption UV-visible, par calculs théoriques de type DFT et par diffraction des rayons X sur monocristaux. Les données de voltampérométrie cyclique et de spectroscopie d'absorption UV-visible (Figure 12) sont en accord avec les calculs de type DFT et prouvent que ces matériaux sont stables dans les conditions ambiantes et possèdent des niveaux d'énergie HOMO et LUMO adéquats pour fonctionner dans des dispositifs à base de semi-conducteurs organiques. En particulier, l'étape de réduction mise en évidence par voltampérométrie cyclique est réversible ce qui constitue un gage de stabilité du canal conducteur en transistor dans un environnement protégé.

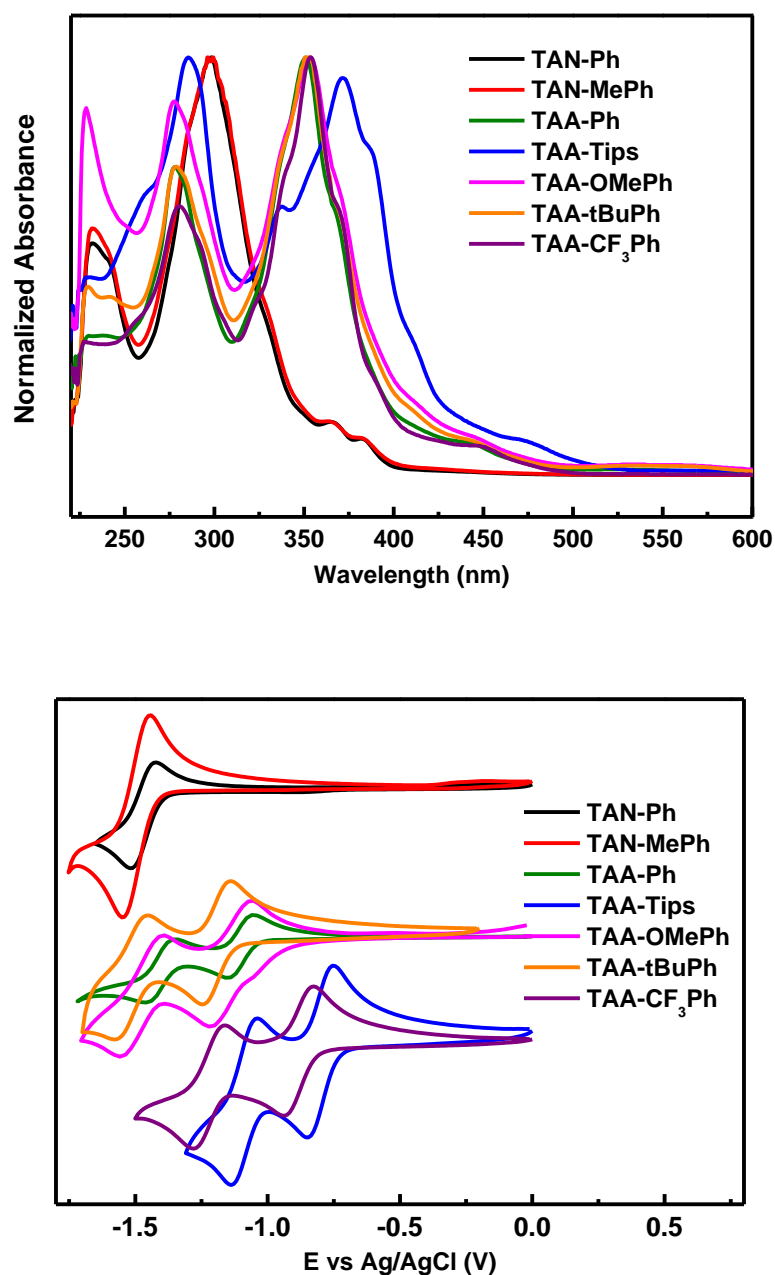


Figure 12. Spectres d'absorption UV-visible dans  $\text{CH}_2\text{Cl}_2$  et cyclovoltammogrammes enregistrés dans le THF des composés TAN et TAA substitués par des carbones  $\text{C}_{\text{sp}2}$  ou  $\text{C}_{\text{sp}}$ .

Les structures cristallines aux rayons X de ces composés (Figure 13) indiquent que les dérivés TAN-Ph et TAN-MePh présentent un empilement moléculaire où les molécules sont toutes décalées du fait de leurs bras relativement courts où le meilleur chemin pour le transport de charge déduit de calculs théoriques ne correspondant à la direction d'empilement. En revanche, les molécules TAA-Tips et TAA-tBuPh ont conduit à un empilement en épi sans chemin efficace pour le transport de charge du fait de l'important encombrement stérique induit par les branches.



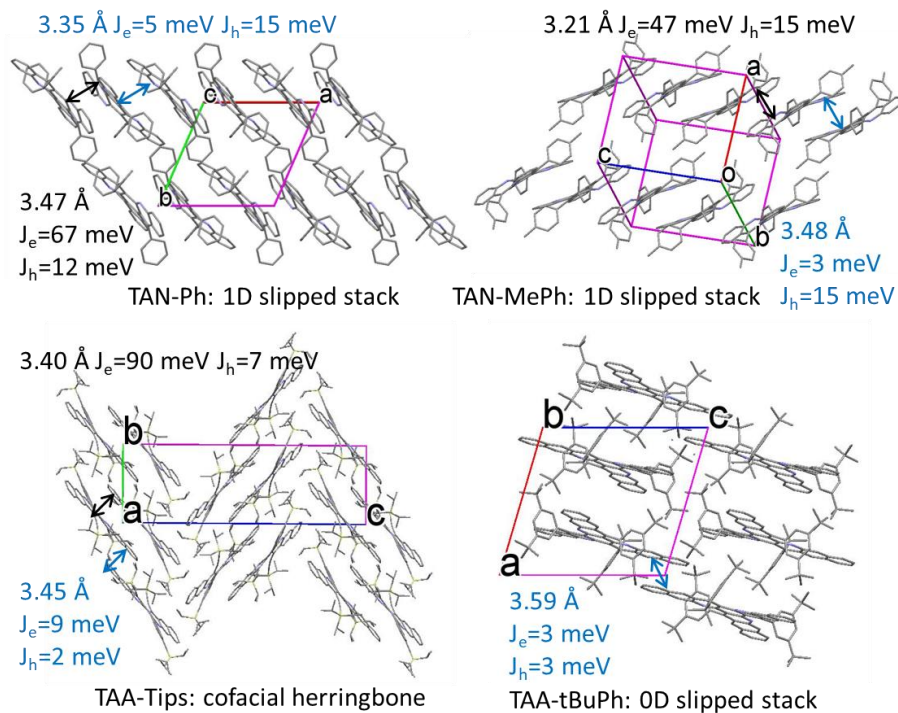


Figure 13. Empilement moléculaire déduit des structures cristallines des composés TAN-Ph, TAN-MePh, TAA-Tips et TAA-tBuPh. Par souci de clarté, les atomes d'hydrogène ont été omis.

Contrairement aux quatre molécules précédentes, les composés TAA-Ph et TAA-OMePh présentent un empilement en colonne entrelacée (“intertwined column packing”) et un empilement via les bras (half “arm packing”) respectivement comme postulé lorsque les molécules ont été conçues. Par ailleurs, nous avons déduit des données issues des structures aux rayons X sur monocristaux que le composé TAA-OMePh pouvait induire un transport de charge 2D tandis que le dérivé TAA-Ph avait le potentiel pour réaliser un transport de charge 3D en phase cristalline. Les intégrales de transfert dans des dimères de la structure cristalline sont en accord avec la dimensionnalité supposée du transport de charge. Cependant des OFETs élaborés à partir de monocristaux ou de films minces élaborés par la méthode de « trempage-retrait » de TAA-Ph n’ont conduit à aucun effet de champ mesurable. En dépit de cet échec, la nouvelle méthode de synthèse développée et l’obtention de deux arrangements moléculaires intéressants à l’état solide pour le transport multidimensionnel pourrait contribuer au développement de matériaux semi-conducteurs organiques performants.

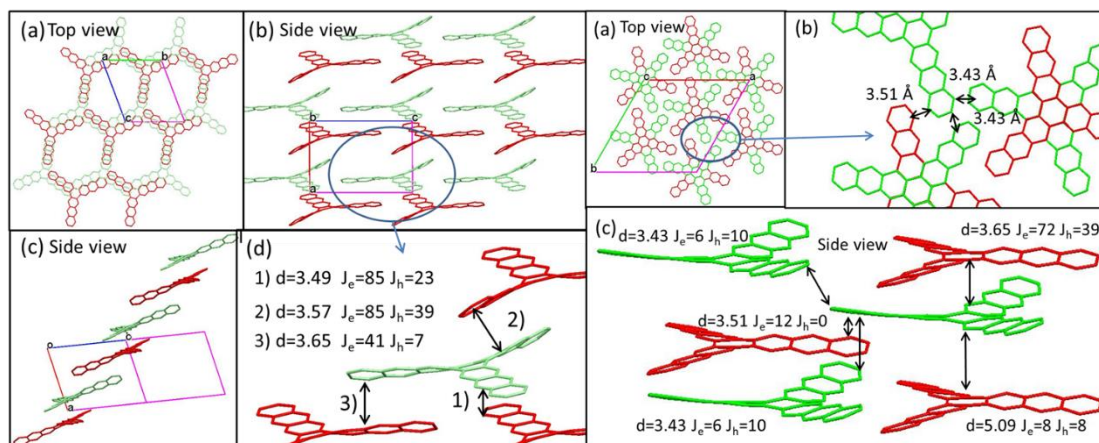
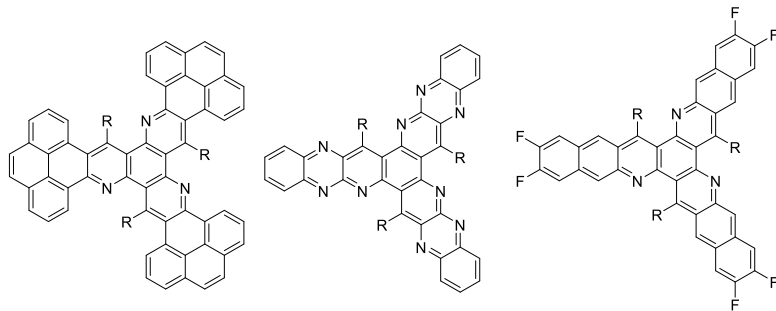


Figure 14. Empilement moléculaire de TAA-OMePh et TAA-Ph. Par souci de claret, les atomes d'hydrogène et les branches latérales ont été omis.

Bien que les matériaux décrits dans cette thèse n'ont pas fourni de performances intéressantes dans les dispositifs que nous avons fabriqués, il y a d'autres méthodes disponibles pour caractériser leurs propriétés de transport de charge. Par exemple, les mobilités peuvent être déterminées par des mesures de temps de vol (TOF) ou par "dark injection space charge limited current" (SCLC). De plus les chromophores de type BODIPY développés dans cette étude devront être étudiés plus en détails avec la synthèse de nouveaux exemples et une caractérisation plus approfondie de leurs propriétés (rendement quantique de fluorescence, durée de vie de l'état excité etc...). Des diodes électroluminescentes (OLEDs) de type TADF mettant en jeu des films minces de TAN-3OH élaborés par voie liquide devront être aussi fabriqués. Certains des matériaux avec une énergie de la LUMO d'environ -3.2 eV pourront être testés comme matériau accepteur non-fullerène en cellules solaires organiques (OPVs). En ce qui concerne les calculs théoriques, les énergies d'association pour chaque dimère et les interactions spécifiques dans les dimères devraient permettre de définir des règles de conception de molécules efficaces pour l'électronique organique ainsi que des simulations de type Monte-Carlo.

Du point de vue de la chimie, quelques suggestions peuvent être proposées pour optimiser ces molécules et concevoir de nouveaux dérivés. Tout d'abord, des molécules avec des bras conjugués plus longs sont nécessaires pour garantir un recouvrement efficace entre molécules voisines. Augmenter la longueur des bras de la molécule pourrait conduire à des problèmes de solubilité et de stabilité des molécules cible, par conséquent l'augmentation du système pi-conjugué des bras non seulement en longueur mais aussi en largeur constitue une meilleure option. D'autre part des molécules de niveau d'énergie LUMO plus faible sont requises pour favoriser l'injection d'électrons dans les OFETs ou pour être employées comme matériaux accepteur non-fullerène en cellules solaires organiques. L'introduction d'hétéroatomes,

la substitution avec des groupements fortement électroaccepteurs ou l'extension des bras constituent trois stratégies pour diminuer le niveau d'énergie de la LUMO de la molécule. Quelques exemples de structures moléculaires cible possibles sont donnés ci-dessous.



## TABLE of CONTENTS

<b>Chapter 1:</b> .....	<b>1</b>
<b>Generalities about Organic Semiconductors</b> .....	<b>1</b>
<b>1.1 Organic Semiconductors</b> .....	<b>3</b>
1.1.1 Semiconductors .....	3
1.1.2 Development of Organic Semiconductors .....	4
1.1.3 Advantages of Small Molecule Organic Semiconductors .....	5
1.1.4 Organic Electronic Devices .....	5
1.1.4.1 Organic Field Effect Transistors .....	5
1.1.4.2 Organic Photovoltaic Cells .....	8
1.1.4.3 Organic Light-Emitting Diodes .....	10
<b>1.2 Mechanism of Charge Transport in OSCs</b> .....	<b>11</b>
1.2.1 $\pi$ Conjugation .....	11
1.2.2 Molecular Packing and Charge Transport .....	13
<b>1.3 High Performance Materials</b> .....	<b>16</b>
1.3.1 P-type, N-type and Ambipolar Transistors .....	16
1.3.2 P-type Materials .....	17
1.3.2.1 Acenes and Their Derivatives. ....	17
1.3.2.2 Heteroacenes and Their Derivatives .....	22
1.3.2.3 TTF and Phthalocyanine Derivatives .....	25
1.3.3 N-type and Ambipolar Materials .....	27
<b>1.4 Two-dimensional and Three-dimensional Conjugated Molecules</b> .....	<b>34</b>
1.4.1 Dimensionality Concept for Molecular Structure and Charge Transport in OFETs ....	34
1.4.2 Two-dimensional Conjugated Molecules .....	36
1.4.3 Three-dimensional Conjugated Molecules .....	37
<b>1.5 Molecular Design for 3D Charge Transport</b> .....	<b>40</b>
<b>1.6 Conclusion</b> .....	<b>42</b>
1.6.1 Molecular Structure .....	43
1.6.2 Molecular Packing .....	43
1.6.3 Energy Levels .....	44
1.6.4 Other Factors .....	44
<b>1.7 Objectives of This Research</b> .....	<b>45</b>
<b>Chapter 2:</b> .....	<b>47</b>
<b>Triazastarphene Substituted by NH as Hole Transport Materials ...</b>	<b>47</b>
<b>2.1 Introduction</b> .....	<b>49</b>

2.2 Synthesis .....	52
2.3 Optical and Electrochemical Properties .....	56
2.4 Theoretical Calculation .....	60
2.5 Single Crystal XRD Result .....	63
2.6 Characterization of Charge Transport .....	72
2.6.1 Spin-coating OFETs .....	72
2.6.2 HTMs in Perovskite Solar Cells .....	74
2.7 BF <sub>2</sub> -rigidified Dyes .....	76
2.8 Trihydroxy-triazatrinaphthylene .....	81
2.9 Conclusion .....	83
<b>Chapter 3: .....</b>	<b>85</b>
<b>Triazastarphene Substituted by C<sub>sp2</sub> and C<sub>sp</sub> as Electron Transport</b>	
<b>Materials .....</b>	<b>85</b>
3.1 Introduction .....	87
3.1.1 Design .....	87
3.1.2 Retrosynthesis .....	87
3.2 Synthesis .....	91
3.3 Optical and Electrochemical Properties .....	93
3.4 Theoretical Calculation .....	96
3.4.1 Optimized Geometries and Electron Density Distributions .....	96
3.4.2 Energy Diagrams .....	99
3.4.3 Electronic Absorption Transitions .....	101
3.5 Single Crystal XRD Result .....	102
3.6 Simulated charge transport properties .....	107
3.7 Thermal Properties .....	114
3.8 OFET Devices .....	116
3.8.1 Thin Film OFETs .....	116
3.8.2 Single Crystal OFETs .....	120
3.9 Conclusion .....	122
<b>Conclusion .....</b>	<b>125</b>
<b>Experiment Part .....</b>	<b>133</b>
1. Materials and Methods .....	135
2. Synthesis .....	136
2.1 Synthesis of Triazastarphene Substituted by NH .....	136
2.2 Synthesis of Triazastarphene Substituted by C <sub>sp2</sub> and C <sub>sp</sub> .....	151
3. Device Fabrication .....	160
3.1 Thin film OFETs Fabricated by Spin-Coating with Triazastarphene Substituted by NH	

(Chapter 2).....	160
<b>3.2 Perovskite Solar Cells (PSCs) with Triazastarphene Substituted by NH as Hole Transport Material (Chapter 2) .....</b>	<b>160</b>
<b>3.3 Thin Film OFETs Prepared by Dip-coating with Triazastarphene Substituted by C<sub>sp2</sub> and C<sub>sp</sub> (Chapter 3).....</b>	<b>161</b>
<b>3.4 Single Crystal OFETs with Triazastarphene Substituted by C<sub>sp2</sub> and C<sub>sp</sub> (Chapter 3) ..</b>	<b>161</b>
<b>4. Crystallographic Data .....</b>	<b>162</b>
<b>References .....</b>	<b>167</b>



**Chapter 1:**  
**Generalities about Organic Semiconductors**





## 1.1 Organic Semiconductors

### 1.1.1 Semiconductors

According to their intrinsic conductivity, all the solid materials can be classified as conductors, semiconductors and insulators (Figure 1-1). Conductors are substances with very high conductivity, usually denoted as  $\sigma$ , between  $10^4 \text{ S.cm}^{-1}$  to  $10^8 \text{ S.cm}^{-1}$  (physical dimension equivalent to  $\text{A.V}^{-1}.\text{m}^{-1}$ ). For example, metals and solvated salts are conductors due to abundant free electrons and free ions respectively. Insulators are substances having no free charge carriers and conductivity lower than  $10^{-8} \text{ S.cm}^{-1}$ . Semiconductors are materials with conductivity in between. In the solid state, these materials are commonly described by their electronic structures (energy and spatial distribution). In detail, insulators have large energy gap between valence and conduction bands, which can be defined as energy states filled by electrons and vacant energy states, respectively (Figure 1-1). In conductors, no more distinction can be found between the two bands. When the gap is small like for semiconductors, an external energy, for instance heat or light, can be easily absorbed by the materials which leads to an addition of electrons in the conduction band (electron charge carriers transport) or to a withdrawing of electrons in the valence band (hole charge carriers transport). Thus, charge carriers become mobile and free. The specific property of semiconductors that make them important materials in the industry of electronic devices is their conductivity which can be controlled by playing with different parameters such as temperature, light, magnetic field, purity or electric field.<sup>[1]</sup>

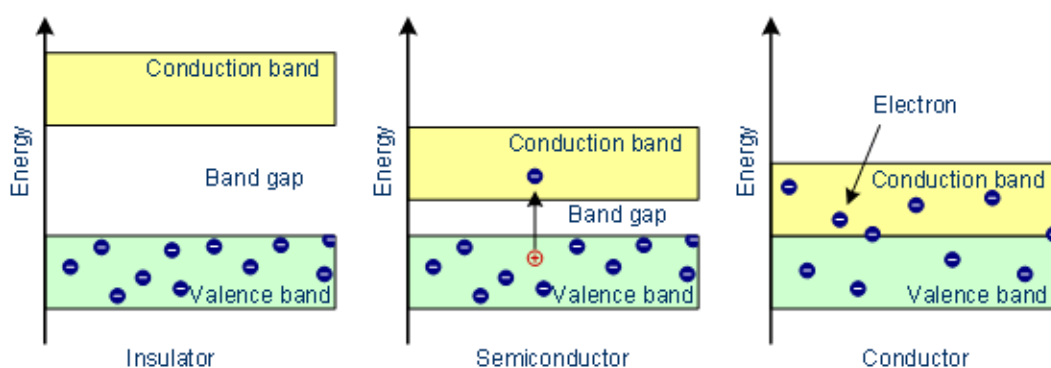


Figure 1-1. The band model of insulators, semiconductors and conductors.<sup>[1]</sup>

From an historical point of view, the semiconductor effect was firstly evidenced by Michael Faraday in 1833, and, few years later, the photovoltaic effect was reported by Alexandre Edmond Becquerel in 1839. The development of semiconductors was quite slow, until solid-state-physics was capable to provide appropriate theoretical

explanation at the beginning of the 20th century. The discovery of Hall effect in 1878 and of electrons in 1897 prompted the establishment of band theory for semiconductor conduction in 1931. The invention of the junction transistor in 1948 by Shockley marked the takeoff of semiconductor industry. Since the invention of transistor radio up to the development of smartphone, semiconductors can be found in every corner of our life (Figure 1-2). So far, most of them are inorganic materials as silicon and metal oxides, but the development of organic semiconductors has attracted more and more attentions.

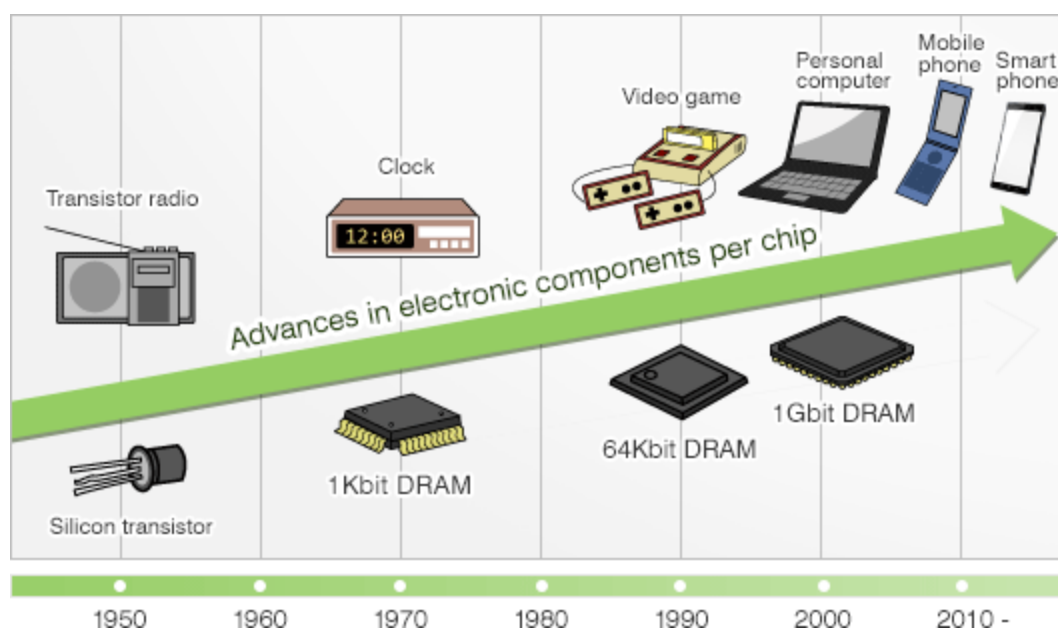


Figure 1-2. Applications of semiconductors in daily life.<sup>[2]</sup>

## 1.1.2 Development of Organic Semiconductors

Organic semiconductors (OSCs) are hydrocarbon-based  $\pi$ -conjugated small molecules or polymers, in which  $\pi$  orbitals delocalize within the molecule and overlap between adjacent molecules to help charge carrier transport. The work of Kallmann and Pope in 1960 proved that organic crystals can act as semiconductors after charge injection.<sup>[3,4]</sup> Alan Heeger, Alan MacDiarmid and Hideki Shirakawa reported in 1977 that the conductivity of iodine-doped polyacetylene can be as high as  $38 \text{ S}\cdot\text{cm}^{-1}$ ,<sup>[5]</sup> which allowed them to be awarded the 2000 Nobel Prize in Chemistry for "The discovery and development of conductive polymers". By now, OSCs are increasingly integrated in electronic devices to replace traditional inorganic materials or fulfill new needs.

### 1.1.3 Advantages of Small Molecule Organic Semiconductors

Compared with inorganic semiconductors, OSCs are lighter and more flexible. Their structures are very versatile and can be designed to possess specific physical, chemical and mechanical properties. OSCs can be categorized in two major classes: small molecules (molecular weight lower than 10000) and polymers (molecular weight higher than 10000). Both types of materials have pros and cons. Polymers decorated with aliphatic side chains show good processability by cheap and well-known printing techniques. By contrast, small molecules are easier to purify and can lead to highly ordered molecular packing. Meanwhile, dense and ordered molecular packing could provide high charge carrier mobility defined as  $\mu = \sigma / Ne$  where  $\sigma$  is the conductivity,  $N$  is the concentration of charge and  $e$  is the elementary charge. For example, in organic field effect transistors the highest hole mobility given by small molecules is in the range of 1–40  $\text{cm}^2 \text{V}^{-1} \text{s}^{-1}$ ,<sup>[6,7]</sup> whereas the best performance given by polymer materials is at least an order of magnitude lower.<sup>[8]</sup> Therefore, this thesis will mainly discuss about small molecule OSCs.

### 1.1.4 Organic Electronic Devices

Over the past decades, OSCs have found widespread applications in large-area displays, solid-state lighting, radio frequency identification tags, and organic solar cells. The most attractive feature about OSCs is their high solubility in organic solvents which makes possible the fabrication of fully flexible devices with low-cost solution-processable thin films. The three main electronic devices made from OSCs are organic field effect transistors (OFETs), organic light emitting diodes (OLEDs) and organic photovoltaic devices (OPVs). Each kind of device has specific requirements on the optical and electrical properties of the OSCs. Generally speaking, OSCs with high charge-carrier mobility are preferable for OFETs; OLEDs require materials with high luminescence efficiency; OPVs need materials with small bandgap and a high absorption coefficient. Furthermore, all devices require adapted HOMO and LUMO energy levels of the OSCs with respect to the work function of electrode materials and frontier orbital energy levels of other neighboring OSCs layers. Finally, it must be underlined that in order to achieve good performance, high charge-carrier mobility is favorable for every kind of device.

#### 1.1.4.1 Organic Field Effect Transistors

OFETs are conventionally used to evaluate the mobility of OSCs. Furthermore they could work as switch units in integrated circuits due to the large difference in current

between their ON and OFF states. In 1986, the first organic solid-state field-effect transistor was fabricated utilizing a thin film of polythiophene with a reported mobility of about  $10^{-5} \text{ cm}^2 \text{ V}^{-1} \text{ s}^{-1}$ .<sup>[9]</sup> After 30 years, with the development of molecular design strategy, and the optimization of both purification technology and device fabrication process, the state-of-the-art mobility value is  $40 \text{ cm}^2 \text{ V}^{-1} \text{ s}^{-1}$  for hole<sup>[7]</sup> and is  $27.8 \text{ cm}^2 \text{ V}^{-1} \text{ s}^{-1}$  for electron.<sup>[10]</sup>

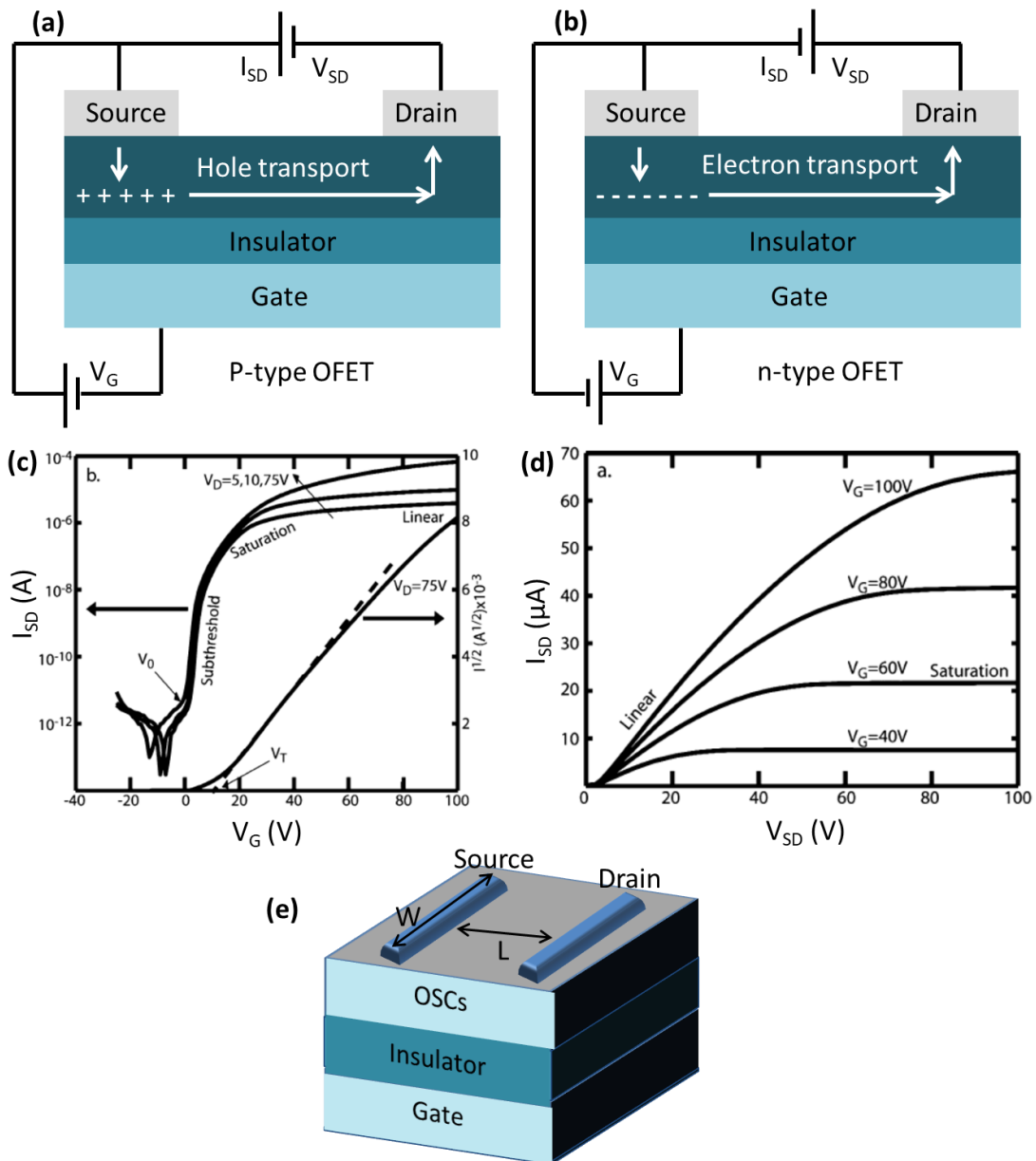


Figure 1-3. P-type (a) and n-type (b) bottom-gate top-contact device architectures, output ( $I_{SD}$ - $V_{SD}$ ) (c) and transfer ( $I_{SD}$ - $V_G$ ) (d) curves of OFETs.<sup>[11]</sup> (e) Schematic representation of the device geometry with the channel width ( $W$ ) and the channel length ( $L$ ).

OFETs are three-terminal devices that consist of source, drain, and gate electrodes.

The working principle of widely used top-contact bottom-gate OFETs is illustrated in Figure 1-3 and can be summarized as follows. The source-drain channel conductivity of OFET is modulated by electrical fields generated by the gate electrode. As shown in Figure 1-3 (a), when a small negative gate to source voltage ( $V_G$ ) is applied in p-type OFETs, holes start to accumulate in the organic semiconductor layer. As this voltage gets more negative, holes start to transport from source to drain increasing dramatically the current (measured by drain to source current ( $I_{SD}$ )) in the organic semiconductor layer. Small change in  $V_G$  causes great difference in  $I_{SD}$  making transistor an amplifier in modern day electronics. Similar to the p-type OFETs, charge carrier transport in n-type OFETs is shown in Figure 1-3 (b).

The performances of OFET devices are generally characterized through two distinct curves, the output ( $I_{SD}$ - $V_{SD}$ ) and transfer ( $I_{SD}$ - $V_G$ ) curves. Both of these curves display a linear and saturation regime that corresponds to different charge carrier concentrations and distributions in the channel of the OFET device (Figure 1-3 (c) and (d)). For an OFET device, the charge mobility ( $\mu$ ) is generally calculated in the saturation regime.<sup>[12]</sup> The OFET saturation current ( $I_{D,sat}$ ) is expressed as:<sup>[13]</sup>

$$I_{D,sat} = \frac{WC_i\mu}{2L}(V_G - V_T)^2 \quad (1)$$

where  $W$  is the channel width,  $L$  is the channel length (Figure 1-3 (e)),  $C_i$  is the dielectric surface capacitance,  $V_G$  and  $V_T$  are the gate voltage, and threshold voltage, respectively.

Equation (1) indicates that the square root of the current is linear with the applied  $V_G$ . The slope of the  $I^{1/2}$  line can be used to calculate the mobility of the semiconductor according to equation (2):<sup>[14]</sup>

$$\mu = \frac{2L}{WC_i} \left( \frac{\partial \sqrt{I_{D,sat}}}{\partial V_G} \right) \quad (2)$$

Another important parameter extracted from OFETs is the on/off current ratio ( $I_{on}/I_{off}$ ). The  $I_{on}/I_{off}$  ratio is the value of the ON current to the OFF current, and is reported in terms of  $10^x$ . In general, it is important to minimize  $I_{OFF}$  through decreasing impurity amounts and leaks, while maximizing  $I_{ON}$  through increasing the mobility of the semiconductor layer.

In thin film OFETs (TFTs), small molecular OSCs are generally thermally evaporated to form a polycrystalline active layer. But during the fabrication procedure, many details affect the performance of thin-film devices, such as surface treatment, temperature, material purity, device structure, and testing and deposition vacuum conditions.<sup>[15]</sup> To minimize the effects of grain boundaries, single-crystal OFETs (SCFETs) are fabricated using single crystals of OSCs. Performances from SCFETs are normally better than TFTs when crystals with sufficiently high quality are applied. However, efficiencies of SCFETs are limited by the anisotropy electrical properties of

organic single crystals.<sup>[16]</sup> Furthermore, conduction of charge carriers through OFET is dependent on the charge carriers at the interface between the organic semiconductor layer and the dielectric layer. As shown in Figure 1-3 (a) and (b), in order to increase the mobility of semiconductor layer, efficient charge carrier transport in both perpendicular and horizontal directions can be necessary depending on device architectures and process technics.<sup>[17]</sup>

### 1.1.4.2 Organic Photovoltaic Cells

Solar cells are devices that can produce electricity by photovoltaic effect. Interestingly, they are able to transform sunlight, which is the most abundant source of energy on earth directly into electrical energy. Basically, most of solar cells are based on p-n semiconductor junctions or heterojunctions in contact with two different electrodes. Light absorption by one of the material constituting the junction leads to the creation of an electron-hole pair which is dissociated at the p-n interface, the resulting electron and hole then migrate towards the positive and negative electrodes, respectively, before being collected by an external circuit. Three basic tasks required for solar cell operation are light harvesting, charge generation and charge transport. Since 1950s,<sup>[18]</sup> traditional silicon-based solar cells and inorganic solar cells have been industrialized with standard power conversion efficiencies (PCEs) of 18% and 20%, respectively.<sup>[19]</sup> In recent decades, OPVs have made remarkable progress,<sup>[20]</sup> leading organic, dye-sensitized and perovskite solar cells became potential alternatives of traditional solar cells. For organic solar cells, the PCEs can be as high as 15% with good stability,<sup>[21]</sup> and recently, the focus in the development of new OSCs for organic solar cells has shifted to organic non-fullerene acceptors (NFAs).<sup>[22]</sup> PCEs achieved from dye-sensitized solar cells have reached up to 13%,<sup>[23]</sup> in which the dye is an organic compound.<sup>[24,25]</sup> Since their discovery in 2012,<sup>[26]</sup> perovskite solar cells have attracted a worldwide interest and remarkably high power conversion efficiencies (PCEs) over 24 % have been achieved within a few years from their advent.<sup>[27]</sup> From material aspect and in the aim of achieving both better performance and stability, perovskites need to be modified as well as the organic hole transport materials (HTMs).<sup>[28]</sup>

Bulk heterojunction (BHJ) solar cells is a representative type of OPVs with PCEs exceeding 15%.<sup>[29]</sup> As shown in Figure 1-4 (a), four steps are included in the energy transfer process: (1) light absorption and exciton formation; (2) exciton diffusion; (3) charge separation; (4) charge transport and collection. Each of these steps is dominated by molecular properties of donor and acceptor materials. Efficient light absorption requires materials with strong absorption ability in the visible and NIR regions; diffusion of charge needs materials with high mobility; charge separation

needs well-matched frontier energy levels of donor and acceptor; efficient charge transport and collection also depends on materials with high mobility. However, the development of novel electron acceptor molecules has been delayed compared to that of new electron donor materials. Fullerenes and their derivatives, especially PC<sub>61</sub>BM and PC<sub>71</sub>BM, have been the best electron acceptors in BHJ OPVs for a long time due to their high electron affinity, high electron mobility, and isotropy of charge transport.<sup>[30]</sup> However, molecules with modified fullerene molecule structure exhibit limited performance. In addition, their synthetic costs are high. As a consequence, design and synthesis non-fullerene electron acceptors with isotropic charge transport pathway for BHJ OPVs has become a hot topic having attracted huge attention in the organic electronic community.<sup>[31–33]</sup>

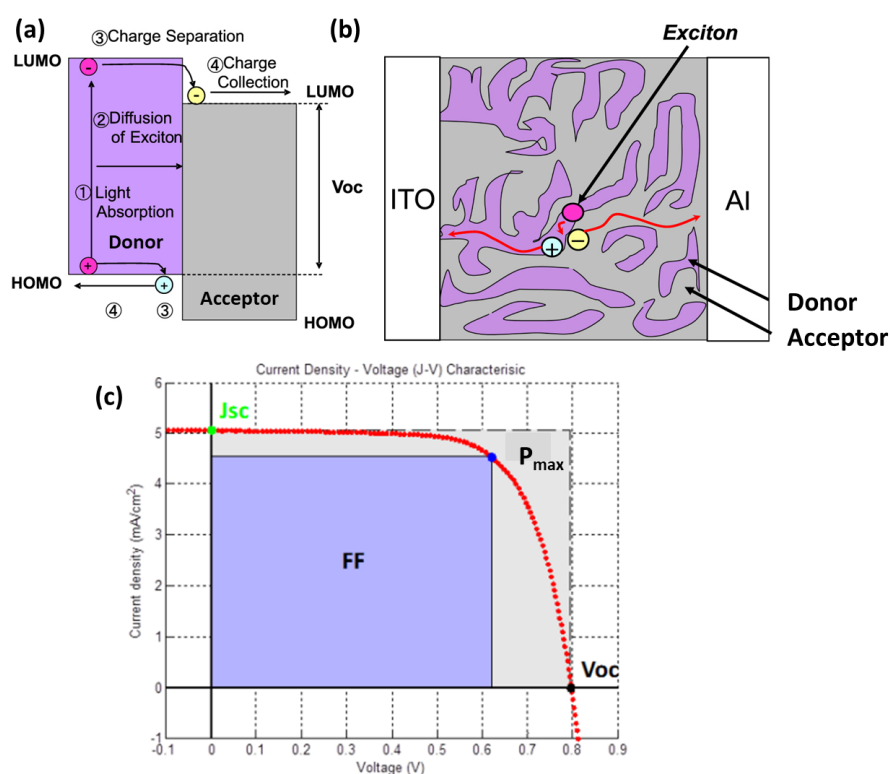


Figure 1-4. Device structure of bulk heterojunction solar cells (a), mechanism of charge separation (b) and typical photocurrent-voltage (J–V) curve of OPVs (c).<sup>[34]</sup>

As mentioned above, PCE ( $\eta$ ) is widely used to compare the performances of different solar cells. And a few parameters are tightly associated with PCE, such as short-current density ( $J_{sc}$ ), open-circuit photovoltage ( $V_{oc}$ ) and a fill factor (FF) which are illustrated in Figure 1-4 (c).  $J_{sc}$  is the photocurrent at the  $V = 0$  V intercept which means the maximum current that the solar cell can deliver. This current is strongly dependent upon the optical properties of the solar cell, such as absorption of the active layer and reflection.  $V_{oc}$  is the voltage at the  $J = 0$  mA cm<sup>-2</sup> intercept which represents the maximum voltage that a solar cell can deliver.  $V_{oc}$  is mainly determined by



saturation current density, which depends on the recombination of charges in the solar cell. FF is the ratio between the maximum power ( $P_{max}$ ) and the product of  $V_{oc}$  with  $J_{sc}$ , thus it has a value between 0 and 1. The effects of these parameters on  $\eta$  are shown in equation (3):

$$\eta = \frac{J_{sc}V_{oc}FF}{P_{in}} \quad (3)$$

where  $P_{in}$  is the power density of the incident light.

### 1.1.4.3 Organic Light-Emitting Diodes

OLEDs are devices that convert electric energy into light energy. Benefited from the features of OLEDs, such as self-emitting ability, transparency, true dark tone, and capability of being made flexible, OLEDs have been commercialized in solid-state display and lighting. As shown in Figure 1-5 (a), the typical device structure of OLEDs consists in a three-layered structure, the so-called double heterostructure, made of a hole-transport layer (HTL), an emissive layer (EML), and an electron-transport layer (ETL). Working principle of OLEDs is illustrated in Figure 1-5 (a) as a four step process. Firstly, when an external voltage is applied across the cathode and the anode, electrons are injected to ETL from cathode and holes are injected to HTL from anode. Secondly, electrons and holes transfer through ETL and HTL respectively and are injected to EML. Thirdly, electrons and holes migrate in EML. Fourthly, electrons and holes recombine and energy is released in the form of light.

In the first-generation OLEDs using fluorescent emitters as EML, the internal quantum efficiency (IQE) is theoretically limited to 25% because triplet excitons created in the fluorescent dyes are non emissive. Then, in the second- and third-generation OLEDs where phosphorescent<sup>[35]</sup> and thermally activated delayed fluorescent (TADF) emitters<sup>[36]</sup> are introduced, the maximum theoretical IQE can reach 100% for both two types of OLEDs.

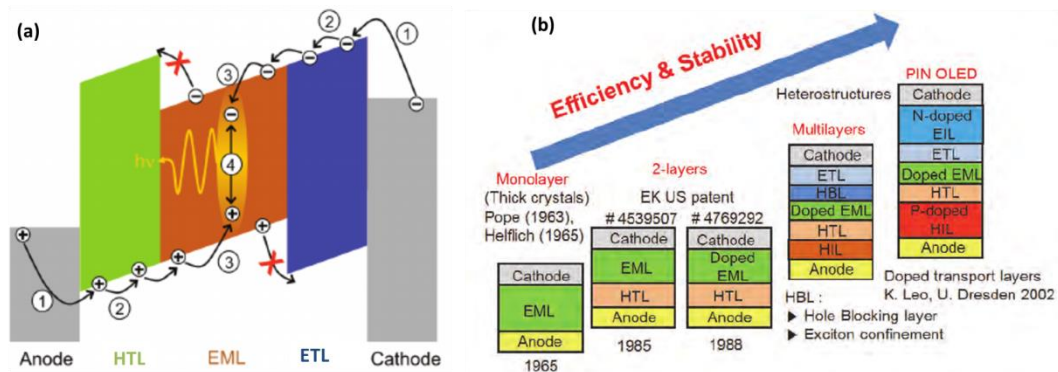


Figure 1-5. Device structure of OLEDs and mechanism of light emitting.<sup>[37]</sup>

As shown in Figure 1-5 (b), in order to improve the performances of OLEDs, the architecture of devices became more and more sophisticated.<sup>[37]</sup> That means before achieving at the emitting layer holes and electrons need to transport a longer distance through different OSCs layers in the device. Consequently, OSCs used in OLEDs need to exhibit high and balanced electron and hole transport mobility.

## 1.2 Mechanism of Charge Transport in OSCs

### 1.2.1 $\pi$ Conjugation

Atom is the basic component of ordinary matter. Every atom is composed of a nucleus and one or more electrons surrounding the nucleus. Electrons are much more mobile than nucleus and their spatial distributions are defined dependent on the nucleus. Electrons are attracted by nucleus by electromagnetic force. The closer an electron is to the nucleus, the greater is the attractive force. In 1913, the physicist Niels Bohr proposed a model in which the electrons of an atom were assumed to orbit the nucleus in some specific orbits with different energies. With the development of quantum mechanics, and the discovery of wave-like behavior of electrons in atoms, atomic orbitals were described by mathematical functions. Based on the wave-particle duality of electrons and the uncertainty principle,<sup>[38]</sup> Mulliken defined, in 1967, an atomic orbital, as a mathematical function that characterizes the probability that an electron appears at a particular location.<sup>[39]</sup>

	s ( $\ell = 0$ )	p ( $\ell = 1$ )			d ( $\ell = 2$ )					f ( $\ell = 3$ )						
	$m = 0$	$m = 0$	$m = \pm 1$		$m = 0$	$m = \pm 1$		$m = \pm 2$		$m = 0$	$m = \pm 1$		$m = \pm 2$		$m = \pm 3$	
	s	$p_z$	$p_x$	$p_y$	$d_{z^2}$	$d_{xz}$	$d_{yz}$	$d_{xy}$	$d_{x^2-y^2}$	$f_{z^3}$	$f_{xz^2}$	$f_{yz^2}$	$f_{xyz}$	$f_x(x^2-y^2)$	$f_x(x^2-3y^2)$	$f_y(3x^2-y^2)$
$n = 1$	•															
$n = 2$	•															
$n = 3$	•															
$n = 4$																
$n = 5$										...	...	...	...	...	...	...
$n = 6$					...	...	...	...	...	...	...	...	...	...	...	...
$n = 7$		...	...	...	...	...	...	...	...	...	...	...	...	...	...	...

Figure 1-6. Atom orbitals and quantum numbers.<sup>[40]</sup>

Each atomic orbital is characterized by a set of values of the three quantum numbers:  $n$  (principal quantum numbers) describes the electron shell,  $\ell$  (angular quantum numbers) describes the subshell, and  $m$  (magnetic quantum number) describes orientation of the subshell's shape. Each orbital can be occupied by two

electrons, each with its own spin quantum number  $s$ . When angular quantum number  $\ell$  is equal to 0, 1, 2 and 3, the names of the orbitals are s orbital, p orbital, d orbital and f orbital respectively.

A molecular orbital (MO) is also a mathematical function which is used to represent the regions of the molecule where an electron can be found with a certain probability. Molecular orbitals are usually constructed by combining atomic orbitals or hybrid orbitals from adjacent atoms in the molecule. In valence bond theory, atomic orbitals are mixed into hybrid orbitals to form chemical bonds.<sup>[41]</sup> Hybrid orbitals are very useful in the explanation of molecular geometry. For example, carbon atom in  $\text{CH}_4$  is  $\text{sp}^3$  hybrid. 4  $\sigma$  bonds are formed by 4 hybrid orbitals overlapped with 4 hydrogen 1s orbitals. This explained well the regular tetrahedron shape of  $\text{CH}_4$  molecule. Carbon atoms in ethene ( $\text{C}_2\text{H}_4$ ) are  $\text{sp}^2$  hybrid. For each carbon, 3  $\sigma$  bonds are constructed from  $\text{sp}^2$  orbitals: two  $\sigma$  bonds by overlapping with 1s orbitals of two hydrogens and another with a  $\text{sp}^2$  orbital of the second carbon. One  $\pi$  bond is also formed by overlapping of the remaining 2p atomic orbital between the two carbons. Geometrically,  $\pi$  bond is distributed on both side of the molecular plane. Moreover, alternation of  $\sigma$  and  $\pi$  bonds leads to extension of  $\pi$  bond over the  $\sigma$  molecular skeleton. The other view is to consider that all  $\pi$  orbitals of neighboring atoms overlap to create extended  $\pi$  molecular orbitals. This phenomenon is known as  $\pi$ -delocalization (Figure 1-7). The new orbitals obtained by delocalization lead to the frontier orbitals. Highest Occupied Molecular Orbital (HOMO) and Lowest Unoccupied Molecular Orbital (LUMO) can be associated to valence and conduction band respectively in the semiconductors model by analogy. In a simplified model for small molecule OSCs, charge carriers (electrons and holes) are localized on LUMO and HOMO of a unique molecule.

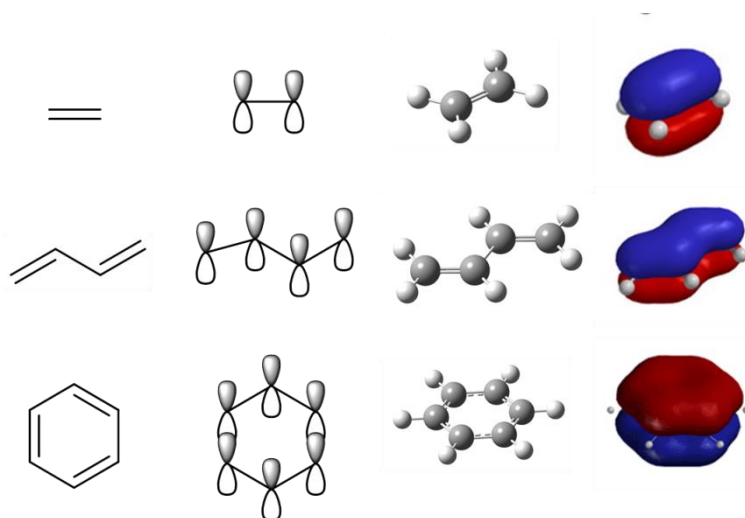


Figure 1-7.  $\pi$  electron delocalization in  $\pi$ -conjugated molecules as ethene (top), but-1,3-diene (middle), benzene (bottom).

## 1.2.2 Molecular Packing and Charge Transport

Contrary to many inorganic materials for which long-range structures are present through covalent- and/or ionic-bonding, the interactions between neighboring organic molecules are noncovalent weak interactions, such as  $\pi$ - $\pi$  stacking, hydrogen bonding, dipole-dipole interactions, and van der Waals (vdW) forces.<sup>[42]</sup> As mentioned in 1.2.1, HOMO and LUMO could be related to valence band and conduction band in inorganic semiconductors, but charge transport in OSCs can rarely be described as band-like transport.<sup>[43]</sup> Indeed, in terms of temperature and inevitable defects, hopping mechanism in OSCs is more widely accepted. In charge hopping process of molecular materials, charge carriers are localized in each molecule and charge transport between molecules is realized by charge carrier hopping process from one molecule to another.<sup>[44]</sup> Thus, in common cases, charge carrier transport between neighboring molecules will be slower than intramolecular transport and depend on  $\pi$ -orbital wavefunction overlap, and electronic coupling.<sup>[45]</sup> The main parameter to describe charge carrier transport property of a material is the mobility. It can be considered as a combination of a charge transfer rate between two close molecules (frequency) with possible pathways (distance).<sup>[46]</sup>

From Marcus theory, charge transfer rate could be calculated according to equation (4):<sup>[47]</sup>

$$\kappa = \left(\frac{4\pi^2}{\hbar}\right) t^2 (4\pi\lambda RT)^{-0.5} e^{\left(-\frac{\lambda}{4RT}\right)} \quad (4)$$

where  $\kappa$  is the charge transfer rate,  $\hbar$  is the reduced Planck constant,  $t$  is the transfer integral,  $\lambda$  is the reorganization energy,  $T$  is the absolute temperature. The most studied factors in this equation are transfer integral and reorganization energy as they are dependent on material structures. Transfer integral ( $t$ ) is related to the intermolecular  $\pi$ -orbital overlaps. It is linked to the distribution of frontier orbitals and molecular packing (relative molecular position as  $\pi$ - $\pi$  stacking distance, angle between aromatic core, etc...)<sup>[48]</sup> For example, a short displacement over the long axis of pentacene in the case of face-to-face packing (the mean planes of the two molecules are parallel) can change the integral transfer from its maximum to zero. (Figure 1-8). Reorganization energy ( $\lambda$ ) is related to the freedom degree of the molecule over vertical transition (the molecular and crystal rigidity, the conjugation length, aromaticity, intermolecular interaction, etc...). Theoretically speaking, large transfer integral and small reorganization energy are favorable for speeding up the charge carrier transfer in OSCs.

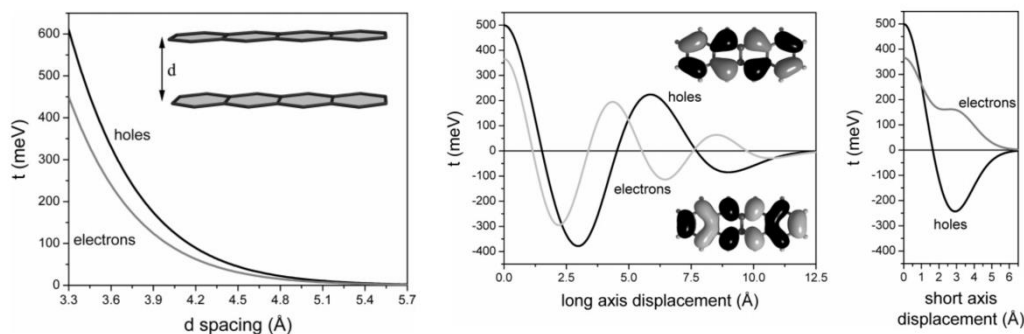


Figure 1-8. Representative diagrams of transfer integrals and molecular packing.<sup>[43]</sup>

In detail, the increase of  $\pi$ - $\pi$  stacking distance significantly decrease transfer integrals of both holes and electrons as shown in Figure 1-8.<sup>[49]</sup> While, displacements of molecules along both long and short axis result in oscillation decay of transfer integral. The oscillations are directly related to HOMO and LUMO distributions of the neighboring molecules. For example in tetracene, along long axis of the molecule structure hole transfer integrals are higher when the displacements are one, two or three benzene rings; while electron transfer integrals are higher when the displacements are half, one and half or two and half benzene rings. In conclusion, dense molecular packing and control of relative position to avoid cancellation between bonding and antibonding interactions can give out a higher transfer integral.<sup>[43,47]</sup>

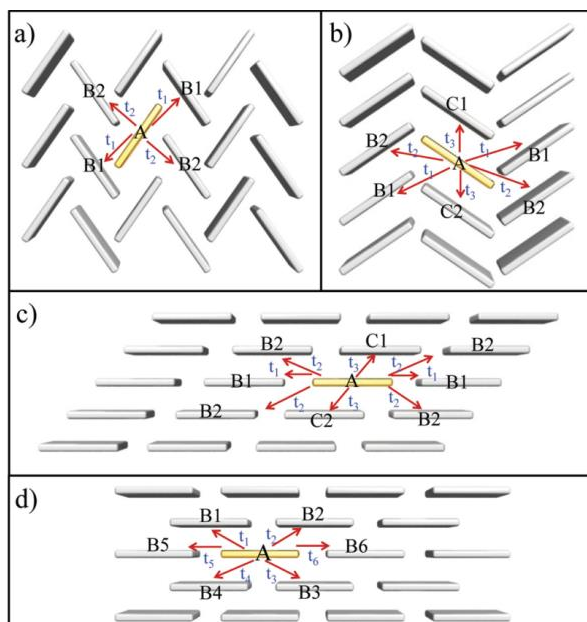


Figure 1-9. Four basic packing motifs of OSCs: a) classical herringbone packing; b) cofacial herringbone packing; c) 1D 'slipped-stacked' arrangement; d) 2D 'bricklayer' arrangement.<sup>[50]</sup>

Based on Marcus theory, higher transfer integral leads to higher mobility.

Therefore, the molecular packing motif has a great impact on mobility. After 50 years of development, many researches about molecule arrangement in crystalline phase have been reported. Finally, most of linear-shaped OSCs can be sorted into four typical packing motifs (Figure 1-9).

- a) Classical herringbone packing. Molecules are present in two orientations and shorter intermolecular distances between them correspond to edge-to-face interactions (the edge of one molecule interacts with the face of the other molecule). In this kind of packing there is no face-to-face overlap between adjacent molecules. Charge carrier transport mainly depends on the edge-to-face overlaps.
- b) Cofacial herringbone packing. Molecules are present in two orientations and shorter intermolecular distances between them correspond to face-to-face interactions. Transfer integral for face-to-face  $\pi$ -stacking is usually larger than that of edge-to-face interaction, so one direction (1D) charge carrier transport along the  $\pi$ -stacking direction can be achieved by this way.
- c) 1D ‘slipped-stacked’ arrangement. Molecules are present in one orientation (or are “parallel”) and shorter intermolecular distances between them correspond to face-to-face interactions. Moreover, the overlap between molecules is much larger in  $\pi$ -stacking direction. Transfer integral along face-to-face  $\pi$  stacking direction is often larger. Therefore, this kind of packing generally yields a 1D charge carrier transport.
- d) 2D ‘bricklayer’ arrangement. Molecules are packed almost the same as 1D ‘slipped-stacked’ arrangement except the overlap between molecules is similar over two directions. Thus, efficient charge transfer to four surrounding molecules can be found. Therefore, this kind of packing can provide a 2D charge carrier transport pathway.

Herringbone packing, cofacial herringbone packing and slipped-stacked arrangement are widely observed in OSCs. However many factors prevent the formation of 2D ‘bricklayer’ arrangement which can be achieved by sophisticated molecular design, such as tips-pentacene<sup>[51]</sup>. Although high mobility can be observed from tips-pentacene, most of the high carrier mobilities are still from those with herringbone and cofacial herringbone packing, such as pentacene and rubrene.<sup>[52]</sup>

## 1.3 High Performance Materials

The first few attempts to fabricate transistors based on conjugated small molecule organic materials were in the 1980s. In 1984, Kudo and co-workers fabricated the first OFET using vacuum-deposited merocyanines films.<sup>[53]</sup> In 1987, M. Madru and C. Clarisse applied metal phthalocyanines (PcZn and Pc<sub>2</sub>Lu) films as active layer in OFETs.<sup>[54]</sup> At that time carrier mobilities measured were around  $10^{-5} \text{ cm}^2 \text{ V}^{-1} \text{ s}^{-1}$ , but with the development of organic chemistry and technique improvement of device fabrication, the mobility of OFETs has increased immensely over the past decades to  $40 \text{ cm}^2 \text{ V}^{-1} \text{ s}^{-1}$  for hole mobility<sup>[7]</sup> and  $27.8 \text{ cm}^2 \text{ V}^{-1} \text{ s}^{-1}$  for electron mobility<sup>[10]</sup>.

### 1.3.1 P-type, N-type and Ambipolar Transistors

In inorganic semiconductor technology, materials are sorted into p-type or n-type depending on dominant carriers are holes or electrons respectively. Physically, hole carriers mean the charge transport occurs in electron-depleted valence band (positively charged) while for electron carriers, the transport results from electron-enriched conduction band (negatively charged). Consequently, the Fermi level (chemical potential) is close to the valence band and conduction band for p-type and n-type respectively. Moreover, Fermi level is commonly lying deeper for p-type than n-type. To reduce contact resistance in devices, the work function of metallic electrodes must be close to Fermi level. By analogy, Fermi level in neutral organic material is at the equidistance of HOMO and LUMO energy level. By extension, if the conductivity increases after depletion of HOMO or enrichment of LUMO, the materials will be called as p-type and n-type OSCs respectively. If both cases are allowed, that means the material possess ambipolar property (Figure 1-10). Most of the materials that have been reported by now are only sufficiently stable to conduct charge carriers of one type, either holes or electrons.

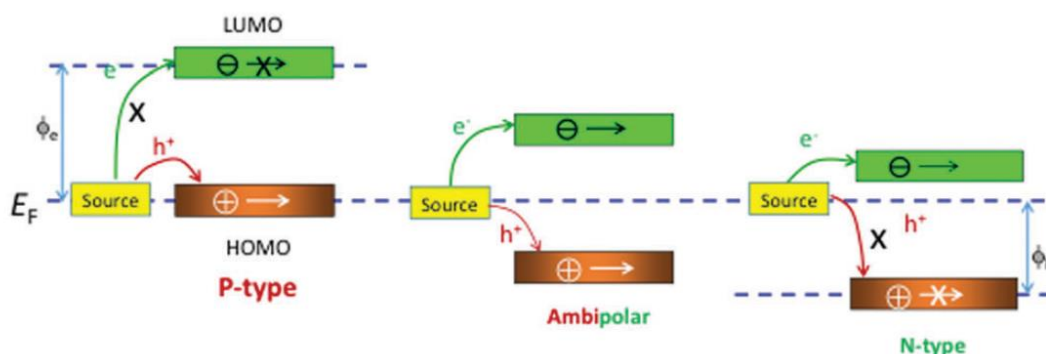


Figure 1-10. Relationships of the frontier energies of the OSCs and the Fermi energy ( $E_F$ ) of the source electrode, where  $\phi_e$  and  $\phi_h$  denote the electron and hole injection barrier, respectively.<sup>[55]</sup>

However, HOMO and LUMO energy levels are just theoretical levels. To evaluate the energy required to remove an electron from the HOMO or to add an electron to the LUMO, ionization potentials and electron affinity can be measured. Thus, for device fabrication, the work function of the electrode must match the ionization potential or electron affinity of the organic semiconductor to reduce contact resistance. There are relatively few metals used as electrode in transistors due to a compromise between their cost and stability. Especially for air-stable devices, gold, aluminum and silver are the most commonly used electrode with work function of -5.1 eV, -4.28 eV and -4.26 eV, respectively. The deep work functions of the electrodes are part of the reason why most of organic materials reported in the literature are p-type. The energy barrier between the work function of the source/drain electrodes and the HOMO of the semiconductor is usually much smaller than the energy barrier between the work function of the electrode and the LUMO. Even if a massive effort has been put into the development of n-type OSCs, it remains more difficult to design and synthesize n-type materials. Ambipolar transistors are transistors that can be operated in both p-channel and n-channel mode by reversing the polarity of the applied gate-source and drain-source voltages. Ambipolar transistors require that the energy barriers between the work function of the electrode and the HOMO/LUMO of the semiconductor are both small enough to permit balanced and efficient charge transfer of both positive and negative carriers. This requires that the bandgap of the material must be smaller than 1 eV.

Representative p-type, n-type and ambipolar materials are summarized and their performances in OFETs are discussed in the following sections. Moreover, the next discussion will mainly focus on single crystal OFETs (SCFET) to be able to compare performances and crystal structures.

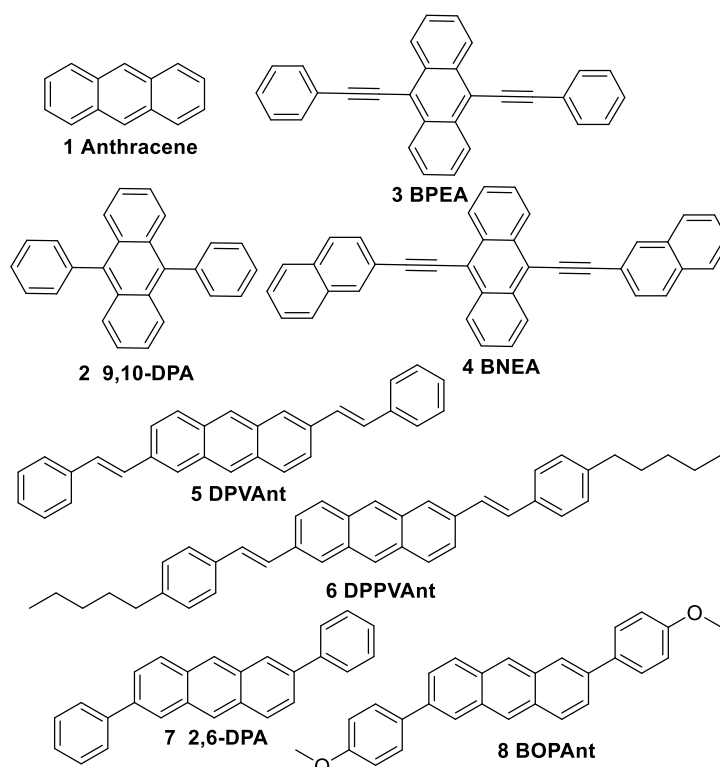
## **1.3.2 P-type Materials**

### **1.3.2.1 Acenes and Their Derivatives.**

Acenes are aromatic hydrocarbons with fused benzene rings, and they are very important candidates for organic semiconductors due to their excellent  $\pi$ -conjugated system and planar molecular structure.



## Anthracene and its derivatives

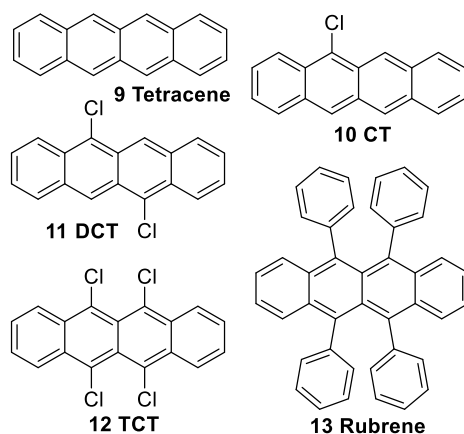


Scheme 1-1: Anthracene and its derivatives

Anthracene (**1**, Scheme 1-1) with three fused benzene rings is the smallest acene compound reported showing transistor effect, however, the mobility reported in 2004 by Aleshin *et al.* for single crystals was only  $0.02 \text{ cm}^2 \text{ V}^{-1} \text{ s}^{-1}$ .<sup>[56]</sup> In 2008 Xiujuan *et al.* synthesized one anthracene derivative, 9,10-diphenylanthracene (9,10-DPA, **2**, Scheme 1-1), and measured its mobility as  $0.16 \text{ cm}^2 \text{ V}^{-1} \text{ s}^{-1}$  in single crystal device, which was one magnitude higher than that of anthracene.<sup>[57]</sup> In 2009, Wang *et al.* synthesized a series of cruciform anthracene derivatives, by incorporating two carbon-carbon triple bonds at the C-9 and C-10 positions of anthracene. Among all these molecules 9,10-bis(phenyl-2-ylethynyl)anthracene (BPEA, **3**, Scheme 1-1), and 9,10-bis(naphthalen-2-ylethynyl)anthracene (BNEA, **4**, Scheme 1-1) led to higher hole mobilities,  $0.73 \text{ cm}^2 \text{ V}^{-1} \text{ s}^{-1}$  and  $0.52 \text{ cm}^2 \text{ V}^{-1} \text{ s}^{-1}$  respectively for **3** and **4**, for their single crystals.<sup>[58]</sup> The higher mobilities could be explained by their coplanar molecule structures and enhanced  $\pi$ - $\pi$  intermolecular interactions in slipped  $\pi$ - $\pi$  stacking arrangement. The mobility break-through of  $1 \text{ cm}^2 \text{ V}^{-1} \text{ s}^{-1}$  for anthracene derivatives was started from di(phenylvinyl)anthracene (DPVAnt, **5**, Scheme 1-1) with phenylenevinylene substituents at both ends of anthracene reported in 2007. OFETs fabricated based on **5** led to mobilities as high as  $1.3 \text{ cm}^2 \text{ V}^{-1} \text{ s}^{-1}$  from thin films<sup>[59]</sup> and  $4.3 \text{ cm}^2 \text{ V}^{-1} \text{ s}^{-1}$  from its single crystals<sup>[60]</sup>. Another similar anthracene derivative 2,6-bis[2-(4-pentylphenyl)vinyl]anthracene (DPPVAnt, **6**, Scheme 1-1) also

showed good performance, with charge carrier mobility of  $1.28 \text{ cm}^2 \text{ V}^{-1} \text{ s}^{-1}$  as thin film.<sup>[61]</sup> The improvement of device performance is due to the fact that: 1) the phenylvinylene substituents extend the  $\pi$ -conjugation of the molecule; 2) the changes at the end of anthracene backbone do not alter the original herringbone molecular packing but lead to a more densely packed crystal structure, and stronger intermolecular electronic couplings for higher carrier mobility; 3) this kind of  $\pi$ -conjugation extension keeps large band gaps of the molecules, thus both **5** and **6** possess band gap around 2.6 eV which is favorable for the environmental stability of the materials. In recent years, the high fluorescent property of anthracene in solid state has drawn more and more attention.<sup>[62]</sup> In 2015, organic light-emitting transistors (OLETs) were fabricated based on 2,6-diphenylanthracene (2,6-DPA, **7**, Scheme 1-1). Single crystal of **7** exhibits not only high emission with absolute fluorescence quantum yield of 41.2% but also high charge carrier mobility with single crystal mobility of  $34 \text{ cm}^2 \text{ V}^{-1} \text{ s}^{-1}$ .<sup>[63]</sup> Then, 2,6-bis(4-methoxyphenyl)anthracene (BOPAnt, **8**, Scheme 1-1) was reported with high mobility of  $16.6 \text{ cm}^2 \text{ V}^{-1} \text{ s}^{-1}$  in SCFETs and a very low anisotropic mobility ratio measured in a plane ( $\mu_{\text{max}}/\mu_{\text{min}}$ ) of 1.23 was obtained.<sup>[64–66]</sup>

### Tetracene and its derivatives

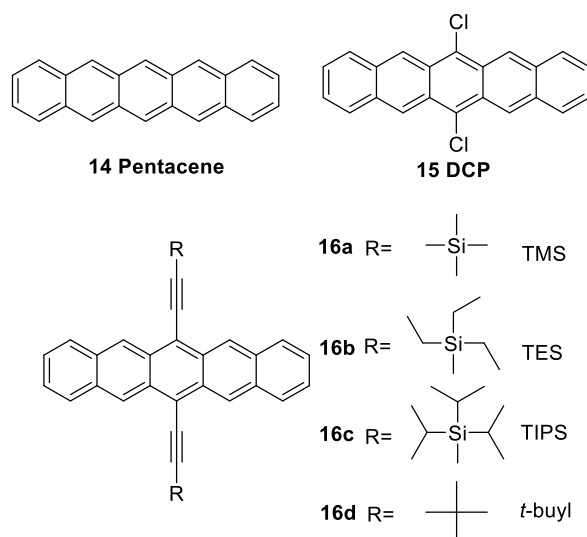


Scheme 1-2: Tetracene and its derivatives.

Tetracene (**9**, Scheme 1-2) is composed of four fused benzene rings. Compared with **5** and **6**, tetracene is another way to extend the  $\pi$ -conjugation system of anthracene. Therefore, the carrier mobility of tetracene is increased to  $0.1 \text{ cm}^2 \text{ V}^{-1} \text{ s}^{-1}$  for measurements from thin films,<sup>[67,68]</sup> and  $2.4 \text{ cm}^2 \text{ V}^{-1} \text{ s}^{-1}$  was obtained from its single crystals.<sup>[69]</sup> In 2004, a series of soluble halogenated tetracene derivatives were synthesized.<sup>[70]</sup> The mono-halo tetracene derivative, 5-chlorotetracene (CT, **10**, Scheme 1-2), exhibited low carrier mobility as  $1.4 \times 10^{-4} \text{ cm}^2 \text{ V}^{-1} \text{ s}^{-1}$  for its single crystals, while the di-halo derivative 5,11-dichlorotetracene (DCT, **11**, Scheme 1-2) led to a hole mobility of  $1.6 \text{ cm}^2 \text{ V}^{-1} \text{ s}^{-1}$  for its single crystals. A few years later in 2008

a tetra-halo derivative 5,6,11,12-tetrachlorotetracene (TCT, **12**, Scheme 1-2) was synthesized and carrier mobility measured from its single crystals was as high as  $1.7 \text{ cm}^2 \text{ V}^{-1} \text{ s}^{-1}$ .<sup>[71]</sup> Compared with **10**, the better performances of **11** and **12** benefited from their slipped-stacking arrangement which demonstrate strong  $\pi$ -stacking overlaps in a face-to-face slipped motif, and face-to-face  $\pi$ -stacks are favorable for efficient charge transport. But the slipped-stacking packing motif induces strong mobility anisotropy, higher mobility is only achieved along the stack direction. The most representative tetracene derivative is 5,6,11,12-tetraphenyltetracene (rubrene, **13**, Scheme 1-2) because of its excellent electronic properties. In 2007, Yamagishi *et al.* reported a very high carrier mobility of  $43 \text{ cm}^2 \text{ V}^{-1} \text{ s}^{-1}$  for rubrene single crystals using double-gate transistor architecture with organic crystal as gate insulators.<sup>[72]</sup> However, early in the 2004 Vikram *et al.* studied very carefully the mobilities of rubrene single crystals and found that mobilities are different along the *a* and *b* axes ( $4.4 \text{ cm}^2 \text{ V}^{-1} \text{ s}^{-1}$  and  $15.4 \text{ cm}^2 \text{ V}^{-1} \text{ s}^{-1}$ , respectively).<sup>[73]</sup> Then in 2005, the strong mobility anisotropy was explained by theoretical calculation. Rubrene adopts a cofacial herringbone arrangement with enhanced  $\pi$ -stacking interactions along the *a*-axis direction in solid state, resulting in efficient electronic couplings and large transfer integral along this direction.<sup>[74]</sup>

### Pentacene and its derivatives



Scheme 1-3: Pentacene and its derivatives.

Pentacene (**14**, Scheme 1-3), with one more benzene ring fused compared to tetracene, has attracted the most interest compared to other acenes. The first report about mobility of pentacene was in 2003 by Butko *et al.* and  $0.3 \text{ cm}^2 \text{ V}^{-1} \text{ s}^{-1}$  was measured for OFET devices built on pentacene crystals using a parylene gate dielectric.<sup>[75]</sup> A higher value of  $2.2 \text{ cm}^2 \text{ V}^{-1} \text{ s}^{-1}$  was reported in 2004 by Roberson *et al.*

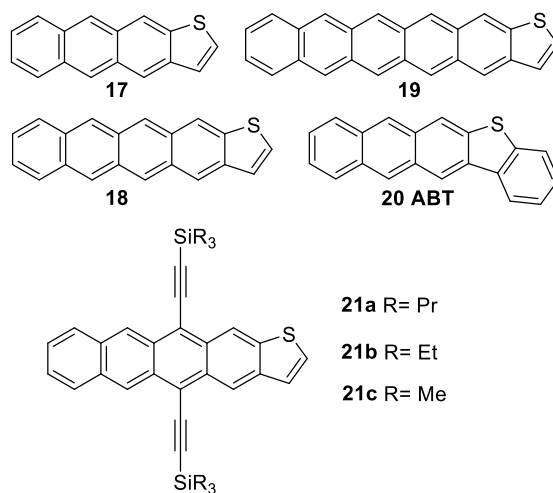
after several purification of pentacene.<sup>[76]</sup> In the same year, a mobility of  $1.4 \text{ cm}^2 \text{ V}^{-1} \text{ s}^{-1}$  was observed for pentacene single crystals by treating  $\text{SiO}_2$  gate dielectric with self-assembled monolayers.<sup>[77]</sup> Jurchescu *et al.* published several papers and proved that by pretreatment using vacuum sublimation to remove the impurity in pentacene single crystals, the mobility can be as high as  $40 \text{ cm}^2 \text{ V}^{-1} \text{ s}^{-1}$ .<sup>[78,7]</sup> The dramatic variation about the mobility of pentacene is caused by the high lying HOMO energy level ( $-5.1 \text{ eV}$ ) and small band gap ( $1.77 \text{ eV}$ ) which make pentacene easily oxidized when exposed to oxygen. When pentacene is oxidized, oxygen atoms replace the hydrogen atoms at C-6 and C-13 positions and form the dominant impurity 6,13-pentacenequinone, in which the oxygen atoms at C-6 and C-13 positions break the conjugation of the whole molecule. Meanwhile, the nonplanar molecule structure of quinone induces a local deformation by distorting the pentacene lattice locally. One representative pentacene derivative is 6,13-dichloropentacene (DCP, **15**, Scheme 1-3) which achieved carrier mobility as high as  $9.0 \text{ cm}^2 \text{ V}^{-1} \text{ s}^{-1}$  for DCP nanoribbon crystals.<sup>[79]</sup> The high mobility of DCP benefited from the densely packed cofacial herringbone arrangement ( $\pi$ - $\pi$  stacking distance of  $3.48 \text{ \AA}$ ) which result from the extension of  $\pi$ -conjugation system as well as the abundant C-H-Cl intermolecular interactions. In order to develop solution-processable, high-mobility, small-molecule OSCs, Anthony and co-workers synthesized a series of pentacene derivatives by introducing bulky solubilizing groups at the peri-positions of pentacene.<sup>[80-82]</sup> Among all the molecules 6,13-bis(triisopropylsilylethynyl)pentacene (TIPS-PEN, **16c**, Scheme 1-3) is one of the most successful examples. The length of the TIPS substituent is approximately half the length of the central pentacene leading to an 2D 'bricklayer' arrangement. Mobilities of  $0.4 \text{ cm}^2 \text{ V}^{-1} \text{ s}^{-1}$ ,<sup>[82]</sup>  $1.42 \text{ cm}^2 \text{ V}^{-1} \text{ s}^{-1}$ <sup>[83]</sup> and  $1.8 \text{ cm}^2 \text{ V}^{-1} \text{ s}^{-1}$ <sup>[84]</sup> were achieved for TIPS-PEN thin film, single nanowire and its drop-cast thin films, respectively. The highest mobility achieved so far for TIPS-PEN is  $4.6 \text{ cm}^2 \text{ V}^{-1} \text{ s}^{-1}$  reported by Gaurav *et al.* in 2011, the  $\pi$ - $\pi$  stacking distance of TIPS-PEN decreased from  $3.33 \text{ \AA}$  to  $3.08 \text{ \AA}$  by introducing strain within the crystal lattice. In recent years, more and more researches focused on the interfaces between OSC single crystals and dielectric layer.<sup>[85,86]</sup>

With the increasing of the number of fused benzene rings in linear shaped acenes the materials become very unstable and difficult to synthesize, such as hexacene, heptacene, octacene and nonacene, making it nearly impossible to apply these materials in field-effect transistors. Therefore, our discussion with acenes stopped with pentacene.

### 1.3.2.2 Heteroacenes and Their Derivatives

Heteroacenes are fused-ring conjugated molecules where one or more benzene rings in acene backbones are replaced by heterocycle, such as thiophene or pyridine moieties. N-Heteroacenes generally improve the n-type character compared to acenes by lowering LUMO energy level, while S-Heteroacenes lead to the inverse behavior.

#### Heteroacenes with one thiophene

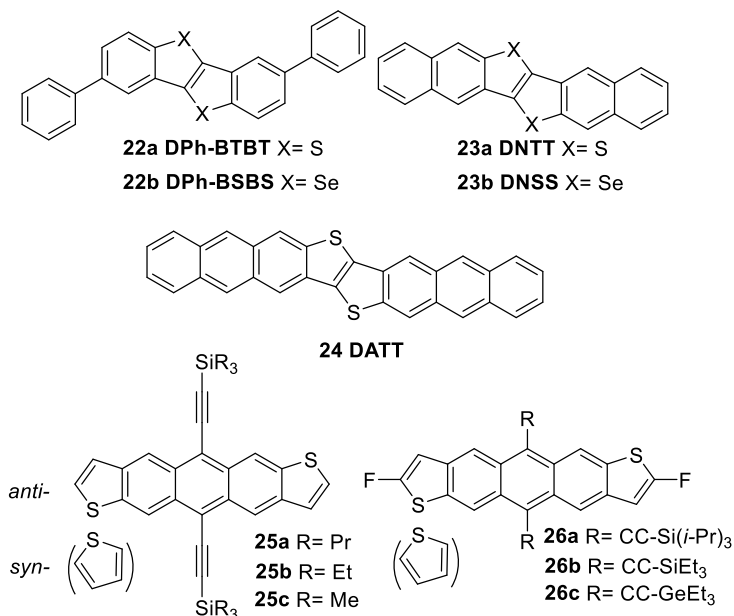


Scheme 1-4: Heteroacenes with one thiophene.

Heteroacenes with one thiophene ring anthra[2,3-*b*]thiophene and tetraceno[2,3-*b*]thiophene (**17**, **18**, Scheme 1-4) were firstly reported by Bao and co-workers in 2006.<sup>[87]</sup> For molecule **17**, the mobility determined as thin films is  $0.15 \text{ cm}^2 \text{ V}^{-1}\text{s}^{-1}$ . For molecule **18**, the mobility observed from its thin films is  $0.47 \text{ cm}^2 \text{ V}^{-1}\text{s}^{-1}$ . Although the mobilities of these two compounds are not higher than their acene counterparts, the HOMO energy levels are lower and their bandgaps are larger. That means with the introduction of one fused thiophene ring at the end of the molecule, the heteroacenes obtained are more stable than the counterpart acenes. In 2009, a heteroacene with more fused rings pentaceno[2,3-*b*]thiophene (**19**, Scheme 1-4) was reported by Bao and co-workers.<sup>[88]</sup> Thin film of molecule **19** exhibited a higher mobility which has reached  $0.57 \text{ cm}^2 \text{ V}^{-1}\text{s}^{-1}$ , because of its extension of  $\pi$ -conjugated system. Another heteroacene with one thiophene ring in the middle of the molecule Anthra[2,3-*b*]benzo[*d*]thiophene (ABT, **20**, Scheme 1-4) was reported by Du *et al.* in 2008.<sup>[89]</sup> The mobility measured for thin films of molecule **20** was  $0.41 \text{ cm}^2 \text{ V}^{-1}\text{s}^{-1}$ . X-ray diffraction study on single crystals revealed that molecules of **20** packed in a herringbone arrangement similar to that of pentacene. In order to improve solubility and investigate the impact of differently bulky side-chain substituents on the packing of the molecules, a series of molecules including tri-isopropylsilyl (TIPS), triethylsilyl

(TES) and trimethylsilyl (TMS) ethynyl tetraceno[2,3-*b*]thiophene units (TIPSEthiotet, TESEthiotet and TMSEthiotet, **21a**, **21b**, **21c**, Scheme 1-4) were synthesized by Bao and co-workers in 2008.<sup>[90]</sup> Among all the compounds, benefited from its 2D bricklayer packing **21a** exhibited mobility as high as  $1.25 \text{ cm}^2 \text{ V}^{-1} \text{ s}^{-1}$  for its thin films, three orders of magnitude higher than **21b** and **21c** which exhibit 1D slip stacking in single crystals.

### Heteroacenes with two thiophenes or selenophenes

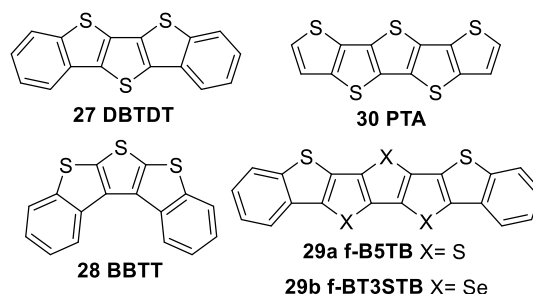


Scheme 1-5: Heteroacenes with two thiophenes or selenophenes.

Heteroacenes with two thiophene rings or two selenophene rings in the middle of the molecule, such as 2,7-diphenyl[1]benzothieno[3,2-*b*][1]benzothienophene and 2,7-diphenyl[1]benzoselenopheno[3,2-*b*][1]benzoselenophene (DPh-BTBT and DPh-BSBS, **22a** and **22b**, Scheme 1-5), were synthesized by Takimiya and co-workers in 2006.<sup>[91]</sup> OFETs fabricated from thin films of **22a** and **22b** yielded mobility of  $2.0 \text{ cm}^2 \text{ V}^{-1} \text{ s}^{-1}$  and  $0.31 \text{ cm}^2 \text{ V}^{-1} \text{ s}^{-1}$  respectively. Heteroacenes with extended  $\pi$ -conjugated systems such as dinaphtho[2,3-*b*:2',3'-*f*]chalcogenopheno[3,2-*b*]chalcogenophene (DNNT and DNSS, **23a** and **23b**, Scheme 1-5) were synthesized by Yamamoto *et al* in 2007.<sup>[92]</sup> Thin film of **23a** exhibited mobility as high as  $2.9 \text{ cm}^2 \text{ V}^{-1} \text{ s}^{-1}$  and mobility for **23b** thin film was found to be  $1.9 \text{ cm}^2 \text{ V}^{-1} \text{ s}^{-1}$ . Additionally, a mobility of  $8.3 \text{ cm}^2 \text{ V}^{-1} \text{ s}^{-1}$  was reported for **23a** single crystals.<sup>[93]</sup> Heteroacene with longer  $\pi$ -conjugated system dianthra[2,3-*b*:20,30-*f*]thieno[3,2-*b*]thiophene (DATT, **24**, Scheme 1-5) was synthesized by Takimiya *et al* in 2011.<sup>[94]</sup> The highest mobility observed from **24** thin films was  $3.1 \text{ cm}^2 \text{ V}^{-1} \text{ s}^{-1}$ . A series of 6,13-functionalized anthradithiophene (ADT)

molecules (**25a**, **25b**, **25c**, Scheme 1-5) were synthesized by Jackson *et al* in 2005.<sup>[95]</sup> Among all the compounds, **25b** exhibited mobility as high as  $1.0 \text{ cm}^2 \text{ V}^{-1}\text{s}^{-1}$  for its solution-deposited thin films. Among these three compounds, only **25b** exhibit a 2D bricklayer packing proving triethylsilyl (TES) branches have suitable size for ADT derivatives. Two Fluorinated anthradithiophenes (**26a**, **26b**, Scheme 1-5) were synthesized by Anthony in 2007,<sup>[96]</sup> the introduction of fluorine atoms in the molecules resulted in strong F-F and F-S interactions which is favorable for dense molecular packing. Finally molecule **26b** formed a 2D bricklayer arrangement with small  $\pi$ -stacking distance. Mobility measured from the thin films of **26b** was  $1.5 \text{ cm}^2 \text{ V}^{-1}\text{s}^{-1}$ . Notably, due to the limitation of synthetic method, results for **25b** and **26b** are all from their inseparable mixtures of *syn*- and *anti*-isomers. In 2015, Anthony and co-workers synthesized the pure *anti*-/*syn*-**26b** and **26c**.<sup>[97]</sup> Maximum mobilities extracted from spin-coating films of pure *anti*-**26b**, *syn*-**26b**, mix **26b**, *anti*-**26c**, *syn*-**26c**, and mix **26c** were  $4.3 \text{ cm}^2 \text{ V}^{-1}\text{s}^{-1}$ ,  $3.0 \text{ cm}^2 \text{ V}^{-1}\text{s}^{-1}$ ,  $2.7 \text{ cm}^2 \text{ V}^{-1}\text{s}^{-1}$ ,  $6.2 \text{ cm}^2 \text{ V}^{-1}\text{s}^{-1}$ ,  $2.8 \text{ cm}^2 \text{ V}^{-1}\text{s}^{-1}$ , and  $2.4 \text{ cm}^2 \text{ V}^{-1}\text{s}^{-1}$ , respectively. In conclusion, purification of ADT derivatives increased the mobility; replacement of silicon by germanium gave out higher performance; the *anti*-isomers were more favorable than the *syn*-isomers to get higher mobility.

### Heteroacenes with more thiophenes or selenophenes

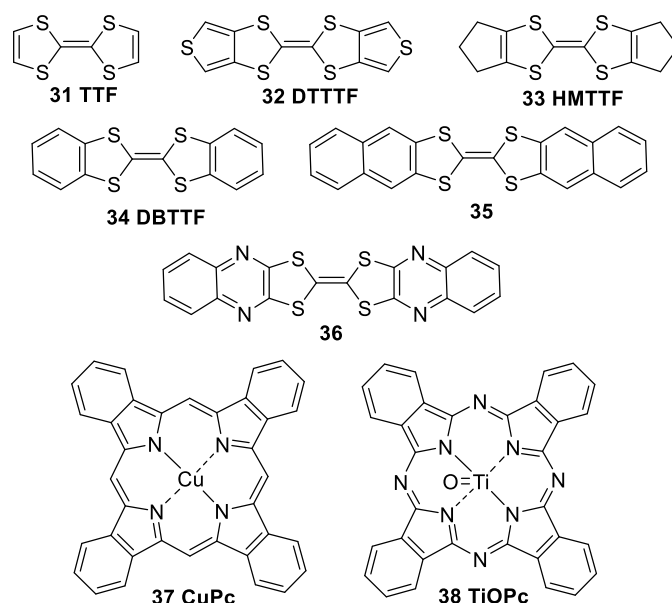


Scheme 1-6: Heteroacenes with more thiophenes or selenophenes.

Two heteroacenes with three thiophene rings dibenzo[*d,d'*]thieno[3,2-*b*;4,5-*b'*]dithiophene and bis(benzo[4,5]-thieno)[2,3-*b*:3',2'-*d*]thiophene (**27** and **28**, Scheme 1-6) were synthesized. For molecule **27** mobility from thin films was  $0.51 \text{ cm}^2 \text{ V}^{-1}\text{s}^{-1}$ , mobility from single crystals grown by physical vapor transport was  $1.8 \text{ cm}^2 \text{ V}^{-1}\text{s}^{-1}$ .<sup>[98]</sup> For molecule **28** mobility for single crystals grown from solution was  $0.6 \text{ cm}^2 \text{ V}^{-1}\text{s}^{-1}$ .<sup>[99]</sup> Larger heteroacenes with five heterocycles benzoannulated pentathienoacene and its selenium analog (f-B5TB and f-BT3STB, **29a** and **29b**, Scheme 1-6) were firstly synthesized by Okamoto *et al.* in 2005.<sup>[100]</sup> Later, in 2007

single crystal transistors were fabricated based on these two materials, and the mobilities determined were  $0.5 \text{ cm}^2 \text{ V}^{-1}\text{s}^{-1}$  and  $1.1 \text{ cm}^2 \text{ V}^{-1}\text{s}^{-1}$  respectively for **29a** and **29b**. Compound **29b** achieved higher mobility due to its considerable Se-Se orbital interactions.<sup>[101]</sup> Finally it is worth noticing that a total thiophene fused molecule pentathienoacene (PTA, **30**, Scheme 1-6) was initially applied in OFETs by Xiao *et al.* in 2005.<sup>[102]</sup> Mobility of PTA thin films was  $0.045 \text{ cm}^2 \text{ V}^{-1}\text{s}^{-1}$ , lower than that of pentacene, but PTA is more stable than pentacene due to its wider band gap (3.29 eV).

### 1.3.2.3 TTF and Phthalocyanine Derivatives



Scheme 1-7: TTF and phthalocyanine derivatives.

Benefited from their electron donating property, tetrathiafulvalene (TTF, **31**, Scheme 1-7) derivatives are excellent candidates for p-type organic semiconductors in OFETs. Moreover, TTFs show a high tendency to form ordered stacks or two-dimensional sheets, which are stabilized by both intermolecular  $\pi$ - $\pi$  and  $\text{S}\cdots\text{S}$  interactions. It was reported in 2007 that devices made from TTF  $\alpha$ -phase single crystals achieved a hole mobility as high as  $1.2 \text{ cm}^2 \text{ V}^{-1}\text{s}^{-1}$ .<sup>[103]</sup> In order to extend the  $\pi$ -conjugation system of TTF, a lot of TTF derivatives were designed and synthesized. There are several TTF derivatives with high mobility. Such as, dithiophene-tetrathiafulvalene (DTTTF, **32**, Scheme 1-7) incorporating two thiophene rings at the end of TTF can give high single crystal mobility as high as  $3.65 \text{ cm}^2 \text{ V}^{-1}\text{s}^{-1}$ .<sup>[104]</sup> Hexamethylenetetrathiafulvalene (HMTTF, **33**, Scheme 1-7) is a TTF derivative showing the highest mobility. Devices fabricated from thin films of HMTTF gave out mobility of  $6.9 \text{ cm}^2 \text{ V}^{-1}\text{s}^{-1}$ ,<sup>[105]</sup> while SCFET of HMTTF achieved hole mobility as high as  $11.2 \text{ cm}^2 \text{ V}^{-1}\text{s}^{-1}$ .<sup>[106]</sup> For molecule dibenzo-tetrathiafulvalene (DBTTF, **34**, Scheme 1-7) mobilities in the range



of  $0.1\text{-}1\text{ cm}^2\text{ V}^{-1}\text{s}^{-1}$  were obtained from solution grown crystals.<sup>[107]</sup> OFETs based on thin films of molecules with larger  $\pi$ -conjugation system dinaphtho TTF and diquinoxalino TTF (**35**, **36**, Scheme 1-7) showed a mobility of  $0.42\text{ cm}^2\text{ V}^{-1}\text{s}^{-1}$  and  $0.2\text{ cm}^2\text{ V}^{-1}\text{s}^{-1}$ , respectively.<sup>[108]</sup>

Phthalocyanines have been known as stable pigments for a long time with high absorption coefficients and remarkably chemical and thermal stabilities, as well as non-toxicity and good field-effect properties.<sup>[109]</sup> The mobility of Cu phthalocyanine (CuPc, **37**, Scheme 1-7) single crystal was up to  $1.0\text{ cm}^2\text{ V}^{-1}\text{s}^{-1}$ .<sup>[110]</sup> Furthermore, the mobility of titanyl phthalocyanine (TiOPc, **38**, Scheme 1-7) thin film OFET was as high as  $10\text{ cm}^2\text{ V}^{-1}\text{s}^{-1}$ , benefiting from its 2D bricklayer arrangement with close  $\pi$ - $\pi$  stacking distance of  $3.21\text{ \AA}$ .<sup>[111]</sup> Metal atom coordination into  $\text{H}_2\text{Pc}$  planes can tune the hole mobility via adjusting the intermolecular distances. Recent work on SCFET of phthalocyanine derivatives showed a hole mobility order of  $\text{ZnPc} > \text{MnPc} > \text{FePc} > \text{CoPc} > \text{CuPc} > \text{H}_2\text{Pc} > \text{NiPc}$ .<sup>[112]</sup>

To conclude, molecules mentioned above together with their mobilities and molecule arrangements are summarized in Table 1-1. There is no clear relationship between mobility and packing mode for SCFET. Moreover, information about mobility along different axis is rare. This could be ascribed to the absence of crystal where molecular packing could lead to high dimensionality of charge transport and the difficulty to elaborate relevant experiment.

Table 1-1. Representative p-type materials, mobilities and molecule arrangements.

Type	Molecule	Mobility ( $\text{cm}^2\text{ V}^{-1}\text{s}^{-1}$ )	Device	Molecular arrangement	Ref.	
Acenes	1 Anthracene	0.02	SC	herringbone packing	[56]	
	2 9,10-DPA	0.16	SC	herringbone packing	[57]	
	3 BPEA	0.73	SC	slipped-stacking	[58]	
	4 BNEA	0.52	SC	slipped-stacking	[58]	
	5 DPVAnt		1.3	TF	herringbone packing	[59]
			4.3	SC		[60]
	6 DPPVAnt	1.28	TF	herringbone packing	[61]	
	7 2,6-DPA	34	SC		[63]	
	8 BOPAnt	16.6	SC		[64–66]	
	9 Tetracene		0.1	TF	herringbone packing	[67,68]
			2.4	SC		[69]
	10 CT	$1.4 \times 10^{-4}$	SC	herringbone packing	[70]	
	11 DCT	1.6	SC	slipped-stacking	[70]	
12 TCT	1.7	SC	slipped-stacking	[71]		
13 Rubrene		4.4 <i>a</i> axes	SC	cofacial herringbone packing	[73]	
		15.4 <i>b</i> axes	SC		[74]	
		43	SC		[72]	

Type	Molecule	Mobility ( $\text{cm}^2 \text{V}^{-1} \text{s}^{-1}$ )	Device	Molecular arrangement	Ref.
	14 Pentacene	0.3	SC	herringbone packing	[75]
		2.2	SC		[76]
		1.4	SC		[77]
		40	SC		[78,7]
	15 DCP	9.0	SC	cofacial herringbone packing	[79]
	16c TIPS-PEN	0.4	TF	bricklayer-packing	[80-82]
1.42		SC			
1.8		TF			
4.6		SC			
<b>Heteroacenes</b>	17	0.15	TF		[87]
	18	0.47	TF		[87]
	19	0.57	TF		[88]
	20 ABT	0.41	TF	herringbone packing	[89]
	21a	1.25	TF		[90]
	22a DPh-BTBT	2.0	TF		[91]
	22b DPh-BSBS	0.31	TF		
	23a DNTT	2.9	TF	herringbone packing	[92]
		8.3	SC		[93]
	23b DNSS	1.9	TF	herringbone packing	[92]
	24 DATT	3.1	TF	herringbone packing	[94]
	25b	1.0	TF	bricklayer-packing	[95]
	26a Anti-26b Anti-26c	1.5	TF	bricklayer-packing	[96]
		4.3	TF		[97]
		6.2	TF		[97]
	27 DBTDT	0.51	TF		[98]
		1.8	SC		
28 BBTT	0.6	SC	slipped-stacking	[99]	
29a 29b	0.5	SC	slipped-stacking	[100]	
	1.1	SC	slipped-stacking		
30 PTA	0.045	TF		[102]	
<b>TTF and phthalocyanine derivatives</b>	31 TTF	1.2	SC	cofacial herringbone packing	[103]
	32 DTTTF	3.65	SC	cofacial herringbone packing	[104]
	33 HMTTF	11.2	SC	bricklayer-packing	[106]
	34 DBTTF	0.1-1	SC	cofacial herringbone packing	[107]
	35	0.42	TF		[108]
	36	0.2	TF		[108]
	37 CuPc	1.0	SC	cofacial herringbone packing	[110]
	38 TiOPc	10	TF	bricklayer-packing 3.21 Å	[111]

### 1.3.3 N-type and Ambipolar Materials

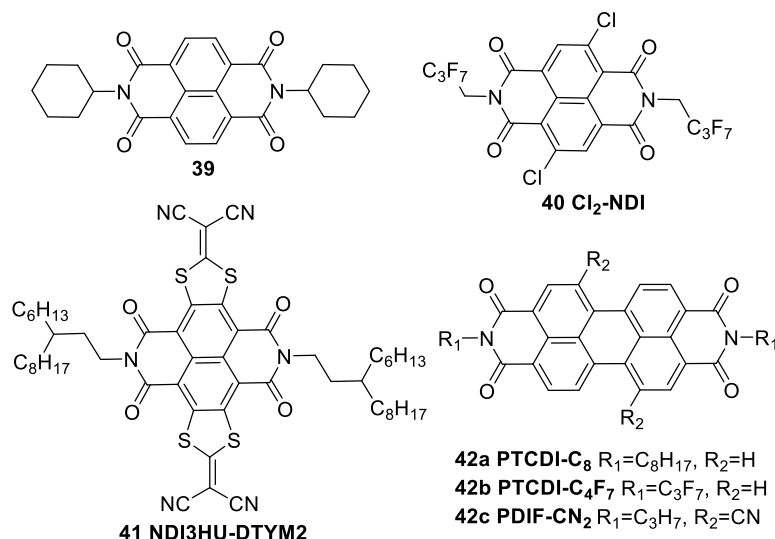
The invention of the first OFET was in 1986,<sup>[9]</sup> while the discovery of n-channel

OFET occurred in 1990.<sup>[113]</sup> Although the performance of n-type OFETs has improved remarkably in the last thirty years with mobility in some cases exceeding amorphous silicon ( $\alpha$ -Si:H, mobility  $\sim 1.0 \text{ cm}^2 \text{ V}^{-1} \text{ s}^{-1}$ ), the overall development of n-type OSCs still lags behind the p-type OSCs. To achieve an ideal n-type OSC, LUMO energy level and molecular packing of semiconducting materials are the most important issues. As we mentioned before, work function of gold is around -5.1 eV. In order to lower the injection barrier from electrode to LUMO of the OSCs, LUMO energy level should be better lower than -4 eV.<sup>[114]</sup> Low lying LUMO is also favorable for anion's stability by decreasing possibilities of electron trapping under ambient condition by  $\text{H}_2\text{O}$  or  $\text{O}_2$ .<sup>[115]</sup> Dense molecular packing is more important for n-type OSCs as it can also act as barrier to prevent the penetration of water and oxygen into the semiconducting layer.<sup>[116]</sup> Representative n-type semiconductors used in OFETs are naphthalene diimide (NDI) and perylene diimide (PDI) derivatives; fluorinated metal phthalocyanines, oligothiophenes and oligoacenes; N-heteroacenes;  $\text{C}_{60}$  and its derivatives.

### 1.3.3.1 Naphthalene Diimide (NDI) and Perylene Diimide (PDI)

#### Derivatives

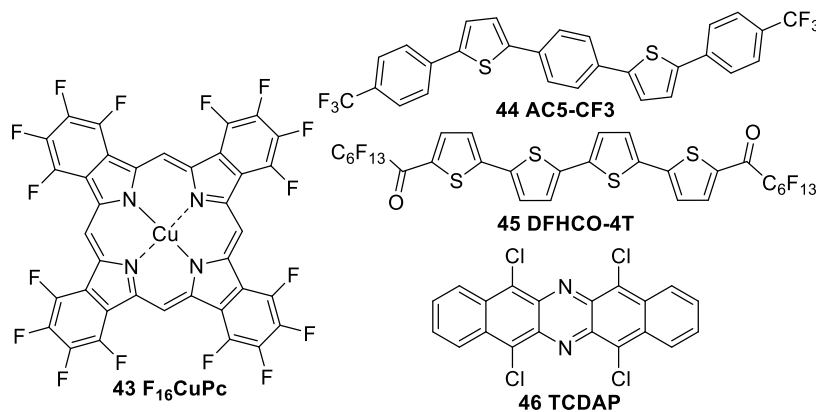
Naphthalene diimides (NDIs) were firstly applied in n-channel OFETs in 1996 with electron mobility reported around  $10^{-4} \text{ cm}^2 \text{ V}^{-1} \text{ s}^{-1}$ .<sup>[117]</sup> When cyclohexyl groups are introduced at the nitrogen positions of diimides in N,N'-bis(cyclohexyl)naphthalene-1,4,5,8-bis(dicarboximide) (**39**, Scheme 1-8), the electron mobility determined from vapor deposited thin film OFETs based on molecule **39** was improved to  $6.2 \text{ cm}^2 \text{ V}^{-1} \text{ s}^{-1}$  under argon.<sup>[118]</sup> Later, a new compound 2,6-Dichloro-1,4,5,8-naphthalene tetracarboxylic diimide ( $\text{Cl}_2$ -NDI, **40**, Scheme 1-8) endowed with fluoroalkyl chains at nitrogen positions of diimides, and chlorine atoms at the naphthalene core was synthesized.<sup>[119]</sup> Compound **40** showed excellent electron transport properties in ambient air with electron mobility up to  $4.26 \text{ cm}^2 \text{ V}^{-1} \text{ s}^{-1}$  achieved from OFETs based on the solution shearing films of **40**.<sup>[120]</sup> Moreover, remarkable high electron mobility in air up to  $8.6 \text{ cm}^2 \text{ V}^{-1} \text{ s}^{-1}$  was obtained from SCFETs of **40**.<sup>[121]</sup> Extension of the NDI planar core was another strategy to design high performance NDI derivatives, such as naphthalene diimides fused with 2-(1,3-dithiol-2-ylidene)malononitrile groups (NDI3HU-DTYM2, **41**, Scheme 1-8). The strong electron deficiency of the malonitrile moieties depressed the LUMO energy level of the molecule which could facilitate the injection of electron from electrode and improve the stability of molecule **41**. The mobility of  $3.5 \text{ cm}^2 \text{ V}^{-1} \text{ s}^{-1}$  was obtained from solution processed thin film OFETs of molecule **41** in air.<sup>[122]</sup>



Scheme 1-8: NDI and PDI derivatives as n-type materials.

Perylene diimides (PDIs) can be considered as NDI derivatives with larger  $\pi$ -conjugated system.<sup>[123]</sup> PDIs with different alkyl chains were therefore synthesized. First of all, thin film of N,N'-dioctyl-3,4,9,10-perylene tetracarboxylic diimides (PTCDI-C<sub>8</sub>, **42a**, Scheme 1-8) with C<sub>8</sub>H<sub>17</sub> yielded an electron mobility as high as 1.7 cm<sup>2</sup> V<sup>-1</sup>s<sup>-1</sup> when tested under a partial pressure of H<sub>2</sub> (10<sup>-4</sup> Torr).<sup>[124]</sup> But when tested in ambient air, mobility obtained from OFETs based on **42a** decreased to 0.36 cm<sup>2</sup> V<sup>-1</sup>s<sup>-1</sup>.<sup>[125]</sup> In order to increase the air stability of the molecule, fluorinated alkyl chains CH<sub>2</sub>C<sub>3</sub>F<sub>7</sub> were introduced to N positions of PDI and led to 2,2,3,3,4,4,4-heptafluorobutyl-substituted PDI (PTCDI-C<sub>4</sub>F<sub>7</sub>, **42b**, Scheme 1-8) which is an excellent n-type OSC with good air stability. Mobility of OFETs based on **42b** thin film measured in air can be as high as 1.24 cm<sup>2</sup> V<sup>-1</sup>s<sup>-1</sup>.<sup>[126]</sup> N,N'-1H,1H-perfluorobutyldicyanoperylene-carboxydiimide (PDIF-CN<sub>2</sub>, **42c**, Scheme 1-8) is one of the most successful PDI derivatives, with two cyano groups at 1 and 7 positions of PDI the LUMO energy level of **42c** decreased to -4.3 eV. Electron mobility of 1.3 cm<sup>2</sup> V<sup>-1</sup>s<sup>-1</sup> was measured in ambient conditions based on solution processed highly crystalline films of molecule **42c**.<sup>[127]</sup> In addition mobility of **42c** single crystals OFETs were found to be even higher, with values reaching 6 cm<sup>2</sup> V<sup>-1</sup>s<sup>-1</sup> and 3 cm<sup>2</sup> V<sup>-1</sup>s<sup>-1</sup> measured in vacuum and in ambient conditions respectively.<sup>[128]</sup>

### 1.3.3.2 Halogen-substituted N-type Materials

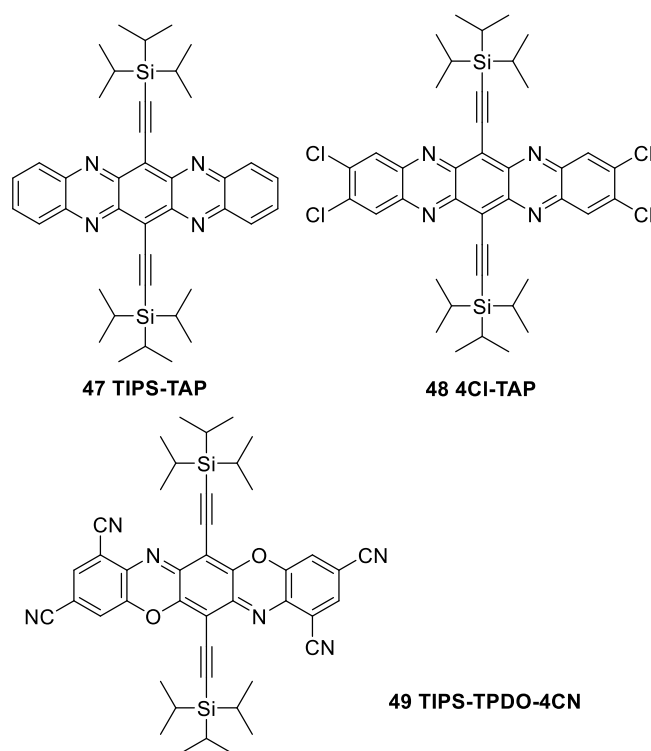


Scheme 1-9: Halogen-substituted n-type materials.

Many n-type OSCs with good performances involve halogen containing compounds. Halogen atoms especially fluorine atom has been widely used as substituent in n-type OSCs because of its electron withdrawing property and high stability in ambient conditions. P-type materials such as CuPc can be modified into n-type material by perfluorination.<sup>[129]</sup> Devices based on thin film of copper-hexadecafluorophthalocyanine (F<sub>16</sub>CuPc, **43**, Scheme 1-9) achieved electron mobility of 0.35 cm<sup>2</sup> V<sup>-1</sup>s<sup>-1</sup> in air.<sup>[130]</sup> Recent study showed that semiconducting property of F<sub>x</sub>CuPc could be tuned from p-type to ambipolar, and finally n-type by increasing the number of fluorine atoms on molecule geometries.<sup>[131]</sup>

Molecule 1,4-bis(5-(4-trifluoromethylphenyl)thiophene-2-yl)benzene (AC5-CF<sub>3</sub>, **44**, Scheme 1-9) is a trifluoromethyl end-capped alternating (thiophene/phenylene)-co-oligomer with good electron transport property. Mobility measured in vacuum of thin film OFET was 0.6 cm<sup>2</sup> V<sup>-1</sup>s<sup>-1</sup>, while 3.1 cm<sup>2</sup> V<sup>-1</sup>s<sup>-1</sup> can be achieved from single crystal OFET.<sup>[132]</sup> Furthermore, molecule α,ω-diperfluorohexylcarbonylquaterthiophene (DFHCO-4T, **45**, Scheme 1-9) is an oligothiophene derivative with carbonyl and fluoroethyl groups. Mobility measured in nitrogen atmosphere was 2 cm<sup>2</sup> V<sup>-1</sup>s<sup>-1</sup> for vacuum deposited thin film OFET.<sup>[133]</sup> On the other hand, introduction of halogen atoms into N-heteroacene is also an efficient strategy to construct n-type semiconductors. Compound 5,7,12,14-tetrachloro-6,13-diazapentacene (TCDAP, **46**, Scheme 1-8) is a chloro-substituted N-heteropentacene with high electron mobility of 3.39 cm<sup>2</sup> V<sup>-1</sup>s<sup>-1</sup> measured from single crystal OFETs in ambient.<sup>[134]</sup>

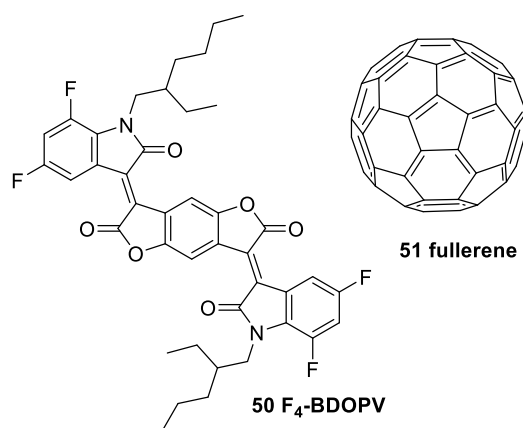
### 1.3.3.3 N-heteroacenes N-type Materials



Scheme 1-10: N-heteroacenes n-type materials.

As shown in part 1.3.2, acenes and S-heteroacenes are excellent p-type OSCs while some N-heteroacenes exhibit n-type property. Based on TIPS-PEN a well-known p-type OSC, compound 6,13-bis((triisopropylsilyl)ethynyl)-5,7,12,14-tetraazapentacene (TIPS-TAP, **47**, Scheme 1-10) was designed by replacing pentacene by N-heteropentacene.<sup>[135]</sup> High mobilities were obtained from vacuum deposited TIPS-TAP OFETs,  $3.3 \text{ cm}^2 \text{ V}^{-1}\text{s}^{-1}$  measured under vacuum and  $0.5 \text{ cm}^2 \text{ V}^{-1}\text{s}^{-1}$  measured in ambient.<sup>[136]</sup> Recently, the mobility has been increased to  $11 \text{ cm}^2 \text{ V}^{-1}\text{s}^{-1}$  measured under vacuum from solution processed TIPS-TAP OFETs,<sup>[137]</sup> and solution-grown single crystal arrays of TIPS-TAP exhibited electron mobility of  $13.3 \text{ cm}^2 \text{ V}^{-1}\text{s}^{-1}$  measured in  $\text{N}_2$  glovebox.<sup>[138]</sup> After halogenation of the tetraazapentacene tetrachloro TIPS-TAP (4Cl-TAP, **48**, Scheme 1-10) was obtained. The mobility measured under vacuum from solution processed OFETs of 4Cl-TAP was as high as  $27.8 \text{ cm}^2 \text{ V}^{-1}\text{s}^{-1}$  which is a new record for n-channel OFETs.<sup>[10]</sup> Triphenodioxazines (TPDOs) is also a decent fragment to construct n-type semiconductors.<sup>[139]</sup> A representative tetracyanotriphenodioxazine compound (TIPS-TPDO-4CN, **49**, Scheme 1-10) was synthesized in our laboratory and achieved electron mobilities of  $0.014$  and  $0.11 \text{ cm}^2 \text{ V}^{-1}\text{s}^{-1}$  for the spin coated and vacuum evaporated films in OFETs under ambient conditions.<sup>[140]</sup>

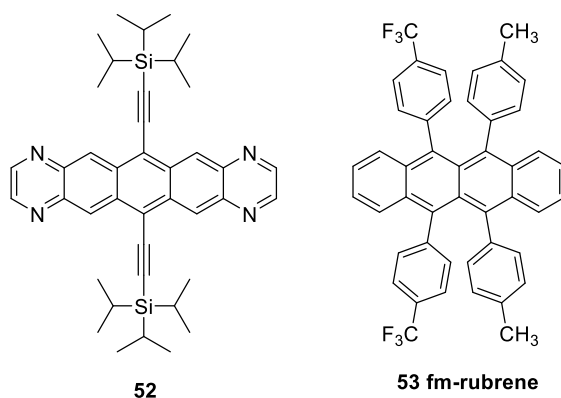
### 1.3.3.4 Other N-type Materials



Scheme 1-11: n-type semiconductors with high mobility.

Benzodifurandione-based oligo(p-phenylene vinylene) (BDOPV) has been used as a good n-type building block for OSCs due to its low LUMO level. Introduction of four fluorine atoms into BDOPV led to a new molecule ( $F_4$ -BDOPV, **50**, Scheme 1-11). Solution processed SCFETs based on  $F_4$ -BDOPV exhibited an electron mobility of  $12.6 \text{ cm}^2 \text{ V}^{-1} \text{ s}^{-1}$  in air, which is among the highest values for n-type OFETs.<sup>[141]</sup> Finally, the most well-known n-type semiconductor is fullerene ( $C_{60}$ , **51**, Scheme 1-11). Since its discovery in 1985,<sup>[142]</sup> fullerene and its derivatives have attracted tremendous attention as n-type OSCs.<sup>[143]</sup> Electron mobilities measured from  $C_{60}$  single crystal OFETs can be as high as  $11 \text{ cm}^2 \text{ V}^{-1} \text{ s}^{-1}$ ,<sup>[144]</sup> however OFETs based on  $C_{60}$  exhibited low stability upon exposure to air.<sup>[145]</sup> In order to improve the stability of the devices, a lot of  $C_{60}$  derivatives were synthesized, but their mobilities are significantly lower than  $C_{60}$  and vary between  $10^{-5}$  and  $10^{-3} \text{ cm}^2 \text{ V}^{-1} \text{ s}^{-1}$ .<sup>[146]</sup>

### 1.3.3.5 Ambipolar Semiconductors



Scheme 1-11: Ambipolar semiconductors with high mobility.

As illustrated before, it is difficult to efficiently inject both holes and electrons

from the same metal electrode due to the wide bandgaps (2–3 eV) of most OSCs. Although many molecules with ambipolar property have been reported, their performances are relatively low.<sup>[147–149]</sup> Finally, two impressive molecules with ambipolar property are demonstrated below. Molecule 6,13-bis((triisopropylsilyl)ethynyl)-1,4,8,11-tetraazapentacene (**52**, Scheme 1-12) is an isomer of **47** with different positions of N atoms. Compared to **47**, molecule **52** exhibited ambipolar property with hole mobility of  $0.22 \text{ cm}^2 \text{ V}^{-1} \text{ s}^{-1}$  and electron mobility of  $1.1 \text{ cm}^2 \text{ V}^{-1} \text{ s}^{-1}$  measured in vacuum.<sup>[136]</sup> Bis(trifluoromethyl)-dimethyl-rubrene (fm-rubrene, **53**, Scheme 1-12) is a rubrene derivative with two trifluoromethyl groups and two methyl groups.<sup>[150]</sup> It behaved as an ambipolar material in single crystal devices with a remarkable hole mobility up to  $4.8 \text{ cm}^2 \text{ V}^{-1} \text{ s}^{-1}$  and equally balanced electron mobility up to  $4.2 \text{ cm}^2 \text{ V}^{-1} \text{ s}^{-1}$  measured in vacuum.<sup>[151]</sup> Recently, more efforts have been done on device architectures to develop new strategies to achieve ambipolar charge transport in OFETs, such as using a blend of p- and n-type OSCs or forming a bilayer p-n junction composed of p-type and n-type OSCs.<sup>[152–154]</sup>

Molecules mentioned above together with their mobilities and measure conditions are summarized in Table 1-2. In summary, impressive progress has been made in the development of n-type organic semiconductors with electron mobilities higher than the values of amorphous silicon. However, available electron withdrawing building blocks for n-type organic semiconductors is still limited compared to electron donating building blocks. Moreover, poor stability of n-type OFETs under ambient conditions remains a critical issue to overcome in the future research of n-type OSCs.

Table 1-2. Representative n-type and ambipolar materials.

Type	Molecule	Mobility ( $\text{cm}^2 \text{ V}^{-1} \text{ s}^{-1}$ )	Device	Measure condition	Ref.
Naphthalene diimides (NDIs)	39	6.2	TF	under argon	[118]
	40 Cl <sub>2</sub> -NDI	4.26	TF	ambient air	[120]
		8.6			[121]
41 NDI3HU-DTYM2	3.5	TF	ambient air	[122]	
Perylene diimides (PDIs)	42a PTCDI-C <sub>8</sub>	1.7	TF	under hydrogen	[124]
		0.36	TF	ambient air	[125]
	42b PTCDI-C <sub>4</sub> F <sub>7</sub>	1.24	TF	ambient air	[126]
	42c PDIF-CN <sub>2</sub>	1.3	TF	ambient air	[127]
6		SC	vacuum	[128]	
Halogen-substituted	43 F <sub>16</sub> CuPc	0.35	TF	ambient air	[130]
	44 AC5-CF3	0.6	TF	vacuum	[132]



Type	Molecule	Mobility ( $\text{cm}^2 \text{V}^{-1} \text{S}^{-1}$ )	Device	Measure condition	Ref.
molecules		3.1	SC	vacuum	
	45 DFHCO-4T	2	TF	under nitrogen	[133]
	46 TCDAP	3.39	SC	ambient air	[134]
N-heteroacenes	47 TIPS-TAP	3.3	TF	vacuum	[135]
		0.5	TF	ambient air	[136]
		11	TF	vacuum	[137]
		13.3	SC	vacuum	[138]
	48 4Cl-TAP	27.8	TF	vacuum	[10]
	49 TIPS-TPDO-4CN	0.014 0.11	TF TF	ambient air ambient air	[140]
Other materials	50 F <sub>4</sub> -BDOPV	12.6	SC	ambient air	[141]
	51 C <sub>60</sub>	11	SC	vacuum	[144]
ambipolar	52	$\mu_h = 0.22$	TF	vacuum	[136]
		$\mu_e = 1.1$	TF	vacuum	
	53 fm-rubrene	$\mu_h = 4.8$ $\mu_e = 4.2$	SC SC	Vacuum vacuum	[151]

## 1.4 Two-dimensional and Three-dimensional Conjugated Molecules

### 1.4.1 Dimensionality Concept for Molecular Structure and Charge Transport in OFETs

1D conjugated molecules are molecules with linear-shaped molecular structure in which  $\pi$ -conjugation (alternating single and double bonds) extends only in one direction, such as tips-pentacene. 2D conjugated molecules are molecules with planar-shaped molecule structure in which  $\pi$ -conjugation extends in two directions and forms a planar conjugated system, such as phthalocyanine derivatives. 3D conjugated molecules are molecules with  $\pi$ -conjugation extending in three directions of the 3D space, such as sphere-shaped fullerene derivatives.

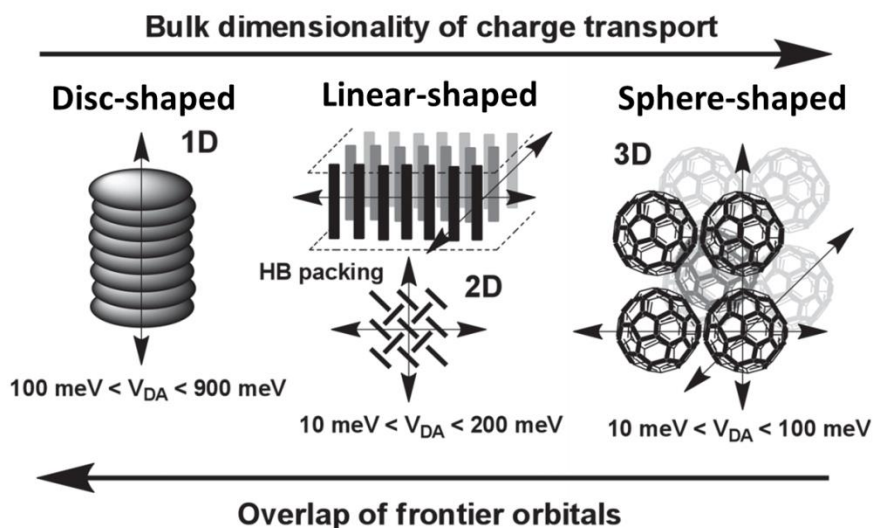


Figure 1-11. 1D, 2D, and 3D charge carrier transport with indicative values of transfer integrals.<sup>[155]</sup>

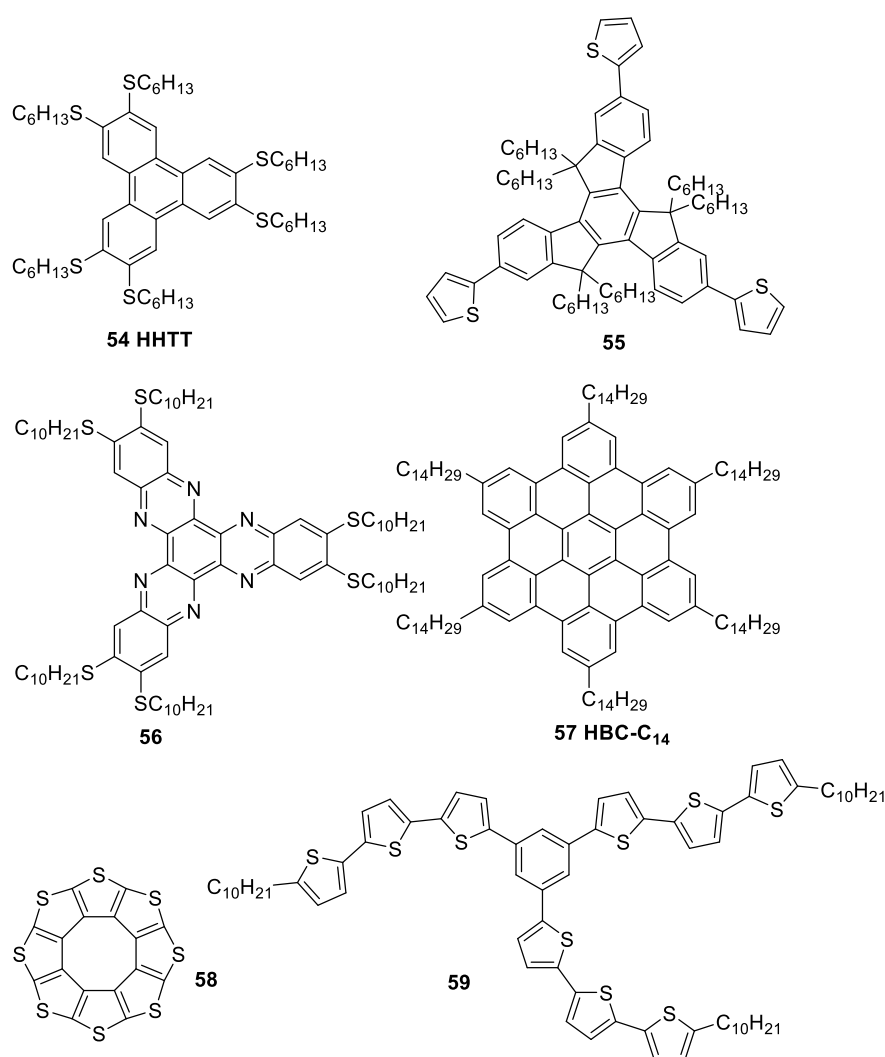
The concept of dimensionality has been widely used in both molecular conjugated dimensionality and bulk charge transport dimensionality, but the meanings behind these two expressions are different. As shown in figure 1-11, disc-shaped molecules are 2D conjugated molecules, but most of the disc-shaped molecules tend to self-assemble into 1D columnar liquid crystal due to the strong face-to-face intermolecular interactions.<sup>[156]</sup> Consequently, this kind of 1D columnar packing generally leads to a 1D charge transport.<sup>[157]</sup> In contrast, some linear-shaped molecules which are 1D conjugated systems can give out 2D charge transport by forming a herringbone or bricklayer packing. The best known examples are rubrene and TIPS-PEN.<sup>[158]</sup> We will summarize 2D and 3D conjugated molecules reported so far in part 1.4, and discuss about strategies to achieve 3D charge transport pathway in part 1.5.

When applied linear-shaped molecules into electronic devices, the unidimensionality of these linearly  $\pi$ -conjugated systems causes a strong anisotropy of electronic properties. For example, in OFET the high mobility can only be observed in one particular direction. Consequently, besides tight molecule packing and strong intermolecular interactions, precise control of the molecule orientation on the substrate become more important. A lot of work has been done to control molecule orientation on substrate, such as chemical decorations of linear alkyl chains at both ends of the molecules, precise control of the thermal evaporation conditions and surface's modification of the substrate by thin layer of organic materials and self-assembled monolayer (SAMs). Although some of these methods worked well for controlling molecule orientation, all these methods complicated the device fabrication

process. Moreover, in OLED and OPV technology, when the active layer is a mixture, the charge transport doesn't follow a straight line. In these cases, the unidimensionality of the transport is detrimental for device performances.

As illustrated before, balanced charge transport in multi dimensions should improve the performance of OFETs. However, in all kinds of packing motifs, 1D conjugated molecule can only achieve 1D and 2D charge transport.<sup>[159]</sup> To go further and reach 3D charge transport, it will be wise to consider the extension to the 2D and 3D conjugated compounds. Indeed, the higher conjugation dimensionality allows greater structure variations.

## 1.4.2 Two-dimensional Conjugated Molecules



Scheme 1-12: Two-dimensional conjugated molecules.

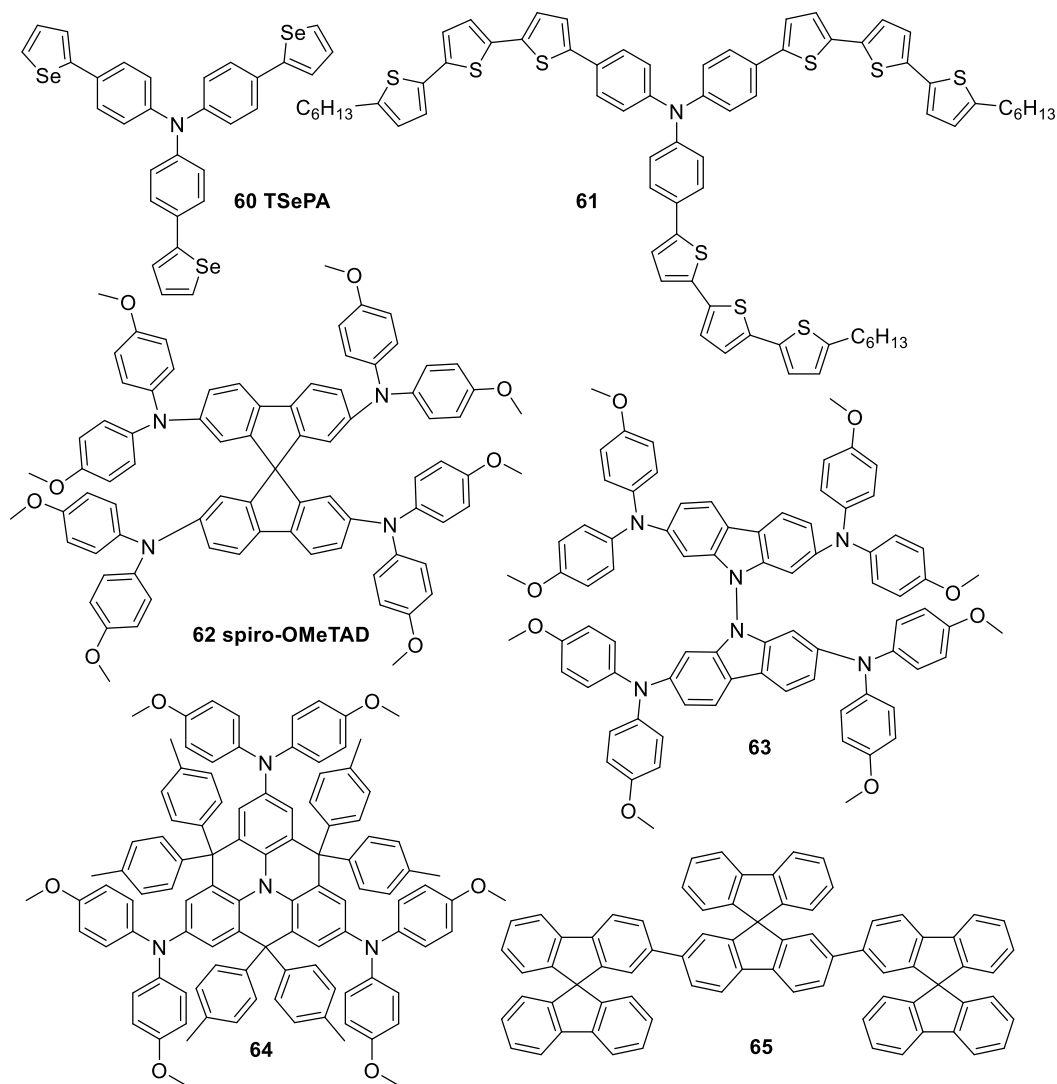
Started from the linear-shaped molecules, in order to increase the conjugation dimensionality, a very straightforward strategy is to add fused benzene rings in all directions to form extended  $\pi$ -conjugated plane. Thus, graphene is the best example of

2D conjugated OSCs, which is composed of 2D fused benzene rings, with mobility as high as  $200,000 \text{ cm}^2 \text{ V}^{-1} \text{ s}^{-1}$ .<sup>[160]</sup> A lot of small 2D conjugated molecules were designed and synthesized. For example, triphenylene which has the same number of benzene rings as tetracene, has a star-shaped planar molecular structure. 2,3,6,7,10,11-Hexahexylthiotriphenylene (HHTT, **54**, Scheme 1-12) is a representative triphenylene derivative with high hole mobility of  $0.1 \text{ cm}^2 \text{ V}^{-1} \text{ s}^{-1}$  in liquid crystalline phase.<sup>[161]</sup> Another way to form a star-shaped molecule is to use truxene as the core of the molecule. Many molecules based on truxene were synthesized, but their mobilities measured in OFETs are relatively modest.<sup>[162]</sup> For example, hole mobility obtained from solution-processed OFETs of thiophene-functionalized truxene (**55**, Scheme 1-12) was  $1.03 \times 10^{-3} \text{ cm}^2 \text{ V}^{-1} \text{ s}^{-1}$ .<sup>[163]</sup> In order to develop n-type OSCs, many hexazatrinaphthylene (HAT) derivatives were synthesized.<sup>[164]</sup> The highest mobility achieved so far was obtained from HAT derivatives with six decylsulfanyl chains (**56**, Scheme 1-12) with a value of  $0.9 \text{ cm}^2 \text{ V}^{-1} \text{ s}^{-1}$  by means of the pulse-radiolysis time-resolved microwave conductivity technique.<sup>[165]</sup> However, most of these compounds are referred to as discotic molecules due to their propension to form columnar packing that can ensure at least high mobility along the columnar packing direction. They are usually designed as a large flat  $\pi$ -conjugated system with linear alkyl chain to ensure solubility. By this way, the best intermolecular interaction is obtained when molecules face each other. Another good example of discotic molecules are hexabenzocoronene (HBC) derivatives.<sup>[166]</sup> Hole mobility measured from HBC-C<sub>14</sub> (**57**, Scheme 1-12) single crystal OFETs exceeded  $1.0 \text{ cm}^2 \text{ V}^{-1} \text{ s}^{-1}$ .<sup>[167]</sup> A novel planar molecule cyclic oligothiophenoacene (**58**, Scheme 1-12) with interesting molecule structure was synthesized. However mobility measured from thermal deposited thin film OFETs of **58** was only  $7.5 \times 10^{-4} \text{ cm}^2 \text{ V}^{-1} \text{ s}^{-1}$ .<sup>[168]</sup> Star-shaped oligothiophenes are 2D conjugated molecules. Solution processed OFETs made from molecule **59** (Scheme 1-12) exhibited a mobility of  $2 \times 10^{-4} \text{ cm}^2 \text{ V}^{-1} \text{ s}^{-1}$ .<sup>[169]</sup> Although mobilities obtained from these compounds are relatively low, functionalized star-shaped oligothiophenes are widely used in OPV and perovskite solar cells as hole transporting materials due to their high flexible molecule structure.<sup>[170]</sup>

### 1.4.3 Three-dimensional Conjugated Molecules

As illustrated before, the best example of 3D conjugated molecule is fullerene which has sphere-shaped molecule architecture with high mobility of  $11 \text{ cm}^2 \text{ V}^{-1} \text{ s}^{-1}$ , but the poor air stability and high synthetic cost of fullerene derivatives limit their application in industry.<sup>[171,172]</sup> Beside fullerene, triphenylamine (TPA) derivatives are also representative examples of 3D conjugated molecules.<sup>[173]</sup> Steric interactions between phenyl groups lead to a nonplanar propeller shape of TPA which is a

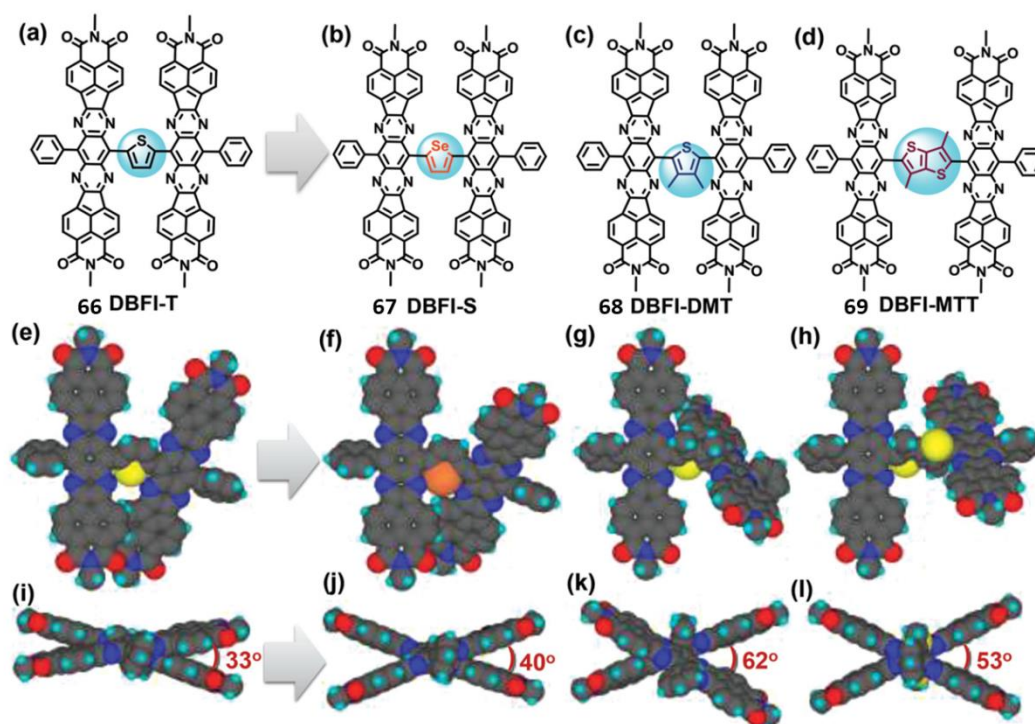
resistance to the crystallization of the compounds. Nonetheless amorphous thin film OFETs of molecule tris[4-(2-selenyl)phenyl]amine (TSePA, **60**, Scheme 1-13) could still give out a high hole mobility of  $0.015 \text{ cm}^2 \text{ V}^{-1} \text{ s}^{-1}$ .<sup>[174]</sup> Spin coating OFETs of triphenylamine-oligothiophene **61** (Scheme 1-13) exhibited a hole mobility of  $0.011 \text{ cm}^2 \text{ V}^{-1} \text{ s}^{-1}$ .<sup>[175]</sup>



Scheme 1-13: Three-dimensional conjugated molecules.

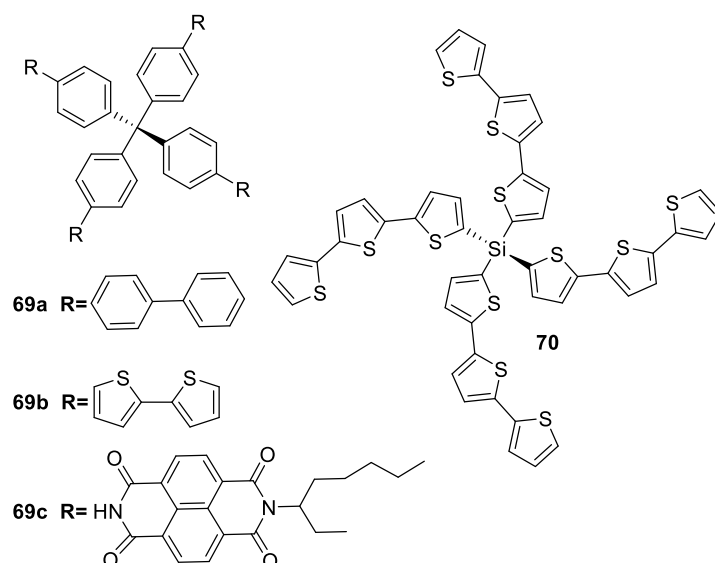
Another famous 3D conjugated molecule is spiro-OMeTAD (**62**, Scheme 1-13) that have been widely used as hole transport material in perovskite solar cells.<sup>[176]</sup> Spirobifluorene units constituting the central part of spiro-OMeTAD thus give the molecule a highly twisted architecture. Mobility of pristine spiro-OMeTAD measured using a space-charge limited current (SCLC) method was around  $9 \times 10^{-5} \text{ cm}^2 \text{ V}^{-1} \text{ s}^{-1}$ .<sup>[177]</sup> Similar molecules with highly twisted central core **63** and **64** (Scheme 1-13) were synthesized with mobility of  $9.5 \times 10^{-5}$  and  $1.4 \times 10^{-4} \text{ cm}^2 \text{ V}^{-1} \text{ s}^{-1}$  respectively.<sup>[178]</sup> Although mobilities achieved from these molecules were low, both materials in the

presence of dopants were applied with success in perovskite solar cells with PCEs reaching up to 16.4% and 17.6%, respectively. A ter(9,9-diarylfuorene) molecule (**65**, Scheme 1-13) composed of spirofluorene units was synthesized and reported as an ambipolar OSC. Hole mobility of  $4 \times 10^{-3} \text{ cm}^2 \text{ V}^{-1} \text{ s}^{-1}$  and electron mobility of  $1 \times 10^{-3} \text{ cm}^2 \text{ V}^{-1} \text{ s}^{-1}$  were measured from vacuum deposited thin film of **65**, by time-of-flight (TOF) transient photocurrent method.<sup>[179]</sup>



Scheme 1-14: Molecular structures (a–d) and the corresponding top view (e–h) and side view (i–l) of the optimized geometries of DBFI-Ars using DFT calculations (B3LYP/6-31G(d)).<sup>[180]</sup>

In 2015 Haiyan Li *et al.* reported a series of molecules (**66**, **67**, **68**, **69**; DBFI-T, DBFI-S, DBFI-DMT, DBFI-MTT; Scheme 1-14) composed of two 7,9,16,18-tetraazabenzodifluoranthene-3,4,12,13-tetracarboxylic acid diimide (BFI) moieties connected by arylene (Ar) linker with nonplanar 3D conformation.<sup>[180]</sup> OFETs based on spin-coating thin films of **68** and **69** exhibited high electron mobility of 0.056 and 0.043  $\text{cm}^2 \text{ V}^{-1} \text{ s}^{-1}$ , relatively higher than that of **66** and **67** ( $0.002 \text{ cm}^2 \text{ V}^{-1} \text{ s}^{-1}$ ).<sup>[181]</sup> Optimized geometries of DBFI-Ars using DFT calculations (B3LYP/6-31G(d)) are shown in Scheme 1-14, showing that the 3D conformation of DBFI-Ar dimer molecules is tuned by choice of the central Ar linker and molecule **68** exhibits the largest interplanar angle between two BFI units. Moreover, these materials were used as nonfullerene acceptors in organic solar cells, and the highest PCE of 6.4% was obtained from **68** which has the largest interplanar angle and electron mobility.



Scheme 1-15: Three-dimensional conjugated molecules with tetrahedral geometry.

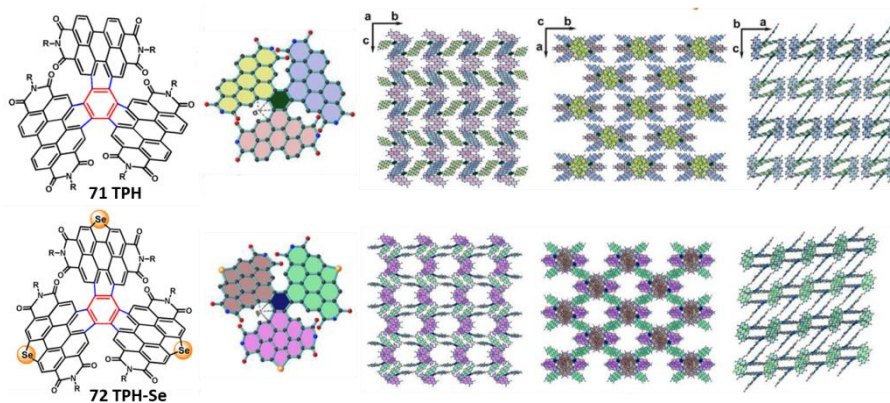
Another strategy to achieve 3D conjugated molecule is attaching 4 conjugated chains onto a tetrahedral central node. The defect of this kind of design is that the generally used central node is silicon or  $sp^3$  carbon, which means the conjugation of the whole molecule is interrupted by the central node. But we have to notice that the probability that a charge tunnels through an  $sp^3$  carbon connecting four conjugated segments might be greater than we could imagine.<sup>[182]</sup> Molecule **69 (a-c)** (Scheme 1-15) were synthesized using tetraphenylmethane as a tetrahedral central core.<sup>[183,184]</sup> Molecule **69a** and **69b** are supposed to be p-type OSCs while molecule **69c** with four naphthalenediimide moieties should exhibit n-type property. Electron mobility of  $0.03 \text{ cm}^2 \text{ V}^{-1}\text{s}^{-1}$  was obtained from spin-coating thin film OFETs of molecule **69c**.<sup>[185]</sup> Finally, 3D conjugated molecules with silicon central node such as molecule **70** (Scheme 1-15) was synthesized, but no mobility data was reported so far.<sup>[186,187]</sup>

## 1.5 Molecular Design for 3D Charge Transport

Molecules discussed in part 1.4 possess 2D or 3D conjugated molecular architectures, but the achievement of an actual 3D charge transport still remains a huge challenge. For example, 2D conjugated “disc-shaped” molecules can only form 1D charge transport by dense face to face  $\pi$ -stacking without frontier orbital interaction on the side. Meanwhile, 3D conjugated molecules described in part 1.4 are mostly highly twisted molecules which are difficult to crystallize and mobilities measured from their amorphous films were relatively modest. Finally, there are few factors that limit the 3D charge transfer measurement: 1) most packing motifs favor 1D or 2D

pathway for charge transport; 2) charge transport measuring methods only allow the measurement in 1D (OFET, SCLC...); 3) highly twisted molecules can be hardly crystallized; 4) crystals cannot be implemented in devices in all directions

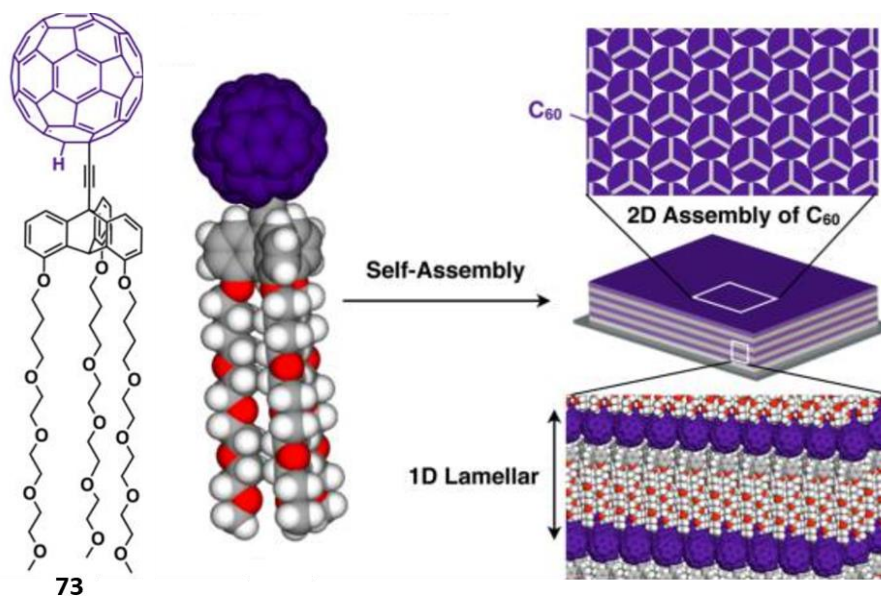
In this section, we will discuss about molecules with 3D charge transport pathway in the crystalline phase and with high charge carrier mobility. It is worth noticing that mobility of single crystal is highly dependent on molecular packing. For instance, a very small molecule as 4-hydroxycyanobenzene (4HCB) showed decent mobility along two of the three crystallographic axes *a* and *b*,  $8 \times 10^{-2}$  and  $9 \times 10^{-3} \text{ cm}^2 \text{ V}^{-1} \text{ s}^{-1}$  for  $\mu_a$  and  $\mu_b$ , respectively.<sup>[188]</sup>



Scheme 1-16: Three-dimensional charge transfer packing motif of TPH and TPH-Se.<sup>[189]</sup>

A good example of 3D charge transport was published by Dong Meng *et al.* in 2016.<sup>[189]</sup> Two  $C_3$ -symmetric propeller-shaped molecules, triperylene hexaimides (TPH, **71**, Scheme 1-16) and selenium annulated triperylene hexaimides (TPH-Se, **72**, Scheme 1-16), were synthesized. Single-crystal X-ray diffraction studies show that a unique 3D network assembly is achieved in both TPH and TPH-Se single crystals in which each conjugated PBI blade of the propeller has dense  $\pi$ - $\pi$  stacking with the PBI blade of another neighboring molecule. Single-crystal OFETs were fabricated from drop-casting and “organic ribbon mask” technique.<sup>[190]</sup> High electron mobilities up to  $0.028 \text{ cm}^2 \text{ V}^{-1} \text{ s}^{-1}$  and  $0.032 \text{ cm}^2 \text{ V}^{-1} \text{ s}^{-1}$  were obtained for TPH and TPH-Se respectively. Combined with their broad and strong absorption ability, TPH and TPH-Se were used as non-fullerene acceptors in organic solar cells and high power conversion efficiency of 8.28% and 9.28% were achieved. Even though the mobility has not been measured in all directions on a single crystal, the high efficiency in OPV combined with the nature of the single crystal structure suggest that the charge transport balance over 3D has been improved.





Scheme 1-17: Three-dimensional charge transfer packing motif of  $2_{\text{TEG}}$ .<sup>[191]</sup>

Franco King-Chi Leung *et al.* reported a tripodal triptycene derivative ( $2_{\text{TEG}}$ , **73**, Scheme 1-17) with isotropic charge-transport property in 2016.<sup>[191]</sup> The bridgehead-substituted tripodal triptycenes self-assembled into a “2D hexagonal + 1D lamellar” structure.<sup>[192]</sup>  $\text{C}_{60}$  which is comparable in diameter to the triptycene framework was introduced in  $2_{\text{TEG}}$  to ensure the mobilities in two directions which are parallel to the surface of the substrate.<sup>[193]</sup> In the end, the mobility of the spin coating film of  $2_{\text{TEG}}$  along the direction parallel to the substrate surface was  $1.0 \times 10^{-2} \text{ cm}^2 \text{ V}^{-1} \text{ s}^{-1}$ , while the mobility in the perpendicular direction was  $1.9 \times 10^{-3} \text{ cm}^2 \text{ V}^{-1} \text{ s}^{-1}$ , measured by flash-photolysis time-resolved microwave conductivity (FP-TRMC) measurements.

## 1.6 Conclusion

In summary, **molecular structure, packing motif and energy level** are three crucial factors about an OSC which are tightly connected. Moreover, they deeply affect theoretical parameters such as reorganization energy, transfer integral, energy level and transport pathway, along with experimental performances of devices such as charge carrier mobility in OFETs and overall energy photoconversion yield in OPVs. Over molecular design consideration, other factors such as purity of materials, use of additives and morphology of the active layers (crystallinity, grain boundary, film thickness...) also affect greatly the device performances. Some of these parameters are summarized in the following.

## 1.6.1 Molecular Structure

Firstly, the basic requirement for high mobility OSCs is to have a molecule structure which possesses a  $\pi$ -conjugated backbone. For instance, fused acenes are promising building blocks as framework for high mobility OSCs by limitation of reorganization energy.<sup>[7,72]</sup> Extension of  $\pi$ -conjugation system can also be an effective strategy to increase intermolecular couplings.<sup>[194]</sup> However, acenes longer than pentacene are poorly stable and soluble. A straightforward approach to solve this problem is to extend the  $\pi$ -conjugation system in different directions such as in star-shaped or disc-shaped molecules. This strategy will not only stabilize the molecules with big  $\pi$ -conjugation system but also increase the  $\pi$ -conjugated dimensionality of the molecules. Secondly, to be able to solubilize the materials, substitutions on the conjugated backbone is necessary. Besides increasing solubility of the molecules, suitable substituents at appropriate positions can modulate the molecular packing mode and frontier orbital energy levels. For example, introduction of two triisopropylsilylethynyl (tips) groups on pentacene leads to a 2D bricklayer packing in tips-pentacene. Thirdly, introduction of heteroatoms in conjugated backbones such as sulfur and nitrogen atoms is a good way to modify the properties of OSCs. Introduction of heteroatoms can induce novel intermolecular interactions (S- $\pi$ , O-H, or N-H, etc.) which is favorable to obtain dense molecular packing and modify the aromaticity of the  $\pi$ -systems.

## 1.6.2 Molecular Packing

In organic semiconductors, charge carriers transport occurs along  $\pi$  orbitals. Therefore, the  $\pi$  orbital overlap degree of neighboring molecules significantly determines the mobility. So far, four dominating packing motifs were found in OSCs, herringbone packing, cofacial herringbone packing, 1D slipped-stack arrangement and 2D bricklayer arrangement. Theoretically speaking, molecular packing with strong intermolecular overlaps such as face-to-face  $\pi$ - $\pi$  stacking is favorable for efficient charge carrier transport. However when the edge-to-face interactions are strong enough some molecules with herringbone and cofacial herringbone packing can also give out high mobility, such as pentacene and rubrene. Limited from 1D charge carrier transport pathway, cofacial herringbone packing and 1D slipped-stack arrangement can only provide high mobility in one direction. Due to the increase of charge transport dimensionality, molecules with 2D bricklayer arrangement with strong  $\pi$ - $\pi$  stacking should provide high mobility. But so far most of the OSCs exhibiting high mobility are still those with herringbone and cofacial herringbone packing. Therefore, in terms of predicting mobility value for a molecule, additional affecting factors should be considered. Meanwhile more OSCs need to be synthesized and analyzed to

study the structure-packing-mobility relationship.

### 1.6.3 Energy Levels

As mentioned in the previous sections, holes move along the HOMOs of neighboring molecules for p-type OSCs and electrons transfer along the LUMOs of neighboring molecules for n-type OSCs. Therefore, HOMO and LUMO energy levels play an important role for charge injection and transport in OSCs. Meanwhile HOMO and LUMO energy levels determine the environmental stability of the molecules. Hence, it is important to design molecules with suitable HOMO, LUMO energy levels and band gaps. For p-type materials, the HOMO levels should be distributed typically from -4.9 to -5.5 eV, while for n-type materials the LUMO levels should be normally located from -3 to -4 eV to obtain stable OSCs for common architecture in OFETs and OPVs. In order to operate in ambient conditions, a narrow scale is required to tolerate water and dioxygen. A simple example to tune the energy levels of OSCs is to use substituents with electron-releasing or electron-withdrawing ability. Incorporation of electron-donating groups (such as double carbon-bond or chalcogen atoms) in the molecules can higher the HOMO energy levels, and result in air-stable p-type OSCs. While introducing electron-withdrawing groups to stabilize the organic anions against oxygen and water is an effective approach to obtain highly stable n-type semiconductors.

### 1.6.4 Other Factors

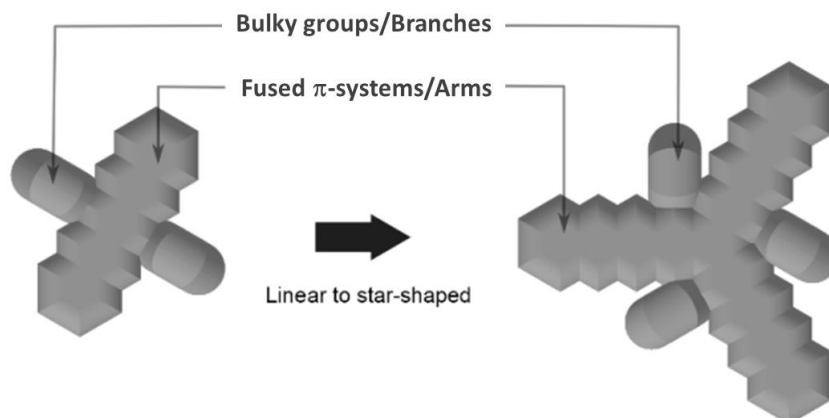
Purity of OSCs is an important factor, because impurities can severely lower the mobility of OFETs. For instance, purification of materials by gradient sublimation has led to improved performances for the devices. Furthermore, additives are added to spiro-derivatives in perovskites solar cell to increase mobility in hole transport layer. Film morphology can also affect the charge transport and OFET performances drastically. For thin film OFETs, better charge transport has been obtained with polycrystalline thin films compared to amorphous thin films. In crystalline thin films, charge hopping across the grain boundaries should be more difficult than charge transfer within ordered domains. Hence, increasing grain sizes in crystalline thin films or improving the charge transfer between grains represents a promising approach to improve OFETs mobility.<sup>[195]</sup> Numerous methods, including optimizing interface quality (such as decoration the interfaces with self-assembled monolayers),<sup>[196]</sup> film treatments (such as thermal or solvent annealing)<sup>[197]</sup> and other strategies<sup>[198,199]</sup> have been introduced to control the morphology of organic thin films. Finally, the mobility records are mostly observed from devices made of single crystal or well-aligned large crystals.

The continuous advances in the field of OSCs speed up the commercialization of

organic electronic devices. However, there are still some fundamental issues that need to be better understood in OSCs, such as chemical structure-packing-mobility relationship and guides for rational design of OSCs with good performance. Among all these topics, achievement of a balanced and efficient 3D charge transport remains a big challenge as well as the experimental determination of mobility over 3D with single crystals.

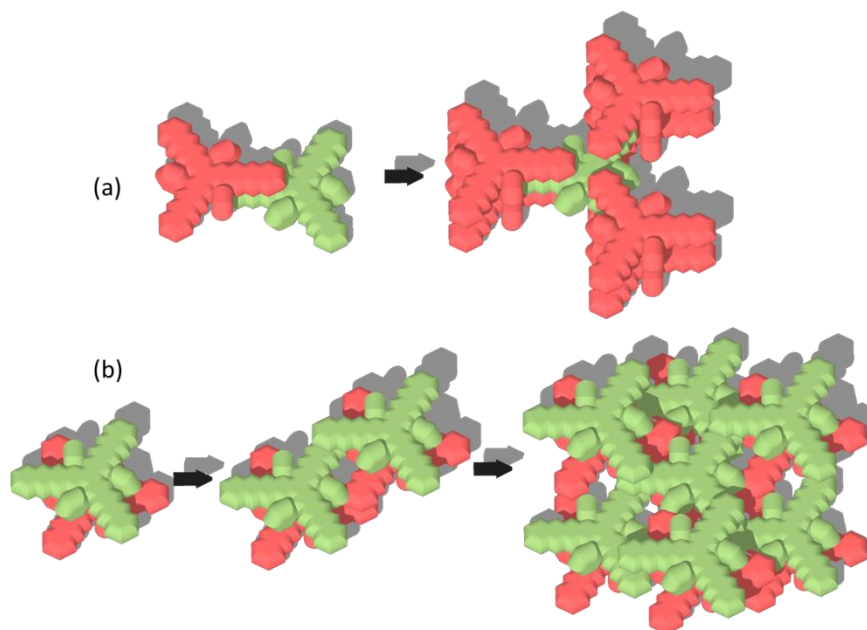
## 1.7 Objectives of This Research

Based on the works and remaining issues about OSCs discussed above, we designed a series of star-shaped molecules to achieve a 3D charge carrier transport pathway in their crystalline phase. Our design strategy is to expand the linear-shaped molecule structure to star-shaped structure, as shown in Scheme 1-18. The design strategy is inspired by Anthony's research on pentacene derivatives. In these pioneer works, the introduction of bulky groups on the central fused benzene ring of pentacene yielded face-to-face  $\pi$ -stacking with large translation along the long molecular axis.<sup>[200]</sup> In some cases, the packing displayed a brick-wall arrangement which increased the charge transport dimensionality into two directions.<sup>[201–203]</sup> This versatile idea has been successfully applied to other fused and linear  $\pi$ -conjugated molecules to reach high performances in OFETs.<sup>[204–207]</sup> With the objective of designing new 3D charge transport materials, we applied similar ideas to star-shaped molecules with  $C_{3h}$  symmetry. The molecules consist of planar core of fused aromatic cycles (referred to as “arms” in the following) and of bulky groups located close to the center (referred to as the “branches”). In this structure,  $\pi$ -conjugated arms are supposed to form efficient  $\pi$ - $\pi$  stacking with neighboring molecules and branches with large steric hindrance are introduced to increase the solubility of the materials, prevent 1D columnar packing and adjust  $\pi$  orbital overlaps and packing distances.



Scheme 1-18. Design strategy of star-shaped molecules.

Based on the structures of the molecules we have designed, two supramolecular arrangements leading to 3D charge transport can be speculated. As shown in scheme 1-19, firstly two molecules can pack either through extended  $\pi$ -stacking along the arms (a “arm packing”) or on top of each other (b “column packing”) to form the first dimer. Extended to larger aggregates, both of these packing modes involve face-to-face  $\pi$ -stating between the central molecule and six neighbors in different directions, so that 3D charge transport pathways might be achieved.



Scheme 1-19. Representative views of speculated molecular arrangements. The two different packing modes are generated from a first dimer obtained either by an extended  $\pi$ -stacking along the arms (“arm packing”) (a) or by staking molecules on top of each other (“column packing”) (b).

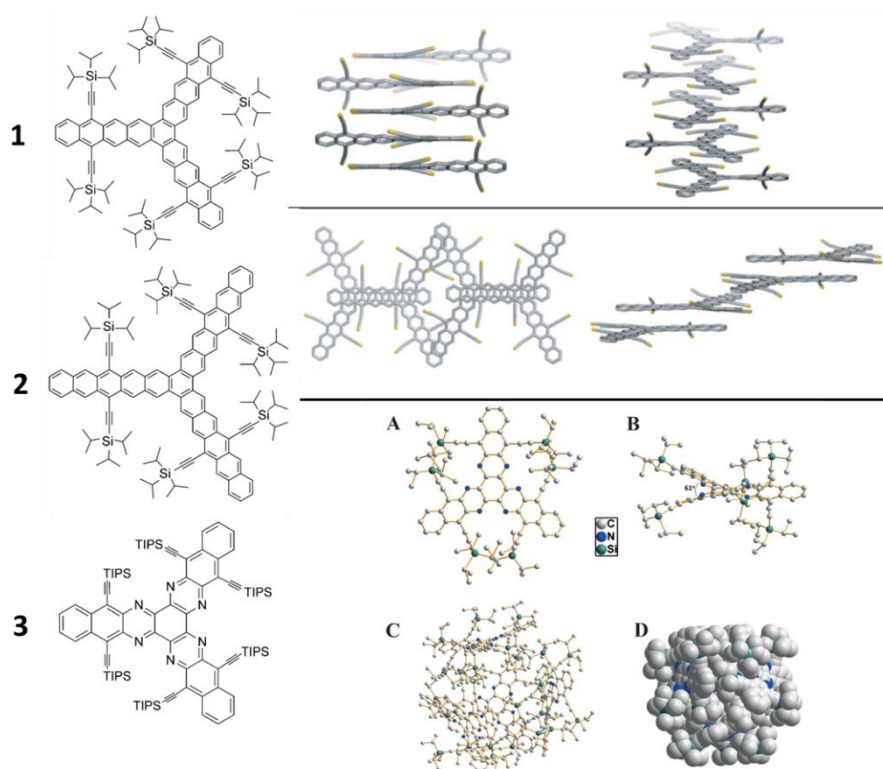
As a consequence, the research objectives of this work are: i) to synthesize star-shaped molecules as designed; ii) to characterize their optical and electronic properties; iii) to study their molecular packing by single crystal X-ray diffraction; iv) to estimate charge transport properties of the molecules by theoretical calculation; v) to characterize charge transport properties of the molecules by fabricating electronic devices. Last but the most important step is to optimize molecule structures to get the packing motif as designed and study about the structure-packing-mobility relationship.

**Chapter 2:**  
**Triazastarphene Substituted by NH as Hole**  
**Transport Materials**



## 2.1 Introduction

As we have mentioned at Chapter 1, we have designed a series of star-shaped molecules which are expected to show a particular packing in the crystalline phase to achieve a 3D charge carrier transport pathway. These star-shaped molecules are composed of a  $\pi$ -conjugated central core and several branches to increase the solubility of the materials. Previous studies proved that both starphenes and hexaazatriphenylene (HAT) derivatives can constitute OSCs with good charge transport mobility and molecular stability.<sup>[208]</sup>

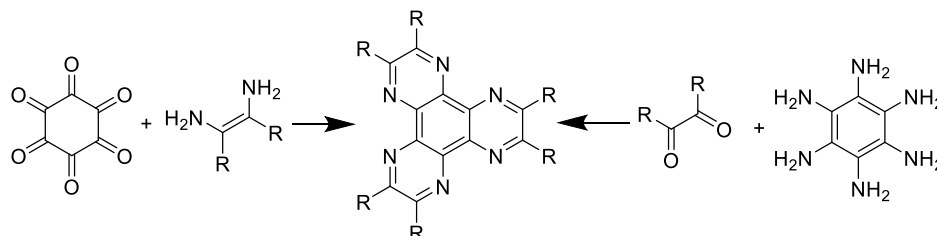


Scheme 2-1. Molecule structures and molecular packings of starphenes and hexaazatriphenylene (HAT) derivatives.<sup>[209] [210]</sup>

In 2014 Elias *et al.* reported two starphene molecules **1** and **2** (Scheme 2-1) with silyl groups as branches which can be considered as star-shaped counterparts of tips-pentacene.<sup>[209]</sup> A tremendous work about linear-shaped acenes and heteroacenes have been done by Anthony and co-workers, and they found out that a very small difference in the molecular structure can cause huge changes in the crystal structure.<sup>[211,212]</sup> The same phenomenon was found for star-shaped molecules, for instance, molecules **1** and **2** which have similar molecular structures but their packing motives in crystalline phase are different. Molecule **1** formed a 1D slipped-stacked arrangement with overlaps between two of the three arms while the third arm of the molecule is twisted out of the plane. Molecule **2** also formed a 1D slipped-stacked

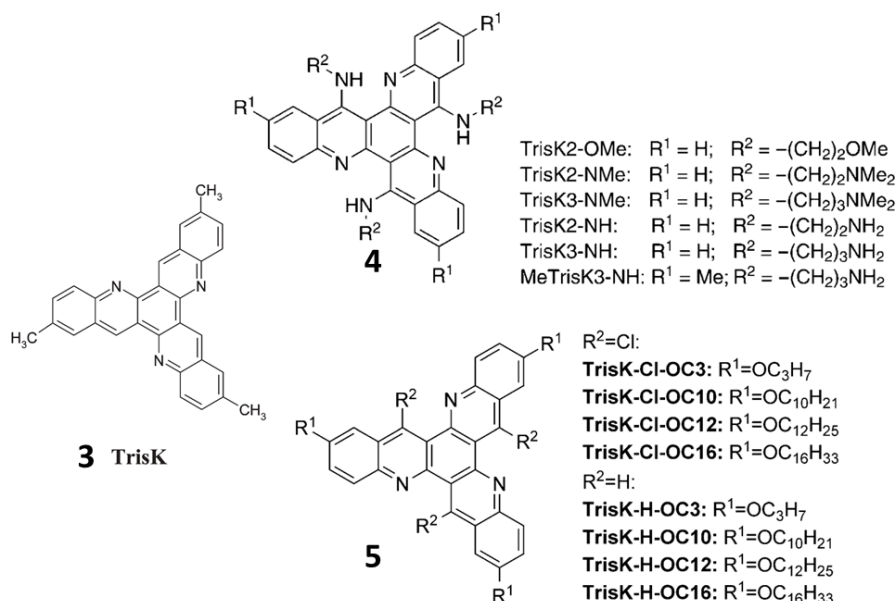


arrangement in which for each molecule there are one large overlap with one planar arm and two small overlaps with two twisted arms. About the synthesis of large starphenes, the difficulty is to keep the intermediate soluble during the process.<sup>[213]</sup> In this paper, molecules **1** and **2** were synthesized from tips-ethynyl-dibromoacene derivatives by using Yamamoto coupling conditions in the last step to avoid insoluble intermediate.



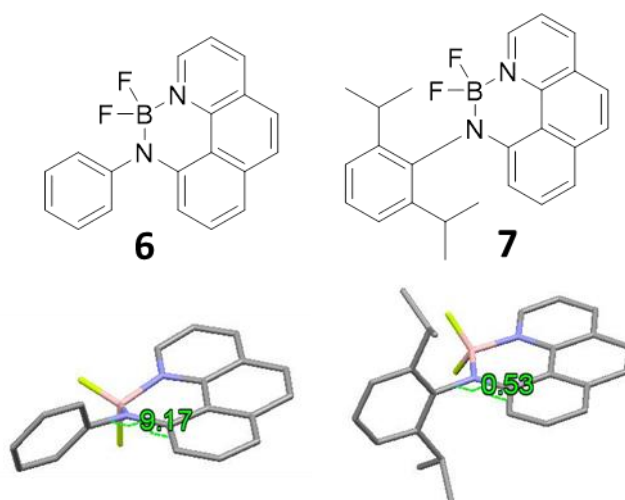
Scheme 2-2. Two synthetic approaches to HAT derivatives

In general, fused aromatic systems containing heteroatoms, could be obtained more easily than their all-carbon counterparts. In 2016 Junbo *et al.* reported a hexazatrianthrylene (HAT) derivative **3** (Scheme 2-1) with good solubility and stability.<sup>[210]</sup> The highly twisted molecule structure leads to a cage-shaped crystal packing motif. Thus, in order to get the packing motif as we designed, it is necessary to reduce the volume and the number of branches to lower the intramolecular steric hindrance. For the synthesis of HAT derivatives, two most widely used strategies are the condensation of hexaketocyclohexane with unsaturated 1,2-diamines<sup>[214]</sup> and the condensation of hexaaminobenzene with  $\alpha$ -diketones<sup>[215]</sup> (Scheme 2-2). Both methods can avoid insoluble intermediates. Therefore a lot of HAT derivatives have been synthesized using these methods and have been thoroughly characterized.<sup>[164]</sup>



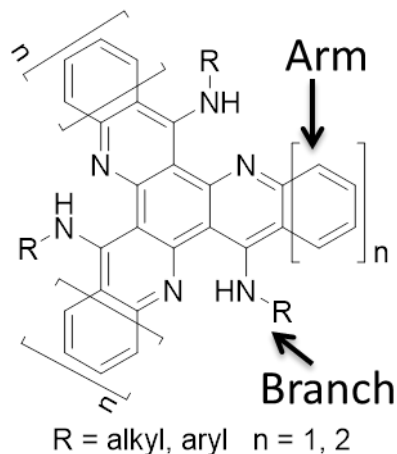
Scheme 2-3. 5,11,17-triazatrinaphthylene derivatives.<sup>[216] [217] [218]</sup>

Triazatrinaphthylene is a molecular design between starphene and hexaazatriphenylene. It possesses three nitrogen atoms which could help the synthesis along and keep three carbons which enable addition of bulky groups close to the central benzene. Denis Fichou group has published a few articles related to 5,11,17-triazatrinaphthylene derivatives. Firstly, 2,8,14-trimethyl-5,11,17-triazatrinaphthylene also named as TrisK (**3**, Scheme 2-3) was synthesized in 2005 as the first molecule based on 5,11,17-triazatrinaphthylene.<sup>[216]</sup> In 2011, a series of 6,12,18 substituted 5,11,17-triazatrinaphthylene derivatives (**4**, Scheme 2-3) were reported for quadruplex DNA recognition.<sup>[217]</sup> In 2013, 5,11,17-triazatrinaphthylene derivatives with chlorine atoms at 6,12,18 positions (**5**, Scheme 2-3) were reported with 2D self-assembling property.<sup>[218]</sup>



Scheme 2-4. Molecule structures and crystal structures of benzo[*h*]quinoline derivatives.<sup>[219]</sup>

On another hand, crystal structure of benzo[*h*]quinoline derivatives that correspond to a truncated star has been resolved.<sup>[219]</sup> As shown in Scheme 2-4, the 10-(phenylamino)benzo[*h*]quinoline derivative that possesses an aminophenyl substituent (molecule **6**) in the internal position keeps its quinoline structure flat. Even more, this structure remains planar even after addition of bulky group (isopropyl) on the phenyl substituent (molecule **7**). Moreover, the addition of substituents, as isopropyl group, in ortho-positions lowers the dihedral angle between quinolone and aminophenyl substituent from 9.17 ° to 0.53 °



Scheme 2-5. Molecular skeleton frame of the designed molecules.

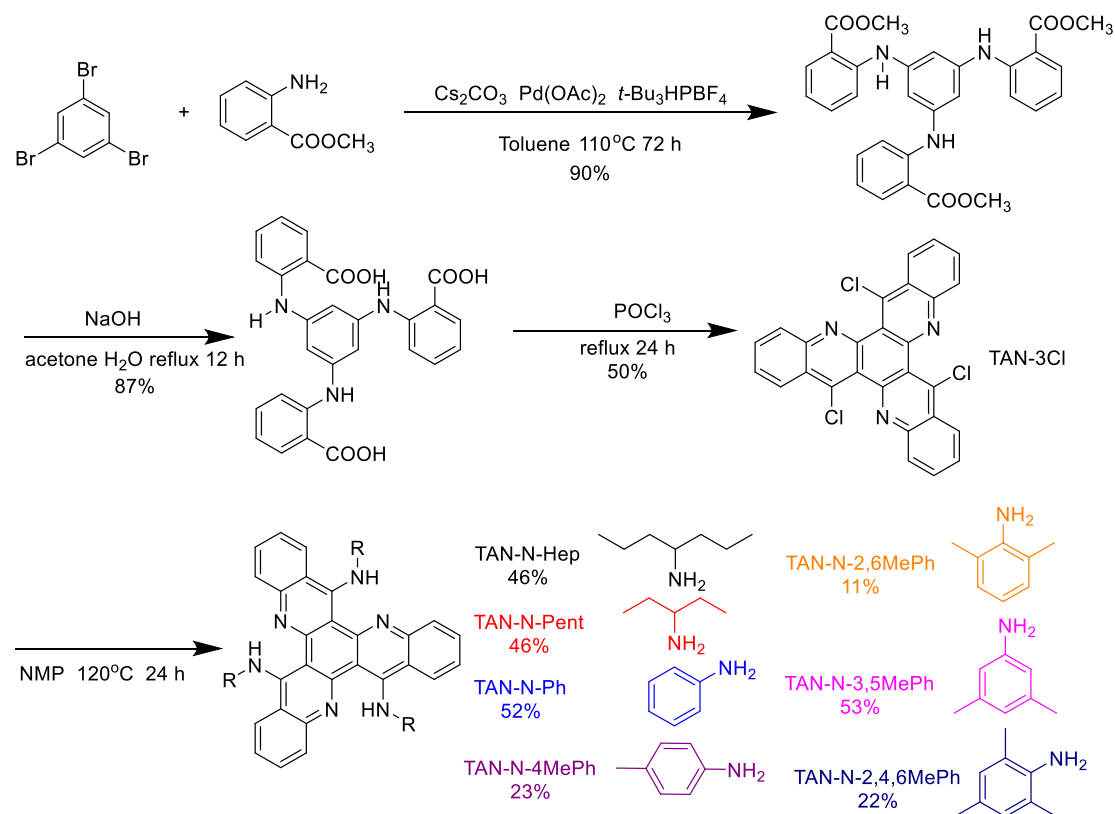
Based on this analysis of the literature data, we presume that 5,11,17-triazatriphthalene (TAN) could be a suitable central core for our molecule design, and chlorine atoms at 6,12,18 positions are favorable for the introduction of branches. As shown in Scheme 2-5 our first design is to use TAN as central core and different amines as branches to increase solubility and control the packing motif in the solid state. Moreover, intramolecular hydrogen bonding between N-H groups and  $N_{sp^2}$  atoms could lock the molecules in a planar structure, which is favorable for face-to-face  $\pi$ - $\pi$  stacking.

## 2.2 Synthesis

The synthetic routes to obtain the final compounds were shown below in Scheme 2-6. Firstly, 6,12,18-trichloro-5,11,17-triazatriphthalene (TAN-3Cl) was synthesized by a three-step process as reported in the literature.<sup>[216]</sup> Afterward final compounds were synthesized by nucleophilic aromatic substitution of chlorine with excess of primary amines and anilines (Method A).

In the first step, a triester compound was obtained from triple Buchwald–Hartwig amination (palladium-catalyzed cross coupling) of 1,3,5-tribromobenzene by methyl anthranilates with high yield of 90%. Then basic hydrolysis of the triester was carried out to produce the triacid compound and the yield can be as high as 87%. TAN-3Cl was then afforded after the cyclization of the triacid compound at reflux with  $POCl_3$ . However the poor solubility of TAN-3Cl has hampered its complete purification. Consequently, crude product of TAN-3Cl was used for the next step. The last step is the same as synthesis of the linear 9-chloroacridine from N-phenylanthranilic acid with phosphorus oxychloride which has been widely used.<sup>[220]</sup> Cyclization can also be done with polyphosphoric acid (PPA) followed by a chlorination with thionyl

chloride<sup>[221]</sup>. We also tried this method with our starting material without success.



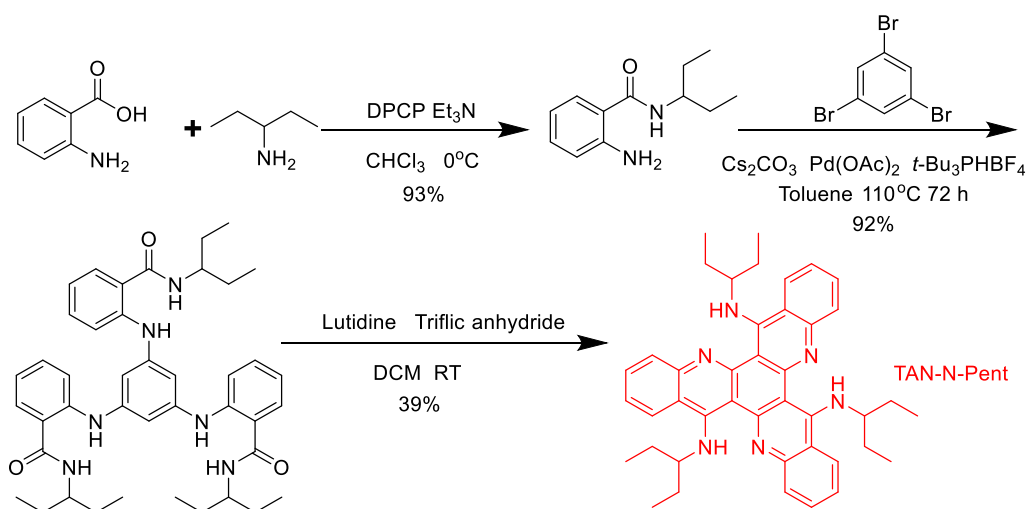
Scheme 2-6. Synthetic routes for TAN derivatives (Method A).

According to the literature, the last step was to reflux TAN-3Cl in the desired amine (large excess) under nitrogen for 70 h to give the target molecules with yields of about 50%.<sup>[217]</sup> That means large amount of amine was needed as reactant and solvent at the same time. We modified the reaction condition by using a high polar aprotic solvent (N-methyl-2-pyrrolidone) to improve the rate of the nucleophilic aromatic reaction. By this way, the reaction time was reduced to 24 h and the quantity of amine was reduced to 6 equivalents. The yields of reactions with two alkyl amines heptan-4-amine and pentan-3-amine were 46%. For aromatic amines, reactions with aniline, 4-methylaniline and 3,5-dimethylaniline were also performed to provide the expected compounds with yields around 50%. But when the 2 and 6 positions of the benzene ring are substituted, such as 2,6-dimethylaniline and 2,4,6-trimethylaniline, the yield of the reactions are much lower due to the higher steric hindrance with last step yield of 11% and 22%, respectively.

The first TAN compound synthesized was TAN-N-Hep, however after purification the compound was obtained as oil at room temperature. As 4-heptyl groups seemed to be a too bulky alkyl chain for the small TAN central core, 3-pentyl groups were tried. In this case, the final product was found to be a light yellow solid. However, these

alkyl groups could be too small and too flexible to avoid direct face-to face packing over the whole structure. As a consequence, five different aryl amines as branches were investigated and obtained for the first time. Within these five aryl amine substituted molecules, relationships between number and position differences of methyl groups on benzene ring and the packing motif of the molecules were investigated.

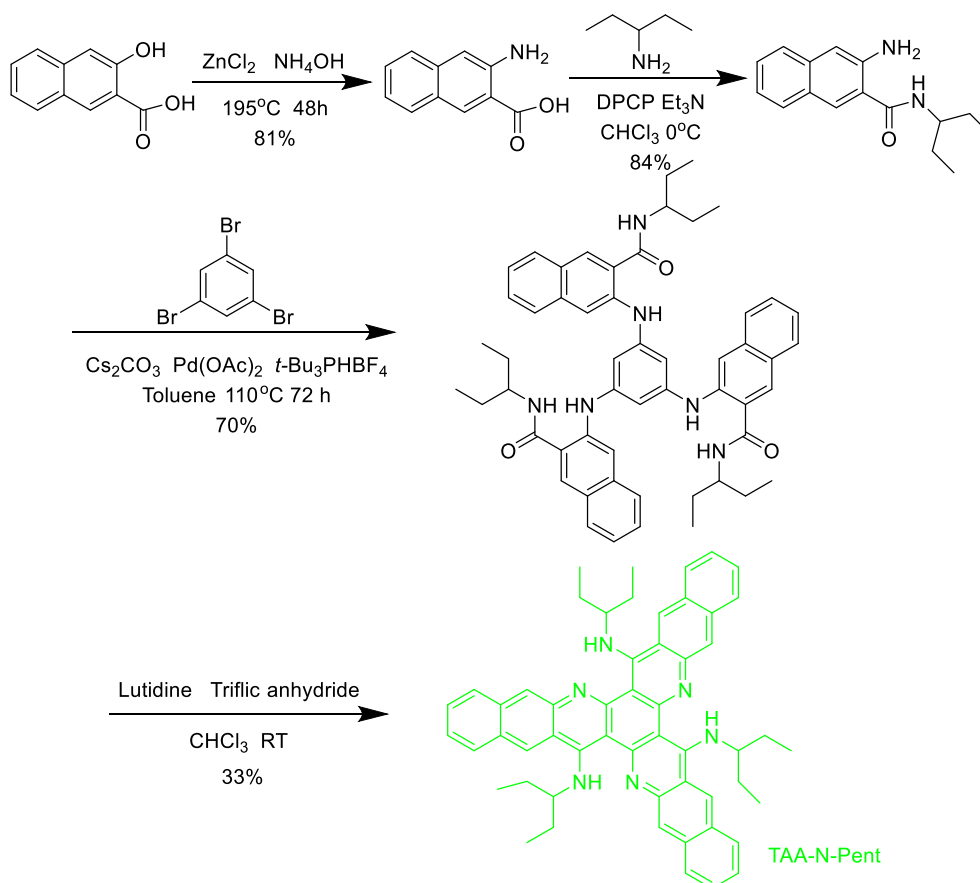
In parallel, we have also tried to synthesize two other molecular structures but without success. Firstly, we tried to enlarge the  $\pi$ -conjugation system of the molecule, but trichloro intermediate of 6,14,22-triazatrianrylene (TAA) cannot be obtained by this method. Secondly, we tried to substitute TAN-3Cl by secondary amines but the nucleophilic aromatic reaction did not occur between chlorine and secondary amine.



Scheme 2-7. Synthetic route with soluble intermediate for TAN-N-Pent (Method B).

As mentioned before, TAN-3Cl shows very low solubility and cannot be purified. It is also the limiting step to enlarge the molecule  $\pi$ -conjugation system since trichloro derivative of TAA cannot be obtained. Moreover, this method does not work with secondary amines. Consequently, a new synthetic route with soluble intermediate is required (Method B). Early in 1946, a series of 4-aminoquinoline derivatives were synthesized by cyclization of a number of  $\beta$ -anilinoacrylamides using phosphorus oxychloride.<sup>[222]</sup> In an article published in 1989, 9-aminoacridines were obtained using the same method.<sup>[223]</sup> As shown in Scheme 2-7, in our case, the synthesis begins by amidation of anthranilic acid inspired from a recent publication (2011).<sup>[224]</sup> Diphenylchlorophosphate (DPCP) was used as a coupling reagent to activate carboxylic acid. Then, palladium-catalyzed triple amination of 1,3,5-tribromobenzene was performed with high yield of 92%. Finally, the cyclization step of the triamide compound was performed with triflic anhydride. This strategy was firstly tested for

the synthesis of TAN-N-Pent. This method increased the overall yield (33%) compared to the previous pathway (20%) and reduced the synthetic route from four steps to three steps. By this method compounds substituted by secondary amine, such as diethylamine (TAN-N-2Et), dipropylamine (TAN-N-2nPr) and diisopropylamine (TAN-N-2iPr) were successfully prepared. However, these molecules were not stable under ambient conditions and they were decomposed into 6,12,18-trihydroxy-5,11,17-triazatrinaphthylene in presence of water.



Scheme 2-8. Synthetic route with soluble intermediate for TAA-N-Pent (Method B).

The success of the second synthetic method allowed us to extend the length of molecule arms. Thus, 6,14,22-triazatryantrylene (TAA) substituted by 3-aminopentyl group was synthesized (Scheme 2-8). As expected, the solubility of all the intermediates and final product TAA-N-Pent are relatively good. Compared with TAN-N-Pent, the extension of  $\pi$ -conjugated system should increase the face-to-face  $\pi$ - $\pi$  stacking. Moreover, TAA-N-Pent is the first TAA derivative that has ever been synthesized.

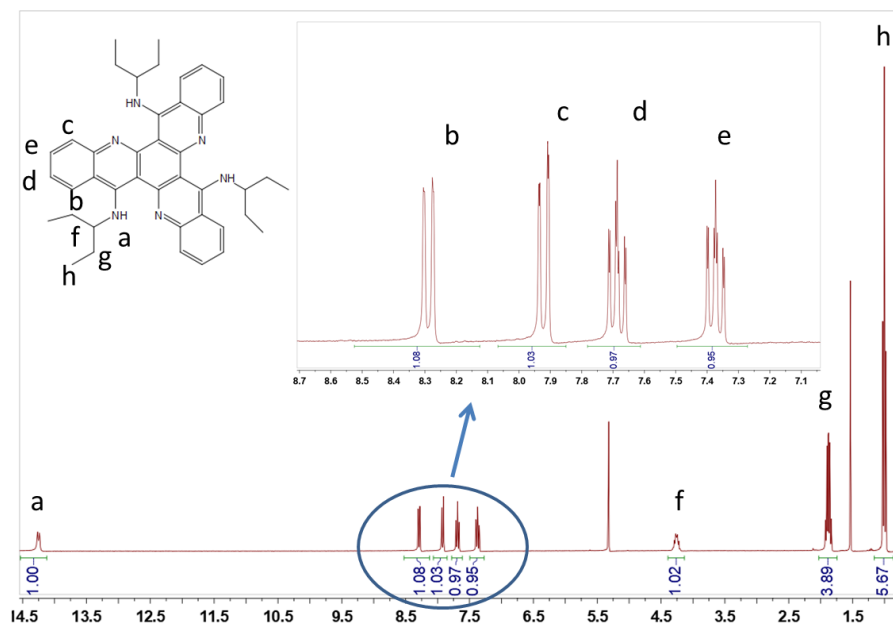


Figure 2-1.  $^1\text{H}$  NMR spectrum of TAN-N-Pent in  $\text{CD}_2\text{Cl}_2$  solution.

$^1\text{H}$  and  $^{13}\text{C}$  NMR data along with high-resolution mass spectrometry analyses were fully consistent with the expected chemical structures (Experiment part). A single set of proton and carbon resonances were detected by  $^1\text{H}$  and  $^{13}\text{C}$  NMR spectroscopy for the arm-branch unit evidencing the  $\text{C}_3$  chemical structure of each star-shaped compound in solution. To illustrate this finding,  $^1\text{H}$  NMR spectra of TAN-N-Pent is shown in Figure 2-1 as an example. It is also worth underlying the high chemical shift value recorded for the N-H protons at about 15 ppm, which can be rationalized by postulating hydrogen bonding with the  $\text{N}_{\text{sp}^2}$  atom in the arm.

## 2.3 Optical and Electrochemical Properties

Optical and electrochemical properties in solution of all compounds were investigated by UV-vis spectroscopy and Cyclic voltammetry (CV).

UV-visible spectra of all compounds were measured in dilute dichloromethane (DCM) solution. UV-visible spectra of three alkylamine substituted molecules TAN-N-Hep, TAN-N-Pent and TAA-N-Pent are shown in Figure 2-2. TAN-N-Hep and TAN-N-Pent have almost the same absorption spectra with main maximum absorption peaks ( $\lambda_{\text{abs}}$ ) at 252 and 353 nm, while absorption spectrum of TAA-N-Pent is 48 nm red shifted to  $\lambda_{\text{abs}} = 287$  and 401 nm due to the extension of the  $\pi$ -conjugated central core. The optical energy bandgaps of TAN-N-Hep and TAN-N-Pent estimated from absorption edges is 2.74 eV, while optical energy bandgap of TAA-N-Pent calculated from the red-shifted spectrum is much smaller (2.42 eV). These results indicated that the extension of alkyl chains does not change the optical property.

Consequently, we can assume the bigger size of alkyl substituents doesn't induce larger distortion of  $\pi$ -central core. Finally, the absorption spectra in solution of molecules substituted by primary alkyl amines are mainly determined by the structure of the central parts.

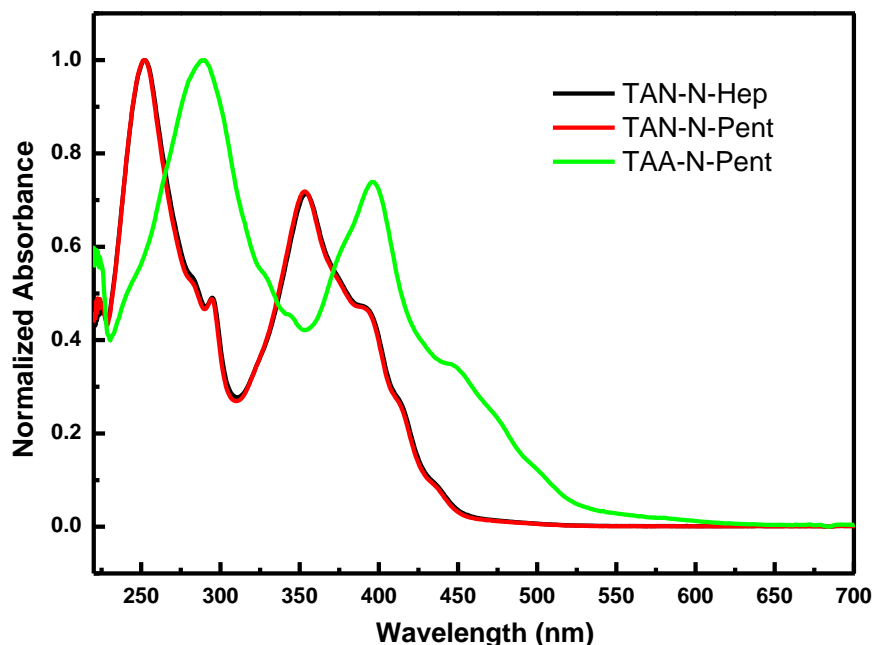


Figure 2-2. UV-visible spectra in DCM of TAN-N-Hep, TAN-N-Pent and TAA-N-Pent.

The absorption spectra of the five other molecules TAN-N-Ph, TAN-N-2,4,6MePh, TAN-N-4MePh, TAN-N-2,6MePh and TAN-N-3,5MePh are shown in Figure 2-3. These five molecules have the same central core (TAN) and very similar branch parts (aromatic amine). Despite these similarities, their absorption spectra can be assorted into two classes. Molecules TAN-N-Ph, TAN-N-4MePh, and TAN-N-3,5MePh showed very similar absorption spectra in the 250-600 nm wavelength range with two main maxima absorption peaks ( $\lambda_{\text{abs}}$ ) at around 260 and 360 nm and less intense features at 400 nm and 300 nm. Bandgaps calculated from the threshold of the absorption spectra are almost the same (2.66, 2.68 and 2.68 eV respectively). Spectra of molecules TAN-N-2,4,6MePh and TAN-N-2,6MePh where aniline are substituted in 2,6-positions exhibit two maxima absorption peaks ( $\lambda_{\text{abs}}$ ) around 255 and 355 nm. Thus, a weak 5 nm blue-shift compared with the other three molecules was observed. Moreover, the effect of substituents is more noticeable for optical bandgaps. Indeed, TAN-N-2,4,6MePh and TAN-N-2,6MePh possess bandgaps at 2.74 and 2.81 eV, respectively, that corresponds to a blue-shift of 20 nm compared to the other three molecules. At this stage, two assumptions can be done to explain this observation. Bulky groups close to the core induce twisting of the  $\pi$ -conjugated



central core or, as observed for small benzo[h]quinoline, a more pronounced tilt between the benzene ring and the  $\pi$ -core is induced. Thus, the  $\pi$ -conjugation over the arms in the first case or between arms and branches in the second case should be reduced.

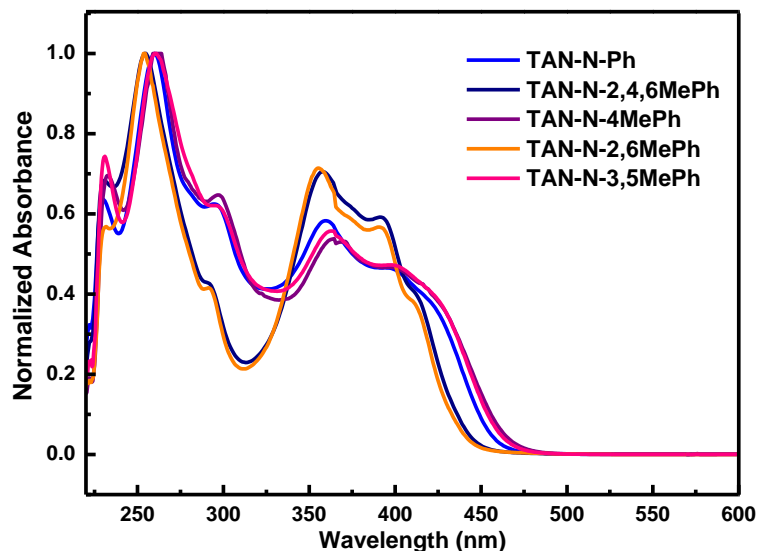


Figure 2-3. UV-visible spectra in DCM of TAN-N-Ph, TAN-N-2,4,6MePh, TAN-N-4MePh, TAN-N-2,6MePh and TAN-N-3,5MePh.

Cyclic voltammetry (CV) was performed at a scan rate of 100 mV/s in 1 mM THF solution, with 0.25 M tetrabutylammonium hexafluorophosphate as supporting electrolyte, glassy carbon as working electrode, platinum as counter electrode, Ag/AgCl as reference electrode and ferrocene/ferrocenium as internal standard. Within the range of the electrochemical window of THF, each compound undergoes a reversible single-electron reduction process except TAN-N-4MePh (Figure 2-4). The high stability of the anionic form in solution during CV indicates that intermolecular reactions won't be generated for the majority of molecules during electronic process if they are used as n-type materials. Reversely, all compounds undergo irreversible oxidation process except TAN-N-2,4,6MePh. Consequently, for most molecules, the charge transport could be limited by the instability of cations over intermolecular reactions if the reactive positions are accessible in the solid state. On the other hand, in organic chemistry and electrochemistry, the aryl amine groups have shown frequently good reactivity for electrophilic substitution in *ortho* and *para* positions. Therefore, the good stability of cations obtained after oxidation of TAN-N-2,4,6MePh was attributed to the substitution in these positions by methyl groups which are worse leaving groups than hydrogens.

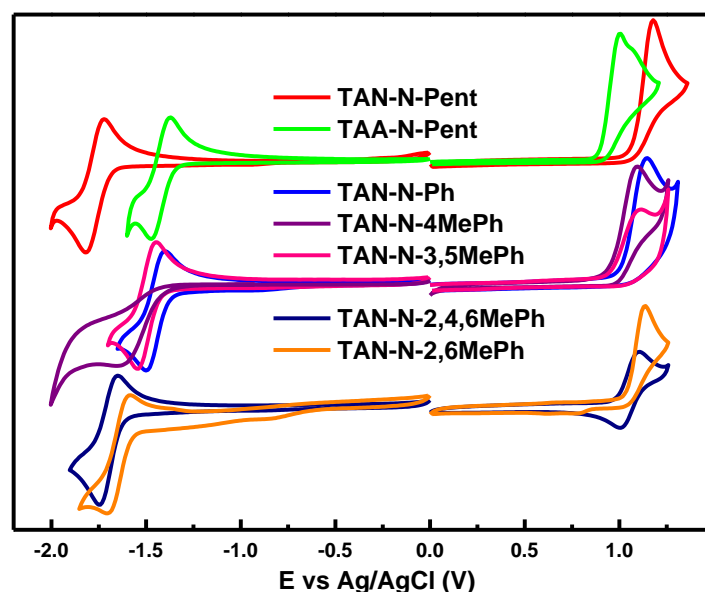


Figure 2-4. Cyclic voltammograms recorded in THF solutions of TAN-N-Pent, TAA-N-Pent, TAN-N-Ph, TAN-N-2,4,6MePh, TAN-N-4MePh, TAN-N-2,6MePh and TAN-N-3,5MePh.

To obtain a homogeneous set of data, LUMO and HOMO energy levels have been estimated from the onset values of the first reduction wave ( $E_{\text{onset}}^{\text{red}}$ ) and of the first oxidation wave ( $E_{\text{onset}}^{\text{ox}}$ ), respectively. The LUMO and HOMO energy levels of these molecules were then inferred from the electrochemical data using the following equation (1) and (2)<sup>[225]</sup>:

$$\text{LUMO} = - (E_{\text{onset}}^{\text{red}} + 4.80 - E_{\text{Fc}/\text{Fc}^+}) [\text{eV}] \quad (1)$$

$$\text{HOMO} = - (E_{\text{onset}}^{\text{ox}} + 4.80 - E_{\text{Fc}/\text{Fc}^+}) [\text{eV}] \quad (2)$$

Half-wave potential of ferrocene/ferrocenium couple  $E_{\text{Fc}/\text{Fc}^+}$  was measured as  $0.615 \text{ V} \pm 0.005 \text{ V}$  versus Ag/AgCl which is close to the experimental value reported in literature<sup>[226]</sup> under the same conditions showing both quality and stability of our reference electrode.

Several conclusions can be drawn from the data summarized in Table 2-1. Firstly, bandgaps calculated from electrochemistry data follow the trend observed by UV-visible spectroscopy even if absolute values are different. For example, alkyl amine substituted molecules TAN-N-Pent and TAA-N-Pent exhibit the largest and smallest bandgap among all the compounds. Moreover, TAN-N-Pent possesses the highest LUMO energy level of -2.50 eV, while TAA-N-Pent shows the lowest LUMO energy level of -2.83 eV due to the extension of conjugation system of central core.

Table 2-1. Optical and electrochemical properties of TAN and TAA derivatives.

Compounds	$\lambda_{\text{abs}}$ (nm) <sup>a</sup>	$E_{\text{g}}^{\text{opt}}$ (eV) <sup>b</sup>	$E_{\text{onset}}^{\text{red}}$ (V) <sup>c</sup>	$E_{\text{onset}}^{\text{ox}}$ (V) <sup>d</sup>	LUMO (eV) <sup>e</sup>	HOMO (eV) <sup>f</sup>	$E_{\text{g}}$ (eV) <sup>g</sup>
TAN-N-Hep	252, 353	2.60					
TAN-N-Pent	252, 353	2.78	-1.69	1.08	-2.50	-5.27	2.77
TAA-N-Pent	287, 401	2.42	-1.36	0.89	-2.83	-5.08	2.25
TAN-N-Ph	260, 360	2.66	-1.37	1.04	-2.82	-5.23	2.41
TAN-N-2,4,6MePh	254, 358	2.74	-1.62	0.98	-2.57	-5.17	2.60
TAN-N-4MePh	260, 362	2.68	-1.42	0.95	-2.77	-5.14	2.37
TAN-N-2,6MePh	254,355	2.76	-1.55	1.04	-2.64	-5.23	2.46
TAN-N-3,5MePh	260, 362	2.68	-1.42	0.95	-2.77	-5.14	2.37

a: Two main absorption features for each compound. b: Optical bandgap calculated from the threshold of UV-vis absorption spectrum. c: Onset reduction potential vs Ag/AgCl. d: Onset oxidation potential vs Ag/AgCl. e: LUMO energy level calculated from  $E_{\text{onset}}^{\text{red}}$  using equation (1). f: HOMO energy level calculated from  $E_{\text{onset}}^{\text{ox}}$  using equation (2). g: Bandgap calculated from reduction and oxidation onset of CV spectrum.

Secondly, compared to alkyl amines, aryl amines lower the LUMO level. Moreover, the LUMO and HOMO values are closer when aryl amines are substituted on *ortho* position. In detail, the five aryl amine substituted molecules can be assorted into two classes similar to those used to discuss the UV-visible spectroscopy data. Molecule TAN-N-Ph, TAN-N-4MePh, and TAN-N-3,5MePh showed very similar CV curves with close LUMO energy levels of -2.82, -2.77 and -2.77 eV respectively. Molecule TAN-N-2,4,6MePh and TAN-N-2,6MePh exhibit larger bandgaps of 2.60 and 2.46 eV, respectively, and higher LUMO energy levels of -2.57 and -2.64 eV, due to the substitutions on 2,6-positions in aromatic branches. As mentioned above in UV-visible spectroscopy paragraph, these findings can be explained by different twisting of the star core or torsion between arms and branches.

As described in bibliographic paragraph, the stability of the materials during electronic process is mainly linked to redox potentials. Therefore, our compounds should be more robust if they are used as a hole transport materials against foreign molecules such as O<sub>2</sub> and H<sub>2</sub>O although the stability of radical cation is not guarantee in solid state. Moreover, the oxidation potential range is compatible with numerous device architectures contrary to reduction potential range.

## 2.4 Theoretical Calculation

Quantum chemical calculations were performed to get deeper insight into the electron density distribution of the frontier molecular orbitals and orbital overlaps and geometries which determine the evolution of the HOMO and LUMO energy levels.

Molecular geometries were optimized using density functional theory (DFT) at B3LYP/6-311G(d,p) level using Gaussian package.<sup>[227]</sup> The electron density distributions of frontier molecular orbitals (MOs) for the various compounds were calculated at the B3LYP/6-311G(d,p) level and the results are shown in Table 2-3 and Table 2-4. Calculated HOMO and LUMO values are summarized in Table 2-2. The values follow the same trend as that observed experimentally within alkylamine substituted and arylamine substituted catalogues. Different starting geometries were used for optimizations and the final geometries are different with very small energy difference. Despite the small geometry difference, the NH hydrogens are always in between the two nitrogen atoms which is consistent with the amazing chemical shift around 15 ppm, measured by solution <sup>1</sup>H NMR for these hydrogen nuclei.

Table 2-2. Experimental and calculated HOMO and LUMO energy levels of TAN and TAA derivatives.

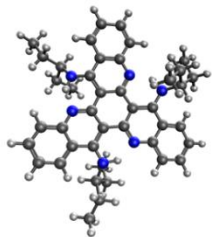
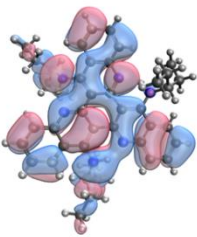
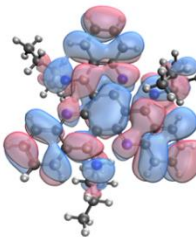
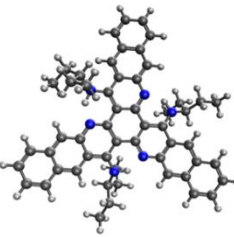
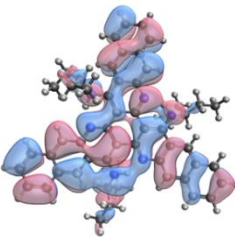
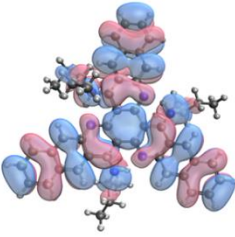
<b>Compounds</b>	<b>LUMO (eV)<sup>a</sup></b>	<b>HOMO (eV)<sup>b</sup></b>	<b>LUMO<sub>calc</sub> (eV)<sup>c</sup></b>	<b>HOMO<sub>calc</sub> (eV)<sup>c</sup></b>
<b>TAN-N-Pent</b>	-2.50	-5.27	-1.55	-5.23
<b>TAA-N-Pent</b>	-2.83	-5.08	-2.09	-5.10
<b>TAN-N-Ph</b>	-2.82	-5.23	-1.98	-5.51
<b>TAN-N-2,4,6MePh</b>	-2.57	-5.17	-1.60	-5.32
<b>TAN-N-4MePh</b>	-2.77	-5.14	-1.87	-5.37
<b>TAN-N-2,6MePh</b>	-2.64	-5.23	-1.68	-5.40
<b>TAN-N-3,5MePh</b>	-2.77	-5.14	-1.90	-5.40

a: LUMO energy level calculated from  $E_{\text{onset}}^{\text{red}}$  using equation (1). b: HOMO energy level calculated from  $E_{\text{onset}}^{\text{ox}}$  using equation (2). c: HOMO and LUMO energy levels calculated at the B3LYP/6-31G(d) level.

For alkylamine substituted molecules TAN-N-Pent and TAA-N-Pent, molecular structures are asymmetric after optimization with two branches on one side of the molecule and one branch on the other side of the molecule with dihedral angles between arm and central core of about 40°. Even though in solution, the NMR results prove the C<sub>3</sub> symmetry of molecules, the modelling show that preferential conformations are not symmetric.

For star-shaped molecule, molecule with C<sub>3h</sub> symmetry, electron density distributions of HOMO and LUMO are sometimes spread over two branches.<sup>[162]</sup> In our case, the distributions are mainly located on the whole star-shaped  $\pi$ -conjugated part as it was expected from the molecular design. For TAN-N-Pent and TAA-N-Pent, electron density distributions of LUMOs are almost following the C<sub>3h</sub> symmetry contrary to HOMOs.

Table 2-3. Electron density distributions of HOMO and LUMO of TAN-N-Pent and TAA-N-Pent with isovalue 0.02.

compound	structure	HOMO	LUMO
TAN-N-Pent			
TAA-N-Pent			

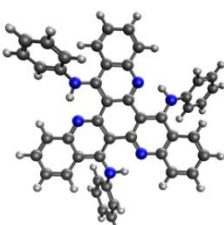
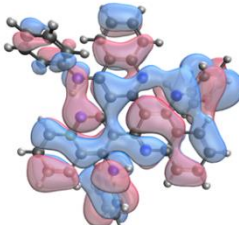
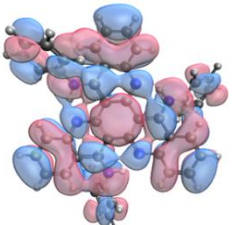
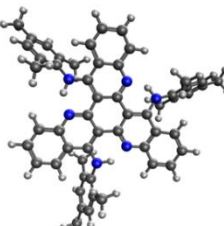
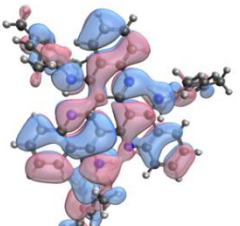
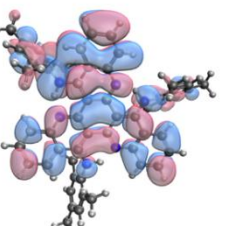
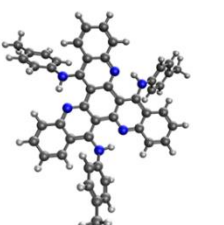
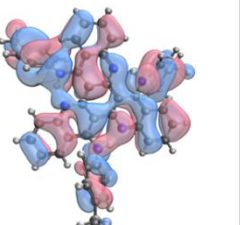
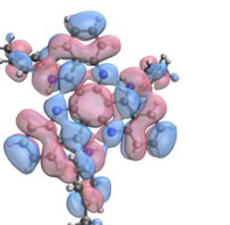
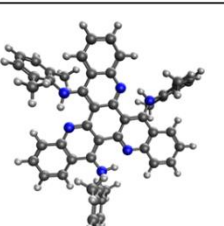
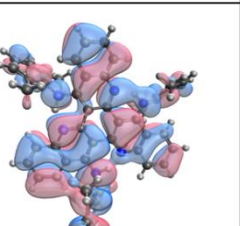
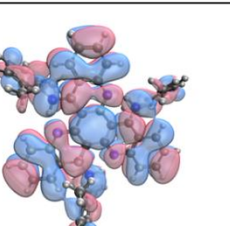
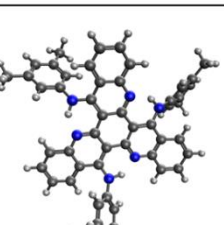
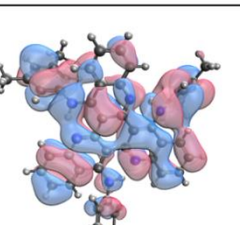
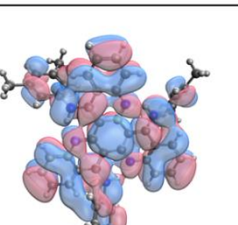
For arylamine substituted molecules, molecular structures after optimization are asymmetric with two branches on one side of the molecule and one branch on the other side of the molecule (dihedral angles around  $40^\circ$ ) except for TAN-N-2,4,6MePh. In this last case, three branches of TAN-N-2,4,6MePh are on the same side of the molecule with smaller dihedral angles around  $20^\circ$ . Corresponding with previous report about small benzo[*h*]quinoline, substituents on phenyl group lower the dihedral angle between arms and branches. <sup>[219]</sup>

These structure differences have significant effect on the electron density distribution of frontier molecular orbitals, as shown in Table 2-4. LUMO orbital of TAN-N-2,4,6MePh is more concentrated on one arm while LUMOs of the other four molecules located on three arms of the molecules as non-substituted TAN (Figure 3-4). In agreement with experimental results, TAN-N-2,4,6MePh and TAN-N-2,6MePh have shallower LUMO due to the steric hindrance of methyl groups in 2,6-positions of branches.

About electron density distribution over branches, both alkyl or aryl amines show molecular orbitals on branches. However, their sizes are sometimes small when they are compared to those of arms and are not equally divided on the three branches. The relative sizes of orbitals are particularly limited in the case of alkyl amines and TAN-N-2,4,6MePh. In the first case, it can be explained by the nature of conjugation which is called hyperconjugation (conjugation between  $\pi$  and  $\sigma$  orbitals). This kind of interaction is often weak, induces little changes in energy level and is commonly limited in space at the first  $sp^3$  atom. In the second case, torsion angle and so the relative dihedral angle between branches and arms disrupt the  $\pi$ -conjugation. Finally, the intermolecular overlap between frontier orbitals could substantially come from

branches for less hindered molecules and, thus, participates to the charge transport.

Table 2-4. Electron density distributions of HOMO and LUMO of TAN-N-Ph, TAN-N-2,4,6MePh, TAN-N-4MePh, TAN-N-2,6MePh and TAN-N-3,5MePh with isovalue 0.02.

compound	structure	HOMO	LUMO
TAN-N-Ph			
TAN-N-2,4,6MePh			
TAN-N-4MePh			
TAN-N-2,6MePh			
TAN-N-3,5MePh			

## 2.5 Single Crystal XRD Result

Single crystals of all the compounds were obtained by solution diffusion method,

using dichloromethane and methanol as solvents. Aline LACOUDRE from CESAMO extracted all the XRD data from these single crystals. Lattice vectors  $a$ ,  $b$  and  $c$  are represented in red, green and blue, respectively. In figures about molecular packing, lateral substituents and hydrogen atoms have been omitted for clarity. In order to show the intermolecular interactions clearly, a random molecule was chosen and coloured in red, named as reference molecule. In some cases, the two molecules which have the strongest intermolecular interactions with the reference molecule are coloured in blue. Due to the non-planarity of the star-shaped molecules, an alternative concept was introduced to describe the intermolecular distances: shortest C-C distance between two neighboring molecules ( $d_{C-C}$ ).

Molecular packing of TAN-N-Pent in single crystal is shown in Figure 2-5. Although solution NMR data evidenced that TAN-N-Pent preserves  $C_3$  symmetry in solution, XRD data revealed that TAN-N-Pent showed asymmetric structure in the solid state (Figure 2-5 (a)) with two branches on one side of the molecule ( $45.68^\circ$  and  $20.99^\circ$ ) and one branch on the other side of the molecule ( $42.51^\circ$ ) which is the same as the structure obtained from theoretical optimization. Moreover, the star-shaped central part is not totally in a plane, three arms of the molecule are bended and twisted in very small angles. As shown in Figure 2-5 (b) side view and Figure 2-5 (c) top view, all the molecules in single crystal are in the same conformation and exhibit two different orientations. Each molecule has efficient face-to-face  $\pi$ - $\pi$  stacking with two neighboring molecules with intermolecular  $d_{C-C}$  3.24 Å. In the end, molecule TAN-N-Pent gives out a 1D cofacial herringbone packing motif which should only provide charge carrier transport pathway in one direction.

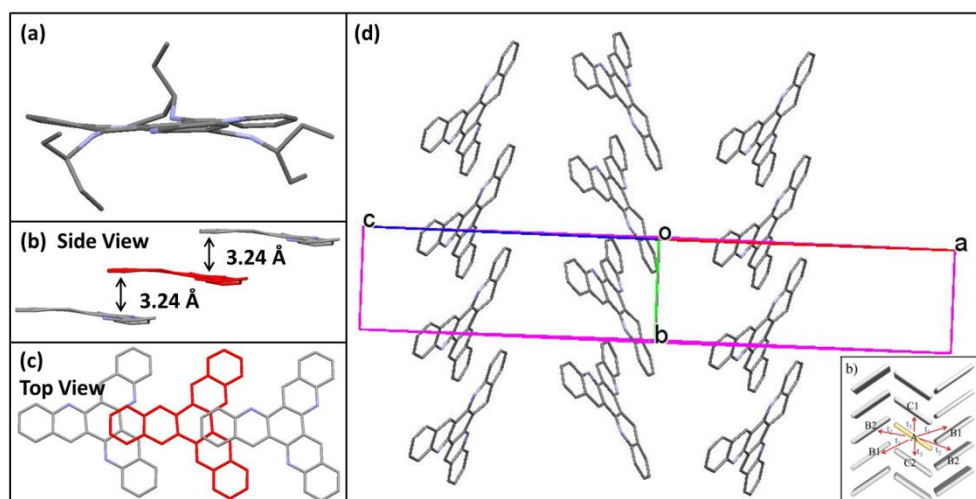


Figure 2-5. Molecular structure (a) and molecular packing (b-d) of TAN-N-Pent in single crystal.

Molecular packing of TAA-N-Pent in single crystal is shown in Figure 2-6. As TAN-N-Pent, TAA-N-Pent exhibits asymmetric structure in the solid state (Figure 2-6

(a) with two branches on one side of the molecule ( $34.15^\circ$  and  $18.36^\circ$ ) and one branch on the other side of the molecule ( $49.87^\circ$ ). As shown in Figure 2-6 (b) side view, each molecule has efficient face-to-face  $\pi$ - $\pi$  stacking with four neighboring molecules from two arms of the molecule. Compare with TAN-N-Pent, longer arms of TAA-N-Pent provide more space and opportunity to the molecule to form  $\pi$ - $\pi$  stacking with neighboring molecules which is favorable to increase the dimensionality of charge carrier transport. As shown in Figure 2-6 (c) top view, all the molecules in single crystal are in the same conformation but in two different orientations. Finally, Figures 2-6 (d) and (e) show that TAA-N-Pent exhibit a 2D bricklayer packing motif which could provide efficient charge carrier transport in two directions.

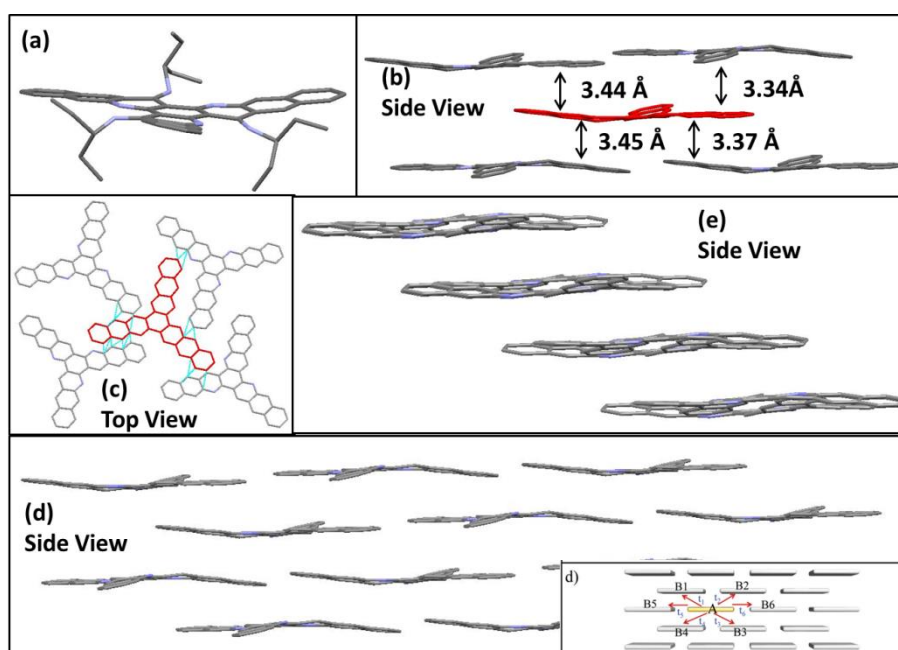


Figure 2-6. Molecular structure (a) and molecular packing (b-e) of TAA-N-Pent in single crystal.

As expected, the introduction of alkyl chains as branches has provided sufficient steric hindrance to prevent disc-like molecule packing and has increased the solubility of the molecules. However, XRD results of arylamine substituted molecules TAN-N-Pent and TAA-N-Pent showed that there are strong interactions between alkyl chains and star-shaped central parts. This kind of interaction will affect the packing motif in the solid state. Therefore, the molecular packings of five arylamine substituted molecules were studied by single crystal XRD and are described below.



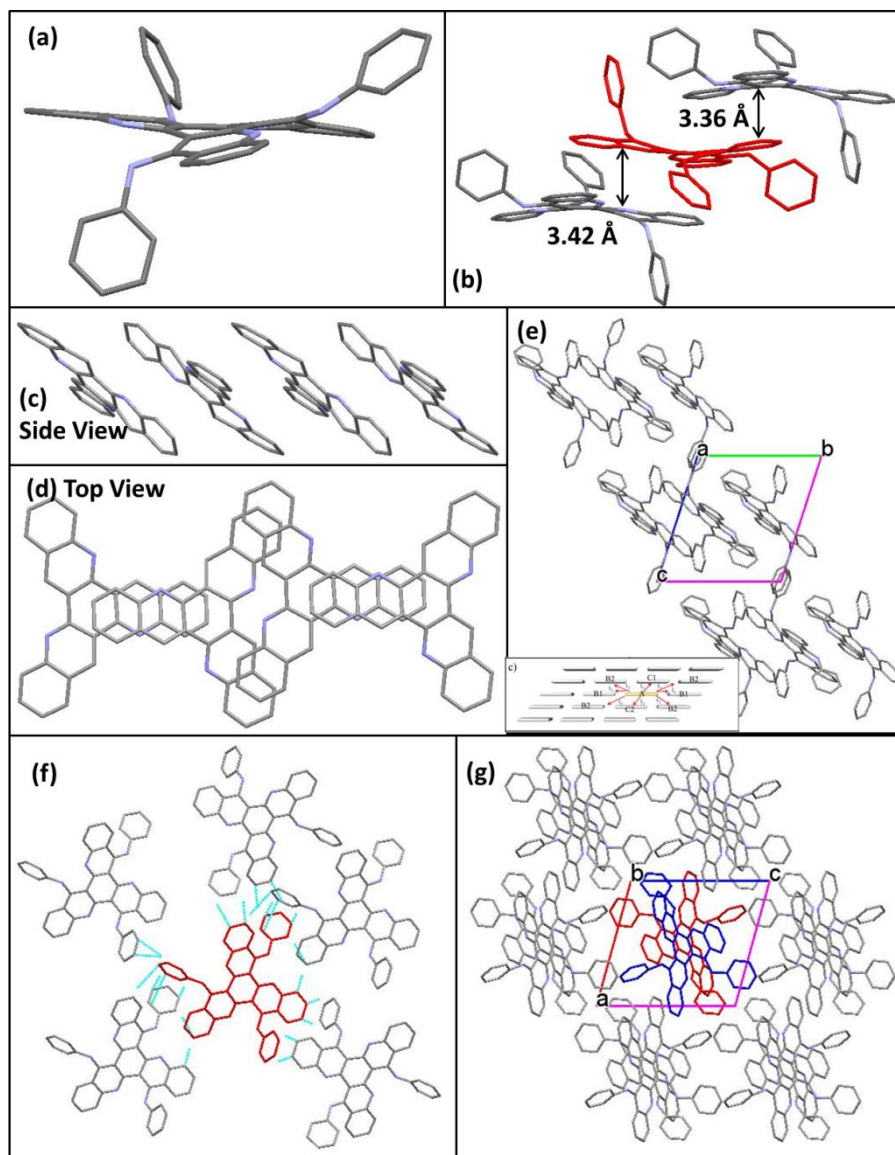


Figure 2-7. Molecular structure (a) and molecular packing (b-g) of TAN-N-Ph in single crystal.

Molecular packing of TAN-N-Ph in single crystal is shown in Figure 2-7. As found for alkylamine substituted molecules, TAN-N-Ph exhibits asymmetric structure in the solid state (Figure 2-7 (a)) with two branches on one side of the molecule ( $47.00^\circ$  and  $36.38^\circ$ ) and one branch on the other side of the molecule ( $68.06^\circ$ ) as suggested by theoretical calculations. In total, dihedral angles between the aromatic branches and central core are much higher than those observed for alkyl branches. It could be due to the cyclic nature of benzene, which induced higher rigidity and larger steric hindrance. As shown in Figure 2-7 (b), each molecule has efficient face-to-face  $\pi$ - $\pi$  stacking with two neighboring molecules and packings with these two molecules are different with intermolecular  $d_{C-C}$  as 3.36 and 3.42 Å along the b axis. In addition, as shown in Figures 2-7 (c) and (d), there are two different orientations of the molecules in single crystal and an alternant molecule packing is constructed, which is very similar to what

it was found for molecule **2** (Scheme 2-1).<sup>[210]</sup> Finally, in (1,0,0) direction molecule TAN-N-Ph exhibits 1D slipped stacking motif (Figure 2-7 (e)) which should favor one direction for the charge transport. However, as shown in Figure 2-7 (f) except the two molecules in (1,0,0) direction the other neighboring molecules have abundant arm-branch and branch-branch interactions with the reference molecule. According to the view from the (1,0,1) plane shown in Figure 2-7 (g), the column including reference molecule has six surrounding columns with edge-to-edge interactions. Moreover, modeling has demonstrated substantial electron density distribution over the benzene branches. Therefore, it can be expected a higher dimensional charge transport in TAN-N-Ph single crystal than in the case of alkyl amine derivatives.

Molecular packing of TAN-N-2,4,6MePh in single crystal is shown in Figure 2-8. Different from all the other molecules, TAN-N-2,4,6MePh exhibits asymmetric structure in solid state (Figure 2-8 (a)) with three branches on the same side of the molecule with different dihedral angles (30.05, 32.73 and 41.19 °) which is consistent with theoretical calculations. The dihedral angles of the 2,4,6MePh branches are smaller than those observed with benzene branches as reported for benzo[*h*]quinoline when benzene ring is more substituted.<sup>[219]</sup> Firstly three branches are on the same side of the molecule mean plane, secondly as shown in Figure 2-8 (b), each molecule has face-to-face  $\pi$ - $\pi$  stacking with three neighboring molecules on the side with three branches, so steric hindrances from these molecules can be a factor that decreases the dihedral angles of 2,4,6MePh branches. Each molecule shows  $\pi$ - $\pi$  stacking with three molecules, and the interactions take place by the arms. Consequently, after extension of the packing, each six molecules give out a shape of hexagon as shown in Figure 2-8 (d). As shown in Figure 2-8 (e) where the view is perpendicular to the top view (Figures 2-8 (c) and (d)), molecule TAN-N-2,4,6MePh exhibits a 2D layer by layer stacking motif. Distances between hexagonal layers are around 4.42 Å. Consequently, charge carrier transport should be favored in two directions within a hexagonal layer while there is no efficient pathway between layers. To the best of our knowledge, this is the first time to bring forward this kind of 2D molecule packing in the crystal phase.

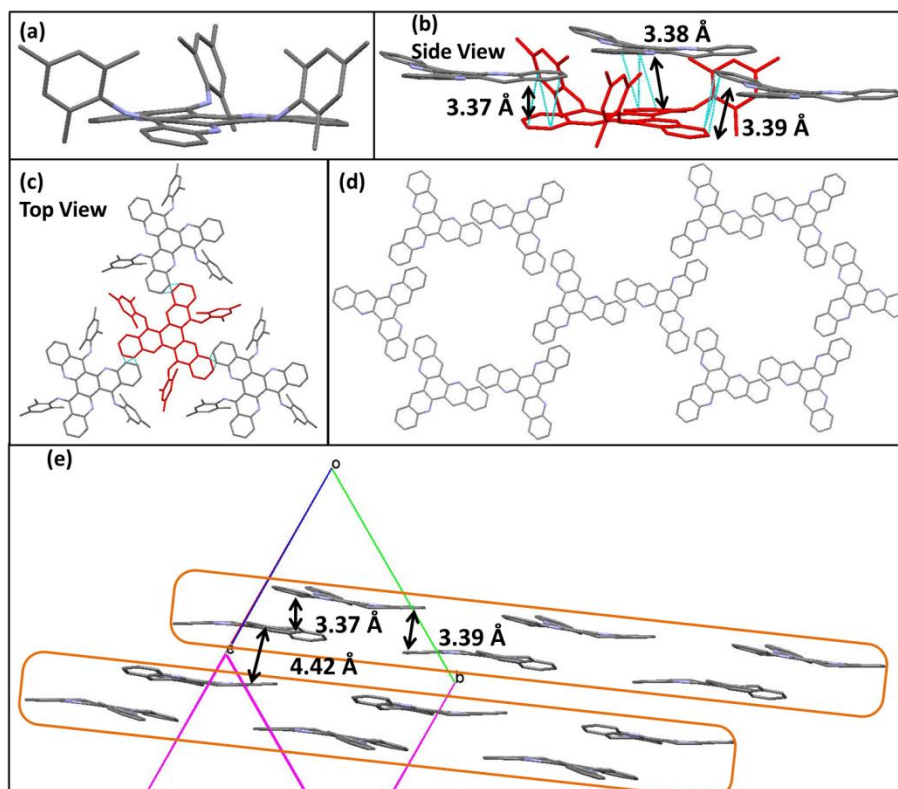


Figure 2-8. Molecular structure (a) and molecular packing (b-e) of TAN-N-2,4,6MePh in single crystal.

Molecular packing of TAN-N-4MePh in single crystal is shown in Figure 2-9. TAN-N-4MePh exhibits asymmetric structure in the solid state (Figure 2-9 (a)) with two branches on one side of the molecule ( $32.41^\circ$  and  $47.87^\circ$ ) and one branch on the other side of the molecule ( $57.46^\circ$ ). As shown in Figure 2-9 (b), each molecule exhibits efficient face-to-face  $\pi$ - $\pi$  stacking with two neighboring molecules and packings with these two molecules are the same with intermolecular  $d_{C-C}$  as small as  $3.27 \text{ \AA}$ . Figure 2-9 (c) proved that there are two different orientations of the molecules in single crystal. As shown in Figure 2-9 (d), molecule TAN-N-4MePh shows 1D slipped stacking motif from (0,1,0) direction. However, as found for molecule TAN-N-Ph and according to Figure 2-9 (e), abundant arm-branch and arm-arm interactions are observed with neighboring molecules. On the other hand, compared with TAN-N-Ph, in (1,1,0) plane there are fewer molecules which have interactions with reference molecule and directions of these interactions are limited (Figure 2-9 (f)). Therefore, from the crystal packing we assumed that charge carrier transport isotropy of TAN-N-4MePh is worse than that of TAN-N-Ph.

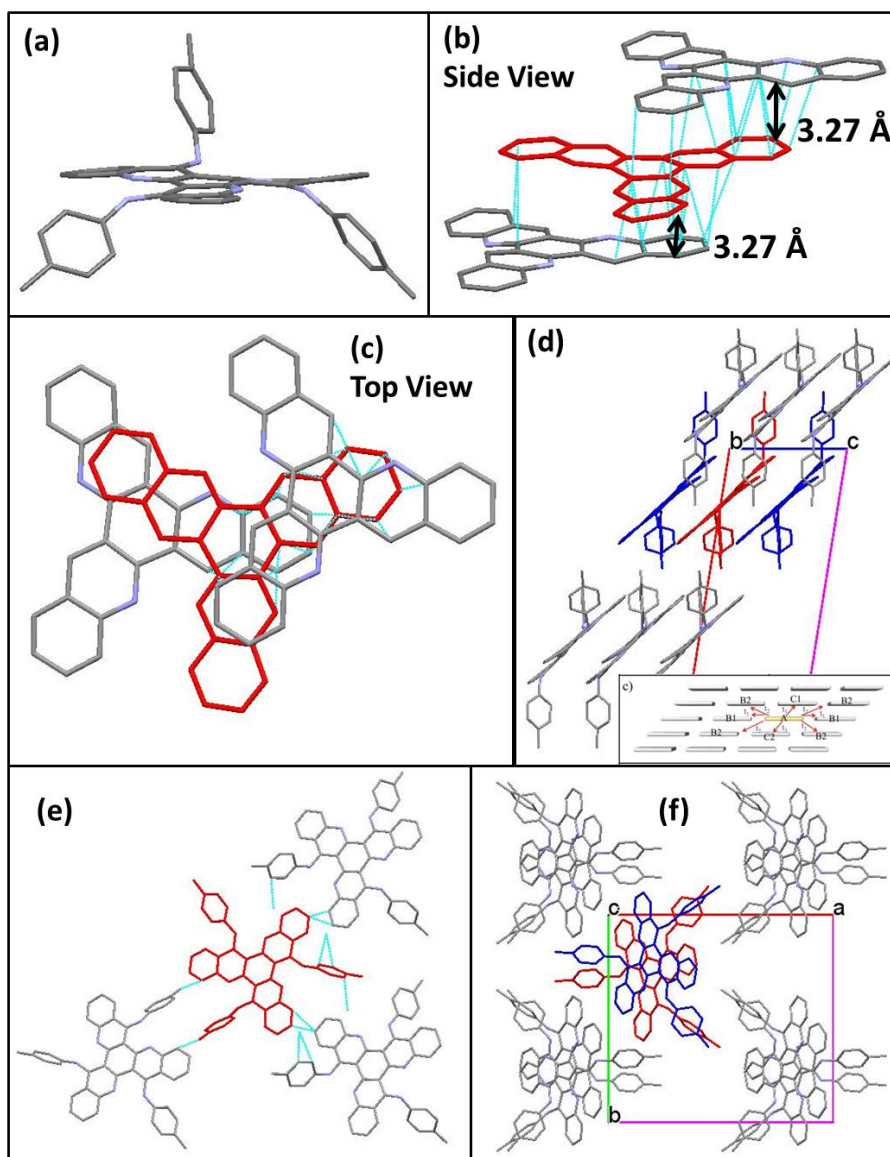


Figure 2-9. Molecular structure (a) and molecular packing (b-f) of TAN-N-4MePh in single crystal.

Molecular packing of TAN-N-2,6MePh in single crystal is shown in Figure 2-10. TAN-N-2,6MePh exhibits asymmetric structure in solid state (Figure 2-10 (a)) with two branches on one side of the molecule ( $29.27^\circ$  and  $31.95^\circ$ ) and one branch on the other side of the molecule ( $30.03^\circ$ ). As shown in Figure 2-10 (b), each molecule has efficient face-to-face  $\pi$ - $\pi$  stacking with two neighboring molecules and packings with these two molecules are different with intermolecular  $d_{C-C}$  as 3.45 and 3.42 Å. Figure 2-10 (c) proved that there are two different orientations of the molecules in single crystal. As shown in Figure 2-10 (d), except the two molecules which have face-to-face  $\pi$ - $\pi$  stacking with reference molecule, quite a lot neighboring molecules have arm-branch and branch-branch interactions with reference molecule. Figure 2-10 (e) show a 1D slipped stacking while Figure 2-10 (f) show that six columns may have

strong edge-to-edge interactions with the column including reference molecule. Therefore, molecule TAN-N-2,6MePh is promising to exhibit 3D charge carrier transport in single crystal. The good charge carrier transport property of TAN-N-2,6MePh was proved by perovskite solar cells and this will be discussed in one of the following section.

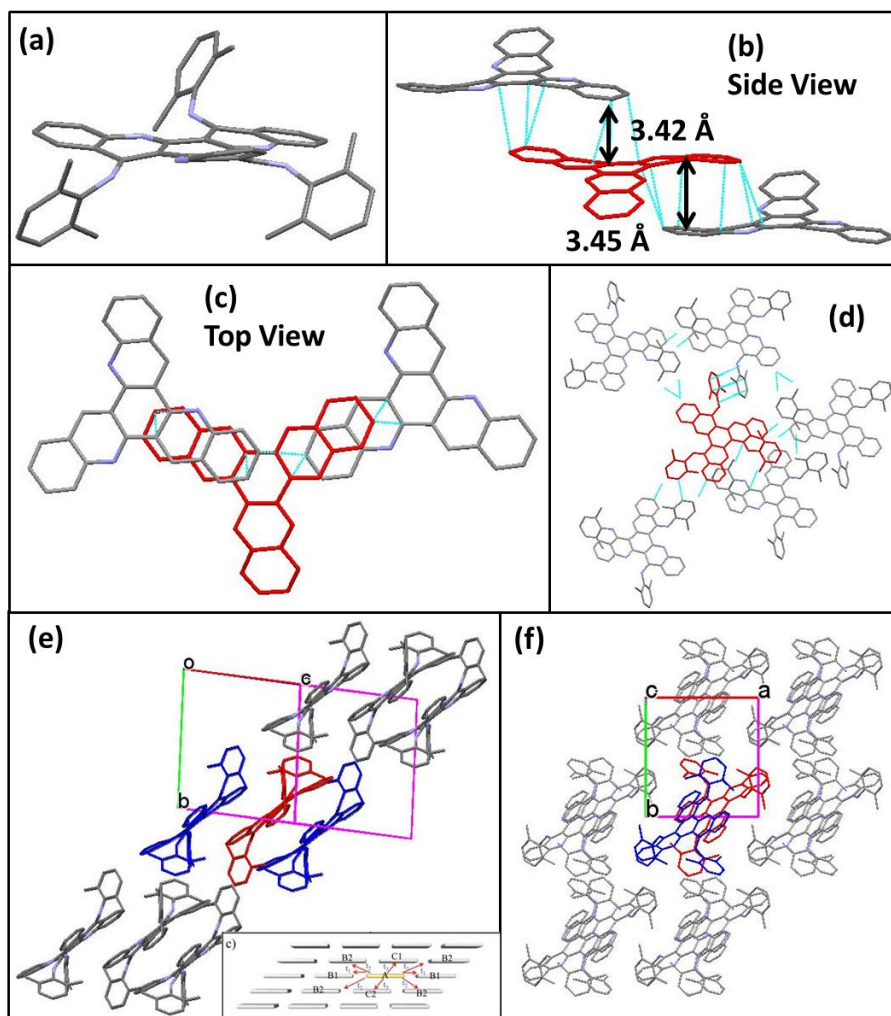


Figure 2-10. Molecular structure (a) and molecular packing (b-f) of TAN-N-2,6MePh in single crystal.

Molecular packing of TAN-N-3,5MePh in single crystal is shown in Figure 2-11. TAN-N-3,5MePh exhibits asymmetric structure in the solid state (Figure 2-11 (a)) with two branches on one side of the molecule ( $39.53^\circ$  and  $56.01^\circ$ ) and one branch on the other side of the molecule ( $32.38^\circ$ ). As shown in Figure 2-11 (b), each molecule has efficient face-to-face  $\pi$ - $\pi$  stacking with two neighboring molecules and packings with these two molecules are different with  $d_{C-C}$  as 3.27 and 3.42 Å. Figure 2-11 (c) proved that there are two different orientations of the molecules in single crystal. Moreover, except the two molecules which have face-to-face  $\pi$ - $\pi$  stacking with reference molecule, the other neighboring molecules do not show efficient

interactions with reference molecule (Figure 2-11 (e) and (f)). Therefore, as shown in Figure 2-11 (d), molecule TAN-N-3,5MePh exhibits 1D slipped stacking motif.

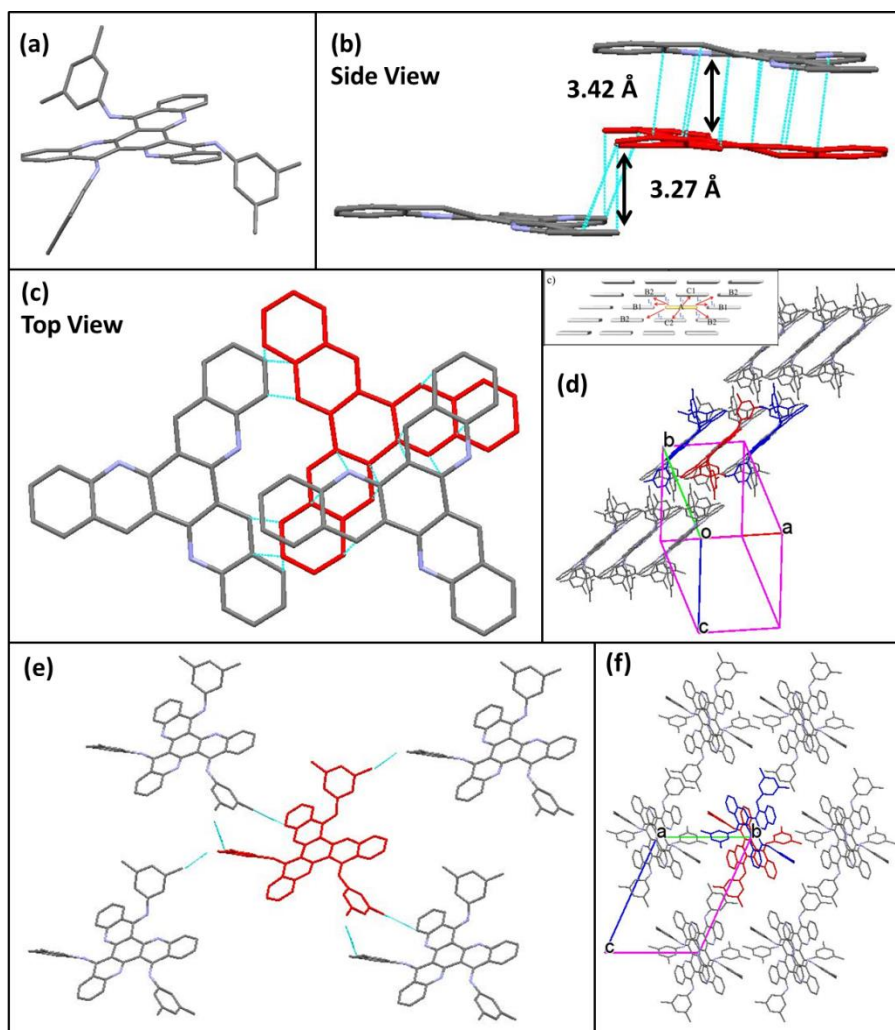


Figure 2-11. Molecular structure (a) and molecular packing (b-f) of TAN-N-3,5MePh in single crystal.

To summarize, from single crystal XRD results, we tried to get some hints about the dimensionality of charge carrier transport in these materials. For alkylamine substituted molecules, TAN-N-Pent exhibits a 1D cofacial herringbone packing motif and TAA-N-Pent shows a 2D bricklayer packing motif benefiting from its longer arms. For arylamine substituted molecules, TAN-N-Ph, TAN-N-4MePh and TAN-N-2,6MePh are promising to exhibit higher charge transport dimensionality due to abundant branch-arm and branch-branch interactions. However, TAN-N-3,5MePh could only exhibit 1D slipped stacking motif due to large distances between neighboring molecules. Most interestingly, TAN-N-2,4,6MePh gives out a new 2D layer by layer packing motif.

## 2.6 Characterization of Charge Transport

Derived from CV results, the HOMO levels of these 7 compounds have been estimated between -5.08 and -5.27 eV which fit with the range of typical hole transport materials for stable OFETs or OPVs.<sup>[228]</sup> For OPVs, the weak absorption in the visible range limits the interest of using these materials as active absorbing materials. However, these compounds can be associated to the last generation of solar cells such as hybrid perovskite solar cells (PSCs). Indeed, their HOMO energy level is very close to that of 2,2',7,7'-tetrakis(N,N-di-*p*-methoxyphenylamine)-9,9'-spirobifluorene (Spiro-OMeTAD), i.e. 5.2-5.4 eV,<sup>[229]</sup> which is one of the most popular hole-transporting materials (HTM) for highly efficient PSCs. On the opposite, their LUMO energy level is not adapted for common OPVs and will require specific architecture for OFETs application. However, these materials can be considered to be promising candidates for hole transport materials based on their high dimensionality molecule packing in the crystalline phase. Consequently, these materials have been integrated in OFETs and as HTM in PSCs and the performances of the corresponding devices are discussed below.

### 2.6.1 Spin-coating OFETs

To investigate the charge transport properties of TAN-N-Pent and TAA-N-Pent, bottom-gate, top-contact p-type OFETs have been fabricated and characterized with the help of Professor Mamatinin ABBAS. The OFETs were fabricated on doped silicon substrates using water soluble spin-coated poly(1-vinyl-1,2,4-triazole) (PVT) layer as gate dielectric. PVT is known both to lead to good wettability with organic ink and to reduce charge trapping in OFETs. Then semiconductor layers were deposited by spin-coating of 10 mg/mL solution in chlorobenzene. 10 nm MoO<sub>3</sub> has been deposited in vacuum before 60 nm of silver source and drain electrodes. MoO<sub>3</sub> is used to align energy level between our OSCs and silver in the aim to reduce resistance contact to the electrode (see details about device fabrication in experiment part).

Device performances were measured directly after device fabrications, but there was no field effect performance for both TAN-N-Pent and TAA-N-Pent based OFETs. In order to optimize the thin-film morphology, a 20 min annealing process under nitrogen was introduced after the spin-coating of the semiconductor layer. Six levels of temperature were applied 80 °C, 100 °C, 120 °C, 140 °C, 160 °C and 180 °C. Visible changes occurred for TAA-N-Pent films at temperature higher than 120 °C while nothing happened to TAN-N-Pent. As shown by optical microscopy in Figure 2-12, film without annealing does not show any evidences of crystallization, while films annealed at 140 °C and 160 °C show nice structures that can be attributed to the formation of crystallites. Thin film X-ray diffraction (XRD) was performed on

TAA-N-Pent thin films annealed at different temperature. A diffraction feature was detected at  $2\theta = 7.6^\circ$  when annealing was carried out at temperature higher than  $140^\circ\text{C}$ .

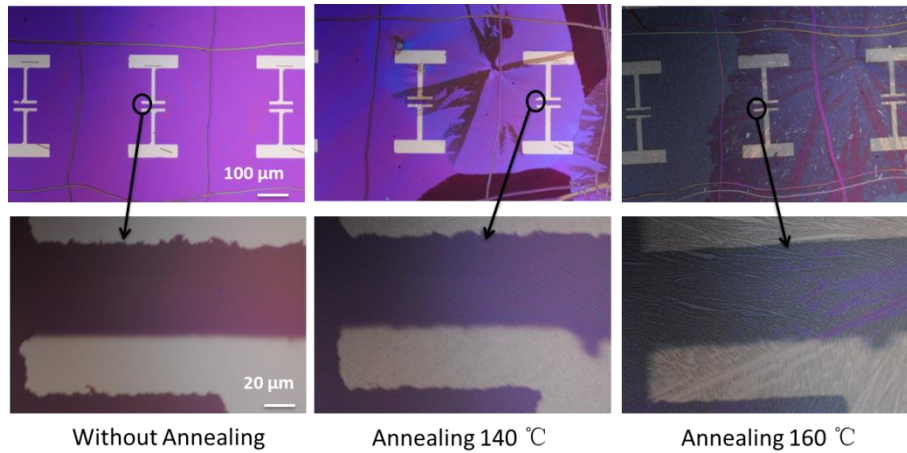


Figure 2-12. Optical microscopy images of spin-coated thin film of TAA-N-Pent annealing at different temperature.

After annealing, these films were integrated into OFETs. Devices based on TAN-N-Pent showed no performance at any temperature. For TAA-N-Pent, device based on film annealing at  $140^\circ\text{C}$  yielded a hole mobility of  $1.2 \times 10^{-4} \text{ cm}^2 \text{ V}^{-1} \text{ s}^{-1}$ , current on/off ratio ( $I_{\text{on}}/I_{\text{off}}$ ) of  $6.7 \times 10^2$  and a threshold voltage ( $V_T$ ) of  $-19 \text{ V}$  (Figure 2-13). When the annealing temperature was even higher, such as  $160^\circ\text{C}$  or  $180^\circ\text{C}$ , the crystallization of the thin films are more obvious, but no field effect performance could be recorded. This is an evidence that small changes in film morphology have a huge effect on the device performances.

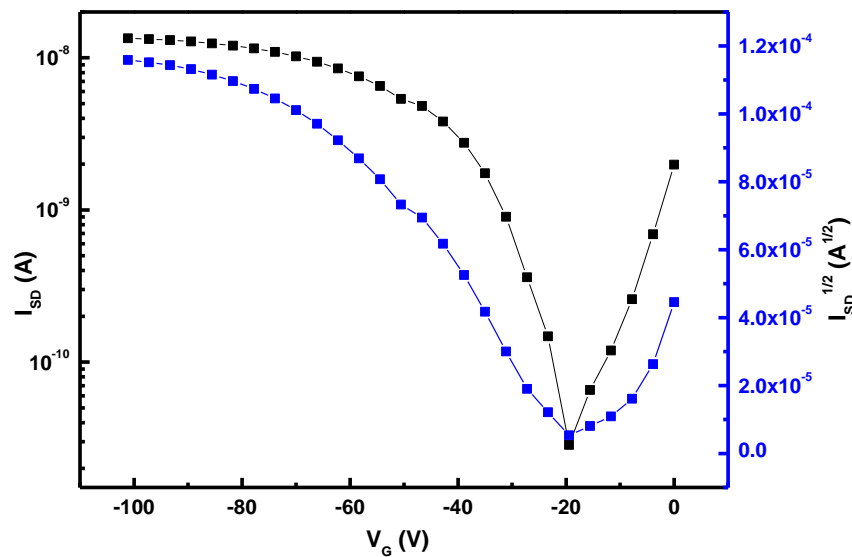


Figure 2-13. Transfer characteristics of OFET based on spin-coating thin film of TAA-N-Pent.



## 2.6.2 HTMs in Perovskite Solar Cells

Organic-inorganic hybrid perovskite solar cells (PSCs)<sup>[26,230]</sup> have attracted worldwide attention due to an unprecedented increase in power conversion efficiency (PCE), which reached 24.2% within less than ten years.<sup>[231,232]</sup> This impressive breakthrough is closely related to the remarkable properties of lead halide hybrid perovskite such as strong light absorption coefficients, tunable band gaps, balance charge transport and long diffusion length of the photo-generated charge carriers.<sup>[233–235]</sup> Thus, due to their intense absorption in the visible spectral region, hybrid perovskite materials were firstly used as sensitizers in dye sensitized solar cells (DSSCs) with liquid electrolyte showing a highest PCE around 4%.<sup>[236]</sup> However, liquid electrolyte based PSCs suffered from fast degradation. That is the reason why the liquid electrolyte was replaced by a solid hole transporting materials (HTM) as Spiro-OMeTAD to yield all solid state device architectures showing energy conversion reaching up to 15% and good performance stability.<sup>[230,237–240]</sup> Beneficiating from the rationalization of the material properties and careful optimization of devices, the energy conversion efficiencies was then pushed up to 24%. In the state-of-the-art devices, spiro-OMeTAD constitutes a standard HTM for PSCs and has inspired the development of the new HTMs.<sup>[241–244]</sup> However, the expensive synthesis and purification cost and complex dopant dependency of Spiro-OMeTAD limited its application for industrialization.<sup>[245–248]</sup>

A typical PSC consists of a conductive substrate, electron transporting layer (ETL), perovskite layer, hole transporting layer (HTL), and back electrode (Au or Ag).<sup>[249]</sup> Ideal HTMs need to exhibit a suitable HOMO energy level for hole extraction, high hole mobility for charge carrier transport, and stable chemical/physical properties to ensure long lifetime of solar cell device.<sup>[250,251]</sup> In recent years, tremendous efforts on developing novel HTMs have been attempted for replacing Spiro-OMeTAD.<sup>[252–255]</sup> Triphenylamine, pyrene, 3,4-ethylenedioxythiophene, linear  $\pi$ -conjugated structure, carbazole, spiro[fluorene-9,90-xanthene] (SFX) and triazines can be employed as building blocks for novel HTMs due to their simple structures, easy functionalization to adjust optoelectronic properties, good photochemical stability, and low price.<sup>[256–260]</sup> In addition, star-shaped hole-transporting materials including carbazole,<sup>[261]</sup> 1,3,5-triphenylbenzene<sup>[262]</sup> or triazine<sup>[263]</sup> core were developed and led in PSCs to energy conversion efficiencies ranging from 12 to 18%. However, the cell performances of reported PSCs with new HTMs are still not comparable with spiro-OMeTAD-based devices. Therefore, much more efforts are needed to develop new low-cost, efficient and stable HTMs for PSCs.

As mentioned before, the five arylamine substituted molecules, TAN-N-Ph, TAN-N-2,4,6MePh, TAN-N-4MePh, TAN-N-2,6MePh and TAN-N-3,5MePh exhibit a

HOMO energy level close to the one of spiro-OMeTAD. In this context, they were applied as HTMs in planar (FAPbI<sub>3</sub>)<sub>0.85</sub>(MAPbBr<sub>3</sub>)<sub>0.15</sub>-based PSCs. PSCs were fabricated by Dr. Paek Sanghyun from the Prof. M. K. Nazeeruddin group (University of Lausanne (Switzerland)). The PSC device configuration consists of a 20 nm-thick TiO<sub>2</sub> compact layer, a 200 - 400 nm thick perovskite layer, a thin HTM layer, and a 70 nm-thick Au electrode.<sup>[264]</sup> The concentration of the chlorobenzene solution used to fabricate hole transport layer was 10 mg mL<sup>-1</sup>. Tert-butylpyridine (Tbp), Tris(2-(1H-pyrazol-1-yl)-4-tert-butylpyridine)cobalt(III) (FK209) and Tris(bis(trifluoromethylsulfon-yl)imide) (Li-TFSI) were added as additives (see details about device fabrication in experiment part).<sup>[265]</sup> The device performances are summarized in Table 2-5. For comparison, PSCs with spiro-OMeTAD as HTM were fabricated as reference and photovoltaic conversion efficiency (PCE) can reach up to 17.7%. First of all, molecules TAN-N-Ph, TAN-N-2,4,6MePh, TAN-N-4MePh, and TAN-N-3,5MePh led to rather fair PCEs of 8.8%, 5.9%, 6.4% and 6.3%, respectively. The best system was this using TAN-N-2,6MePh as HTM which led to PCEs up to 10.4% with a short-current density ( $J_{sc}$ ) of 18.58 mA cm<sup>-2</sup>, an open-circuit photovoltage ( $V_{oc}$ ) of 0.92 V and a fill factor (FF) of 0.61 (Figure 2-14). Nonetheless, all photovoltaic parameters for TAN-N-2,6MePh are weaker than those obtained with spiro-OMeTAD. The corresponding J-V characteristic showed almost no hysteresis which is promising for further investigations.

Table 2-5. Photovoltaic characteristics of TAN-N-Ph, TAN-N-2,4,6MePh, TAN-N-4MePh, TAN-N-2,6MePh and TAN-N-3,5MePh.

Material	$J_{sc}$ (mA/cm <sup>2</sup> )	$V_{oc}$ (V)	FF	PCE (%)
<b>TAN-N-Ph</b>	16.1	0.89	0.61	8.8
<b>TAN-N-2,4,6MePh</b>	12.5	0.89	0.53	5.9
<b>TAN-N-4MePh</b>	11.3	0.89	0.64	6.4
<b>TAN-N-2,6MePh</b>	18.6	0.92	0.61	10.4
<b>TAN-N-3,5MePh</b>	12.3	0.92	0.55	6.3
<b>Spiro-OMeTAD</b>	22.1	1.07	0.75	17.7

Even though dopants were used in this study, the PCE obtained with these materials should depend on their hole mobility and stability. The first evidence is that the two highest efficiencies, 8.8 and 10.4%, were obtained with TAN-N-Ph and TAN-N-2,6MePh, respectively, which are expected to provide higher charge transport dimensionality according to XRD results. These higher PCEs are mainly due to much higher  $J_{sc}$  values which are determined by the charge transport properties of the HTMs in PSCs. As a consequence, the higher  $J_{sc}$  measured with TAN-N-Ph and

TAN-N-2,6MePh can be related to the numerous branch-arm and branch-branch interactions found by XRD measurements in the solid state. On the other hand, the compound without substitution on 3, 4 and 5 positions led to the highest PCE. The following hypothesis can also be formulated to explain this finding: a substantial part of the charge carrier transport pass through the branches and more probably between branches. A careful determination of the conductivity of these materials should be carried out in the future to confirm this assumption.

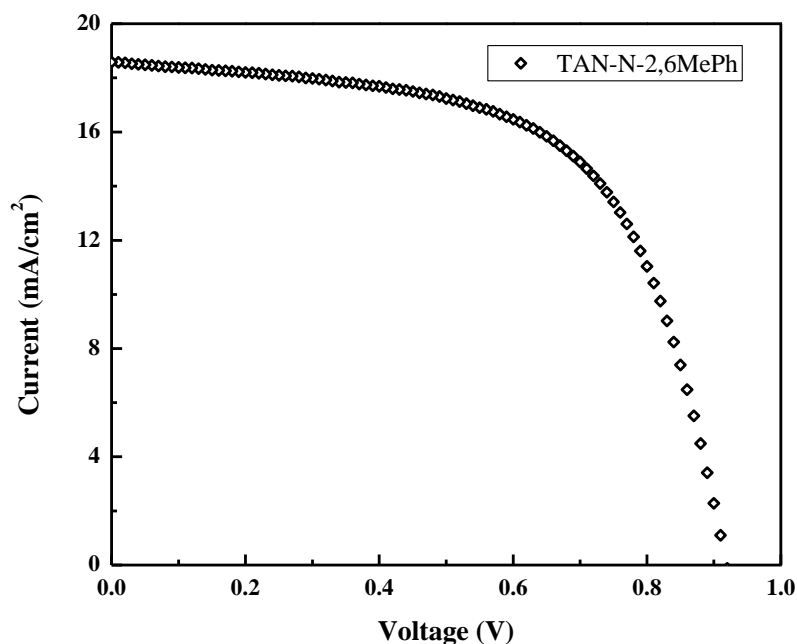


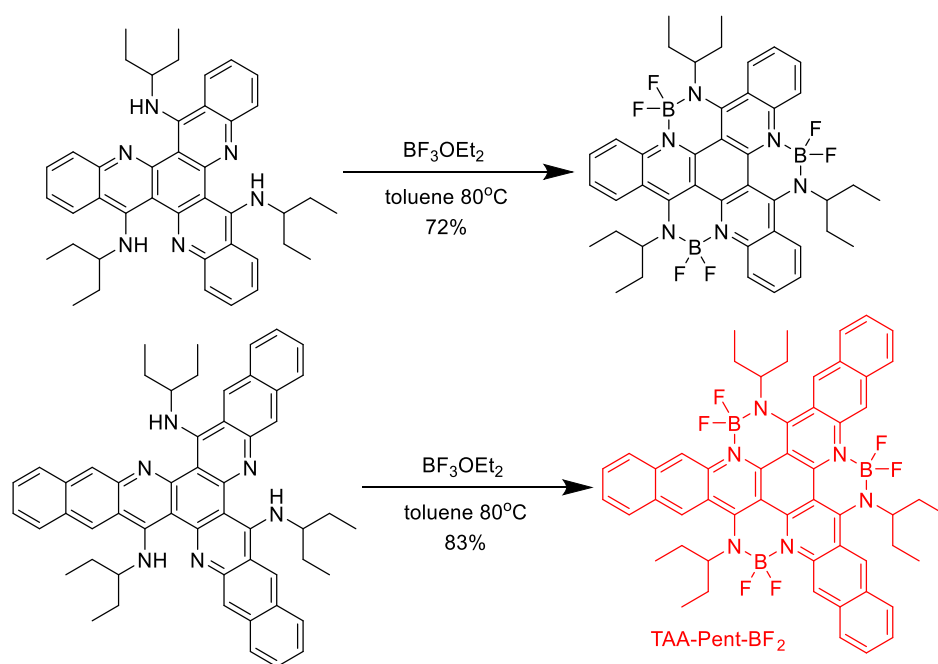
Figure 2-14. Photocurrent-voltage (J-V) characteristic of PSC based on the TAN-N-2,6MePh.

## 2.7 BF<sub>2</sub>-rigidified Dyes

Boron dipyrromethene (BODIPY) dyes were first reported in 1968 by Treibs and Kreuzer.<sup>[266]</sup> Since then, BODIPY moiety has been widely utilized in organic solar cells, organic light-emitting diodes, sensing, imaging, owing to its rich optoelectronic properties.<sup>[267,268]</sup> BODIPY dyes are outstanding fluorescent dyes featuring with strong absorption in the UV-visible wavelength range, relatively sharp fluorescence emission and high quantum yields of fluorescence emission. However, BODIPY dyes suffer from some limitations for application purpose due to their low Stokes shift (7–15 nm) which allows re-absorption of the emitted photons. The low Stokes shift observed for BODIPY dyes can be ascribed to their rigid molecular structures. Desymmetrization of the bidentate nitrogen ligand and replacement of rigid heterocycle pyrrole by substituted amines constitute a promising method to enlarge

Stokes shift.<sup>[219]</sup> Therefore, the molecular structure we introduced in this chapter can be considered as a perfect multidentate ligand which is able to complex with boron centers to form dyes with large Stokes shift. The same strategy has been used by Feng Qiu *et al.* in a paper published in 2016 to constitute triple boron-cored chromophores<sup>[269]</sup> and latter these chromophores cross-linked via exposure to white and UV light<sup>[270]</sup>.

We tried both alkylamine substituted molecules and arylamine substituted molecules to react with boron trifluoride diethyl etherate in the presence of triethylamine.<sup>[271]</sup> First of all, TAN-N-Pent and TAA-N-Pent actually reacted with three equivalents of boron trifluoride diethyl etherate ( $\text{BF}_3\text{OEt}_2$ ) to yield two novel chromophores, TAN-Pent- $\text{BF}_2$  and TAA-Pent- $\text{BF}_2$ , including three chelated boron centers (Scheme 2-9). By contrast, the tris-adduct cannot be obtained by using the arylamine substituted molecules due to steric hindrance and the electron withdrawing effect of  $\text{BF}_2$  moiety. In this case, only two boron atoms were chelated by the multidentate ligand.



Scheme 2-9. Synthetic routes towards TAN-Pent- $\text{BF}_2$  and TAA-Pent- $\text{BF}_2$ .

Optical properties of TAN-Pent- $\text{BF}_2$  and TAA-Pent- $\text{BF}_2$  in diluted dichloromethane solution were investigated by UV-visible and photoluminescence (PL) spectroscopy. The longest wavelength for absorption maximum of TAN-Pent- $\text{BF}_2$  was found to be 376 nm while that of TAA-Pent- $\text{BF}_2$  was measured at 399 nm. The 23 nm red-shift can reasonably be attributed to the extension of  $\pi$ -conjugated system in TAA-Pent- $\text{BF}_2$ . Both TAN-Pent- $\text{BF}_2$  and TAA-Pent- $\text{BF}_2$  show broad absorption bands

which reveal more flexible molecular structures compared with BODIPY.<sup>[272]</sup> Interestingly, absorption maximum of TAN-Pent-BF<sub>2</sub> is 23 nm red-shifted compared with TAN-N-Pent, while it is almost the same for TAA-Pent-BF<sub>2</sub> and TAA-N-Pent. No emission can be observed for TAN-N-Pent and TAA-N-Pent, but after incorporation of BF<sub>2</sub> moieties, TAN-Pent-BF<sub>2</sub> exhibits blue emission at 476 nm and TAA-Pent-BF<sub>2</sub> shows green emission at 541 nm. Moreover, large Stokes shifts have been observed for both TAN-Pent-BF<sub>2</sub> and TAA-Pent-BF<sub>2</sub> (100 nm and 142 nm respectively) which indicates energy losses due to conformational changes related to the flexible structure of this family of molecules.

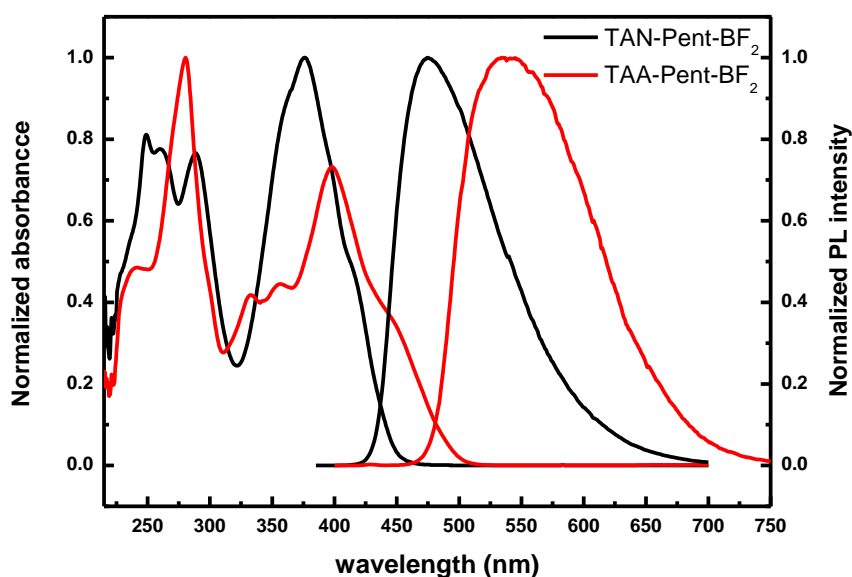


Figure 2-15. UV-visible and PL spectra of TAN-Pent-BF<sub>2</sub> and TAA-Pent-BF<sub>2</sub> in DCM.

Cyclic voltammetry (CV) studies were carried out in THF solution to investigate the electronic properties of these new compounds. Both TAN-Pent-BF<sub>2</sub> and TAA-Pent-BF<sub>2</sub> showed a reversible reduction wave whereas no oxidation wave could be observed. Accordingly, LUMO energy levels were derived based on the onset values of the reduction potential (-3.1 eV and -3.31 eV for TAN-Pent-BF<sub>2</sub> and TAA-Pent-BF<sub>2</sub>, respectively). HOMO energy levels were then estimated from the optical band gaps (2.76 eV and 2.49 eV, respectively) and the LUMO energy values. Cyclovoltammograms of TAN-N-Pent and TAA-N-Pent are also depicted in Figure 2-16 for sake of comparison. Introduction of BF<sub>2</sub> moieties lowered the HOMO and LUMO energy levels by around 0.6 eV, consequently these molecules are potential n-type material due to their electron-deficient properties.

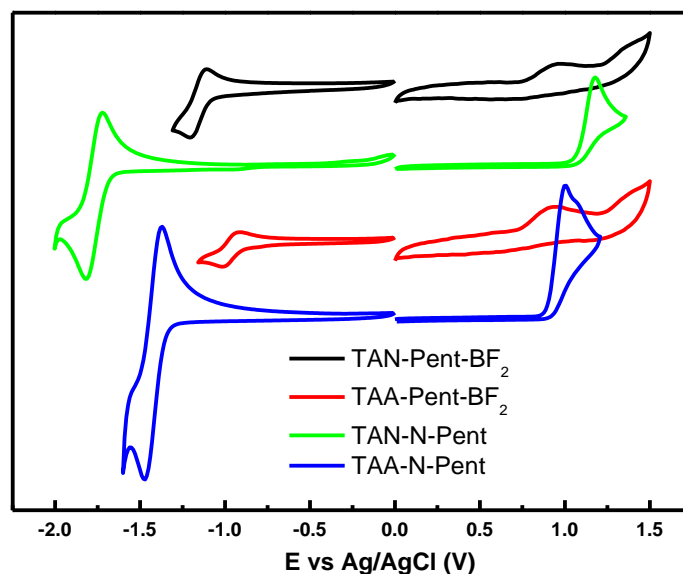


Figure 2-16. Cyclic voltammograms of TAN-Pent-BF<sub>2</sub>, TAA-Pent-BF<sub>2</sub>, TAN-N-Pent and TAA-N-Pent in THF.

Table 2-6. Optical and electrochemical properties of TAN-Pent-BF<sub>2</sub> and TAA-Pent-BF<sub>2</sub>.

Compounds	$\lambda_{\text{abs}}$ (nm) <sup>a</sup>	$\lambda_{\text{em}}$ (nm) <sup>b</sup>	$E_{\text{g}}^{\text{opt}}$ (eV) <sup>c</sup>	$E_{\text{onset}}^{\text{red}}$ (V) <sup>d</sup>	LUMO (eV) <sup>e</sup>	HOMO (eV) <sup>f</sup>
TAN-Pent-BF <sub>2</sub>	289, 376	476	2.76	-1.16	-3.1	-5.82
TAA-Pent-BF <sub>2</sub>	279, 399	541	2.49	-0.97	-3.31	-5.8

a: Two main absorption features for each compound. b: Emission maximum upon excitation at the longest absorption maximum. c: Optical bandgap calculated from the threshold of UV-vis absorption spectrum. d: Onset reduction potential vs Ag/AgCl. e: LUMO energy level calculated from  $E_{\text{onset}}^{\text{red}}$  using equation (1). f: HOMO energy level calculated from  $E_{\text{onset}}^{\text{ox}}$  using equation (2).

Molecule structure and molecular packing of TAN-Pent-BF<sub>2</sub> in single crystal are shown in Figure 2-17. Solution NMR data evidenced that TAN-Pent-BF<sub>2</sub> preserves  $C_3$  symmetry in solution, but single crystal X-ray structure showed that TAN-Pent-BF<sub>2</sub> exhibits asymmetric structure in the solid state. As shown in Figure 2-17 (a), three branches and BF<sub>2</sub> moieties are placed on one side of the molecule mean plane (dihedral angles 34.04 °, 32.1 ° and 28.45 °) and three arms of the molecules bend to the other side of the plane (bending angles of the arms are calculated from the mean plane of the central ring and the line connecting the centroids of the third and central phenyl rings, 2.77 °, 7.66 ° and 8.02 °). The bending angles derived from TAN-N-Pent single crystal (1.3 °, 2.3 ° and 3.36 °) are much smaller. The congested circumstances after the introduction of BF<sub>2</sub> moieties enhanced the non-planar property of the molecule.

Consequently as shown in Figure 2-17 (c) the bowl-shaped molecule shows a compact  $\pi$ - $\pi$  stacking with another molecule on the side without branches and these two molecules constitute a dense dimer with  $d_{C-C}$  as 3.39 Å. However, as shown in Figures 2-17 (d) and (e) there is no efficient interactions between dimers which is detrimental for the charge carrier transport in OSCs.

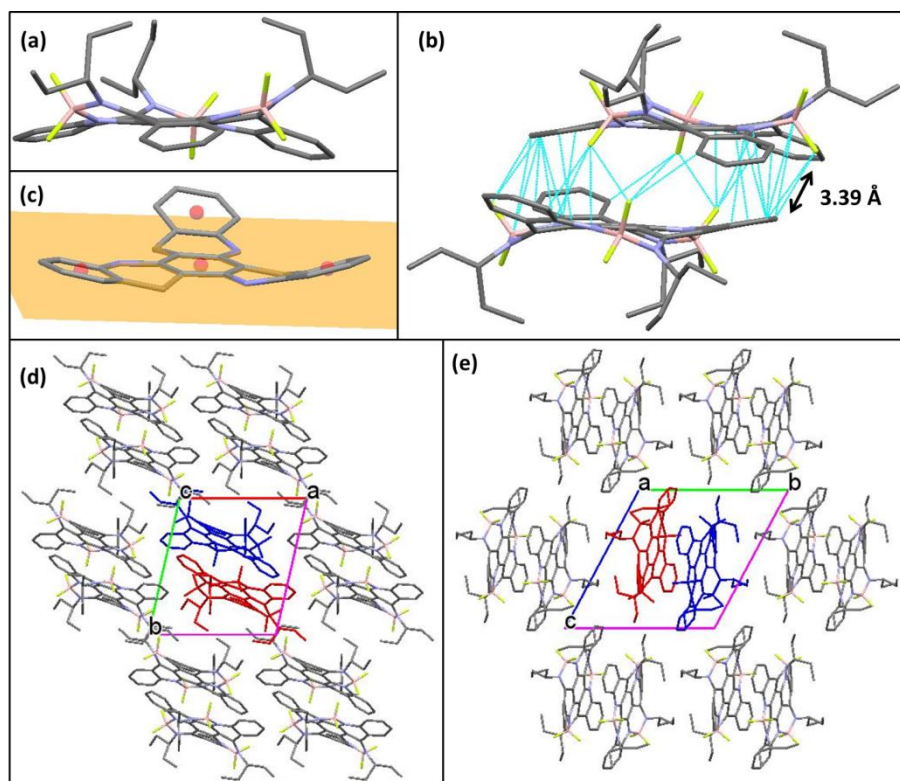


Figure 2-17. Molecular structure (a, c) and molecular packing (b, d-f) of TAN-Pent-BF<sub>2</sub> in single crystal.

Molecular structure and packing of TAA-Pent-BF<sub>2</sub> in single crystal are shown in Figure 2-18. As found for TAN-Pent-BF<sub>2</sub>, TAA-Pent-BF<sub>2</sub> exhibits asymmetric structure in the solid state. With three branches on one side of the molecule (dihedral angles 6.55°, 25.96° and 27.54°) and three arms bending to the other side of the molecule (5.04°, 5.32° and 13.08°), a bowl-shaped molecule configuration was also observed for TAA-Pent-BF<sub>2</sub> (displayed in Figure 2-18 (a)). The bending angles of the arms are larger compared with those of TAA-N-Pent (1.22°, 3.24° and 3.46°). As shown in Figure 2-18 (b), each molecule has efficient face-to-face  $\pi$ - $\pi$  stacking with two neighboring molecules and thus forms a column with fully  $\pi$  stacking. However, due to the large steric hindrance of branches the interactions between columns are weak, as shown in Figure 2-18 (c) and (d), thus TAA-Pent-BF<sub>2</sub> may possess a 1D charge carrier transport pathway.

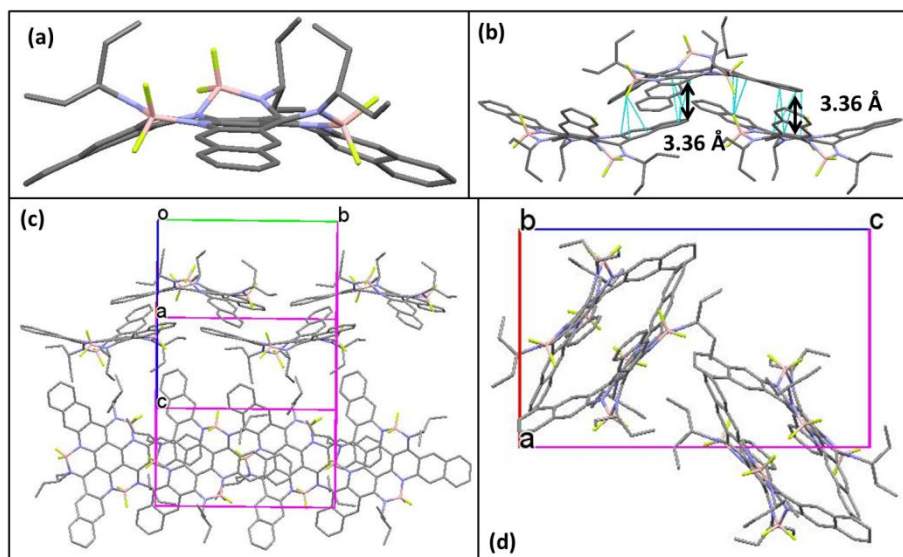


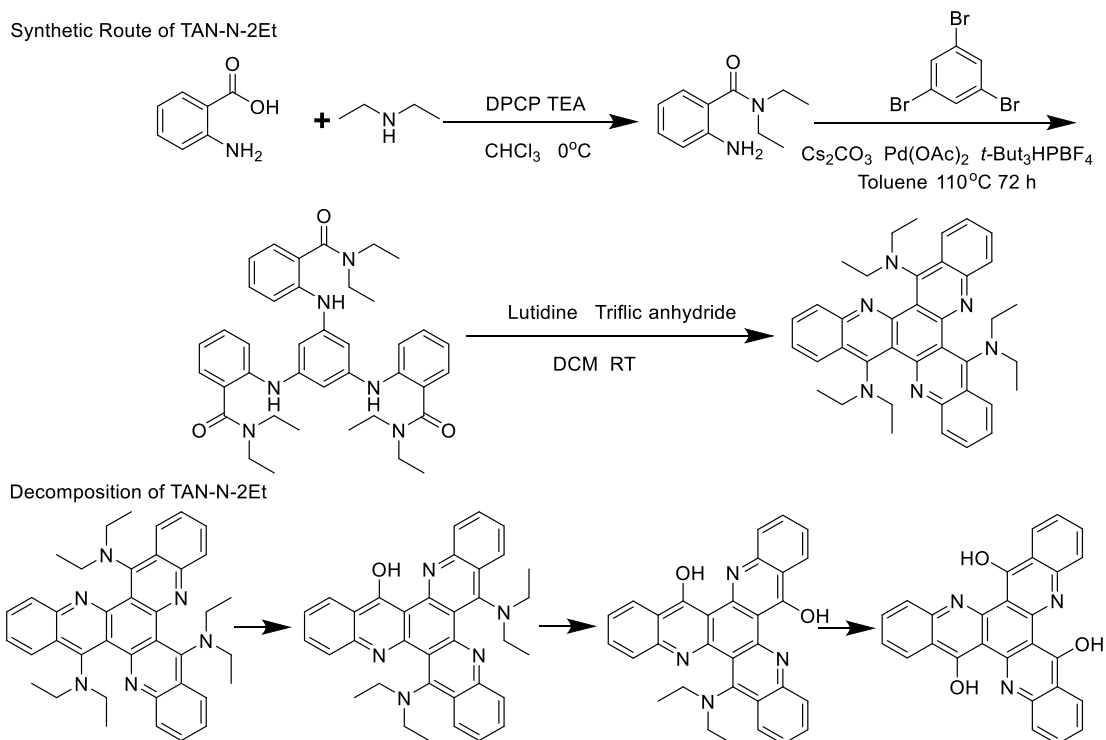
Figure 2-18. Molecule structure (a) and molecular packing (b-d) of TAA-Pent-BF<sub>2</sub> in single crystal.

To summarize, in this part we rigidified the molecule structures of TAN-N-Pent and TAA-N-Pent with BF<sub>2</sub> moieties to provide two new compounds TAN-Pent-BF<sub>2</sub> and TAA-Pent-BF<sub>2</sub>. After careful characterization of the molecule properties, two promising applications of these materials can be proposed. Firstly, as BODIPY type dyes these materials possess large Stokes shift which opens new avenues for applications in luminescence. Secondly, due to the introduction of BF<sub>2</sub> moieties, the LUMO energy levels are much lower which makes these materials possible to work as n-type semiconductors.

## 2.8 Trihydroxy-triazatrinaphthylene

As we reported before, compounds substituted by secondary amine, such as diethylamine (TAN-N-2Et), dipropylamine (TAN-N-2nPr) and diisopropylamine (TAN-N-2iPr) were successfully synthesized. However, these molecules were not stable under ambient conditions especially in the presence of water. When they were dissolved in dichloromethane, they were easily decomposed in a few hours and precipitation was observed. According to mass spectroscopy and <sup>1</sup>H NMR, hydroxyl groups are present in the decomposition products. Mass spectra of decomposed mixture of 6,12,18-Tris(diethylamino)-5,11,17-triazatrinaphthylene (TAN-N-2Et) showed that in the mixture there are three compounds with diethylamino groups replaced by hydroxyl groups once, twice and three times respectively. The decomposition process of TAN-N-2Et is depicted in Scheme 2-9.





Scheme 2-9. Synthetic route (up) and decomposition process (below) of TAN-N-2Et.

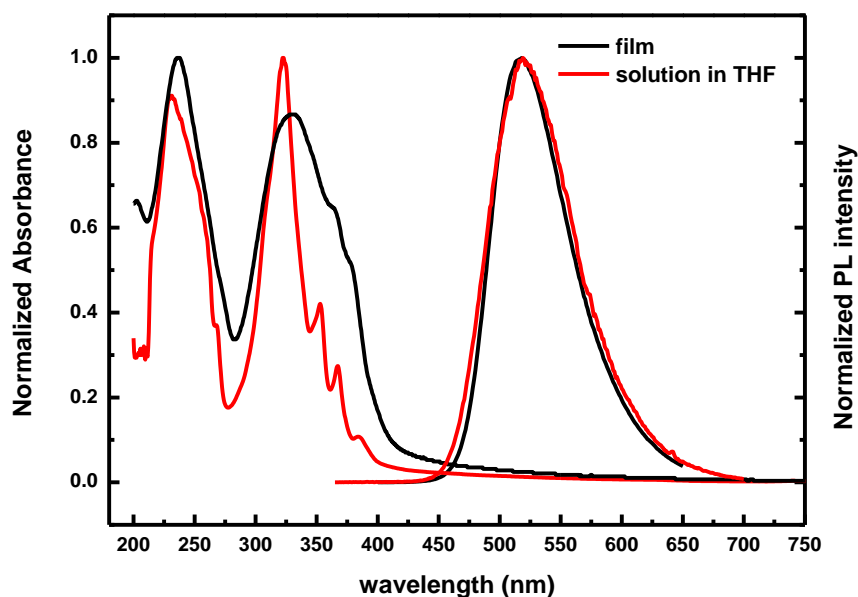


Figure 2-19. UV-visible and PL spectra of TAN-3OH in THF (red) and in film (black).

Most interestingly, the final compound isolated after complete decomposition, 6,12,18-trihydroxy-5,11,17-triazatrinaphthylene (TAN-3OH), is highly fluorescent both in diluted solution and the solid state. Due to the low solubility of TAN-3OH, UV-visible spectra can only be recorded in diluted THF solution. Thin films of

TAN-3OH on quartz were obtained by thermal evaporation. As shown in Figure 2-19, absorption spectrum in solution is acuter compared with that of thin film due to the more flexible molecule vibration in solution. Fluorescent spectra are the same in solution and film with high luminescence at 520 nm. The direct quantum yield measured by integration sphere from thin film of TAN-3OH was found to be 8.6%.

A paper published in 2017 by Adachi's group studied TAN-3OH thoroughly by both theoretical simulation and experiment.<sup>[273]</sup> In this paper they explained that the high fluorescent property of TAN-3OH originated from thermally activated delayed fluorescence (TADF) which is normally induced by HOMO and LUMO separation.<sup>[274]</sup> In the fully fused, planar and rigid  $\pi$ -system of TAN-3OH, the HOMO and LUMO separation is achieved by excited-state intramolecular proton transfer (ESIPT) within TAN-3OH molecule.<sup>[275,276]</sup> This is the first example of OLED using an ESIPT-based TADF material and it provided a new method to construct TADF materials without using a donor-acceptor system.

In the paper mentioned above, the OLEDs were fabricated by thermal evaporation due to the low solubility of TAN-3OH. In our case, we can benefit from the decomposition of secondary amine substituted TAN and fabricate the device by cheaper and easier solution method. For example, solution of TAN-N-2Et could be used to spin-coat thin film and after decomposition the diethyl amine with boiling point at 89 °C will be very easily to remove. By this way, we can fabricate the device using solution method and modify the thin film morphology by using different branches.

## 2.9 Conclusion

In this chapter, new star-shaped molecules were firstly introduced with a molecular design to achieve 3D charge carrier transport in solid state. Then, common and new synthetic pathways were reported to reach a series of star-shaped molecules with arms based on acridine structure and branches composed of aromatic or aliphatic amine. For all pure compounds, molecular and material properties were investigated by NMR spectroscopy, UV-Visible absorption spectroscopy, XRD crystallography, modeling, optical microscopy and these new materials were investigated in organic electronic devices (OFETs and PSCs).

Even though the performances obtained with the devices based on these materials did not reach state of the art performances, some interesting fundamental conclusions can be drawn and a few suggestions to optimize these molecules and design new molecules are proposed below.

- 1) Small differences in the chemical structure change totally the packing mode. Indeed, all interactions are Van der Waals interaction or  $\pi$ -stacking which are in similar energy range. In our case, these interactions are balanced.

- 2) The comparison of the TAN-N-Pent and TAA-N-Pent crystallographic structures indicates that longer arms are favorable to form efficient  $\pi$ - $\pi$  stacking between arms and to increase dimensionality of charge carrier transport. Consequently, in order to obtain 2D or 3D charge carrier transport in the solid state, longer arms have to be tested.
- 3) Molecular structures deduced from single crystal X-ray crystallography show that the  $sp^3$  hybrid nitrogen atoms, which work as flexible nodes, allow numerous arrangements of branches. Therefore, replace the N-H moieties in branches by  $sp^2$  carbons could lead to a more rigid molecular structure which allows for limiting the number of possible conformations.
- 4) Modeling and crystal structures have shown that charge transport could be done through the arms and participate to balance charge transport in 2 or 3 directions. The decent PCEs obtained in PSCs are also an indication of a balanced charge transport.
- 5) For alkylamine substituted molecules, there are strong interactions between alkyl chains. For arylamine substituted molecules, aromatic hydrogens in branch parts have a lot of unexpected interactions with the adjacent molecules such as edge-to-face  $\pi$ -stacking. Usually,  $CH_2$ - $CH_2$  interaction (around 1.5 kcal/mol in linear chain<sup>[277,278]</sup> ) and  $CH_3$ - $\pi$  are estimated to be weaker than edge-to-face (around 2.5 kcal/mol for benzene<sup>[279]</sup> ) and face-to face  $\pi$ - $\pi$  interaction. So, replacement of aromatic hydrogens by other groups, such as  $CH_3$  group should reduce the energy gain by interactions with branches and lead to a packing mostly driven by arms interactions. In perspective, theoretical calculation could give the gain in energy for each dimer as well as for each specific interaction. These results will help us to understand packing rules and design new molecules

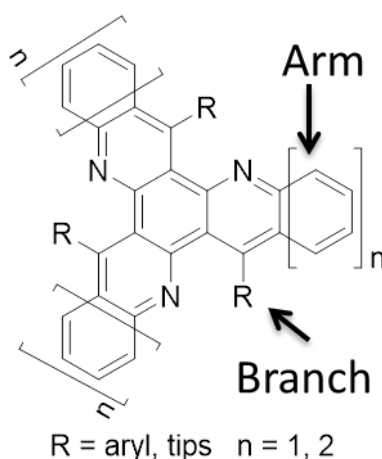
**Chapter 3:**  
**Triazastarphene Substituted by C<sub>sp2</sub>**  
**and C<sub>sp</sub> as Electron Transport Materials**



## 3.1 Introduction

### 3.1.1 Design

As mentioned in chapter 2,  $sp^3$  hybrid nitrogen atoms (NH) lead to flexible branches. Thus, the relative position of bulky substituents is difficult to fix and to foresee in the solid state as well as molecular packing. In order to reach the arrangement we were targeting (Chapter 1.7), the star-shaped central core design used in Chapter 2 has been kept. Then, the NH moiety has been replaced by  $sp^2$  or  $sp$  carbon which is small and has bonds inscribed in a plan (Scheme 3-1). Crystallographic data of similar smaller molecules have been gathered and compared.<sup>[280,281]</sup> It suggests the fused  $\pi$ -system should remain planar with benzene as branches. Moreover, two different lengths for the arms were investigated as we already did in the previous chapter.



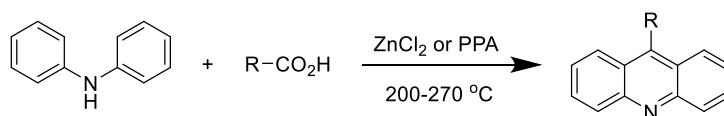
Scheme 3-1. Molecular skeleton frame of the designed molecules.

### 3.1.2 Retrosynthesis

Two synthetic methods were introduced in chapter 2. Triazatrinaphthylene (TAN) derivatives were indeed synthesized by nucleophilic reaction between amines and trichloro TAN or by cyclization of the corresponding triamide compounds, while triazatrianthyrene (TAA) molecule with larger  $\pi$ -conjugation system could only be synthesized by the second method. In this chapter where we intend to obtain original large  $\pi$ -conjugation systems, we have to find synthetic routes and keep in mind the possible solubility issues. As in the previous chapter, the formation of the 6 atoms ring including a nitrogen atom is the key step of the synthesis. Indeed, 9-substituted acridines are often obtained by cyclisation of the cycle containing the nitrogen. Moreover, to keep molecules soluble even with extended arms, the branches have to

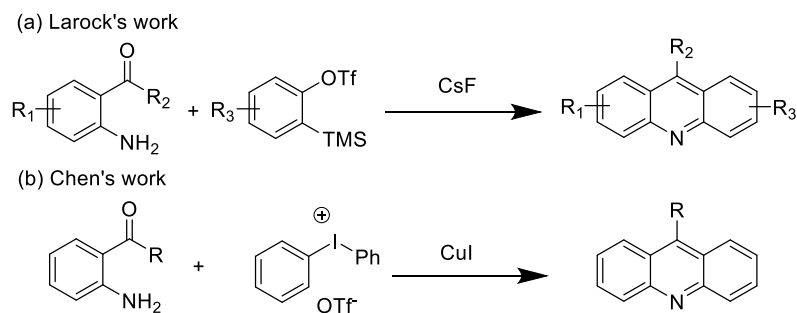
be bonded before extension of  $\pi$ -conjugated system and cyclisation. Therefore, it is crucial to find a simple and straightforward way to synthesize 9-substituted acridines with cyclization reaction as the last step.

Acridines are important nitrogen-containing moieties that have been widely used in biological and medicinal areas owing to their inhibition of DNA-related enzymes by intercalation.<sup>[282]</sup> Many antibacterial, antileukemic, antimalarial, and anticancer drugs based on acridine derivatives have been synthesized and commercialized.<sup>[283–286]</sup> Beneficiating from their rigid conjugated structures, acridine derivatives with extended conjugated systems have also been applied as building blocks in dyes and pigments,<sup>[287]</sup> ligands,<sup>[288]</sup> fluorescent sensors,<sup>[289]</sup> and even in semiconductor materials<sup>[290]</sup>. Therefore, huge efforts have been devoted to searching for efficient synthetic methodologies towards acridines over several decades. Bernthsen reaction (Scheme 3-2), one of the earliest synthetic methods for acridine derivatives was published in 1878. In this method acridines were synthesized under harsh reaction conditions: heating diphenylamine and carboxylic acids at 200–270 °C for about twenty hours with zinc chloride as the catalyst.<sup>[291,292]</sup> In 1962, this method was modified by Popp's work (Scheme 3-2) in which polyphosphoric acid was used instead of zinc chloride and the reaction time was reduced to 15 minutes.<sup>[293]</sup>



Scheme 3-2. Bernthsen and Popp's work.

Since then, a series of useful methods have been developed for the construction of acridines. A convenient and mild synthetic method for acridines was [4 + 2] annulation (Scheme 3-3) with benzyne intermediate. In 2010, Larock reported a reaction between 2-aminoaryl ketones and in situ arynes generated by the treatment of *o*-(trimethylsilyl)aryl triflates with CsF resulted in [4 + 2] annulation to afford substituted acridines in good yields (Scheme 3-3 (a)).<sup>[294]</sup> In 2015, a modular method to synthesize acridine derivatives was developed by Chen with *o*-acylanilines and diaryliodonium salts (Scheme 3-3 (b)). The reactions proceeded smoothly under Cu-catalyzed or metal-free reaction conditions at elevated temperature through tandem arylation/Friedel–Crafts reactions.<sup>[295]</sup>

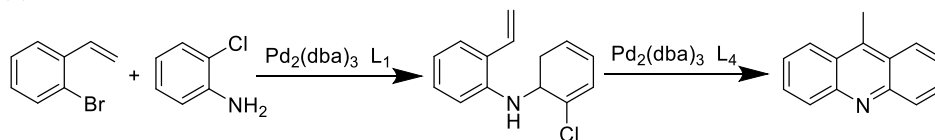


Scheme 3-3. [4 + 2] annulation method to synthesize acridines.

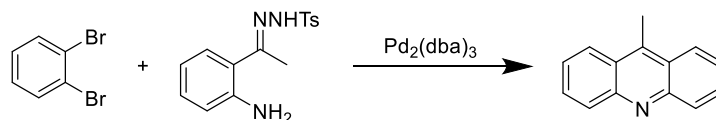
Another widely studied synthetic method of acridines is Pd-catalyzed auto-tandem synthesis (Scheme 3-4). In 2010, Buchwald reported that Pd-catalyzed condensation of 2-bromostyrene and 2-chloroaniline derivatives yielded stable diphenylamine intermediates, and these intermediates were converted into acridines using another ligand for the palladium catalyst (Scheme 3-4 (a)).<sup>[296]</sup> Later in 2012, Wang developed a facile palladium-catalyzed synthesis of acridines by consecutive C-C and C-N cross-coupling (Scheme 3-4 (b)). By this method, a variety of functionalized acridines are accessible from easily available *o*-dihalobenzenes and N-tosylhydrazones in one step.<sup>[297]</sup> In 2013, Qu developed a Pd-catalyzed one-pot amination/cyclization/ elimination reaction of 2-formyl-phenyl triflate and anilines to construct acridines (Scheme 3-4 (c)). With Pd(OAc)<sub>2</sub>-X-Phos as the catalyst, a series of unsymmetric acridines were obtained in moderate yields.<sup>[298]</sup> In 2015, Xu demonstrated an efficient tandem coupling/cyclization approach for facile synthesis of diversely substituted acridines (Scheme 3-4 (d)). The reactions were accomplished with ease under Pd(0)-catalysis by using commercial available substituted 2-bromobenzaldehydes and 3,5-dimethoxyaniline as starting materials. The Lewis acid AlCl<sub>3</sub> was required to promote the sequential cyclization for less electron-rich anilines.<sup>[299]</sup> In 2017, Deng developed an approach for the synthesis of 9-aryl-substituted acridines from 2-aminobenzophenones and cyclohexanones involving a condensation/cyclization/aromatization sequence (Scheme 3-4 (e)). Cheap and readily available cyclohexanones were used as the aryl source through a dehydrogenation/tautomerization process under oxygen atmosphere.<sup>[300]</sup> In the same year, Wu developed a new aerobic oxidative annulation of cyclohexanones and 2-aminophenyl ketones (Scheme 3-4 (f)). With the use of non-symmetric 3-substituted cyclohexanones as substrates, a high regioselectivity was observed for this Pd-catalyzed acridine synthesis.



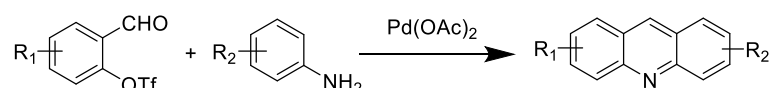
(a) Buchwald's work



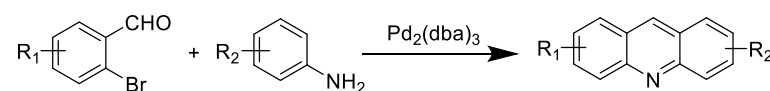
(b) Wang's work



(c) Qu's work



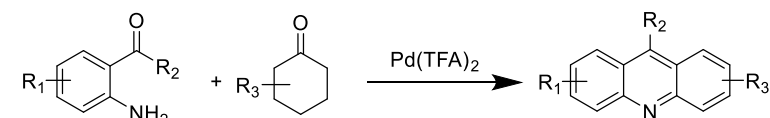
(d) Xu's work



(e) Deng's work

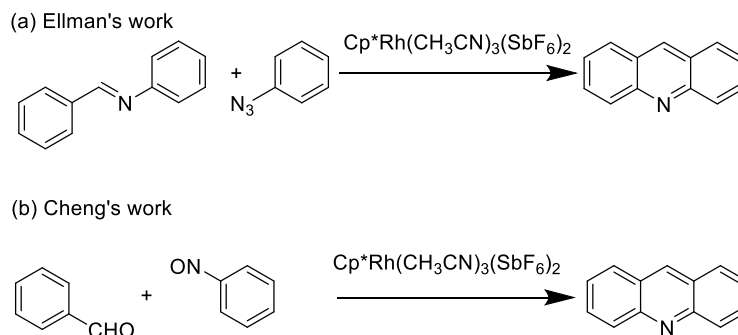


(f) Wu's work



Scheme 3-4. Pd-catalyzed auto-tandem cyclization method for acridines.

There are also some other methods to synthesize acridines, such as Ru(III)-catalyzed annulations (Scheme 3-5). In 2013, Ellman reported Ru(III)-catalyzed [3 + 3] annulations of aromatic azides and aromatic imines to give acridines (Scheme 3-5 (a)).<sup>[301]</sup> In 2017, Cheng demonstrated a straightforward, highly efficient, and sustainable procedure to access acridine analogues starting from aromatic aldehydes and aryl nitrosos enabled by C–H functionalization bilateral cyclization (Scheme 3-5 (b)). This procedure proceeded with the in situ formation and removal of an imino transient directing group in the presence of catalytic amount of  $\text{BnNH}_2$ .<sup>[302]</sup>



Scheme 3-5. Ru(III)-catalyzed annulations for acridines.

In the molecular structures we designed, three 9-substituted acridines are included. On the other hand, a reactant with 3 nitrogens in 1,3,5 position of benzene ring to induce the  $C_{3h}$  symmetry is not available and its synthesis is dangerous. Therefore, the nitrogen must be on the other substrate and an aminonaphthalene will be required for large star-shaped molecules. To be sure about the regioselectivity of our last reaction with aminonaphthalene, we only selected reaction with a substituent in *ortho* position of nitrogen which conducts the annulation. Thus, Ru(III)-catalyzed annulation are not suitable for our system. We assumed that Pd-catalyzed auto-tandem cyclization method could be a good method for our star-shaped molecules.

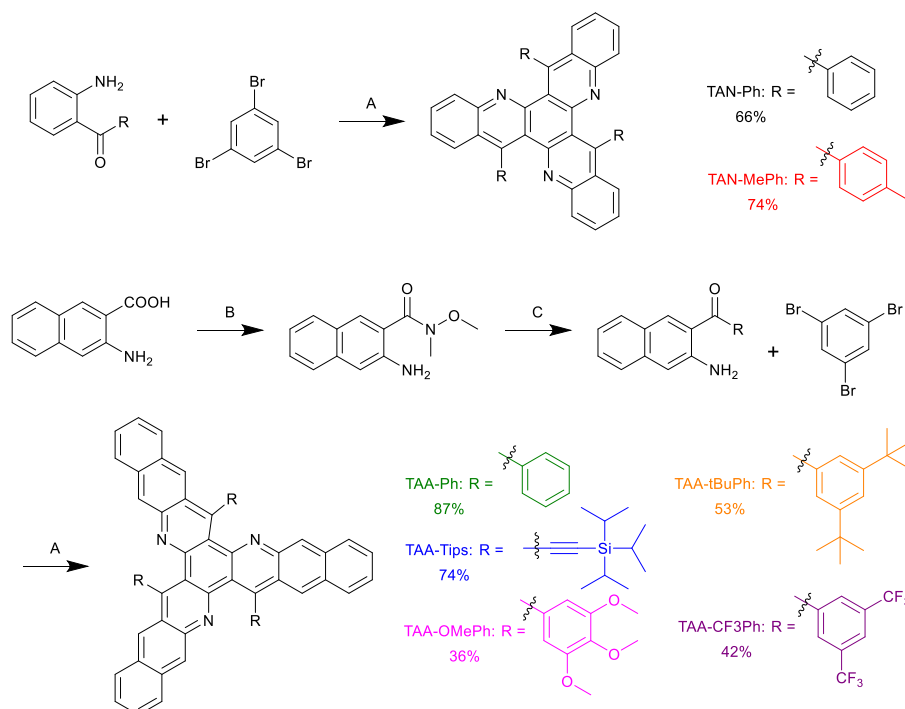
## 3.2 Synthesis

In the beginning of our synthesis, we used a traditional Buchwald reaction condition:  $Pd_2(dba)_3$  ( $dba =$  dibenzylideneacetone) as Pd(0) source, BrettPhos (2-(dicyclohexylphosphanyl)-3,6-dimethoxy-2,4,6-triisopropylbiphenyl) as ligand,  $K_2CO_3$  as base, and *t*-BuOH as solvent to realize the first cross-coupling reaction between two commercial available compounds, 2-aminobenzophenone and 1,3,5-tribromobenzene (Scheme 3-6). The final TAN derivative was obtained in one-step with good yield (66%), suggesting that amination coupling and cyclization occurred in tandem.

In order to get deeper understanding of the reaction mechanism, reactions of 2-aminobenzophenone with both bromobenzene and 1,4-dibromobenzene were carried out. In this case, the reactions were stopped after the first amination steps without acridine formation, evidencing a two-step reaction mechanism. In conclusion, the three substitutions on 1,3,5 positions of a benzene by electron releasing groups, such as amine in our case or methoxy group in Xu's study (Scheme 3-4 (d)), activate carbons in *ortho* positions to achieve the cyclization and aromatization in mild basic conditions. Other derivatives of 2-aminobenzophenone have been applied to increase the branch size. When benzene branches were substituted twice in *ortho* positions, the cyclization steps did not occur, while the final compounds were obtained for other

regioisomers.

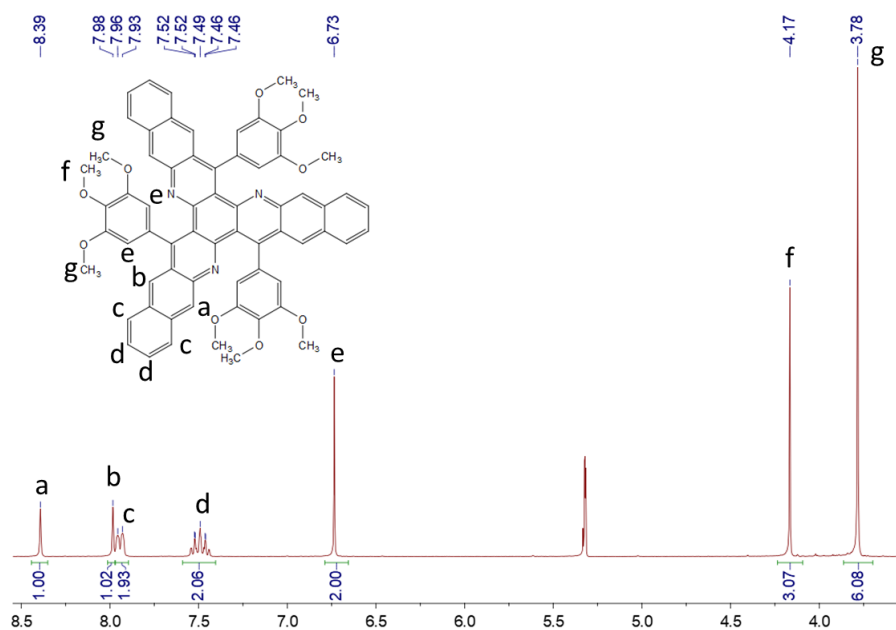
As shown in Scheme 3-6, this synthetic pathway was extended to 2-amino-3-benzoylnaphthalene derivatives to construct TAA derivatives. Thus, the arms of star-shaped molecules were successfully lengthened without encountering solubility issues, which are frequently observed for large  $\pi$ -conjugated systems. For the synthesis of TAA derivatives, 3-amino-2-naphthoic acid was transferred to Weinreb amide before being reacted with Grignard or organolithium reagents to make sure to get ketone compounds. Then, the final products were synthesized by one-pot reactions between aminoketones and 1,3,5-tribromobenzene with quite high yield. Furthermore, the versatility of this one-step reaction was pushed forward with triple bond substitutions as branches to lead to  $C_{3h}$  equivalents of Tips-pentacene with high yield of 74%.



Scheme 3-6. Synthetic routes towards the TAN and TAA derivatives. A:  $Pd_2(dba)_3$ , Brettphos,  $K_2CO_3$ , *t*-BuOH,  $100^\circ C$ , 24 h. B: MeNHOMe $\cdot$ HCl, DPCP,  $Et_3N$ , DCM,  $0^\circ C$ ., overnight. C: Br-R / H-R, *n*-BuLi, THF,  $-78^\circ C$ . / PhMgCl, THF,  $0^\circ C$ .

Finally, seven new star-shaped molecules with different arm lengths and branch sizes (Scheme 3-6) have been efficiently synthesized with a last tandem step reaching up to 87% yield.  $^1H$  and  $^{13}C$  NMR data along with high-resolution mass spectrometry analyses were in agreement with the expected chemical structures. A single set of proton and carbon signals were observed by  $^1H$  and  $^{13}C$  NMR spectroscopy for the arm-branch unit confirming the  $C_3$  chemical structure of each star-shaped compound in solution. To illustrate this finding,  $^1H$  NMR spectra of TAN-OMePh is shown in

Scheme 3-7 as an example.



Scheme 3-7. <sup>1</sup>H NMR spectra of TAN-OMePh

### 3.3 Optical and Electrochemical Properties

Optical and electrochemical properties of all the compounds were investigated by UV-visible spectroscopy and cyclic voltammetry (CV).

UV-visible spectra of the seven compounds were recorded in dichloromethane (DCM) solutions (Figure 3-1). The spectra of the two triazatrinaphthylene derivatives (TAN-Ph and TAN-MePh), are very similar, with main absorption peaks at 232 and 298 nm, and two small absorption bands at longer wavelength (365 and 383 nm). The highest-wavelength absorption band ( $\lambda_{\max}$ ) at 383 nm reflects the  $\pi$ - $\pi^*$  transition absorption of the starphene conjugated core. The optical energy bandgaps of TAN-Ph and TAN-MePh estimated from the thresholds of the absorption spectra were found to be 3.10 and 3.05 eV, respectively. These bandgaps are close to the values reported for 2,8,14-trimethyl-5,11,17-triazatrinaphthylene (TrisK-H-Me) in which the central starphene is not substituted.<sup>[218]</sup> These results indicate that electron conjugations do not extend over the benzene and toluene branches, and are mainly localized on the central core in solution. This also holds true for four of the five triazatriantrylene (TAA) derivatives, TAA-Ph, TAA-OMePh, TAA-tBuPh and TAA-CF<sub>3</sub>Ph, which display identical absorption bands around 230 nm, 285 nm and 355 nm whatever the substitution of branches. On another hand, the extension of the conjugated core leads to red-shifting of the maximum absorption band of these four TAA derivatives by 57 nm compared to TAN derivatives. As shown on Figure 3-1, the UV-visible spectrum

of TAA-Tips differs from those of benzene-substituted TAA derivatives where main absorption band is red-shifted by 20 nm. It should result from the conjugation between the triple bonds of the Tips substituents and the TAA core. Finally, all absorption spectra exhibit weak absorption bands at higher wavelength, which might be attributed to forbidden  $S_0-S_1$  transition due to the three-fold symmetry.<sup>[303–305]</sup> Consequently, optical energy bandgaps calculated from the thresholds of the UV-vis spectra lie far in the visible part of spectrum (2.38 eV for TAA-Tips, and around 2.55 eV for the other four TAA derivatives). Finally, the maximum wavelength for all spectra is small compared to the size of molecule. Indeed, for molecules owing  $C_{3h}$  or  $D_{3h}$  point groups, their absorption spectra are blue-shifted compared to linear compound with the same number of  $C_{sp^2}$ . For example, maximum absorption wavelengths have been reported at 287 and 476 nm for triphenylene and tetracene in cyclohexane and benzene, respectively.<sup>[306]</sup>

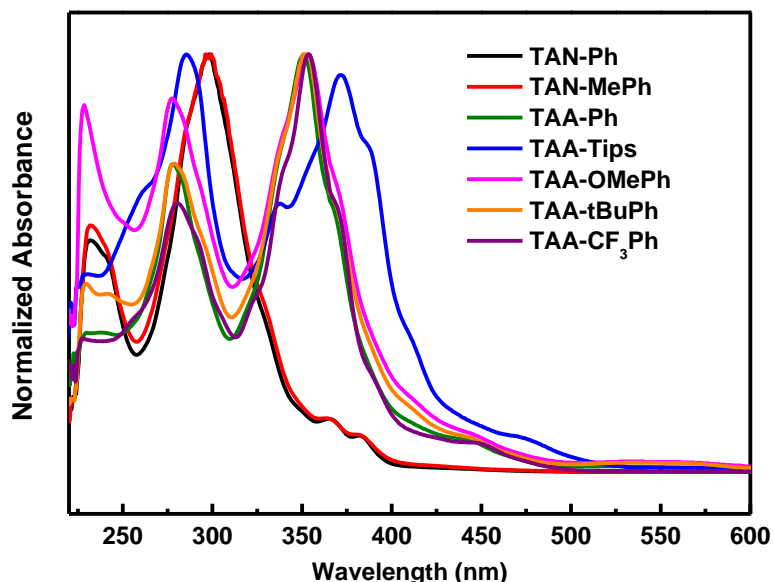


Figure 3-1. UV-visible spectra in DCM of TAN-Ph, TAN-MePh, TAA-Ph, TAA-Tips, TAA-OMePh, TAA-tBuPh and TAA-CF<sub>3</sub>Ph.

Then, cyclic voltammetry (CV) measurements were performed for going further in the investigation of electronic properties. Within the electrochemical window of THF and under a nitrogen atmosphere, all compounds undergo a reversible single-electron reduction wave, which reveals the high stability of radical anions (Figure 3-2). Thus, the radical anion (negatively charged molecule) will be stable under inert atmosphere. Reversely, no oxidation process could be detected.

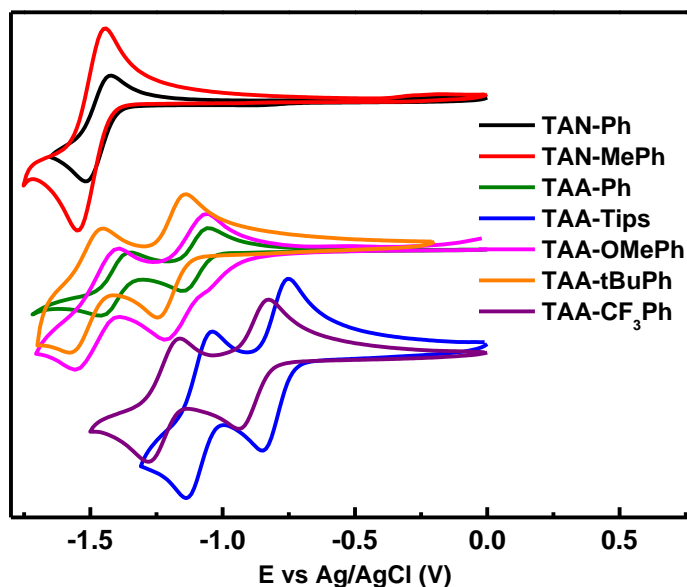


Figure 3-2. CV spectra in THF of TAN-Ph, TAN-MePh, TAA-Ph, TAA-Tips, TAA-OMePh, TAA-tBuPh and TAA-CF<sub>3</sub>Ph

The LUMO energy levels of these molecules were then inferred from the electrochemical data using the following equation (1):<sup>[225]</sup>

$$\text{LUMO} = - (E_{1/2}^{\text{red}} + 4.80 - E_{\text{Fc}/\text{Fc}^+}) \text{ [eV]} \quad (1)$$

where  $E_{\text{Fc}/\text{Fc}^+}$  (0.6 V)<sup>[307]</sup> is the redox potential of the ferrocene/ferrocenium (Fc/Fc<sup>+</sup>) couple measured under the same conditions for each experience and  $E_{1/2}^{\text{red}}$  is the half-wave reduction potential of each compound. Then, HOMO energy levels were eventually estimated from the LUMO values and optical bandgaps. The half-wave reduction potentials versus Ag/AgCl measured for TAN-Ph and TAN-MePh were found to be -1.47 V and -1.49 V, respectively, giving out similar energy diagrams for these two compounds with HOMO levels at -5.83 and -5.76 eV respectively (Table 3-1). The low-lying HOMO levels suggest that these compounds should exhibit high stability under ambient condition over oxidation. Contrary, the oxidized state will be less stable in contact with water and could prevent hole transport. For the TAA derivatives, a second reversible single-electron reduction process is observed. In addition, TAA-Ph, TAA-OMePh and TAA-tBuPh exhibit very similar frontier orbital energy levels while those of TAA-CF<sub>3</sub>Ph and TAA-Tips are deeper (Table 3-1). Consequently, the conjugation between OMe group and star-shape core is weak as already deduced from the UV-visible spectroscopy study. However, even though conjugation between branches and arms are almost null, the six CF<sub>3</sub> groups decrease the oxidation and reduction potential by about 0.2 eV. The smaller optical band gap observed by UV-visible absorption spectroscopy goes along with lower redox

potential for TAA-Tips. Especially, reduction potential decreases about 0.3 eV showing the electron withdrawing character of triple bonds. The high reversibility of the reduction process in solution suggests that these molecules could support electron transport. However, the reduction potentials are not in the range of air stable OSC,<sup>[308]</sup> thus electronic devices and semi-conductive layer should be protected from sources of proton such as water or silanol.

Table 3-1. Optical and electrochemical properties of TAN and TAA derivatives.

Compounds	$\lambda_{\text{abs}}$ (nm) <sup>a</sup>	$E_g^{\text{opt}}$ (eV) <sup>b</sup>	$E_{1/2}^{\text{red}}$ (V) <sup>c</sup>	LUMO (eV) <sup>d</sup>	HOMO (eV) <sup>e</sup>
TAN-Ph	232, 298	3.10	-1.47	-2.73	-5.83
TAN-MePh	233, 297	3.05	-1.49	-2.71	-5.76
TAA-Ph	278, 351	2.56	-1.11	-3.09	-5.65
TAA-Tips	286, 371	2.38	-0.80	-3.40	-5.78
TAA-OMePh	278, 354	2.53	-1.15	-3.05	-5.58
TAA-tBuPh	279, 352	2.55	-1.21	-2.99	-5.54
TAA-CF <sub>3</sub> Ph	280, 353	2.56	-0.88	-3.32	-5.88

a: Two main absorption features for each compound. b: Optical bandgap calculated from the threshold of UV-vis absorption spectrum. c: Half-wave reduction potential vs Ag/AgCl. d: LUMO energy level calculated from  $E_{1/2}^{\text{red}}$  using equation 1. e: HOMO energy level estimated from LUMO energy and optical bandgap values.

## 3.4 Theoretical Calculation

Theoretical calculations were performed for each compound to get an insight into their optical and electrochemical properties. Optimized ground state geometries as well as energy diagrams and electron density distributions have been determined. Meanwhile electronic absorption transitions in UV-visible energy range were simulated.

### 3.4.1 Optimized Geometries and Electron Density Distributions

Molecular geometries were optimized using density functional theory (DFT) at B3LYP/6-311G(d,p) level in gas phase using Gaussian 09 package.<sup>[227]</sup> As found for NH containing molecules introduced in Chapter 2, all the 7 molecules exhibit asymmetric geometry after optimization with small geometrical difference of each arm. However, due to the rigidity of C-C bond, branches do not bend out of the mean plane of the molecules. When compared with NH containing molecules, the higher

steric hindrances caused by the branches in carbon  $sp^2$  or  $sp$  containing molecules force the arms to twist and bend out of mean plane of the molecule. Consequently, all the 7 molecules tend to exhibit a propeller-shaped molecule geometry. For instance, as shown in Figure 3-3 for TAN-N-Ph, the star-shaped central core is almost planar and three branches bend out of the molecular mean plane due to the flexibility of C-N bond. While in its carbon  $sp^2$  counterpart, TAN-Ph, branches do not bend out of the mean plane of the molecules and star-shaped central core exhibit a propeller-shaped geometry with small bending and twisting of the arms. The same geometry was also found in TAA-Ph where the lengths of arms are extended.

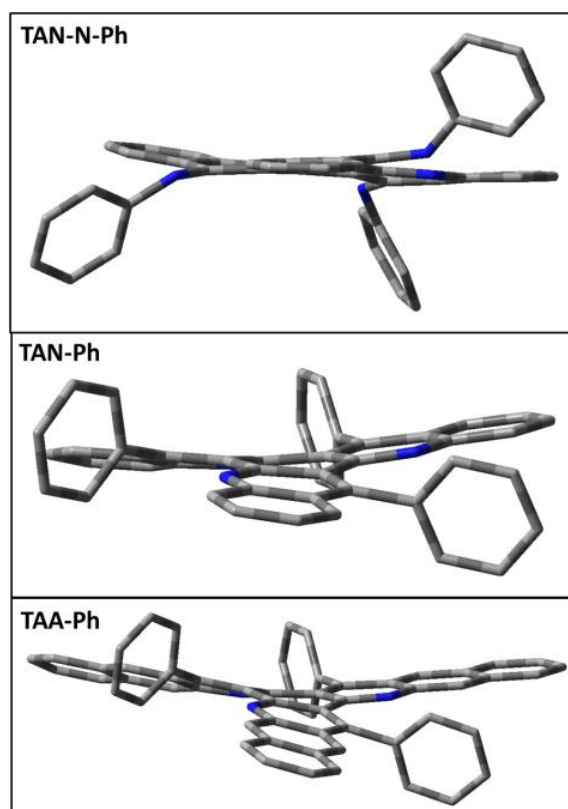


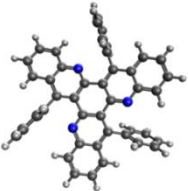
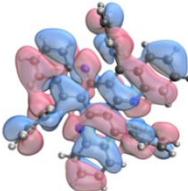
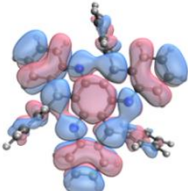
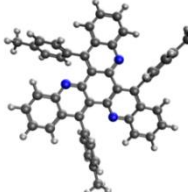
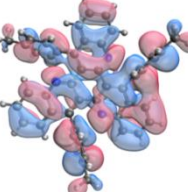
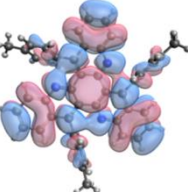
Figure 3-3. Molecular geometries of TAN-N-Ph, TAN-Ph and TAA-Ph, optimized by Gaussian at B3LYP/6-311G(d,p) level

Distributions of electron density in molecular orbitals (MOs) of various compounds are derived and summarized in Tables 3-2 and 3-3.

For TAN derivatives, electron density distributions in HOMO do not respect the  $C_{3h}$  symmetry, while LUMO orbitals are symmetrically localized on the molecules. As expected from UV-visible spectroscopy, LUMO orbitals of TAN-Ph and TAN-MePh are mainly distributed on the conjugated central core. However, HOMOs of these two molecules are widely expanded to the branches although the dihedral angles between branches and arms are almost  $90^\circ$ .



Table 3-2. HOMO and LUMO orbitals of TAN-Ph and TAA-MePh with isovalue 0.02.

compound	structure	HOMO	LUMO
TAN-Ph			
TAN-MePh			

In order to study the relation between the introduction of branches and the electron density distributions, HOMO and LUMO orbitals of unsubstituted trinaphthylene (TNA), TAN and TAA have been calculated. As shown in Figure 3-4, only the HOMO orbital of TAN is not distributed following the point group symmetry of its molecular structure. The same phenomenon has been found in the series of molecules herein studied. In addition, introduction of nitrogen atoms has a double impact. Firstly, all energy levels decrease and, secondly, HOMO-LUMO gap increases.

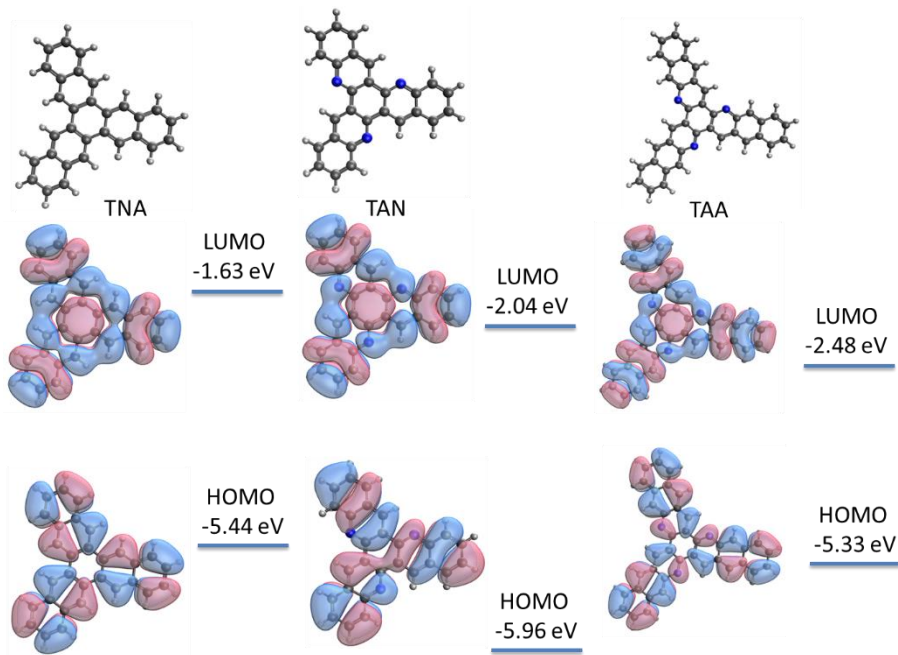
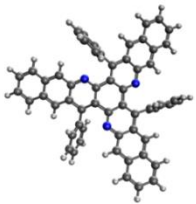
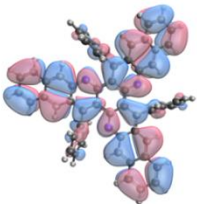
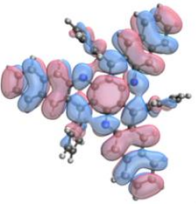
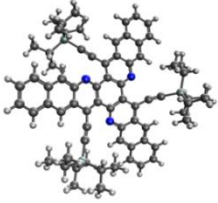
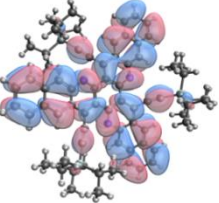
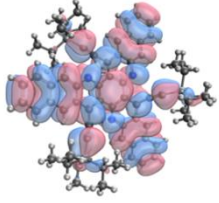

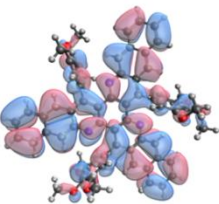
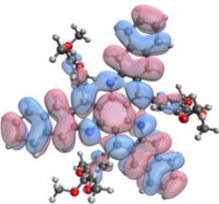
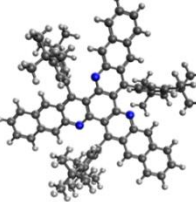
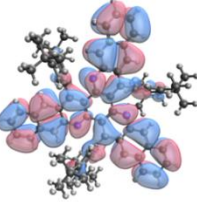
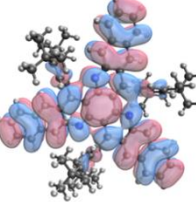
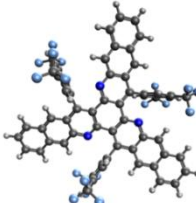
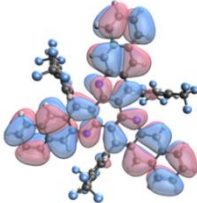
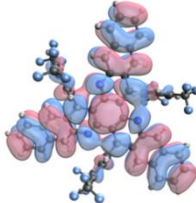


Figure 3-4. HOMO and LUMO orbitals of non-substituted TNA, TAN and TAA with isovalue 0.02.

For TAA derivatives, HOMO and LUMO orbitals are symmetrically localized on the molecules and are mainly distributed on the conjugated central core as expected. It is worth noting that in TAA-Tips electronic density distributions over triple bonds have an equivalent size to those of arms which could explain the extension of conjugation expected in the optical absorption part.

Table 3-3. HOMO and LUMO orbitals of TAA derivatives with isovalue 0.02.

compound	structure	HOMO	LUMO
TAA-Ph			
TAA-Tips			
TAA-OMePh			
TAA-tBuPh			
TAA-CF <sub>3</sub> Ph			

### 3.4.2 Energy Diagrams

About energy diagrams, HOMO and LUMO energy levels calculated at the B3LYP/6-31G(d) level in THF of all the compounds are summarized in Table 3-4.

Table 3-4. Experimental and calculated maximum UV absorption, HOMO and LUMO energy levels of TAN and TAA derivatives.

Compounds	$\lambda_{\text{abs}}$ (nm) <sup>a</sup>	LUMO (eV) <sup>b</sup>	HOMO (eV) <sup>c</sup>	LUMO <sub>calc</sub> (eV) <sup>d</sup>	HOMO <sub>calc</sub> (eV) <sup>d</sup>	$\lambda_{\text{calc}}$ (nm) <sup>e</sup>
TAN-Ph	232, 298	-2.73	-5.83	-2.12	-5.99	284
TAN-MePh	233, 297	-2.71	-5.76	-2.10	-5.88	284
TAA-Ph	278, 351	-3.09	-5.65	-2.56	-5.39	330
TAA-Tips	286, 371	-3.40	-5.78	-2.86	-5.44	357
TAA-OMePh	278, 354	-3.05	-5.58	-2.56	-5.39	330
TAA-tBuPh	279, 352	-2.99	-5.54	-2.50	-5.36	331
TAA-CF <sub>3</sub> Ph	280, 353	-3.32	-5.88	-2.76	-5.55	334

a: Two main absorption features for each compound. b: LUMO energy level calculated from  $E_{1/2}^{\text{red}}$  using equation 1. c: HOMO energy level estimated from LUMO energy and optical bandgap values. d: HOMO and LUMO energy level calculated at the B3LYP/6-31G(d) level in THF. e: Maximum absorption wavelength calculated at the CAM-B3LYP/6-311G(d) level in DCM.

A very good correlation is found between the LUMO energy levels derived from CV measurements and values calculated at the B3LYP/6-31G(d) (with a correlation coefficient  $R^2 = 0.977$ , see Figure 3-4 left), although the latter are systematically larger by  $\sim 0.6$  eV. Meanwhile, a very good correlation is also found between calculated and experimental optical (deduced from UV-visible spectroscopy) band-gaps ( $R^2 = 0.993$ , see Figure 3-5 right), confirming the reliability of the experimental procedure employed for extracting the MO energy levels.

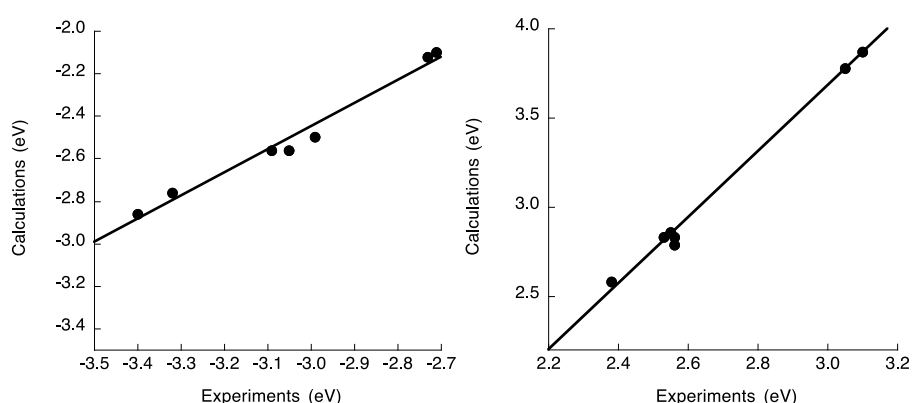
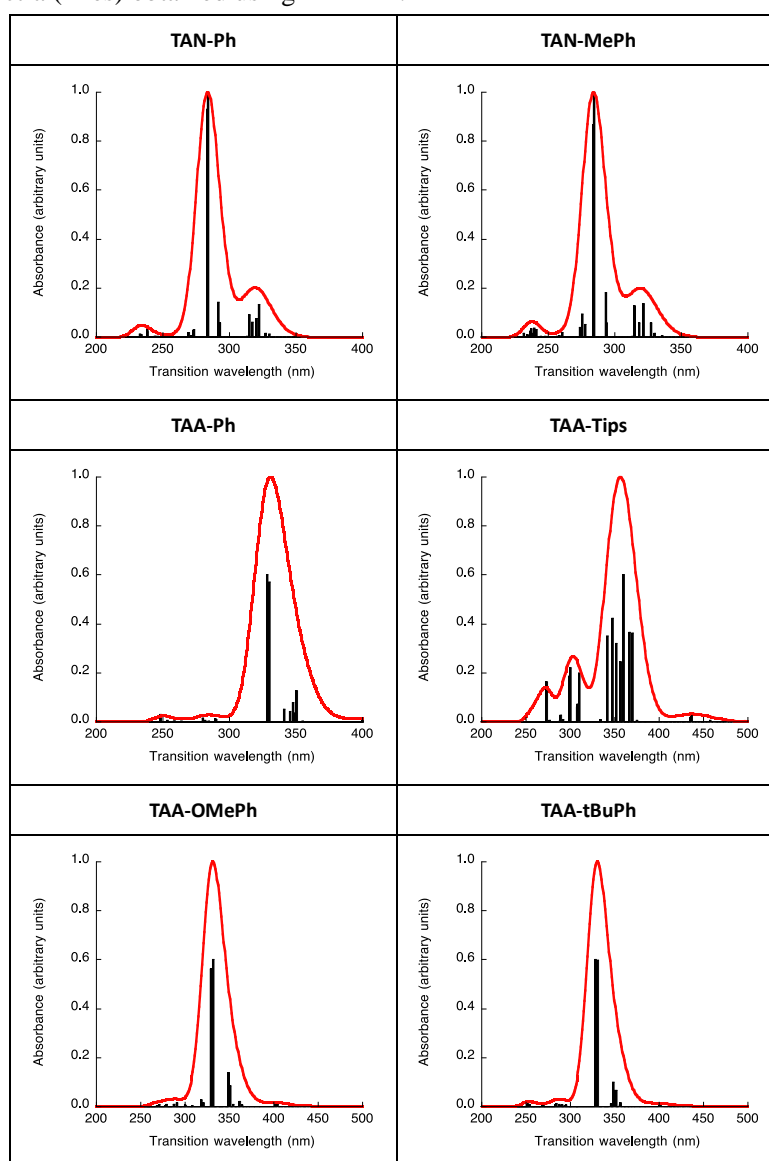


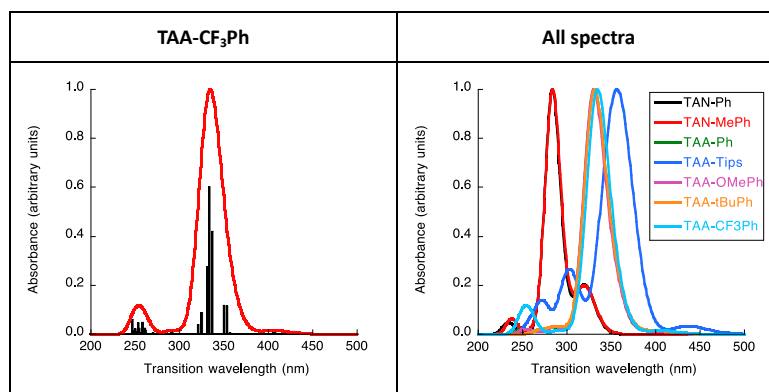
Figure 3-5. Correlation between experimental and IEFPCM:B3LYP/6-31G(d) calculations in THF for (left) LUMO energies and (right) HOMO-LUMO gaps.

### 3.4.3 Electronic Absorption Transitions

Transition energies towards the first optically allowed excited states were computed by means of time-dependent DFT at the B3LYP/6-311G(d) level. Solvent effects were taken into account in these calculations by using the Integral Equation Formalism of the Polarizable Continuum Model (IEF-PCM).<sup>[309]</sup> Each transition has been enlarged by using a Gaussian function with a full width at half maximum (FWHM) equal to 0.3 eV to obtain normalized spectra (Table 3-5). All calculations were performed with the ORCA<sup>[310]</sup> and Gaussian<sup>[227]</sup> programs.

Table 3-5. Oscillator strengths (black bars) associated to electron excitations and normalized absorption spectra (lines) obtained using TD-DFT.





As indicated by TD-DFT calculations, the maximum absorption band mainly originates from  $\pi$ - $\pi^*$  electron transitions towards two degenerate excited states (owing to the near  $C_{3h}$  symmetry). The low-intensity absorption bands at larger wavelengths result from a set of electron excitations associated to oscillator strengths one order of magnitude smaller. These bands also involve transitions within  $\pi$  molecular orbitals (MOs) localized on the star-shaped  $\pi$ -conjugated core. DFT calculations also revealed that these low energy bands include additional contributions due to electron transitions from the peripheral phenyls to the fused arms, which are made possible owing to deviations from ideal  $C_{3h}$  symmetry. Experimentally, such contributions could arise from dynamical geometry fluctuations.

### 3.5 Single Crystal XRD Result

In order to investigate molecular packing in single crystal, X-ray measurements were carried out on single crystals of these molecules. Single crystals were obtained for all compounds by solution diffusion method. However, even though crystals of TAA- $CF_3Ph$  were obtained, XRD record did not lead to resolvable data.

Firstly, single crystal X-ray measurements confirm the chemical structures of the synthesized compounds and reveal large dihedral angles between arms and aromatic branches (around  $70^\circ$ ) as expected due to steric hindrance. Secondly, the crystalline structures showed that the fused aromatic rings (the arms of the molecule) are propeller-shaped with bending or twisting (Table 3-6). Twisting angles (defined as the dihedral angles between the mean plane of the fused star-shaped core and the mean plane of each arm) range from  $3^\circ$  to  $27^\circ$ , while bending angles (defined as the angles between the mean plane of the central ring and the line connecting the centroids of third and central phenyl ring) range from  $0.8^\circ$  to  $10.3^\circ$ . TAA-OMePh is used to explain dihedral angle, twisting angle and bending angle in Figure 3-6.

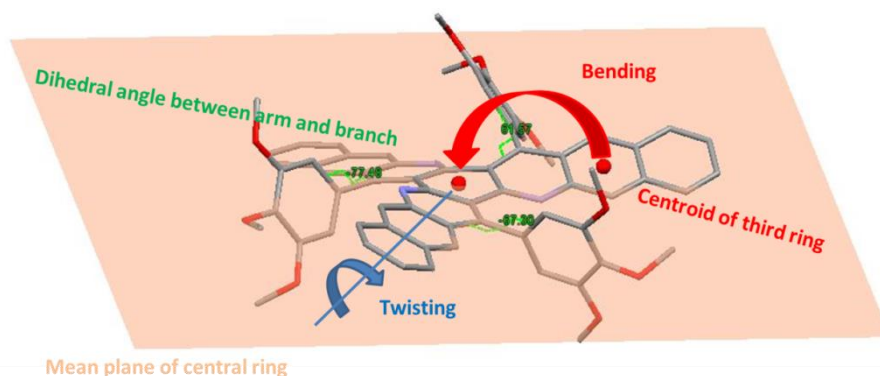


Figure 3-6. Schematic diagram of dihedral angle, twisting angle and bending angle.

Table 3-6. Molecular structural parameters deduced from single crystal XRD measurements.

	Twisting angles ( $^{\circ}$ ) <sup>a</sup>	Distance ( $\text{\AA}$ ) <sup>b</sup>	Bending angles ( $^{\circ}$ ) <sup>c</sup>	Bending radius ( $\text{\AA}$ ) <sup>d</sup>
<b>TAN-Ph</b>	19, 11, 4	0.73, 0.3, 0.28	-8.7, 3.5, 3.3	16, 40, 42
<b>TAN-MePh</b>	24, 8, 8	0.73, 0.65, 0.02	-8.7, 7.7, 0.2	16, 18, 821
<b>TAA-Ph</b>	13, 13, 13 11, 11, 11	0.12, 0.12, 0.12 0.27, 0.27, 0.27	1.4, 1.4, 1.4 3.2, 3.2, 3.2	101, 101, 101 43, 43, 43
<b>TAA-Tips</b>	13, 13, 10	0.48, 0.39, 0.17	-5.7, 4.6, 2.0	24, 30, 70
<b>TAA-OMePh</b>	27, 25, 3	0.87, 0.32, 0.32	-10.3, 3.8, 3.8	14, 36, 36
<b>TAA-tBuPh</b>	5, 3, 3	0.2, 0.17, 0.07	2.4, 2.0, 0.8	57, 70, 180
<b>TAA-CF<sub>3</sub>Ph</b>	/	/	/	/

a: Twisting angles between the mean plane of the fused star-shaped core and the mean plane of each arm; b: distances from the centroid of the third phenyl ring and the mean plane of central ring; c: Bending angles between the mean plane of the central ring and the line connecting the centroids of third and central phenyl ring. d: Bending radius ( $\text{\AA}$ ) calculated as the radius of circle connecting the centroid of the first and third ring and tangent to the mean plane of the first ring.

Figure 3-7 illustrates the two extreme cases: the most distorted derivative (TAA-OMePh, with twisting angles up to  $27^{\circ}$  and bending angles up to  $10.3^{\circ}$ ) and the most regular one (TAA-Ph, with twisting and bending angles of  $13^{\circ}$  and  $3.2^{\circ}$ , respectively). It is worth noticing that except for TAA-Ph, the bending or twisting angles are different for each arm of a given molecule, which means that only TAA-Ph keeps a  $C_3$  symmetry structure in the solid state, whereas solution NMR data evidenced that all molecules display  $C_3$  symmetry in solution. Moreover, the compound bearing the largest peripheral substituents (TAA-tBuPh) unexpectedly exhibits the flattest molecular structure. In fact, no correlation could be established between the nature of the branches and the distortion of molecular arms in the solid

state, suggesting that small differences of planarity within a molecule is mainly driven by intermolecular interactions induced by the different packing modes. X-Ray patterns also revealed that molecules display a single geometry in all crystals, except TAA-Ph that exists in two non-equivalent forms (or two different conformations).

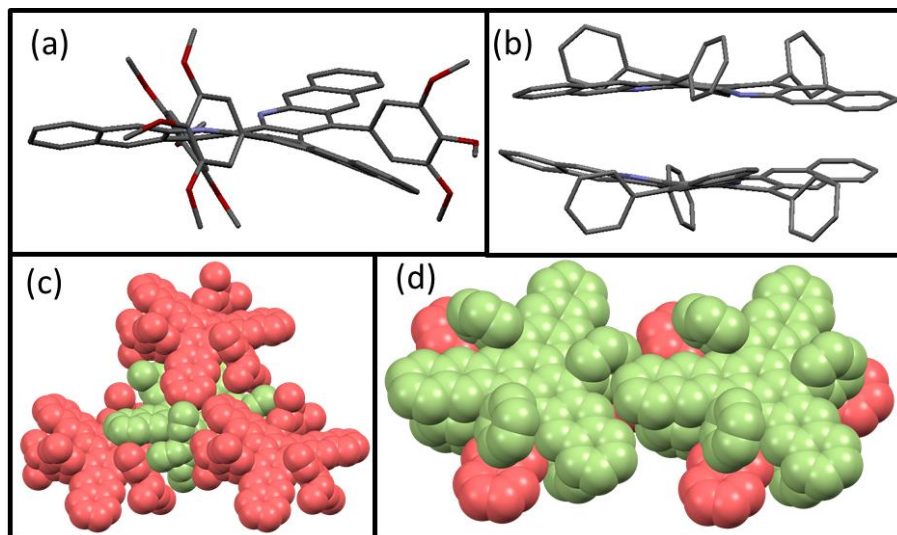


Figure 3-7. Molecular structures of TAA-OMePh (a) and TAA-Ph (b) extracted from single crystals, and space-filling representations of the molecular packing of the same crystals (c and d).

For clarity, hydrogen atoms have been omitted.

Molecular packings of TAN-Ph, TAN-MePh, TAA-Tips and TAA-tBuPh in single crystal are displayed in Figure 3-8. TAN-Ph and TAN-MePh exhibit typical 1D slipped stacking due to relatively planar molecular structures and strong  $\pi$ - $\pi$  stacking interactions. Each molecule shows efficient face-to-face  $\pi$ - $\pi$  stacking with two neighboring molecules. Moreover, packing with these two molecules are different with  $d_{C-C}$  (shortest C-C distance between two neighboring molecules) of 3.47 and 3.35 Å for TAN-Ph, 3.21 and 3.48 Å for TAN-MePh. Dimers of molecule with larger branches have relatively smaller intermolecular  $d_{C-C}$  distance. TAA-Tips molecules exhibit cofacial herringbone packing with  $d_{C-C}$  of 3.40 and 3.45 Å. Although the distances are similar, the  $\pi$ - $\pi$  stacking extents are quite different for the two neighboring molecules. As shown in Figure 3-8, one side has large packing area while the other side has only overlap about one benzene ring. In the case of TAA-tBuPh, the large steric hindrance caused by the bulky branches prevent  $\pi$ - $\pi$  stacking of the molecular units, which adopt a packing motif similar to hexa(p-tolyl)truxene.<sup>[311]</sup>

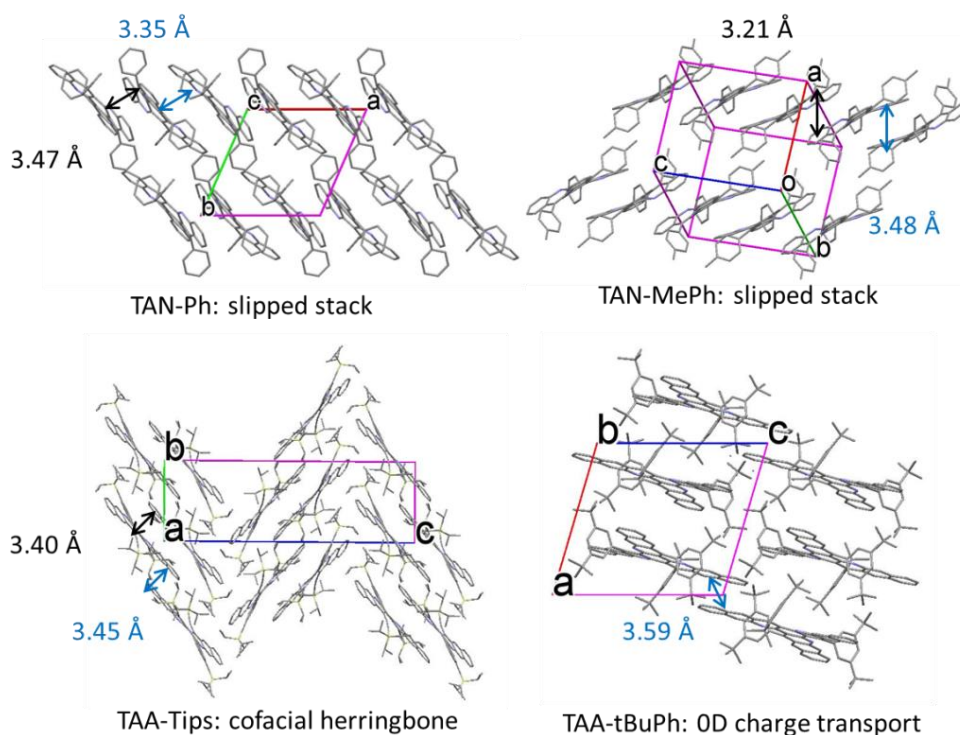


Figure 3-8. Molecular packing in the TAN-Ph, TAN-MePh, TAA-Tips and TAA-tBuPh single crystals. For sake of clarity, hydrogen atoms have been omitted.

From the packing motifs of TAN-Ph, TAN-MePh, TAA-Tips and TAA-tBuPh, we assume these four molecules could only lead to 1D or 0D charge transport. But packing motifs of TAA-OMePh and TAA-Ph are more interesting and could lead to higher dimensionality for charge transport. Molecule packing of TAA-OMePh is displayed in Figure 3-9 with top view, side view and partial zoom in. Two inverted orientations of the molecules are found in the crystal. They are colored in red and green respectively. It is worth noting that from the top view, TAA-OMePh molecules arrange in a hexagon pattern. As illustrated in Chapter 1.7, TAA-OMePh presents an “arm packing” organization in which every single molecule  $\pi$ -stacks with three neighbors through overlap of the arms. An important difference with respect to the speculated packing mode shown in Scheme 1-19 lies in the fact that only three dimers with large overlap exist around one molecule instead of six, thus reducing the crystal isotropy and prefiguring 2D rather 3D charge transport.



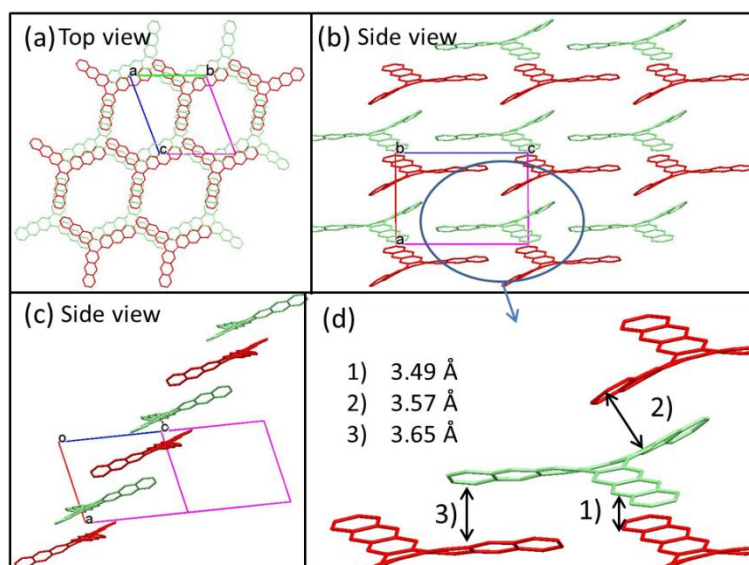


Figure 3-9. Molecular packing of TAA-OMePh. For sake of clarity, hydrogen atoms and lateral branches have been omitted.

TAA-Ph presents a very different crystallographic structure (Figure 3-10), in which molecules develop face-to-face interactions within a “column packing” arrangement. As speculated, six face-to-face  $\pi$ -interactions are observed with identically oriented neighboring molecules even if the overlap is weak. Moreover, an extra interaction on each arm is found at small distance (3.51 Å). Beyond particular face-to-face  $\pi$ -stacking, numerous edge-to-face interactions between arms and branches are observed. At this point, charge transport should be better spread around all directions for TAA-Ph.

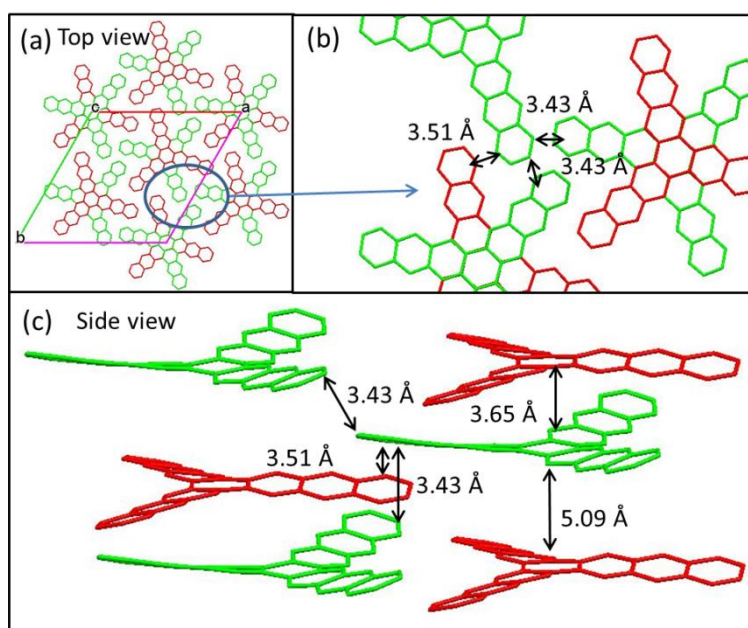


Figure 3-10. Molecule packing of TAA-Ph. For sake of clarity, hydrogen atoms and lateral branches have been omitted.

### 3.6 Simulated charge transport properties

In section 3.5, we assumed the charge transport dimensionality of the materials just from their molecule arrangements. Moreover, we mostly focused on the face-to-face  $\pi$ -stacking and obliterate other  $\pi$ - $\pi$  interactions. In order to get a deeper insight into the amplitude and dimensionality of charge transport within the six crystal structures described above, electronic parameters characterizing the migration of charge carriers in the hopping regime were evaluated at the B3LYP/6-31G(d) level. The corresponding calculations were carried out by Prof. Frédéric CASTET (ISM, University of Bordeaux). Hereby, ionization energies (IEs), electron affinities (EAs) as well as internal reorganization energies ( $\lambda_i$ ), which measure the changes in geometry of the molecules involved in hole and electron transfer processes, are reported in Table 3-7.

Table 3-7. Ionization energies (IE), Electron affinities (AE) and internal reorganization energies ( $\lambda_i$ ), for hole (h) and electron (e) transport.

Compounds	IE (eV) <sup>a</sup>	EA (eV) <sup>a</sup>	$\lambda_h$ (eV) <sup>b</sup>	$\lambda_e$ (eV) <sup>b</sup>
TAN-Ph	6.753	0.916	0.231	0.095
TAN-MePh	6.613	0.877	0.216	0.099
TAA-Ph	6.126	1.470	0.083	0.071
TAA-Tips	6.122	1.868	0.079	0.108
TAA-OMePh	6.049	1.535	0.168	0.094
TAA-tBuPh	6.030	1.464	0.075	0.079
Pentacene			0.097	

a: calculated from differences in the total energies of the charged and neutral molecules in their optimized geometries. b: calculated using the four point adiabatic potential approach.

Internal reorganization energies for holes ( $\lambda_h$ ) and electrons ( $\lambda_e$ ) were calculated using the expression derived from the four point adiabatic potential approach:<sup>[312–315]</sup>

$$\lambda_h = E^{(+)}(M) - E^{(0)}(M) + E^{(+)}(M^+) - E^{(0)}(M^+) \quad (2)$$

$$\lambda_e = E^{(-)}(M) - E^{(0)}(M) + E^{(-)}(M^-) - E^{(0)}(M^-) \quad (3)$$

where  $E^{(0)}(M)$ ,  $E^{(+)}(M^+)$  and  $E^{(-)}(M^-)$  denote the ground-state energy of the neutral, positively and negatively charged states, respectively;  $E^{(+)}(M)$  [ $E^{(-)}(M)$ ] is the energy of the neutral molecule in the optimized geometry of the

cation [anion], and  $E^{(0)}(M^+)$  [ $E^{(0)}(M^-)$ ] is the energy of the cation [anion] in the optimized geometry of the neutral molecule. Ionization energies (IE) and electron affinities (EA) are defined as:

$$IE = E^{(+)}(M^+) - E^{(0)}(M) \quad (4)$$

$$EA = E^{(0)}(M) - E^{(-)}(M^-) \quad (5)$$

The IEs (EAs) calculated in the gas phase lie in the range of 6.0-6.8 eV (0.9-1.9 eV). As expected, TAN derivatives display larger IEs and smaller EAs than TAA derivatives, owing to the smaller spatial extension of the aromatic core. Lateral substitution has a relatively weak impact on IE and EA values, which show variations smaller than 0.1 eV with respect to the nature of the peripheral functional groups. A noticeable exception is observed for TAA-Tips, which exhibits a much larger EA than the other compounds, consistently with its LUMO energy we calculated and reduction potential we measured. Apart from this compound (and to a lesser extent TAA-tBuPh), internal reorganization energies for electron transport are smaller than the ones calculated for holes. Since  $\lambda$  must be minimized to achieve high transfer rates according to Marcus theory, this suggests that this series of materials should favor electron transport over hole transport. Moreover,  $\lambda_e$  (from 71 meV to 108 meV) have similar values to  $\lambda_h$  obtained with the well-known pentacene.

Transfer integrals  $J_{ij}$  characterizing hole (electron) coupling between molecular pairs  $ij$  within the crystals were obtained by employing the projection method involving the HOMOs (LUMOs) of monomers  $i$  and  $j$ .<sup>[316]</sup> Since the TAN-Ph compound possesses nearly degenerate HOMO (H) and HOMO-1 (H-1) levels ( $E_{H-1} = -5.657$  eV and  $E_H = -5.637$  eV, as calculated at the B3LYP/6-31G(d) level using the crystal geometry), effective transfer integrals for hole transport in this compound were also computed as:

$$J_h = \frac{1}{\sqrt{2}} \{J_{H-1,H-1}^2 + J_{H-1,H}^2 + J_{H,H-1}^2 + J_{H,H}^2\}^{1/2} \quad (6)$$

in line with previous works.<sup>[317-319]</sup>

Transfer integrals  $J_{ij}$ , are collected in Table 3-8. As discussed above, the nature of peripheral substituents has a strong impact on the molecular arrangement within the crystals, which translates into large variations in hole and electron transfer integrals. Moreover, the maximum calculated transfer integrals are larger for electrons than for holes in all compounds. Consequently, both integral transfer and internal reorganization energies favored negative charge transport.

Table 3-8. Transfer integrals (with absolute values larger than 2 meV) between a reference molecule (i) and its first neighbors (j), calculated for holes (h) and electrons (e) at the B3LYP/6-31G(d) level.

Compound	$\vec{v}_{ij}^a$	$d_{i,j} (\text{\AA})^b$	$J_h$ (meV) <sup>c</sup>	$J_e$ (meV) <sup>c</sup>	Dimer relation <sup>d</sup>
<b>TAN-Ph</b> <b>P<math>\bar{1}</math></b>	(0.52, 0.02, 0.13)	5.853	12 (68)	67	$\bar{1}$
	(-0.48, 0.02, 0.13)	6.075	15 (24)	5	$\bar{1}$
	(-0.52, -1.02; -0.12)	10.888	0	2	$\bar{1}$
	$\pm(0, 0, 1)$	13.640	7 (10)	5	1
	(-0.52, -1.02, -1.13)	13.721	1 (4)	2	$\bar{1}$
	$\pm(1, 1, 0)$	13.777	1 (9)	2	1
	$\pm(1, 1, 1)$	13.748	7 (6)	2	1
<b>TAN-MePh</b> <b>P<math>\bar{1}</math></b>	(0.02, 0.03, 0.46)	6.162	15	3	$\bar{1}$
	(0.02, 0.03, -0.53)	7.272	15	47	$\bar{1}$
	(0.02, -0.96, -0.53)	12.952	8	3	$\bar{1}$
	(0.02, 1.03, 0.46)	13.181	7	14	$\bar{1}$
	(1.02, 0.03, -0.53)	13.812	13	1	$\bar{1}$
	$\pm(1, 1, 0)$	13.907	0	6	1
	(1.02, 1.03, 0.46)	14.540	6	1	$\bar{1}$
<b>TAA-Ph</b> <b>R3</b>	(0, 0, -0.45)	4.194	39	72	A-B
	(0, 0, 0.55)	5.177	8	8	A-B
	(-2/3, -1/3, 0.22)	15.660	0	12	A-B
	(1/3, 2/3, 0.22)	15.660	0	12	A-B
	(1/3, -1/3, 0.22)	15.660	0	12	A-B
	$\pm(-1/3, 1/3, 1/3)$	15.836	10	6	1
	$\pm(-1/3, -2/3, 1/3)$	15.836	10	6	1
	$\pm(2/3, 1/3, 1/3)$	15.836	10	6	1
<b>TAA-OMePh</b> <b>P<math>\bar{1}</math></b>	(-0.43, 0.61, -1/3)	9.522	23	85	$\bar{1}$
	(0.57, -0.39, -1/3)	10.464	39	85	$\bar{1}$
	(-0.43, -0.39, -1/3)	11.771	2	1	$\bar{1}$
	(-0.43, -0.39, 2/3)	11.933	7	41	$\bar{1}$
	(0.57, 0.61, -1/3)	12.150	1	1	1
	$\pm(0, 1, 0)$	15.712	5	3	1
	$\pm(0, 0, 1)$	16.961	4	7	1
	$\pm(0, -1, 1)$	18.432	3	0	

Compound	$\vec{v}_{ij}$ <sup>a</sup>	$d_{i,j}$ (Å) <sup>b</sup>	$J_h$ (meV) <sup>c</sup>	$J_e$ (meV) <sup>c</sup>	Dimer relation <sup>d</sup>
<b>TAA-Tips</b>	(0.09, 0.22, -0.22)	7.881	7	90	$\bar{1}$
<b>P2<sub>1</sub>/n</b>	(-0.41, $\pm 1/2$ , 0.28)	13.131	0	2	2 <sub>1</sub>
	(0.09, 1.22, -0.22)	14.792	2	9	1
	(0.59, $\pm 1/2$ , 0.28)	15.036	3	2	2 <sub>/1</sub>
<b>TAA-tBuPh</b>					
<b>P<math>\bar{1}</math></b>	(-0.46, -0.96, -0.94)	15.902	3	3	$\bar{1}$
<b>Pentacene</b> <sup>e[320]</sup>	$\pm(0.5, 0.5, 0)$	4.73	85		A $\bar{}$ -B
<b>P<math>\bar{1}</math></b>	$\pm(-0.5, 0.5, 0)$	5.20	51		A $\bar{}$ -B
	$\pm(1, 0, 0)$	6.27	37 and 34		1

<sup>a</sup> The crystallographic directions corresponding to intermolecular vectors joining one central molecule with its neighbours are given in the basis of direct lattice vectors. <sup>b</sup>  $d_{i,j}$  is the distance (in Å) between the centers of mass of molecules  $i$  and  $j$ . <sup>c</sup> values in parentheses are calculated using equation SI5 accounting for the close degeneracy of the two highest occupied MOs. <sup>d</sup> relationship linking molecules  $i$  and  $j$ . When  $i$  and  $j$  have the same configuration, symmetry operations are given, otherwise dimers are described as A $\bar{}$ -B. B $\bar{}$ -B dimers do not have close contacts, so that all integral transfers are negligible. <sup>e</sup> data from reference.

To give a better view about integral transfer and its related dimer, molecular packings of TAN derivatives are displayed in Table 3-9 where values of the main electron and hole transfer integrals between the reference molecule (in red) and its first neighbors are shown. Lattice vectors  $a$ ,  $b$  and  $c$  are represented in red, green and blue, respectively. In each structure, lateral substituents and hydrogen atoms have been omitted for sake of clarity. TAN-Ph and TAN-MePh exhibit significant electron transfer integrals along the  $\pi$ -staging direction while they are one order of magnitude lower along the other directions which suggests 1D electron transport. However, both crystals display an alternation of non-equivalent dimers along the  $\pi$ -staging direction ((1,0,0) direction for TAN-Ph and (0,0,1) for TAN-MePh) that are associated to very different  $J_e$  values (67 vs. 5 meV in TAN-Ph, 47 vs. 3 meV in TAN-MePh), which should hamper the electron mobility. Interestingly, the largest transfer integrals for holes are 3-5 times lower ( $\sim 15$  meV) than for electrons but do not show the same detrimental alternation between large and small  $J$  values. Consequently, the orbital  $\pi$ -interactions should favor hole transport over electron transport in these materials. Moreover, in (0,0,1) and (1,1,1) directions, the hole integral transfers are half of that observed in (1,0,0) direction for TAN-Ph, while intermolecular distances are doubled. Thus, the mobility of charge carriers could be equivalent in all these directions although it should be very weak. The same observation can be done for TAN-MePh

where dimers have the same ratio between integral transfer and distance. On another hand, the mobility of holes in TAN-Ph should be enhanced, as large increasing of  $J_h$  values is obtained when accounting for the contributions of the two degenerated MOs (Table 3-7). In the case of TAN-MePh, a counterintuitive observation can be done. Despite of 1D-sliped-stack due to face-to face  $\pi$ -staging in (0,0,1) direction, the fastest pathway should follow (0,1,1) direction for negative charges as the two highest intermolecular distances and transfer integrals are obtained for dimer linked by (0.02, 0.03,-0.53) and (0.02, 1.03, 0.46) vectors and inversion symmetry. The pathway direction has been calculated as one vector  $\vec{v}$  colinear of the direction line from two intermolecular vectors  $\vec{v}_1$  and  $\vec{v}_2$  concerning dimers of inverted molecules (Eq. 7).

$$\vec{v} = \vec{v}_1 - \vec{v}_2 \quad (7)$$

Compared with  $J_h$  and  $d_{i-j}$  of pentacene, negative charge transport for both TAN derivatives should be widely hampered whatever the direction as the pathway pass through one dimer with small distance or integral transfer.

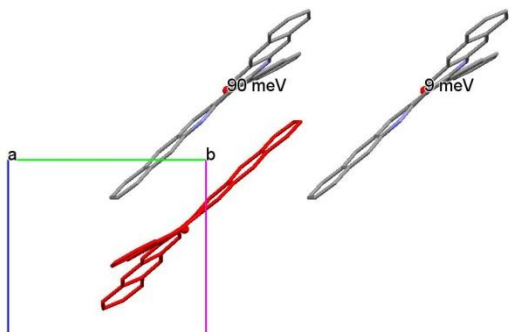
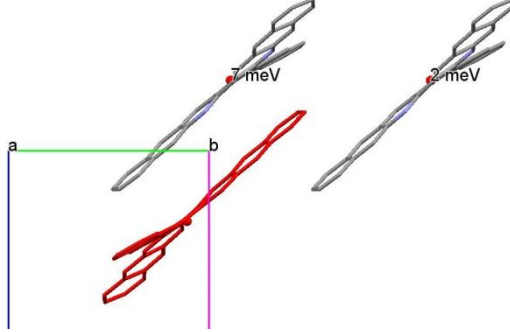
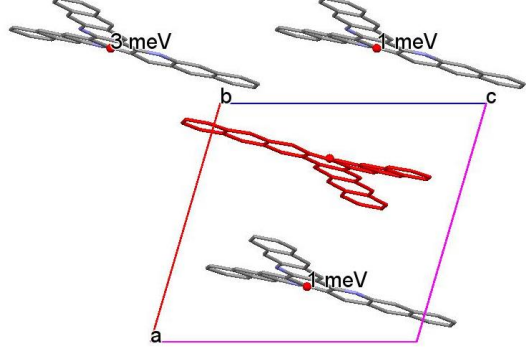
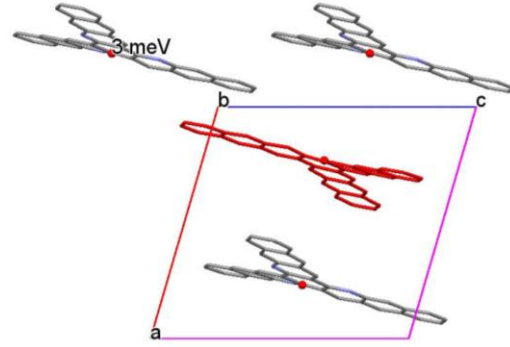
Table 3-9. Molecular packings and main electron and hole transfer integrals of TAN derivatives.

TAN-Ph (Electrons)	TAN-Ph (Holes)
TAN- MePh (Electrons)	TAN- MePh (Holes)

Molecular packings and main electron and hole transfer integrals of TAA-Tips

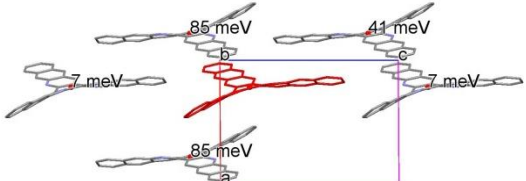
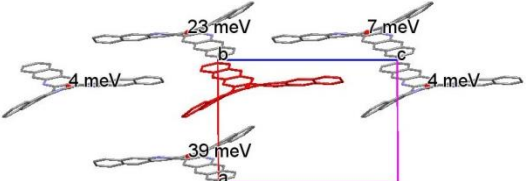
and TAA-tBuPh are displayed in Table 3-10. TAA-Tips molecules adopt herringbone packing, with negligible electronic couplings between molecules belonging to different layers. Within a layer, the extended spatial overlap between the conjugated arms of the first molecular neighbor gives rise to a large coupling term (90 meV). However, a second weak coupling has to be associated to create a charge transport pathway. In this case, we suppose a 1D slow charge transport will occur. In the case of TAA-tBuPh, all electronic couplings are negligible due to the lack of  $\pi$ -interactions between molecular units suggesting no pathway for charge carrier transport in TAA-tBuPh single crystal.

Table 3-10. Molecular packings and main electron and hole transfer integrals of TAA-Tips and TAA-tBuPh.

TAA-Tips (Electrons)	TAA-Tips (Holes)
	
TAA-tBuPh (Electrons)	TAA-tBuPh (Holes)
	

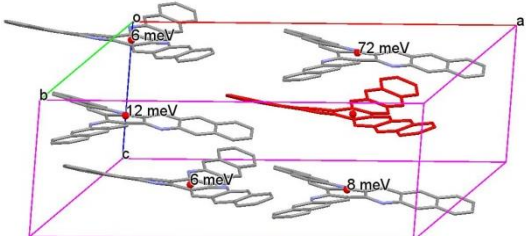
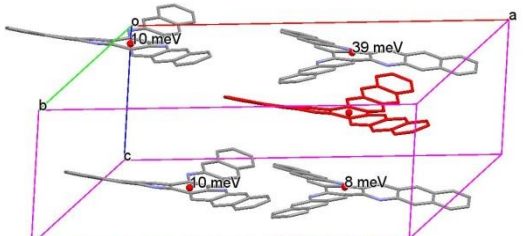
Molecular packing and main electron and hole transfer integrals of TAA-OMePh are displayed in Table 3-11. As we predicted from the XRD result, the three neighbouring molecules directly involved in “arm packing” with the reference molecule (in red), are associated to large electron transfer integrals, clearly suggesting a 2D electron transport in this material following the plane  $\vec{n}$  (1;1;1). This plane has been identified in figure 3-9(c).

Table 3-11. Molecular packing and main electron and hole transfer integrals of TAA-OMePh.

TAA-OMePh (Electrons)	TAA-OMePh (Holes)
	

Molecular packing and main electron and hole transfer integrals of TAA-Ph are displayed in Table 3-12. TAA-Ph displays the maximum couplings (72 meV) along the  $\pi$ -stacking direction (0,0,1) with consecutive dimers stacked in staggered conformation and consisted of 2 different conformations. However, the other dimer in column leads to small integral transfer (8 meV). In addition, secondary coupling terms (12 meV for three dimers) between the two conformations are also obtained with large intermolecular distances around 16 Å, which indicates that charge transport pathways also exist perpendicular to the column axis and could lead to 3D electron transport. In details, the three  $\vec{v}_{ij}$ , associated with those dimers can be regarded as an addition of two components : one colinear to the column stack (0,0,1) and another perpendicular to it. Consequently, charge transport pathways also exist in the plane perpendicular to the column axis and could lead to 3D electron charge transport. Moreover, the colinear component points out the opposite direction to the  $\vec{v}_{ij}$  (0,0,-0.45) associated to the highest integral transfer. Thus, these three dimers will positively contribute to the charge transport following the c axis.

Table 3-12. Molecular packing and main electron and hole transfer integrals of TAA-Ph.

TAA-Ph (Electrons)	TAA-Ph (Holes)
	

To conclude, the highest overlaps lead to the highest integral transfers. However, a large overlap does not guarantee a good coupling. Moreover, it will decrease the intermolecular distance. As discussed with crystallographic data, small change in chemical structure induced huge modification of intensity and anisotropy of charge transport. Furthermore, counterintuitive pathways have been revealed by calculation. Finally, the level of calculation does not allow us to conclude about the theoretical



degree of anisotropy even if 2D and 3D charge transport are possible with reasonable successful values for internal reorganization energy, transfer integral and distance. In perspective, simple analytical solution such as that used by William A. Goddard III<sup>[321]</sup> cannot be employed due to the mix between dimers with and without inversion of molecular orientation. That is the reason why the versatile Kinetic Monte Carlo method (KMC) will be tested next months.

### 3.7 Thermal Properties

Thermal stability of organic materials constitutes a key requirement for potential applications in organic electronics. In this context, thermal behaviors of newly synthesized star-shaped molecules were studied by thermogravimetric analysis coupled to mass spectrometry (TGA-MS) and differential scanning calorimetry (DSC) under argon atmosphere (Figures 3-11 and 3-12).

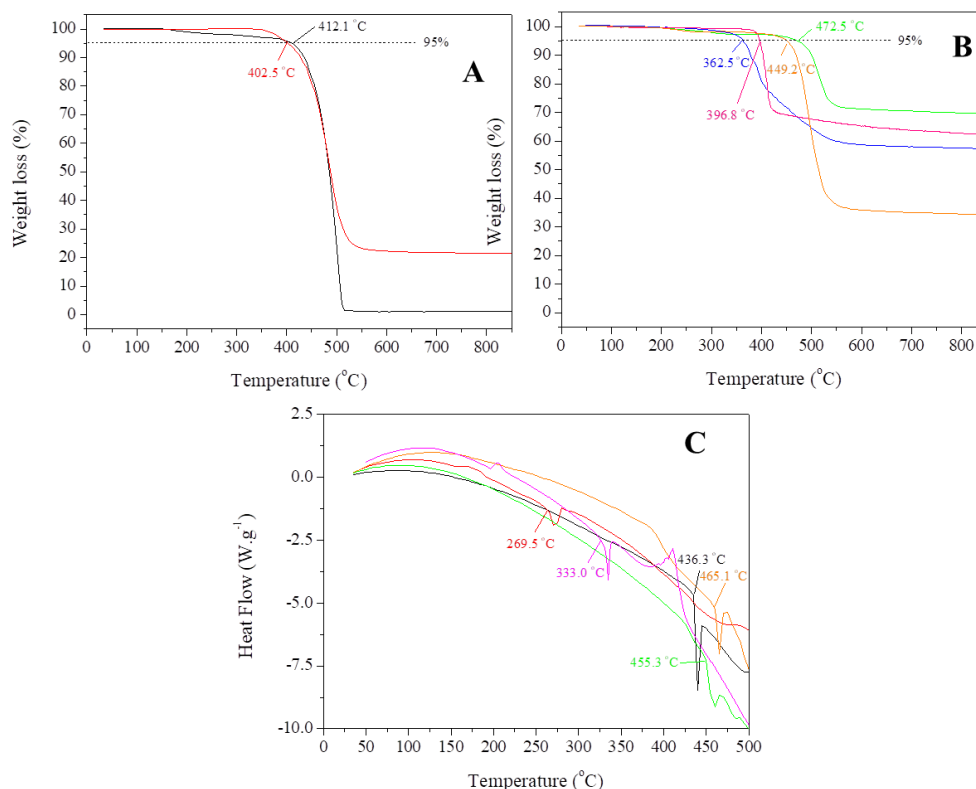


Figure 3-11. TGA (A,B) and DSC (C) curves for TAN-Ph (black), TAN-MePh (red), TAA-Ph (green), TAA-Tips (blue), TAA-OMePh (pink) and TAA-tBuPh (Orange).

TAN-Ph and TAN-MePh showed high thermal stability with decomposition temperature ( $T_d$ ) of 412.1 and 402.5 °C, respectively, the decomposition process occurring in a steep single stage. Moreover, TAA-Ph and TAA-tBuPh appeared to be even more thermally stable with decomposition temperature of 449.2 and 472.5 °C,

respectively, and, once again, through a steep single decomposition stage. This suggests that the introduction of azaanthrylene arms has a beneficial effect on the thermal stability. Nonetheless, the nature of the branches also strongly affects the thermal stability. Thus, TAA-OMePh and TAA-Tips were less stable with decomposition temperature of 396.8 °C and 362.5 °C, respectively, the decomposition pathway involving at least two different steps in the last case.

Moreover, TGA-MS traces indicated that the main fragments detected during the decomposition step are tolyl ( $m/z = 91$ ) for TAN-MePh, phenyl ( $m/z = 77$ ) for TAA-Ph, isopropyl ( $m/z = 43$ ) for TAA-Tips, methoxy ( $m/z = 31$ ) for TAA-OMePh and tert-butyl ( $m/z = 57$ ) for TAA-tBuPh. These features confirm that the main decomposition process corresponds to the loss of branches.

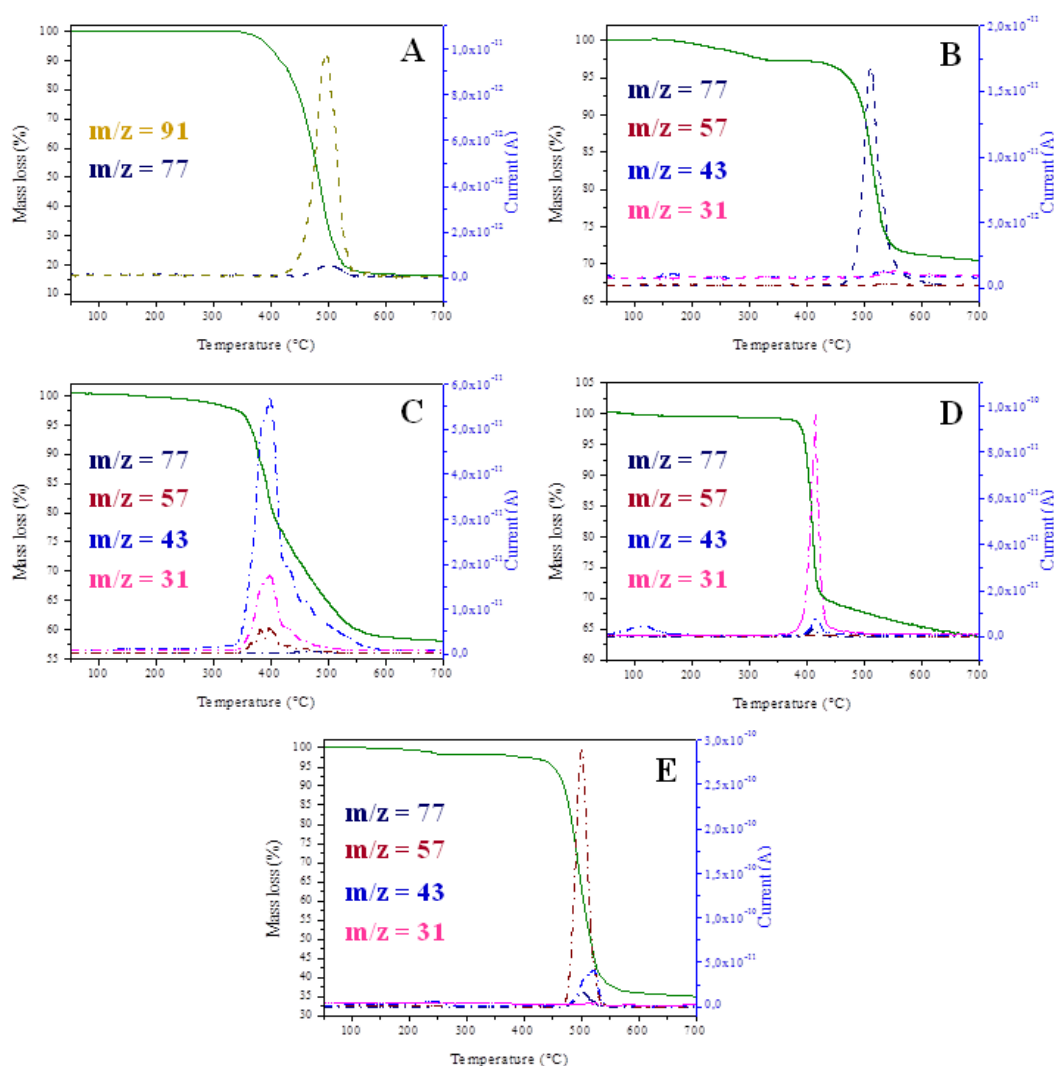


Figure 3-12. TGA-MS traces for TAN-MePh (A), TAA-Ph (B), TAA-Tips (C), TAA-OMePh (D) and TAA-tBuPh (E).

On the other hand, DSC curves of TAA-OMePh and TAA-Tips exhibited no

feature of any phase transition before the decomposition stage. By contrast, the DSC trace of TAN-MePh and TAA-OMePh showed an endothermic feature at 269.5 °C ( $\Delta H = -53.6 \text{ J.g}^{-1}$ ) and 333.0 °C ( $\Delta H = -34.3 \text{ J.g}^{-1}$ ), respectively, that can be unambiguously assigned to melting since this temperature is far below the decomposition temperature. Similar features were also found for TAN-Ph, TAA-Ph and TAA-tBuPh at 436.3 °C ( $\Delta H = -92.4 \text{ J.g}^{-1}$ ), 455.3 °C ( $\Delta H = -44.2 \text{ J.g}^{-1}$ ) and 465.1 °C ( $\Delta H = -85.6 \text{ J.g}^{-1}$ ) indicating that melting took place just before the decomposition process.

### 3.8 OFET Devices

In order to investigate charge transport properties of the synthesized molecules, thin film OFETs and single crystal OFETs were fabricated.

#### 3.8.1 Thin Film OFETs

To fabricate thin film OFETs devices, there are generally two types of techniques: thermal evaporation and solution-processable deposition for OSCs. Due to the high molecular weight of our molecules (around 1000) and pretty decent solubility in organic solvent, obviously solution-processable deposition should be a better choice to fabricate thin film OFETs.

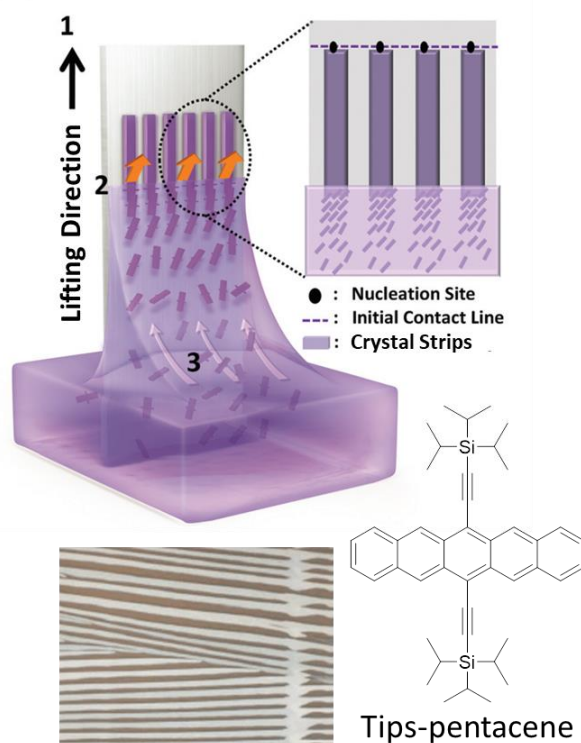


Figure 3-13. Simplified schematic illustration of fast evaporation-induced crystal growth during dip-coating and example of crystal strips of tips-pentacene.<sup>[330]</sup>

In terms of solution-processable deposition, spin-coating is the most commonly

used method. However, the films generated by spin-coating generally show low crystallinity because self-organization must finish within a short processing time.<sup>[322]</sup> In order to get highly crystalline thin films in OFETs, various deposition methods have been introduced, such as drop-casting,<sup>[323,324]</sup> ink-jet printing,<sup>[325,326]</sup> solution shearing,<sup>[327]</sup> spray coating,<sup>[328]</sup> and zone-casting<sup>[329]</sup>. In this study, the dip-coating method has been chosen to fabricate thin film OFETs.

Dip-coating has been a promising method for achieving highly crystalline organic thin films for a long time benefited from its simplicity and easiness to operate.<sup>[331]</sup> As shown in Figure 3-13, there are three steps to form crystallized strips. Firstly, substrate was lifted at an optimized rate concerning evaporation and surface tension of the solvent. Secondly, nucleation sites formed at the air-substrate-solvent conduct line. Thirdly, following molecules self-organized after the nucleation sites to form strips. Therefore, a few critical parameters need to be taken into account, such as lifting speed, temperature, solvent nature and concentration of the solution.<sup>[332]</sup>

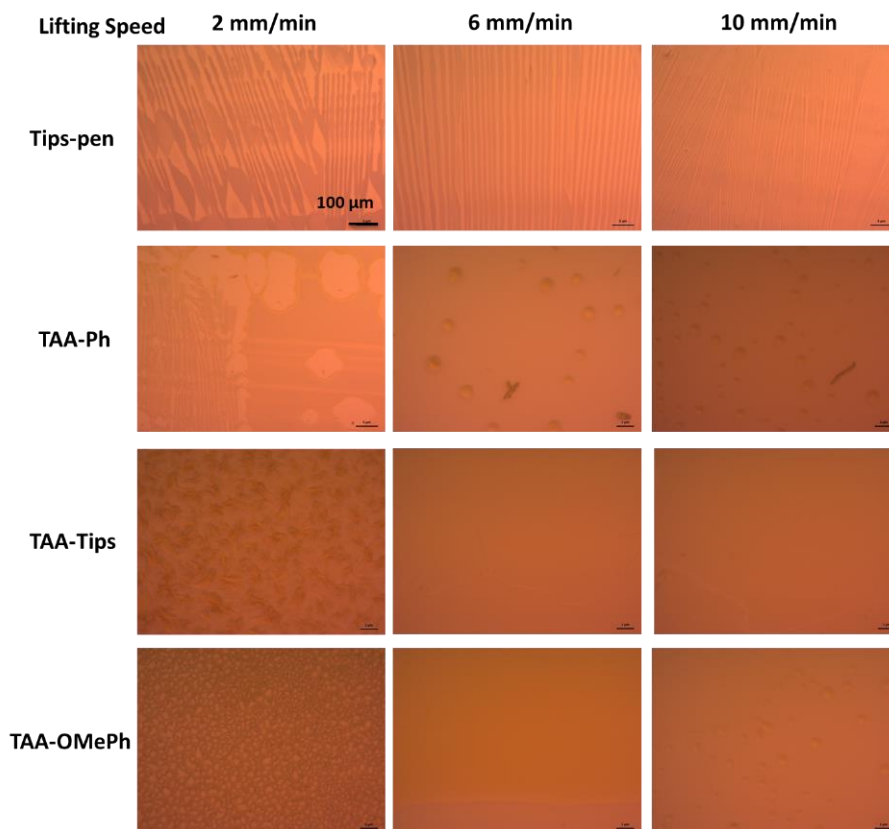


Figure 3-14. Optical microscopy images of dip-coated Tips-Pen, TAA-Ph, TAA-Tips and TAA-OMePh thin films prepared from dichloromethane solution under lifting speed of 2, 6, and 10 mm/min.

The first parameter we studied about is lifting speed. Three different speeds 2, 6 and 10 mm/min were tested with three of our molecules with interesting molecule

packing (TAA-Ph, TAA-Tips and TAA-OMePh), and Tips-Pen was used as reference. All the experiments were performed on glass substrates at 25 °C with air conditioning to ensure a stable atmosphere. Dichloromethane was used as solvent and solution concentration was 5 mg/mL for Tips-Pen, TAA-Tips and TAA-OMePh, while 2 mg/mL for TAA-Ph due to the limitation of solubility.

As shown in Figure 3-14, Tips-Pen formed crystalized strips under all the tested speeds, with the increase of lifting speed strips on the substrates became thinner. For TAA-Ph, TAA-Tips and TAA-OMePh, only TAA-Ph formed strips partially under low lifting speed. Thus, we focused on TAA-Ph and investigated thin films prepared from different solvents.

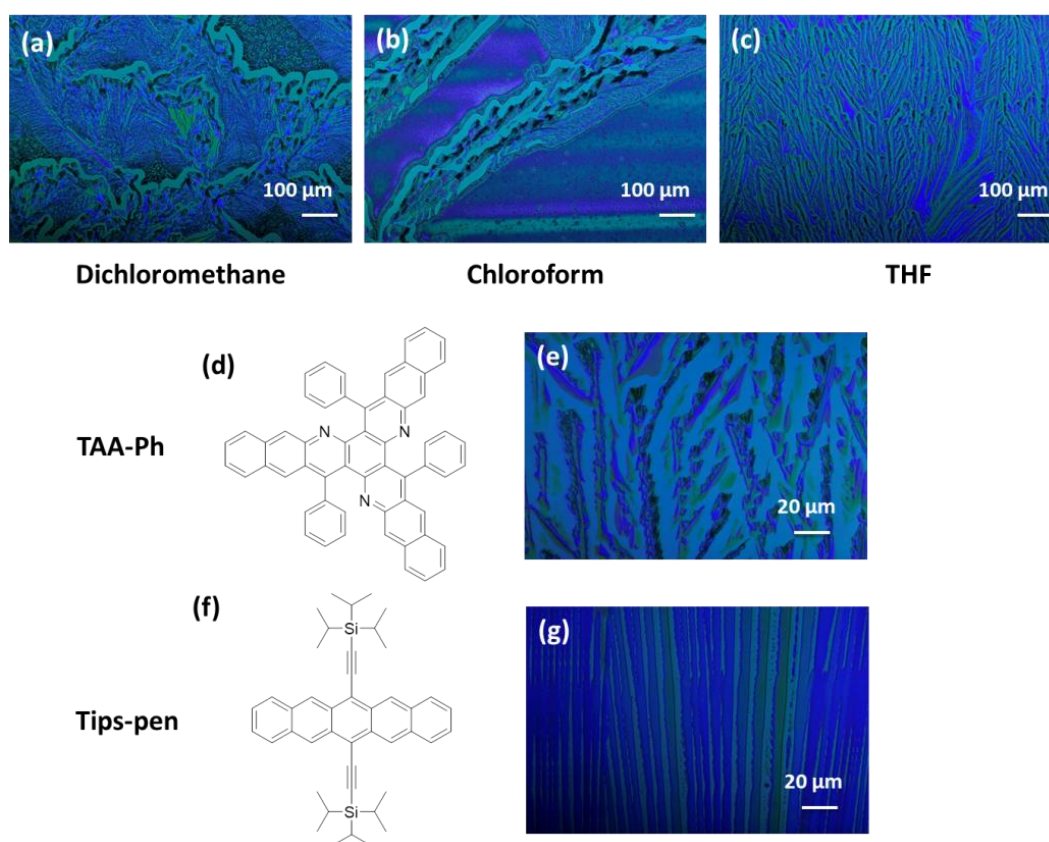


Figure 3-15. POM images of dip-coated TAA-Ph thin films from dichloromethane, chloroform and THF solution (a-c) and magnification of TAA-Ph strips from THF (e) and Tips-Pen strips (g).

Polarized optical microscopy (POM) images of dip-coated TAA-Ph thin films from dichloromethane, chloroform and THF solution are shown in Figure 3-15. Compared with strips from dichloromethane (a) and chloroform (b), strips from THF (c) are relatively consecutive. However, the strips are interrupted into small pieces of crystals as shown in the magnification graph (e). Although the strips from TAA-Ph are not perfectly constant as Tips-pen (g), considering the channel length of the mask we used to fabricate OFETs is only 50 μm the crystals on the substrate are long enough to

be used in OFETs. Therefore, we fabricated OFETs with dip-coated TAA-Ph thin films to investigate its charge transport properties.

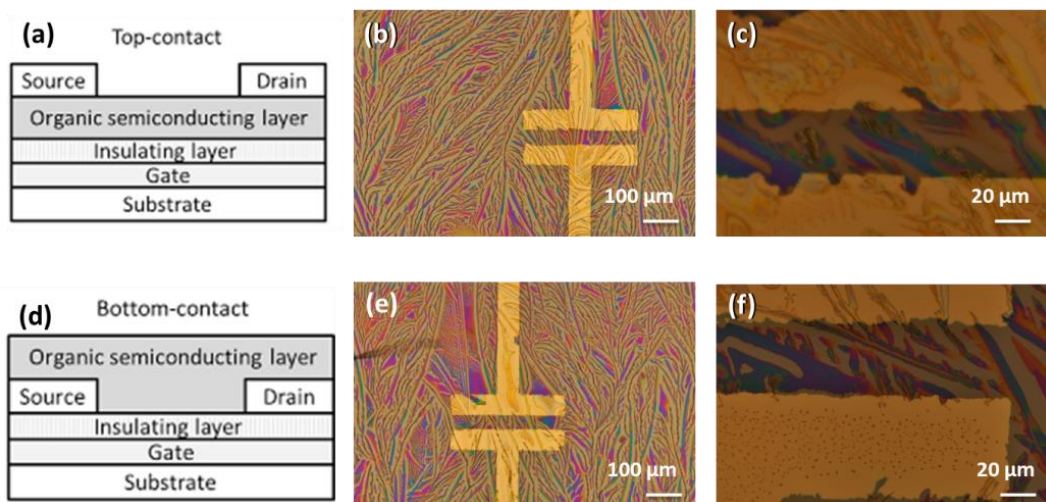


Figure 3-16. Device architectures of top-contact and bottom-contact OFETs (a, d), optical microscopy images of whole transistors (b, e) and magnifications of the channels (c, f).

As shown in Figure 3-16, top-contact and bottom-contact OFET devices were fabricated respectively with dip-coated TAA-Ph thin films. In both cases gold source and drain electrodes were deposited by thermal evaporation, and poly(1-vinyl-1,2,4-triazole) PVT insulating layer was formed by spin-coating. For top-contact device, the Si/SiO<sub>2</sub> substrates were firstly spin-coated with PVT, then dip-coated with TAA-Ph. At the end, electrodes were deposited. For bottom-contact device, Si/SiO<sub>2</sub> substrates were spin-coated with PVT firstly, and then electrodes were deposited. Finally, the active material (TAA-Ph or tips-pentacene) was dip-coated. First of all, both top-contact and bottom-contact OFETs based on dip-coating Tips-pen thin films give out a decent performance with highest mobility of 0.1 cm<sup>2</sup> V<sup>-1</sup> s<sup>-1</sup>, current on/off ratio ( $I_{on}/I_{off}$ ) of  $1.3 \times 10^4$  and a threshold voltage ( $V_T$ ) of -19 V (Figure 3-17). These results validate the experimental procedure employed to fabricate OFETs.

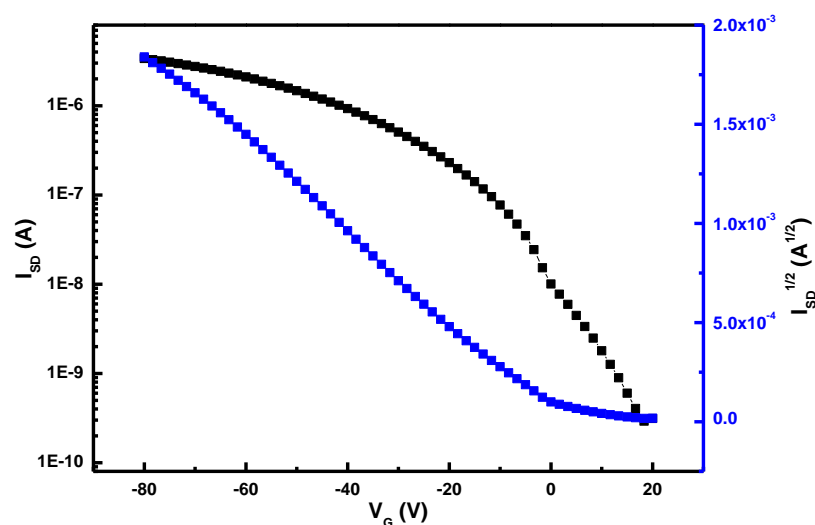


Figure 3-17. Transfer characteristics of OFET based on dip-coated Tips-pen thin film.

The same experiments were reproduced with dip-coated TAA-Ph layers. Obviously, in bottom-contact device crystals growth was interrupted on the gold-PVT frontier. Indeed, free space is observed at the electrode boundary. This contact issues could not be solved by modification of the process. Consequently, top-contact devices were measured and did not obtain OFET performance in positive or negative gate-bias voltage.

### 3.8.2 Single Crystal OFETs

Single crystal OFETs is a good method to investigate charge transport anisotropy of the materials.<sup>[333]</sup> Single crystal OFETs based on TAA-Ph single crystal and two types of rubrene single crystals were fabricated. Si/SiO<sub>2</sub> substrates were spin-coated with PVT firstly, then gold electrodes were deposited under vacuum. A single crystal was placed on the substrate in ambient and went through the length of the OFET channel as shown in Figure 3-18 (a). Methanol lamination was applied to increase the contact between crystal and electrodes.

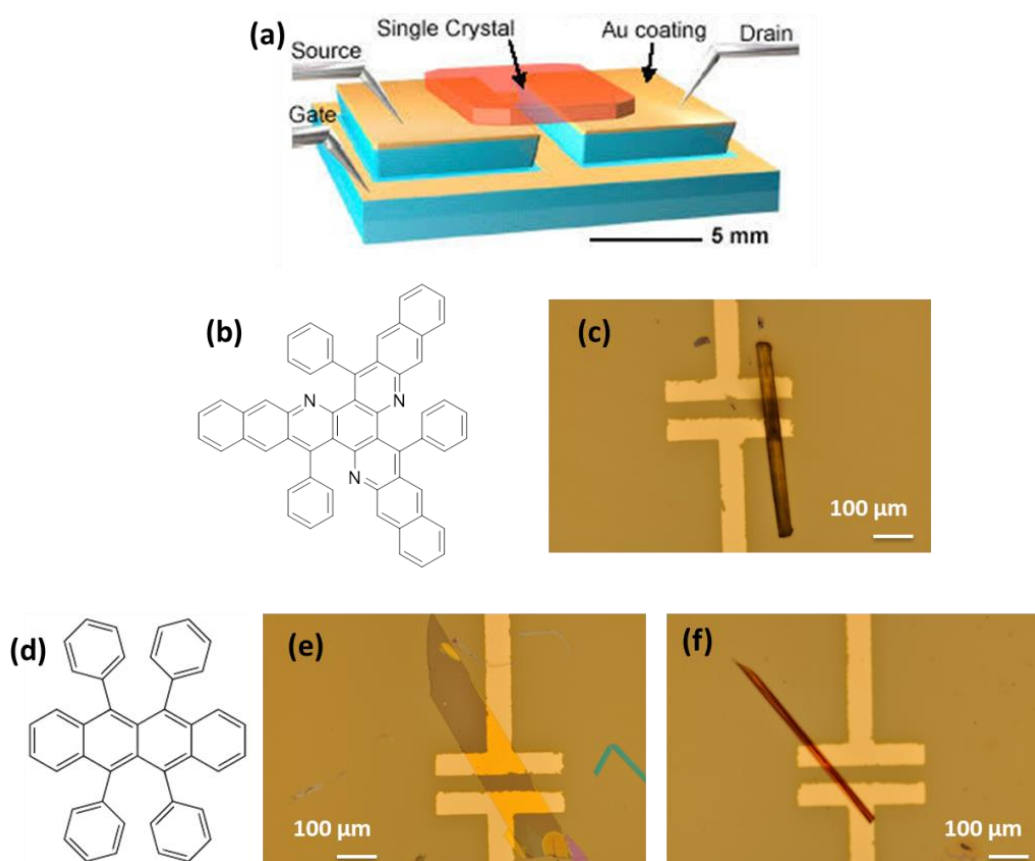


Figure 3-18. Single crystal OFETs architecture (a), chemical structure of TAA-Ph (b) and rubrene (d) and optical microscopy images of single crystal OFETs based on TAA-Ph (c) and rubrene (e and f).

TAA-Ph single crystals were grown by solution diffusion and rubrene single crystals were obtained by physical vapor transport. As reported in the literature, the morphology of rubrene single crystals is controlled by tuning growth parameters.<sup>[334]</sup> Lath-like (Figure 3-18 (e)) and needle-like (Figure 3-18 (f)) rubrene single crystals were obtained and applied in devices. Device in Figure 3-18 (e) led to hole mobilities as high as  $8 \text{ cm}^2 \text{ V}^{-1} \text{ s}^{-1}$  with current on/off ratio ( $I_{\text{on}}/I_{\text{off}}$ ) of  $1.4 \times 10^5$  and a threshold voltage ( $V_T$ ) of 10 V (Figure 3-19) in ambient conditions, while device in Figure 3-18 (f) did not show OFET performance. That means in single crystal OFETs, the device performance is strongly dependent on the morphology of the single crystals or polymorphism. Finally, the micro-ribbon-shaped TAA-Ph single crystal device (Figure 3-18 (c)) did not exhibit OFET performance in positive or negative gate-bias voltage in ambient conditions.



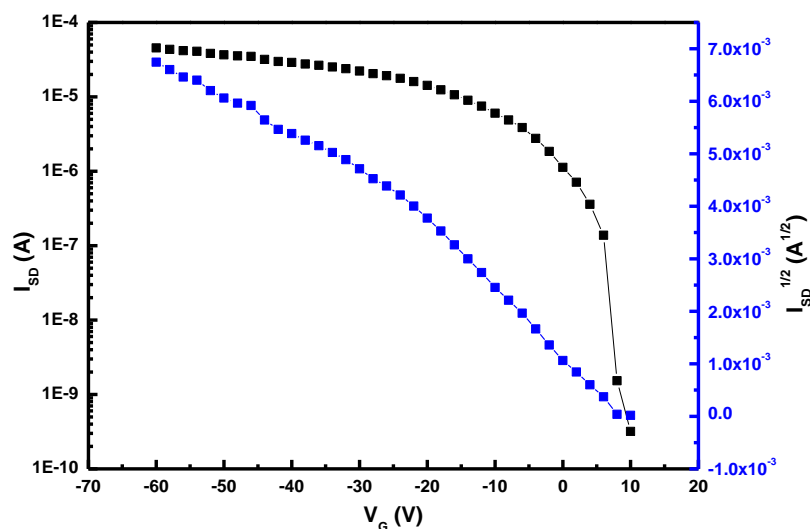


Figure 3-19. Transfer characteristics of single crystal OFET based on rubrene.

### 3.9 Conclusion

In summary, a series of star-shaped molecules with  $C_{3h}$  symmetry were designed and two molecular arrangements were proposed from their molecule structures, named as “arm packing” and “column packing”. An original and efficient synthetic method has been developed to form the acridine moiety of the targeted TAN and TAA derivatives. To the best of our knowledge, this work constitutes the first report about straightforward synthesis of extended  $C_{3h}$  acridine derivatives. Their molecular properties were thoroughly investigated through cyclic voltammetry, UV-visible spectroscopy, DFT calculations and single crystal X-Ray Diffraction. Cyclic voltammetry and UV-visible spectroscopy data are consistent with DFT calculations and proved that all these materials are ambient stable and possess suitable HOMO and LUMO energy levels to work in organic semiconducting devices. In particular, the reduction step is reversible that will guarantee stable channel in protected environment. Single crystal XRD results demonstrated that TAA-Ph and TAA-OMePh exhibit “column packing” and half “arm packing” respectively as speculated in the very beginning. From the XRD results, we assumed that TAA-OMePh could give out 2D charge transport pathway while TAA-Ph has the potential to achieve 3D charge transport pathway in the crystal phase. Calculated transfer integrals between molecular pairs in single-crystals supported the assumed dimensionality of charge transport. The novel synthetic method and the achievement of two interesting molecular arrangement motifs in single crystal can contribute to the development of high-performance OSCs.

Based on the aforementioned results, two suggestions can be made to design

better n-type semiconductors:

1) Molecules with longer conjugated arms are necessary to pledge efficient overlap between neighboring molecules. Further enlargement of  $\pi$ -conjugation system of the molecule might encounter with low stability and solubility problems, so new molecule design strategy and efficient synthesis pathway are required.

2) Molecules with lower LUMO energy level are needed to enable electron injection in OFETs. The lowest LUMO we got with TAA derivatives is -3.32 eV which is too high for ordinary electrodes for OFETs. Introduction of heteroatoms, substitution with strong electron-withdrawing groups or extension of arms are three good strategies to lower the LUMO energy level.

Consequently, this work should be continued by the synthesis of new molecules following the previous suggestions. In addition, these molecules should be introduced in electronic devices, which require 3D mobilities such as OPVs. Then, calculation of association energy for each dimer and specific interaction in dimer should help the edition of design rules as well as Kinetic Monte-Carlo simulation.



## **Conclusion**



Over the past few decades, huge efforts have devoted to the development of organic semiconductors (OSCs) and numerous novel p- and n-type semiconductors have been reported with better mobility performances than those exhibited by amorphous silicon. Nonetheless, most of the high mobilities reported so far for OSCs were extracted from single crystals or highly crystalized thin films in one direction. Therefore, one remaining drawback that limits the application of OSCs is the high anisotropy of their charge transport properties in the crystalline phase. To overcome the unidimensionality of charge transport in most OSCs, the objective of this thesis was to design and synthesize molecules that could provide balanced three dimensional charge transport pathway.

In this aim, our design strategy is expanding the generally linear-shaped molecular structure into star-shaped structure with  $C_{3h}$  symmetry. The designed molecules consist of a planar core of fused aromatic cycles (referred to as the “arms”) and of bulky groups located close to the center (referred to as the “branches”). In such molecular structures,  $\pi$ -conjugated arms are supposed to form efficient  $\pi$ - $\pi$  stacking with neighboring molecules while branches with large steric hindrance are introduced to increase the solubility of the materials, to prevent 1D columnar packing and to adjust  $\pi$  orbital overlaps and packing distances. Based on the structures of the molecules we have designed, two supramolecular arrangements that lead to 3D charge transport can be expected. Firstly two molecules can pack either through extended  $\pi$ -stacking along the arms (“arm packing”) or on top of each other (“column packing”) to form the primary dimer. When the arm packing and column packing are extended to large scale, both of these packing modes involve face-to-face  $\pi$ -stacking between the original molecule and six neighbors in different directions, so that 3D charge transport pathways might be achieved.

In the second chapter, eight new star-shaped molecules were firstly synthesized based on the 5,11,17-triazatrinaphthylene (TAN) and 6,14,22-triazatriantrylene (TAA)  $\pi$ -conjugation systems in respect to the previous design rules. Among all these eight molecules, seven TAN derivatives were obtained by nucleophilic aromatic reaction between 6,12,18-trichloro-TAN (TAN-3Cl) and the desired amines (Method A). Due to the low solubility of TAN-3Cl, another synthetic route involving a one-pot cyclisation reaction as the last step (Method B) was reported for TAN-N-Pent. Method B which keeps all the intermediates soluble during the process allowed us to design larger  $\pi$ -conjugation systems. Thus, TAA-N-Pent was also synthesized according to method B. For each compound, the molecular structure was confirmed by NMR spectroscopy and high-resolution mass spectroscopy. Thus, a single set of proton and carbon resonances were detected by  $^1\text{H}$  and  $^{13}\text{C}$  NMR spectroscopy for the arm-branch unit evidencing the  $C_3$  chemical structure of each star-shaped compound

in solution. Meanwhile, electronic properties and molecular organization in the solid state of these original organic materials were determined by UV-visible absorption spectroscopy, cyclic voltammetry, single crystal X-ray crystallography, DFT calculations and optical microscopy. Finally charge transport properties of these new materials were investigated in solution processed organic field effect transistors (OFETs) and their ability to be used as hole transport materials in photovoltaic devices was evaluated in organic-inorganic hybrid perovskite solar cells (PSCs).

Derived from UV-visible absorption spectroscopy and cyclic voltammetry results, the HOMO levels of TAN derivatives (TAN-N-Pent, TAN-N-Ph, TAN-N-2,4,6MePh, TAN-N-4MePh, TAN-N-3,5MePh and TAN-N-2,6MePh) and TAA-N-Pent have been estimated to be comprised between -5.08 and -5.27 eV which fit with the range of typical hole transport materials for stable OFETs or organic photovoltaic devices (OPVs). On the other hand, molecular packings extracted from single crystal XRD results highlighted that high dimensionality charge carrier transport in the crystalline phase can be obtained for some of these molecules. For alkylamine substituted molecules, TAN-N-Pent exhibits a 1D cofacial herringbone packing motif while TAA-N-Pent shows a 2D bricklayer packing motif benefiting from its longer arms. For arylamine substituted molecules, TAN-N-Ph, TAN-N-4MePh and TAN-N-2,6MePh are promising to exhibit higher charge transport dimensionality due to abundant branch-arm and branch-branch interactions. However, TAN-N-3,5MePh could only exhibit 1D slipped stacking motif due to large distances between neighboring molecules. Most interestingly, TAN-N-2,4,6MePh yielded a new 2D layer by layer packing motif.

Bottom-gate, top-contact p-type OFETs have been fabricated based on spin-coated thin films of TAN-N-Pent and TAA-N-Pent. Devices fabricated at room temperature led to no field effect performance. Then thermal annealing was introduced after the spin-coating of the active layer and thin film of TAA-N-Pent showed visible crystallization after 20 min annealing at 140 °C. Devices based on crystallized thin films exhibited a hole mobility of  $1.2 \times 10^{-4} \text{ cm}^2 \text{ V}^{-1} \text{ s}^{-1}$ . Even though the mobilities obtained with these devices did not reach state of the art performances, this result constitutes a clear evidence that film morphology strongly affects the device performance. Furthermore, five arylamine substituted derivatives, TAN-N-Ph, TAN-N-2,4,6MePh, TAN-N-4MePh, TAN-N-2,6MePh and TAN-N-3,5MePh which exhibit a HOMO energy level close to that of spiro-OMeTAD were applied as hole transporting materials (HTM) in mesoscopic  $\text{TiO}_2/(\text{FAPbI}_3)_{0.85}(\text{MAPbBr}_3)_{0.15}$ -based PSCs. A photovoltaic effect was observed for each compound tested with power conversion efficiencies (PCEs) ranging from 6 to 10% and the best performance was obtained using TAN-N-2,6MePh as HTM which led to PCEs up to 10.4% with a

short-current density ( $J_{sc}$ ) of  $18.58 \text{ mA cm}^{-2}$ , an open-circuit photovoltage ( $V_{oc}$ ) of  $0.92 \text{ V}$  and a fill factor (FF) of  $0.61$ . Besides, new fluorescent molecules were also synthesized using some of these compounds as reactant to form organoboron molecules. Thus, TAN-N-Pent and TAA-N-Pent were reacted with boron trifluoride diethyl etherate leading to two molecules (TAN-Pent-BF<sub>2</sub> and TAA-Pent-BF<sub>2</sub>) with 3 new fused cycles with boron atoms as observed in BODIPY derivatives. Visible-light emission features were observed in the blue and the green for TAN-Pent-BF<sub>2</sub> and TAA-Pent-BF<sub>2</sub>, respectively, with large Stokes shifts ( $100 \text{ nm}$  for TAN-Pent-BF<sub>2</sub> and  $142 \text{ nm}$  for TAA-Pent-BF<sub>2</sub>). As a result, two promising applications can be proposed for these compounds. Firstly, since they show large Stokes shifts they can be used as BODIPY type dyes for applications in luminescence. Secondly, due to the introduction of BF<sub>2</sub> moieties, the LUMO energy levels are much lower (around  $-3.2 \text{ eV}$ ) which makes these materials as potential n-type semiconductors. Another interesting molecule we have introduced in Chapter 2 is 6,12,18-trihydroxy-5,11,17-triazatrinaphthylene (TAN-3OH) which is a promising excited-state intramolecular proton transfer (ESIPT)-based thermally activated delayed fluorescence (TADF) material. The low solubility of TAN-3OH prevents its application by solution processable techniques. Based on the decomposition of our secondary amine substituted TAN derivatives, it is possible to fabricate TAN-3OH thin film through solution routes which opens new avenues in the field of liquid-processing of OLEDs.

On the basis of the results described in the second chapter, the nitrogen atoms on branches were removed and a series of triazastarphenes substituted directly by C<sub>sp2</sub> were designed and synthesized as n-type semiconductors in the third chapter. An original and efficient synthetic method has been developed to form the acridine moiety of the targeted TAN (TAN-Ph and TAN-MePh) and TAA (TAA-Ph, TAA-OMePh, TAA-tBuPh and TAA-CF<sub>3</sub>Ph) derivatives. This work constitutes the first example of a straightforward synthesis towards extended C<sub>3h</sub> acridine derivatives. Their molecular properties were thoroughly investigated through cyclic voltammetry, UV-visible spectroscopy, DFT calculations and single crystal X-Ray crystallography. Cyclic voltammetry and UV-visible spectroscopy data were consistent with DFT calculations and proved that all these materials are stable under ambient conditions and possess suitable HOMO and LUMO energy levels to work in organic semiconducting devices. In particular, the reduction step in CV is reversible that will guarantee stable channel in protected environment.

Single crystal XRD results revealed that TAN-Ph and TAN-MePh showed 1D slipped stacking due to their relatively shorter arms where the best charge transport pathway deduced from modeling does not follow the packing direction. On other hand,



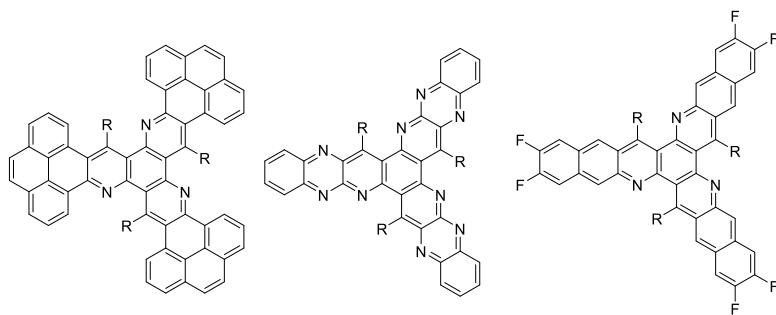
TAA-Tips and TAA-tBuPh led to herringbone packing without efficient pathway for charge transport due to the large steric hindrance induced by branches. Contrary to the four compounds above, TAA-Ph and TAA-OMePh exhibit “column packing” and half “arm packing” respectively as speculated when the molecules were designed. Furthermore, we deduced from the single crystal X-ray structure data that TAA-OMePh could give out 2D charge transport pathway while TAA-Ph had the potential to achieve 3D charge transport pathway in the crystal phase. Calculated transfer integrals between molecular pairs in single-crystals supported the assumed dimensionality of charge transport. Dip-coating OFETs and single crystal OFETs were fabricated using TAA-Ph, but no field effect performance could be measured. Despite all of this, the novel synthetic method and the achievement of two interesting molecular arrangement motifs in single crystal can contribute to the development of high-performance OSCs.

Even though the materials reported in this thesis did not give out decent performances in the devices we fabricated, there are other methods that could be used to characterize these materials. For instance, mobility can be tested by time of flight (TOF), dark injection space charge limited current (SCLC) and many other method. Moreover, the BODIPY type dyes developed in this study should be investigated in more details with the synthesis of new examples and a deeper understanding of their emission properties (quantum yield of fluorescence, emission life time etc...) should be performed. TADF OLED based on solution processed TAN-3OH thin film should also be fabricated. Some of the materials with LUMO level around -3.2 eV could be tested in OPVs as non-fullerene acceptors. As far as theoretical calculations are concerned, the association energy for each dimer and specific interaction in dimer should help the edition of design rules as well as Kintec Monte-Carlo simulations.

From the chemistry point of view, a few suggestions to optimize these molecules and design new molecules can be proposed. First of all, molecules with longer conjugated arms are necessary to pledge efficient overlap between neighboring molecules. Increase the arm length of the molecule might encounter with low stability and solubility issues, so enlarge the  $\pi$ -conjugation system of the arm not only in length but also in width is better choice. Secondly, molecules with lower LUMO energy level are needed to help electron injection in OFETs or to be considered as non-fullerene acceptors. Introduction of heteroatoms, substitution with strong electron-withdrawing groups or extension of arms represent three promising strategies to lower the LUMO energy level of the molecule. A few primary molecule design strategies are given below.

## Conclusion

---





## **Experiment Part**



## 1. Materials and Methods

All the chemical reagents were purchased and used without any further purification. Solvents used below were dried (over sodium for pentane, diethyl ether and THF; over calcium hydride for dichloromethane, chloroform and methanol) and freshly distilled before use. All reactions using organolithium and Grignard reagents were performed under an inert atmosphere of nitrogen gas and with anhydrous solvents.

$^1\text{H}$  and  $^{13}\text{C}$  spectra were recorded on Bruker Avance I 300 MHz, Avance II 400 MHz and Avance III 600 MHz spectrometers at CESAMO (ISM, UMR 5255 CNRS). Chemical shift values were given in ppm versus tetramethylsilane with reference to solvent residual signals. Mass spectra analyses were performed at CESAMO (ISM, UMR 5255 CNRS). Electron-spray ionization (ESI) mass spectra were recorded on a QStar Elite mass spectrometer. The electrospray needle was maintained at 5000 V and operated at room temperature. Samples were introduced by injection through a 20  $\mu\text{L}$  sample loop into a 400  $\mu\text{L}/\text{min}$  flow of methanol from the LC pump. Field Desorption (FD) spectra were recorded on a TOF mass spectrometer AccuTOF GCv by JEOL using an FD emitter with an emitter voltage of 10 kV. One to two microliters solution of the compound was deposited on a 13  $\mu\text{m}$  emitter wire.

UV-visible absorption spectra in solution were carried out with UV-1650PC Shimadzu spectrophotometer with diluted solution in dichloromethane. Fluorescence emission spectra were recorded on a FluoroMax-4 HORIBA spectrofluorometer. Cyclic voltammetry analyses were performed using potentiostat/galvanostat Autolab PGSTAT100 and a three-electrode device with a glassy carbon working electrode, a platinum counter electrode and an Ag/AgCl reference electrode. 0.25 M tetrabutylammonium hexafluorophosphate ( $n\text{-Bu}_4\text{NPF}_6$ ) was employed as supporting electrolyte. Ferrocene/ferrocenium couple was used as internal standard. All compounds were analysed in THF solution with concentration of 1 mM at a scan rate of 100  $\text{mV s}^{-1}$ . Bubbling with nitrogen flow before cyclic voltammetry and scanning under a blanket of nitrogen to avoid the effect of oxygen were achieved to obtain reliable data. The optical microscopy images have been captured on Zeiss Axio Imager A1 microscope mounted with: Ec Epiplan-Neofluar x50 lens.

Thermogravimetric (TG) and differential scanning calorimetry (DSC) analyses were performed by using a STA 449 F5 Jupiter Simultaneous Thermal Analyzer (TG-DTG, DTA, DSC) from NETZSCH under an argon flow at a heating rate of 20  $\text{K}\cdot\text{min}^{-1}$ . The evolved gases were analyzed on NETZSCH, Aeolos, QMS 403D mass spectrometer coupled to the TG instrument. The transfer line was heated to 250  $^\circ\text{C}$ . Mass Spectrometry was carried out in the scan mode for mass ranging from 16 to 130 amu.

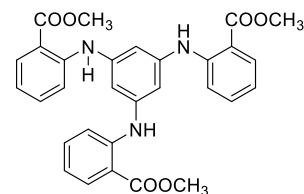
DFT and TD-DFT calculations were carried out by Dr. Frédéric Castet (ISM,

Bordeaux) using Gaussian 09 package and ORCA. Molecular geometries were optimized using the density functional theory (DFT) at the B3LYP/6-31G(d) level. Internal reorganization energies for holes ( $\lambda_h$ ) and electrons ( $\lambda_e$ ) were calculated at the same level of theory. Absorption spectra were calculated at the IEFPCM/B3LYP/6-311G(d) level.

Cristallographic data were acquired at CESAMO (ISM, UMR 5255 CNRS) on a Bruker APEX 2 DUO. A single crystal was mounted and immersed in a stream of nitrogen gas [ $T = 150(2)$  K]. Data were collected, using a microfocus sealed tube of Mo K $\alpha$  radiation ( $k = 0.71073$  Å) on a KappaCCD diffractometer. Data collection and cell refinement were performed using APEX2 2013.10-0 (Bruker AXS Inc.), and SAINT v8.34A (Bruker AXS Inc.). Data reduction was performed using SAINT v8.34A (Bruker AXS Inc.). Correction for absorption was performed using multi-scan integration as included in SADABS V2012/1 (Bruker AXS). Structure solutions were found by charge flipping methods (SUPERFLIP (Palatinus & Chapuis, 2007) EDMA (Palatinus et al., 2012)) and refined with (SHELXL) (G.M. Sheldrick, A short history of SHELX, Acta Crystallographica Section A, 64 (2008), pp. 112–122).

## 2. Synthesis

### 2.1 Synthesis of Triazastarphene Substituted by NH

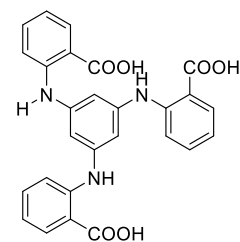


#### 1,3,5-Tris(2-carbomethoxyphenylamino)benzene

1.00 g (3.18 mmol, 1.0 eq.) of 1,3,5-tribromobenzene, 1.68 g (11.12 mmol, 3.5 eq.) of methyl anthranilate, 5.17 g (15.88 mmol, 5.0 eq.) of cesium carbonate, 0.043 g (0.19 mmol, 0.06 eq.) of Pd(OAc)<sub>2</sub> and 0.17 g (0.57 mmol, 0.18 eq.) of tri-*tert*-butylphosphonium tetrafluoroborate were added into a dry round-bottom flask. 50 mL freshly distilled toluene were added into the flask. The mixture was stirred at reflux 72 h under nitrogen. After cooling to room temperature, the reaction mixture was filtered and the filtrate was dried under reduced pressure. The residue was purified by column chromatography over silica gel with pentane : dichloromethane (3:2) as eluent to give 1.50 g of a white solid (90%).

<sup>1</sup>H NMR (300 MHz, CDCl<sub>3</sub>):  $\delta = 9.46$  (s, 3H; NH), 7.96 (d, 3H,  $J = 7.9$  Hz; Ar-H), 7.36 (m, 6H; Ar-H), 6.84 (s, 3H; Ar-H), 6.75 (m, 3H; Ar-H), 3.90 (s, 9H; OCH<sub>3</sub>).

$^1\text{H}$  NMR corresponds with published data.<sup>[269]</sup>

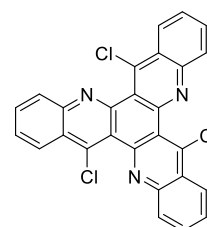


### 1,3,5-Tris(2-carboxyphenylamino)benzene

1.00 g (1.90 mmol, 1.0 eq.) of 1,3,5-Tris(2-carboxyphenylamino)benzene was dissolved in acetone. 17 ml of 5% aqueous solution of NaOH (0.91 g, 22.81 mmol, 12.0 eq.) were added to the solution. The reaction mixture was stirred at reflux under nitrogen for 12 h. After cooling to room temperature, acetone was removed under reduced pressure. 50 mL of  $\text{H}_2\text{O}$  was added to the residue then washed with dichloromethane. The aqueous phase was acidified to pH 1 by addition of aq. HCl solution (1 M). The obtained suspension was filtered and dried under vacuum at 100 °C for 2 h to afford 0.80 g of a white solid (87%).

$^1\text{H}$  NMR (300 MHz, DMSO):  $\delta$  = 13.11 (s, 3H; COOH), 9.57 (s, 3H; NH), 7.89 (dd, 3H,  $J$  = 7.9, 1.5 Hz; Ar-H), 7.42 (m, 6H; Ar-H), 6.81 (m, 3H; Ar-H), 6.76 (s, 3H; Ar-H).

$^1\text{H}$  NMR corresponds with published data.<sup>[269]</sup>



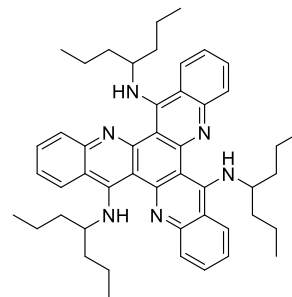
### TAN-3Cl: 6,12,18-trichloro-5,11,17-triazatrinaphthylene

0.50 g (1.03 mmol, 1.0 eq.) of 1,3,5-Tris(2-carboxyphenylamino)benzene was dried under vacuum at 110 °C for 4 h, 0.65 g (3.09 mmol, 3.0 eq.) of  $\text{PCl}_5$  and 20 mL  $\text{POCl}_3$  (large excess) were added. The solution was stirred and refluxed under nitrogen for 24 h. After reaction, the excess of  $\text{POCl}_3$  was removed under reduced pressure, the residue was dissolved in dichloromethane and slowly poured into ice-cooled water. After stirring for 2 h, the mixture was filtered and the filtrate was thoroughly washed with acetone and dried to afford 0.4 g of a black solid with yield around 50%.

$^1\text{H}$  NMR (600 MHz, TCE):  $\delta$  = 8.74 (d, 3H,  $J$  = 8.5 Hz; Ar-H), 8.43 (d, 3H,  $J$  = 8.3 Hz; Ar-H), 7.99 (t, 3H,  $J$  = 7.1 Hz; Ar-H), 7.87 (t, 3H,  $J$  = 7.2 Hz; Ar-H).

$^1\text{H}$  NMR corresponds with published data.<sup>[269]</sup>





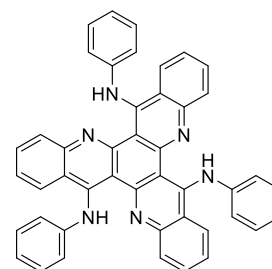
**TAN-N-Hep: 6,12,18-Tris(heptan-4-yl)-5,11,17-triazatrinaphthylene**

0.15 g (0.31 mmol, 1.0 eq.) of 6,12,18-trichloro-5,11,17-triazatrinaphthylene was dissolved in 10 mL of 1-Methyl-2-pyrrolidinone. 0.21 g (1.86 mmol, 6 eq.) of 4-Aminoheptane was added. The solution was stirred at 150 °C under nitrogen for 24 h. After cooling to room temperature, the reaction mixture was poured into water and stirred for 1 hour. After extraction into ethyl acetate and then drying over anhydrous MgSO<sub>4</sub>, the organic phase was concentrated under reduced pressure. The residue was purified by column chromatography over silica gel with pentane : ethyl acetate (9:1) as eluent to give 0.10 g of a yellow solid (45%).

<sup>1</sup>H NMR (600 MHz, TCE):  $\delta$  = 11.15 (d, 3H,  $J$  = 8.6 Hz; NH), 8.31 (d, 3H,  $J$  = 8.3 Hz; Ar-H), 7.95 (d, 3H,  $J$  = 8.3 Hz; Ar-H), 7.76 (t, 3H,  $J$  = 7.5 Hz; Ar-H), 7.44 (t, 3H,  $J$  = 7.5 Hz; Ar-H), 4.37 (m, 3H; CH), 1.85 (m, 12H; CH<sub>2</sub>), 1.47 (m, 12H; CH<sub>2</sub>), 0.89 (t, 18H; CH<sub>3</sub>).

<sup>13</sup>C NMR (75 MHz, TCE):  $\delta$  = 157.4, 152.4, 146.1, 130.0, 126.9, 126.1, 122.1, 118.7, 106.9, 58.8, 38.9, 19.2, 14.2.

+TOF HRMS (m/z): calculated for [C<sub>48</sub>H<sub>60</sub>N<sub>6</sub>Na]<sup>+</sup>: 743.4771, found: 743.4786.



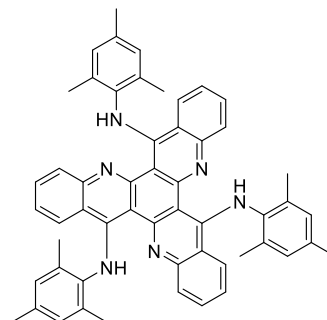
**TAN-N-Ph: 6,12,18-Tris(phenylamino)-5,11,17-triazatrinaphthylene**

0.40 g (0.82 mmol, 1.0 eq.) of 6,12,18-trichloro-5,11,17-triazatrinaphthylene was dissolved in 15 mL of 1-Methyl-2-pyrrolidinone. 0.46 g (4.95 mmol, 6 eq.) of aniline was added. The solution was stirred at 150 °C under nitrogen for 24 h. After cooling to room temperature, the reaction mixture was poured into water and stirred for 1 hour. After extraction into ethyl acetate and then drying over anhydrous MgSO<sub>4</sub>, the organic phase was concentrated under reduced pressure. The residue was purified by column chromatography over silica gel with pentane : ethyl acetate (4:1) as eluent to yield 0.28 g of a yellow solid (52%).

$^1\text{H}$  NMR (300 MHz,  $\text{CD}_2\text{Cl}_2$ ):  $\delta$  = 15.94 (s, 3H; NH), 7.95 (m, 6H; Ar-H), 7.67 (ddd, 3H,  $J$  = 8.3, 6.8, 1.4 Hz; Ar-H), 7.29 (dd, 6H,  $J$  = 8.3, 7.4 Hz; Ar-H), 7.20 (m, 3H; Ar-H), 7.08 (m, 9H; Ar-H).

$^{13}\text{C}$  NMR (75 MHz,  $\text{CD}_2\text{Cl}_2$ ):  $\delta$  = 152.5, 151.9, 146.2, 144.8, 130.9, 129.6, 128.1, 127.4, 123.7, 123.3, 121.3, 119.0, 109.3.

FD+ HRMS (m/z): calculated for  $[\text{C}_{45}\text{H}_{30}\text{N}_6]^+$ : 654.25319, found: 654.25475.



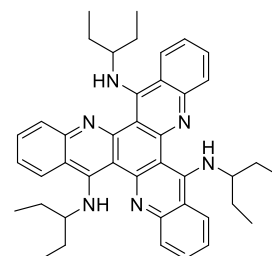
**TAN-N-2,4,6MePh:**  
**6,12,18-Tris(2,4,6-trimethylphenylamino)-5,11,17-triazatrinaphthylene**

0.70 g (1.44 mmol, 1.0 eq.) of 6,12,18-trichloro-5,11,17-triazatrinaphthylene was dissolved in 20 mL of 1-Methyl-2-pyrrolidinone. 1.17 g (8.66 mmol, 6 eq.) of 2,4,6-trimethylaniline was added. The solution was stirred at 150 °C under nitrogen for 24 h. After cooling to room temperature, the reaction mixture was poured into water and stirred for 1 hour. After extraction into ethyl acetate and then drying over anhydrous  $\text{MgSO}_4$ , the organic phase was concentrated under reduced pressure. The residue was purified by column chromatography over silica gel with pentane : ethyl acetate (4:1) as eluent to give 0.25 g of a yellow solid (22%).

$^1\text{H}$  NMR (300 MHz,  $\text{CD}_2\text{Cl}_2$ ):  $\delta$  = 17.09 (s, 3H; NH), 7.77 (dd, 3H,  $J$  = 8.4, 0.8 Hz; Ar-H), 7.54 (m, 6H; Ar-H), 7.02 (s, 6H; Ar-H), 6.95 (m, 3H; Ar-H), 2.38 (s, 9H;  $\text{CH}_3$ ), 2.20 (s, 18H;  $\text{CH}_3$ ).

$^{13}\text{C}$  NMR (75 MHz,  $\text{CD}_2\text{Cl}_2$ ):  $\delta$  = 154.2, 153.3, 145.5, 138.9, 135.6, 133.9, 130.5, 129.7, 127.4, 124.7, 122.7, 118.5, 104.2, 21.2, 19.2.

FD+ HRMS (m/z): calculated for  $[\text{C}_{54}\text{H}_{48}\text{N}_6]^+$ : 780.39404, found: 780.39339.



**TAN-N-Pen: 6,12,18-Tris(pentan-3-yl)-5,11,17-triazatrinaphthylene (method A)**

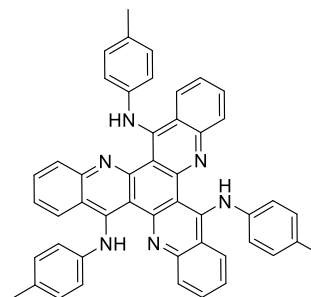
0.20 g (0.41 mmol, 1.0 eq.) of 6,12,18-trichloro-5,11,17-triazatrinaphthylene was dissolved in 20 mL of 1-Methyl-2-pyrrolidinone. 0.22 g (2.47 mmol, 6 eq.) of

3-aminopentane was added. The solution was stirred at 150 °C under nitrogen for 24 h. After cooling to room temperature, the reaction mixture was poured into water and stirred for 1 hour. After extraction into ethyl acetate and then drying over anhydrous MgSO<sub>4</sub>, the organic phase was concentrated under reduced pressure. The residue was purified by column chromatography over silica gel with pentane : ethyl acetate (4:1) as eluent to give 0.12 g of a yellow solid (46%).

<sup>1</sup>H NMR (300 MHz, CD<sub>2</sub>Cl<sub>2</sub>): δ = 14.25 (d, 3H, *J* = 8.9 Hz; NH), 8.29 (d, 3H, *J* = 8.5 Hz; Ar-H), 7.92 (dd, 3H, *J* = 8.4, 0.9 Hz; Ar-H), 7.69 (ddd, 3H, *J* = 8.3, 6.8, 1.4 Hz; Ar-H), 7.37 (ddd, 3H, *J* = 8.3, 6.8, 1.3 Hz; Ar-H), 4.25 (m, 3H; CH), 1.88 (m, 12H; CH<sub>2</sub>), 1.00 (t, 18H, *J* = 7.4 Hz; CH<sub>3</sub>).

<sup>13</sup>C NMR (75 MHz, CD<sub>2</sub>Cl<sub>2</sub>): δ = 158.0, 153.1, 146.7, 130.4, 127.4, 126.7, 122.4, 119.2, 107.3, 62.2, 29.2, 10.6.

FD+ HRMS (m/z): calculated for [C<sub>42</sub>H<sub>48</sub>N<sub>6</sub>]<sup>+</sup>: 636.39404, found: 636.39497.



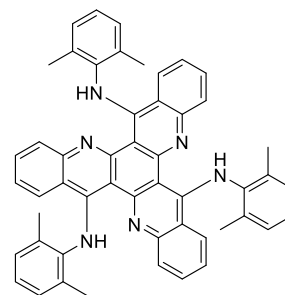
#### TAN-N-4MeP: 6,12,18-Tris(4-methylphenylamino)-5,11,17-triazatrinaphthylene

0.60 g (1.24 mmol, 1.0 eq.) of 6,12,18-trichloro-5,11,17-triazatrinaphthylene was dissolved in 20 mL 1-Methyl-2-pyrrolidinone. 1.0 g (9.35 mmol, 7.5 eq.) of *p*-toluidine was added. The solution was stirred at 150 °C under nitrogen for 24 h. After cooling to room temperature, the reaction mixture was poured into water and stirred for 1 hour. After extraction into ethyl acetate and then drying over anhydrous MgSO<sub>4</sub>, the organic phase was concentrated under reduced pressure. The residue was purified by column chromatography over silica gel with pure chloroform as eluent to give 0.20 g of a yellow solid (23%).

<sup>1</sup>H NMR (300 MHz, CDCl<sub>3</sub>): δ = 15.97 (s, 3H; NH), 7.89 (dd, 6H, *J* = 7.5, 4.3 Hz; Ar-H), 7.59 (t, 3H, *J* = 7.2 Hz; Ar-H), 7.07 (m, 15H; Ar-H), 2.34 (s, 9H; CH<sub>3</sub>).

<sup>13</sup>C NMR (75 MHz, CD<sub>2</sub>Cl<sub>2</sub>): δ = 152.7, 152.2, 146.2, 142.3, 133.2, 130.8, 130.2, 128.0, 127.4, 123.4, 121.6, 119.0, 109.0, 21.0.

ESI+ HRMS (m/z): calculated for [C<sub>48</sub>H<sub>37</sub>N<sub>6</sub>]<sup>+</sup>: 697.30742, found: 697.30684.



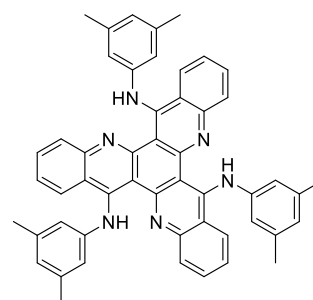
**TAN-N-2,6MePh:**  
**6,12,18-Tris(2,6-dimethylphenylamino)-5,11,17-triazatrinaphthylene**

0.60 g (1.24 mmol, 1.0 eq.) of 6,12,18-trichloro-5,11,17-triazatrinaphthylene was dissolved in 20 mL of 1-Methyl-2-pyrrolidinone. 1.0 g (8.26 mmol, 6.7 eq.) of 2,6-dimethylaniline was added. The solution was stirred at 150 °C under nitrogen for 24 h. After cooling to room temperature, the reaction mixture was poured into water and stirred for 1 hour. After extraction into ethyl acetate and then drying over anhydrous MgSO<sub>4</sub>, the organic phase was concentrated under reduced pressure. The residue was purified by column chromatography over silica gel with pentane : ethyl acetate (4:1) as eluent to yield 0.10 g of a yellow solid (11%).

<sup>1</sup>H NMR (300 MHz, CDCl<sub>3</sub>): δ = 17.25 (s, 3H; NH), 7.81 (d, 3H, *J* = 8.3 Hz; Ar-H), 7.19 (m, 9H; Ar-H), 6.97 (dd, 3H, *J* = 8.4, 6.8 Hz; Ar-H), 2.28 (s, 18H; CH<sub>3</sub>).

<sup>13</sup>C NMR (75 MHz, CD<sub>2</sub>Cl<sub>2</sub>): δ = 154.2, 153.3, 145.7, 141.6, 134.2, 130.6, 129.1, 127.4, 126.0, 124.6, 123.0, 118.6, 104.4, 19.4.

ESI+ HRMS (m/z): calculated for [C<sub>51</sub>H<sub>43</sub>N<sub>6</sub>]<sup>+</sup>: 739.35437, found: 739.35334.



**TAN-N-3,5MePh:**  
**6,12,18-Tris(3,5-dimethylphenylamino)-5,11,17-triazatrinaphthylene**

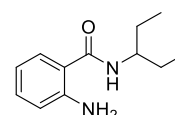
0.50 g (1.03 mmol, 1.0 eq.) of 6,12,18-trichloro-5,11,17-triazatrinaphthylene was dissolved in 20 mL of 1-Methyl-2-pyrrolidinone. 0.50 g (4.13 mmol, 4.0 eq.) of 3,5-dimethylaniline was added. The solution was stirred at 150 °C under nitrogen for 24 h. After cooling to room temperature, the reaction mixture was poured into water and stirred for 1 hour. After extraction into ethyl acetate and then drying over anhydrous MgSO<sub>4</sub>, the organic phase was concentrated under reduced pressure. The residue was purified by column chromatography over silica gel with pentane : ethyl

acetate (4:1) as eluent to lead to 0.40 g of a yellow solid (53%).

$^1\text{H}$  NMR (300 MHz,  $\text{CDCl}_3$ ):  $\delta$  = 15.88 (s, 3H; NH), 8.00 (d, 6H,  $J$  = 8.3 Hz; Ar-H), 7.71 (t, 3H,  $J$  = 7.7 Hz; Ar-H), 7.23 (t, 3H,  $J$  = 7.6 Hz; Ar-H), 6.78 (m, 9H; Ar-H), 2.30 (s, 18H;  $\text{CH}_3$ ).

$^{13}\text{C}$  NMR (75 MHz,  $\text{CD}_2\text{Cl}_2$ ):  $\delta$  = 152.6, 152.1, 146.2, 144.8, 139.3, 130.8, 128.0, 127.4, 125.2, 123.4, 119.3, 119.2, 109.1, 21.5.

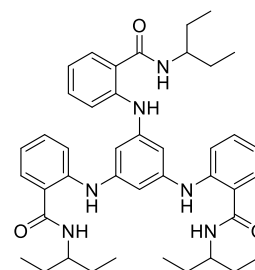
ESI+ HRMS (m/z): calculated for  $[\text{C}_{51}\text{H}_{43}\text{N}_6]^+$ : 739.35437, found: 739.35360.



### 2-amino-*N*-(pentan-3-yl)-benzamide

1.00 g (7.30 mmol, 1.0 eq.) of 2-aminobenzoic acid was dissolved in 50 mL chloroform and cooled down to 0 °C. 2.32 g (8.76 mmol, 1.2 eq.) of diphenyl chlorophosphate was added drop wise and stirred for 10 min. 1.75 g (17.52 mmol, 2.4 eq.) of triethylamine was added and stirred for 10 min. 0.76 g (8.76 mmol, 1.2 eq.) of 3-aminopentane was then added. The mixture was stirred under nitrogen overnight with the temperature rising to room temperature. After reaction, the reaction mixture was poured into water and extracted into dichloromethane, the organic phase was evaporated under reduced pressure. The residue was purified by column chromatography over silica gel with dichloromethane : ethyl acetate (1:1) as eluent to give 1.4 g of a yellow solid (93%).

$^1\text{H}$  NMR (300 MHz,  $\text{CDCl}_3$ ):  $\delta$  = 7.23 (m, 3H; Ar-H), 6.67 (m, 1H; Ar-H), 5.73 (s, 3H; NH), 3.95 (m, 1H; CH), 1.55 (m, 4H;  $\text{CH}_2$ ), 0.96 (t, 6H,  $J$  = 7.4 Hz;  $\text{CH}_3$ ).

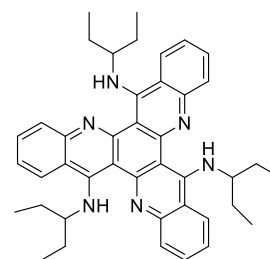


### 1,3,5-tris((2-(*N*-pentan-3-yl)carbamoyl)phenylamino)benzene

0.68 g (2.08 mmol, 1.0 eq.) of 1,3,5-tribromobenzene, 1.50 g (7.28 mmol, 3.5 eq.) of 2-amino-*N*-(pentan-3-yl)-benzamide, 3.39 g (10.40 mmol, 5.0 eq.) of cesium carbonate, 0.028 g (0.19 mmol, 0.06 eq.) of  $\text{Pd}(\text{OAc})_2$  and 0.12 g (0.37 mmol, 0.18 eq.) of tri-*tert*-butylphosphonium tetrafluoroborate were added into a dry round-bottom flask. 50 mL freshly distilled toluene was added into the flask. The mixture was stirred at reflux 72 h under nitrogen. After cooling to room temperature,

the reaction mixture was filtered and the filtrate was concentrated under reduced pressure. The residue was purified by column chromatography over silica gel with dichloromethane : ethyl acetate (9:1) as eluent to yield 1.29 g of a white solid (92%).

$^1\text{H}$  NMR (300 MHz,  $\text{CDCl}_3$ ):  $\delta$  = 9.16 (s, 3H; NH), 7.40 (t, 6H,  $J$  = 8.9 Hz; Ar-H), 7.26 (m, 3H; Ar-H), 6.74 (t, 3H,  $J$  = 7.5 Hz; Ar-H), 6.64 (s, 3H; Ar-H), 5.96 (d, 3H; NH), 3.92 (m, 3H; CH), 1.54 (m, 12H;  $\text{CH}_2$ ), 0.93 (t, 6H,  $J$  = 7.4 Hz;  $\text{CH}_3$ ).



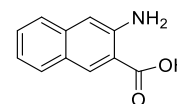
### TAN-N-Pent: 6,12,18-Tris(pentan-3-yl)-5,11,17-triazatrinaphthylene (method B)

1,3,5-Tris((2-(N-pentan-3-yl)carbamoyl)phenylamino)benzene 1.49 g (2.16 mmol, 1.0 eq.) was dissolved in 30 mL of chloroform, 1.3 g (12.94 mmol, 6.0 eq.) lutidine was added in the solution at room temperature, 1.7 g (6.47 mmol, 3 eq.) trifluoromethanesulfonic anhydride was added to the solution. The reaction finished in 30 min. The reaction mixture was then poured into water and extracted into dichloromethane, the organic phase was concentrated under reduced pressure. The residue was purified by column chromatography over silica gel with pentane : ethyl acetate (4:1) as eluent to lead to 0.5 g of a yellow solid (39%).

$^1\text{H}$  NMR (300 MHz,  $\text{CD}_2\text{Cl}_2$ ):  $\delta$  = 14.25 (d, 3H,  $J$  = 8.9 Hz; NH), 8.29 (d, 3H,  $J$  = 8.5 Hz; Ar-H), 7.92 (dd, 3H,  $J$  = 8.4, 0.9 Hz; Ar-H), 7.69 (ddd, 3H,  $J$  = 8.3, 6.8, 1.4 Hz; Ar-H), 7.37 (ddd, 3H,  $J$  = 8.3, 6.8, 1.3 Hz; Ar-H), 4.25 (m, 3H; CH), 1.88 (m, 12H;  $\text{CH}_2$ ), 1.00 (t, 18H,  $J$  = 7.4 Hz;  $\text{CH}_3$ ).

$^{13}\text{C}$  NMR (75 MHz,  $\text{CD}_2\text{Cl}_2$ ):  $\delta$  = 158.0, 153.1, 146.7, 130.4, 127.4, 126.7, 122.4, 119.2, 107.3, 62.2, 29.2, 10.6.

FD+ HRMS (m/z): calculated for  $[\text{C}_{42}\text{H}_{48}\text{N}_6]^+$ : 636.39404, found: 636.39497.



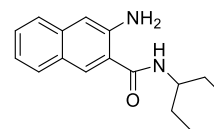
### 3-amino-2-naphthoic acid

100 mL (1.57 mole, 15 eq.) of 30% aqueous ammonia was charged into an autoclave, 14 g (0.10 mole, 1 eq.) of zinc chloride was added gradually with stirring, 30 g (0.16 mole, 1.5 eq.) of 3-hydroxy-2-naphthoic acid was added. The autoclave was closed, heated to 200 °C for 36 h with stirring; the pressure is about 14 bar. After reaction, the

autoclave was allowed to cool to room temperature. The cover was removed and the reaction mixture was transferred to a flask. The autoclave was rinsed two times with 150 mL of water, and the resulting solutions were added to the reaction mixture. 100 mL concentrated hydrochloric acid were added to the mixture, the suspension was refluxed for 30 min. The mixture was filtered while hot through a Buchner funnel. The residual cake was extracted again with 100 mL of boiling water and 5 mL concentrated hydrochloric acid, filtered while hot. Filtrates were combined and cooled down with an ice-bath, the remaining 3-hydroxy-2-naphthoic acid was deposited out, the mixture was filtered to remove the deposition. Filter cake was placed in a flask with 200 mL water, 20 mL 40% sodium hydroxide solution was added with stirring to make the solution at pH = 11~12. The mixture was heated to 85 °C and filtered to remove the insoluble solid. The filtrate was made acid to pH = 4~5 with 15 mL acetic acid, the mixture was filtered and the residue was washed with water. The product was dried under vacuum to get 24.1 g of a yellow powder (81%).

$^1\text{H}$  NMR (300 MHz,  $(\text{CD}_3)_2\text{CO}$ ):  $\delta$  = 8.55 (s, 1H; Ar-H), 7.78 (dd, 1H,  $J$  = 8.5, 0.7 Hz; Ar-H), 7.53 (dd, 1H,  $J$  = 8.4, 0.7 Hz; Ar-H), 7.38 (ddd, 1H,  $J$  = 8.3, 6.7, 1.3 Hz; Ar-H), 7.15 (ddd, 1H,  $J$  = 8.0, 6.7, 1.2 Hz; Ar-H), 7.07 (s, 1H; Ar-H).

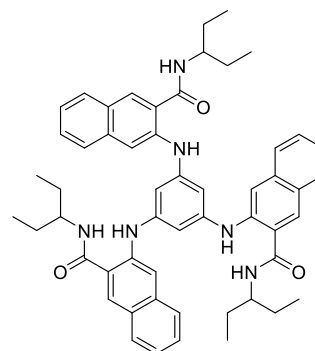
$^{13}\text{C}$  NMR (75 MHz,  $(\text{CD}_3)_2\text{CO}$ ):  $\delta$  = 132.5, 130.4, 129.8, 126.8, 110.8.



### 3-amino-N-(pentan-3-yl)-2-naphthamide

1.00 g (5.35 mmol, 1.0 eq.) of 3-amino-2-naphthoic acid was dissolved in 50 mL chloroform and cooled down to 0 °C. 1.72 g (6.42 mmol, 1.2 eq.) of diphenyl chlorophosphate was added drop wise and stirred for 10 min. 1.30 g (12.83 mmol, 2.4 eq.) of triethylamine was added and stirred for 10 min. 0.56 g (6.42 mmol, 1.2 eq.) of 3-aminopentane was added. The mixture was stirred under nitrogen overnight with the temperature rising to room temperature gradually. After reaction, the reaction mixture was poured into water and extracted into dichloromethane, the organic phase was evaporated under reduced pressure. The residue was purified by column chromatography over silica gel with dichloromethane : ethyl acetate (7:3) as eluent to give 1.2 g of a yellow solid (84%).

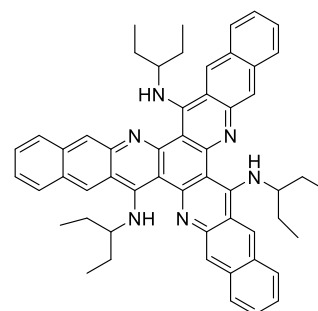
$^1\text{H}$  NMR (300 MHz,  $\text{CDCl}_3$ ):  $\delta$  = 7.83 (s, 1H; Ar-H), 7.69 (d, 1H,  $J$  = 8.2 Hz; Ar-H), 7.57 (d, 1H,  $J$  = 8.3 Hz; Ar-H), 7.40 (ddd, 1H,  $J$  = 8.2, 6.8, 1.3 Hz; Ar-H), 7.23 (ddd, 1H,  $J$  = 8.1, 6.8, 1.2 Hz; Ar-H), 7.05 (s, 1H; Ar-H), 5.93 (d, 1H,  $J$  = 7.8 Hz; NH), 4.02 (m, 1H; CH), 1.63 (m, 4H;  $\text{CH}_2$ ), 1.01 (t, 6H,  $J$  = 7.4 Hz;  $\text{CH}_3$ ).



### 1,3,5-tris((2-(3-(*N*-pentan-3-yl)carbamoyl)naphthyl)amino)benzene

0.70 g (2.22 mmol, 1.0 eq.) of 1,3,5-tribromobenzene, 2.00 g (7.80 mmol, 3.5 eq.) of 3-amino-*N*-(pentan-3-yl)-2-naphthamide, 4.5 g (13.81 mmol, 6.0 eq.) of cesium carbonate, 0.038 g (0.17 mmol, 0.075 eq.) of Pd(OAc)<sub>2</sub> and 0.15 g (0.52 mmol, 0.23 eq.) of tri-*tert*-butylphosphonium tetrafluoroborate were added into a dry round-bottom flask. 50 mL freshly distilled toluene was added into the flask. The mixture was stirred at reflux 72 h under nitrogen. After reaction, the reaction mixture was poured into water and extracted into dichloromethane, the organic phase was evaporated under reduced pressure. The residue was purified by column chromatography over silica gel with dichloromethane : ethyl acetate (9:1) as eluent to yield 2.10 g of a white solid (70%).

<sup>1</sup>H NMR (300 MHz, CDCl<sub>3</sub>): δ = 8.65 (s, 3H; NH), 7.91 (s, 3H; Ar-H), 7.78 (s, 3H; Ar-H), 7.62 (t, 6H, *J* = 7.9 Hz; Ar-H), 7.37 (t, 3H, *J* = 7.6 Hz; Ar-H), 7.20 (m, 3H; Ar-H), 6.83 (s, 3H; Ar-H), 6.40 (dd, 3H, *J* = 8.5, 6.0 Hz; NH), 3.95 (m, 3H; CH), 1.54 (m, 12H; CH<sub>2</sub>), 0.95 (t, 18H, *J* = 7.4 Hz; CH<sub>3</sub>).



### TAA-N-Pent: 6,12,18-Tris(pentan-3-yl)-5,11,17-triazatrianthrylene

1,3,5-tris((2-(3-(*N*-pentan-3-yl)carbamoyl)naphthyl)amino)benzene 1.30 g (1.55 mmol, 1.0 eq.) was dissolved in 30 mL of chloroform, 0.99 g (9.25 mmol, 6.0 eq.) lutidine was introduced at room temperature and finally 1.3 g (4.61 mmol, 3.0 eq.) trifluoromethanesulfonic anhydride was added to the solution. The reaction was completed within 30 min. The reaction mixture was then poured into water and extracted into dichloromethane, the organic phase was evaporated under reduced

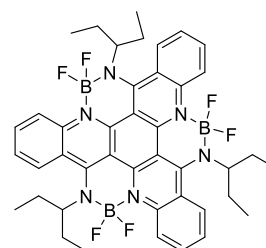


pressure. The residue was purified by column chromatography over silica gel with dichloromethane : ethyl acetate (9:1) as eluent to provide 0.4 g of a yellow solid (33%).

$^1\text{H}$  NMR (300 MHz,  $\text{CDCl}_3$ ):  $\delta$  = 14.90 (d, 3H,  $J$  = 9.4 Hz; NH), 8.86 (s, 3H; Ar-H), 8.36 (s, 3H; Ar-H), 8.03 (d, 6H,  $J$  = 8.6 Hz; Ar-H), 7.49 (dt, 6H,  $J$  = 14.2, 6.7 Hz; Ar-H), 4.47 (m, 3H; CH), 2.02 (m, 12H;  $\text{CH}_2$ ), 1.10 (t, 18H,  $J$  = 7.3 Hz;  $\text{CH}_3$ ).

$^{13}\text{C}$  NMR (75 MHz,  $\text{CD}_2\text{Cl}_2$ ):  $\delta$  = 158.4, 154.7, 143.9, 135.1, 129.5, 129.4, 127.6, 127.3, 127.0, 124.8, 123.0, 120.0, 105.2, 62.4, 30.0, 10.9.

ESI+ HRMS (m/z): calculated for  $[\text{C}_{54}\text{H}_{55}\text{N}_6]^+$ : 787.44827, found: 787.44718.



#### TAN-Pent-BF<sub>2</sub>:

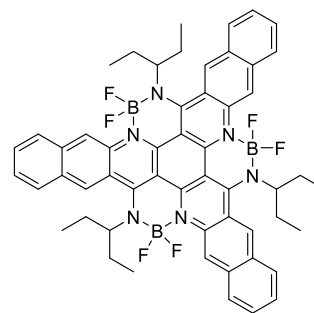
**5,5,11,11,17,17-hexafluoro-6,12,18-tri(pentan-3-yl)-5,6,11,12,17,18-hexahydro-4b $\lambda^4$ ,6,10b $\lambda^4$ ,12,16b $\lambda^4$ ,18-hexaaza-5 $\lambda^4$ ,11 $\lambda^4$ ,17 $\lambda^4$ -triboratribenzo[*fgh,pqr,za<sub>1</sub>b<sub>1</sub>*]trinaphthylene**

6,12,18-Tris(pentan-3-yl)-5,11,17-triazatrinaphthylene 0.20 g (0.31 mmol, 1.0 eq.) was dissolved in 20 ml of toluene, 0.29 g (2.83 mmol, 9.0 eq.) triethylamine was added in the solution and stirred for 10 minutes, 0.67 g (4.71 mmol, 15.0 eq.) boron trifluoride diethyl etherate was added dropwise to the solution. The reaction mixture was heated to 80 °C overnight. After reaction, the reaction mixture was quenched with 5 mL water and extracted with dichloromethane, the organic phase was dried under reduced pressure. The residue was purified by silica gel column chromatography with eluent dichloromethane : pentane = 1 : 1 to give 0.18 g yellow solid as product in 72% yield.

$^1\text{H}$  NMR (300 MHz,  $\text{CDCl}_3$ ):  $\delta$  = 8.72 (d, 3H,  $J$  = 8.8 Hz; Ar-H), 8.11 (dd, 3H,  $J$  = 8.4, 1.2 Hz; Ar-H), 7.81 (ddd, 3H,  $J$  = 8.7, 7.0, 1.4 Hz; Ar-H), 7.50 (t, 3H,  $J$  = 7.3 Hz; Ar-H), 4.37 (m, 3H; CH), 2.19 (m, 12H;  $\text{CH}_2$ ), 0.78 (t, 18H,  $J$  = 7.4 Hz;  $\text{CH}_3$ ).

$^{13}\text{C}$  NMR (75 MHz,  $\text{CDCl}_3$ ):  $\delta$  = 161.6, 142.3, 142.0, 133.4, 127.3, 124.4, 124.2, 119.7, 102.0, 69.5, 28.2, 11.8.

+TOF HRMS (m/z): calculated for  $[\text{C}_{42}\text{H}_{45}\text{B}_3\text{F}_6\text{N}_6\text{Na}]^+$ : 803.3781, found: 803.3764.

**TAA-Pent-BF<sub>2</sub>:**

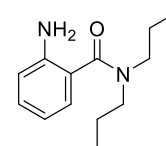
**6,6,14,14,22,22-hexafluoro-7,15,23-tri(pentan-3-yl)-6,7,14,15,22,23-hexahydro-5bλ<sup>4</sup>,7,13bλ<sup>4</sup>,15,21bλ<sup>4</sup>,23-hexaaza-6λ<sup>4</sup>,14λ<sup>4</sup>,22λ<sup>4</sup>-triborabenzox[xyz]benzo[6,7]triphenyl eno[2,1,12,11-hijkl]heptaphene**

6,12,18-Tris(pentan-3-yl)-5,11,17-triazatrianthrylene 0.10 g (0.13 mmol, 1.0 eq.) was dissolved in 15 ml of toluene, 0.12 g (1.14 mmol, 9.0 eq.) triethylamine was added in the solution and stirred for 10 minutes, 0.27 g (1.91 mmol, 15.0 eq.) boron trifluoride diethyl etherate was added dropwise to the solution. The reaction mixture was heated to 80 °C overnight. After reaction, the reaction mixture was quenched with 5 mL water and extracted with dichloromethane, the organic phase was dried under reduced pressure. The residue was purified by silica gel column chromatography with eluent dichloromethane : pentane = 1 : 1 to give 0.10 g yellow solid as product in 83% yield.

<sup>1</sup>H NMR (300 MHz, CDCl<sub>3</sub>): δ = 9.12 (s, 3H; Ar-H), 8.70 (s, 3H; Ar-H), 8.11 (d, 3H, *J* = 8.3 Hz; Ar-H), 8.01 (d, 3H, *J* = 8.1 Hz; Ar-H), 7.66 (m, 3H; Ar-H), 7.56 (m, 3H; Ar-H), 4.61 (m, 3H; CH), 2.36 (m, 12H; CH<sub>2</sub>), 0.90 (t, 18H, *J* = 7.1 Hz; CH<sub>3</sub>).

<sup>13</sup>C NMR (75 MHz, CDCl<sub>3</sub>): δ = 162.1, 143.8, 137.5, 135.6, 129.1, 129.0, 128.5, 128.2, 126.5, 121.4, 119.0, 100.2, 69.6, 28.2, 11.8.

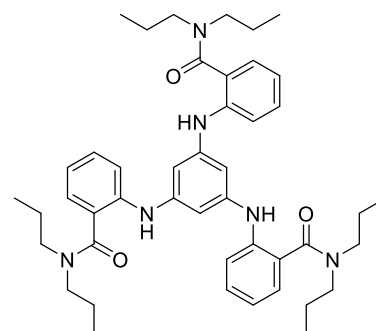
+TOF HRMS (*m/z*): calculated for [C<sub>54</sub>H<sub>51</sub>B<sub>3</sub>F<sub>6</sub>N<sub>6</sub>]<sup>+</sup>: 953.4250, found: 953.4206.

**2-amino-*N,N*-dipropylbenzamide**

2.00 g (14.60 mmol, 1.0 eq.) of 2-aminobenzoic acid was dissolved in 60 mL chloroform and cooled down to 0 °C. 4.71 g (17.52 mmol, 1.2 eq.) of diphenyl chlorophosphate was added drop wise and stirred for 10 min. 3.55 g (35.04 mmol, 2.4 eq.) of triethylamine was added and stirred for 10 min. 1.77 g (17.52 mmol, 1.2 eq.) of dipropylamine was then added. The mixture was stirred under nitrogen overnight with the temperature rising to room temperature slowly. After reaction, the reaction mixture was poured into water and extracted into dichloromethane, the organic phase was evaporated under reduced pressure. The residue was purified by column

chromatography over silica gel with dichloromethane : ethyl acetate (4:1) as eluent to give 2.5 g of a yellow oil (78%).

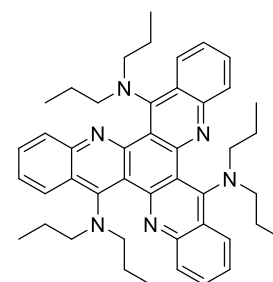
$^1\text{H NMR}$  (300 MHz,  $\text{CDCl}_3$ ):  $\delta$  = 7.13 (ddd, 1H,  $J$  = 8.1, 7.3, 1.6 Hz; Ar-H), 7.05 (dd, 1H,  $J$  = 7.8, 1.6 Hz; Ar-H), 6.70 (m, 2H; Ar-H), 4.15 (s, 2H; NH), 3.33 (br.s, 4H;  $\text{CH}_2$ ), 1.60 (br.s, 4H;  $\text{CH}_2$ ), 0.85 (br.s, 6H;  $\text{CH}_3$ ).



### 1,3,5-tris((2-(*N,N*-dipropyl)carbamoyl)phenylamino)benzene

1.12 g (3.56 mmol, 1.0 eq.) of 1,3,5-tribromobenzene, 2.50 g (11.39 mmol, 3.2 eq.) of 2-amino-*N,N*-dipropylbenzamide, 5.78 g (17.79 mmol, 5.0 eq.) of cesium carbonate, 0.048 g (0.21 mmol, 0.06 eq.) of  $\text{Pd}(\text{OAc})_2$  and 0.19 g (0.64 mmol, 0.18 eq.) of tri-*tert*-butylphosphonium tetrafluoroborate were added into a dry round-bottom flask. 50 mL freshly distilled toluene was added into the flask. The mixture was stirred at reflux 72 h under nitrogen. After cooling to room temperature, the reaction mixture was filtered and the filtrate was concentrated under reduced pressure. The residue was purified by column chromatography over silica gel with dichloromethane : ethyl acetate (2:3) as eluent to yield 2.3 g of a white solid (88%).

$^1\text{H NMR}$  (300 MHz,  $\text{CDCl}_3$ ):  $\delta$  = 7.42 (d, 3H,  $J$  = 8.1 Hz; Ar-H), 7.15 (m, 6H; Ar-H), 6.86 (t, 3H,  $J$  = 7.4 Hz; Ar-H), 6.77 (s, 3H; Ar-H), 6.36 (s, 3H; NH), 3.35 (br, 12H;  $\text{CH}_2$ ), 1.54 (br, 12H;  $\text{CH}_2$ ), 0.86 (br, 18H;  $\text{CH}_3$ ).

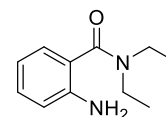


### TAN-N-2Pro: 6,12,18-Tris(*N,N*-dipropyl)-5,11,17-triazatrinaphthylene (method B)

1,3,5-tris((2-(*N,N*-dipropyl)carbamoyl)phenylamino)benzene 1.95 g (2.66 mmol, 1.0 eq.) was dissolved in 30 mL of chloroform, 1.75 g (15.96 mmol, 6.0 eq.) lutidine was added in the solution at room temperature, 2.3 g (7.98 mmol, 3 eq.) trifluoromethanesulfonic anhydride was added to the solution. The reaction finished in

30 min. The reaction mixture was then poured into water and extracted into dichloromethane, the organic phase was concentrated under reduced pressure. The residue was purified by column chromatography over silica gel with pentane : ethyl acetate (4:1) as eluent to lead to 0.5 g of a light yellow solid (28%).

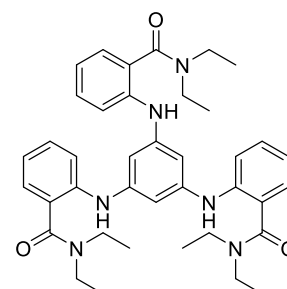
$^1\text{H NMR}$  (300 MHz,  $\text{CDCl}_3$ ): 8.42 (d, 3H,  $J = 8.4$  Hz; Ar-H), 8.14 (d, 3H,  $J = 8.3$  Hz; Ar-H), 7.70 (t, 3H,  $J = 7.5$  Hz; Ar-H), 7.51 (t, 3H,  $J = 7.6$  Hz; Ar-H), 3.50 (t, 12H,  $J = 7.5$  Hz;  $\text{CH}_2$ ), 1.67 (m, 12H;  $\text{CH}_2$ ), 0.77 (t, 18H,  $J = 7.3$  Hz;  $\text{CH}_3$ ).



### 2-amino-*N,N*-diethylbenzamide

2.00 g (14.60 mmol, 1.0 eq.) of 2-aminobenzoic acid was dissolved in 60 mL chloroform and cooled down to 0 °C. 4.71 g (17.52 mmol, 1.2 eq.) of diphenyl chlorophosphate was added drop wise and stirred for 10 min. 3.55 g (35.04 mmol, 2.4 eq.) of triethylamine was added and stirred for 10 min. 1.28 g (17.52 mmol, 1.2 eq.) of dipropylamine was then added. The mixture was stirred under nitrogen overnight with the temperature rising to room temperature slowly. After reaction, the reaction mixture was poured into water and extracted into dichloromethane, the organic phase was evaporated under reduced pressure. The residue was purified by column chromatography over silica gel with dichloromethane : ethyl acetate (4:1) as eluent to give 2.11 g of a yellow solid (75%).

$^1\text{H NMR}$  (300 MHz,  $\text{CDCl}_3$ ):  $\delta = 7.11$  (t, 1H,  $J = 7.7$  Hz; Ar-H), 7.04 (d, 1H,  $J = 7.9$  Hz; Ar-H), 6.70 (m, 2H; Ar-H), 3.94 (s, 2H; NH), 3.40 (br.s, 4H;  $\text{CH}_2$ ), 1.16 (br.s, 6H;  $\text{CH}_3$ ).

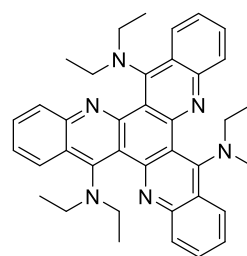


### 1,3,5-tris((2-(*N,N*-diethyl)carbamoyl)phenylamino)benzene

1.08 g (3.43 mmol, 1.0 eq.) of 1,3,5-tribromobenzene, 2.11 g (10.97 mmol, 3.2 eq.) of 2-amino-*N,N*-diethylbenzamide, 5.55 g (17.14 mmol, 5.0 eq.) of cesium carbonate, 0.046 g (0.21 mmol, 0.06 eq.) of  $\text{Pd}(\text{OAc})_2$  and 0.18 g (0.62 mmol, 0.18 eq.) of tri-*tert*-butylphosphonium tetrafluoroborate were added into a dry round-bottom flask.

50 mL freshly distilled toluene was added into the flask. The mixture was stirred at reflux 72 h under nitrogen. After cooling to room temperature, the reaction mixture was filtered and the filtrate was concentrated under reduced pressure. The residue was purified by column chromatography over silica gel with dichloromethane:ethyl acetate (2:3) as eluent to yield 2.03 g of a white solid (91%).

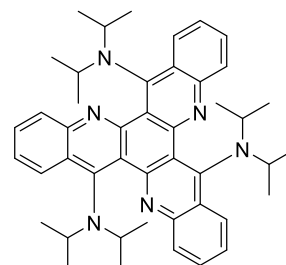
$^1\text{H}$  NMR (300 MHz,  $\text{CD}_2\text{Cl}_2$ ):  $\delta$  = 7.42 (d, 3H,  $J$  = 8.2 Hz; Ar-H), 7.26 (ddd, 3H,  $J$  = 7.4, 4.6, 1.5 Hz; Ar-H), 7.17 (dd, 3H,  $J$  = 7.6, 1.6 Hz; Ar-H), 6.90 (td, 3H,  $J$  = 7.5, 1.1 Hz; Ar-H), 6.77 (s, 3H; Ar-H), 6.37 (s, 3H; NH), 3.41 (br, 12H;  $\text{CH}_2$ ), 1.15 (br.s, 18H;  $\text{CH}_3$ ).



**TAN-N-2Et: 6,12,18-Tris(*N,N*-diethyl)-5,11,17-triazatrinaphthylene (method B)**

1,3,5-tris((2-(*N,N*-diethyl)carbamoyl)phenylamino)benzene 0.4 g (0.62 mmol, 1.0 eq.) was dissolved in 10 mL of chloroform, 0.40 g (3.70 mmol, 6.0 eq.) lutidine was added in the solution at room temperature, 0.52 g (1.85 mmol, 3 eq.) trifluoromethanesulfonic anhydride was added to the solution. The reaction finished in 30 min. The reaction mixture was then poured into water and extracted into dichloromethane, the organic phase was concentrated under reduced pressure. The residue was purified by column chromatography over silica gel with pentane : ethyl acetate (4:1) as eluent to lead to 0.12 g of a light yellow solid (33%).

$^1\text{H}$  NMR (300 MHz,  $\text{CDCl}_3$ ): 8.72 (d, 3H,  $J$  = 8.4 Hz; Ar-H), 8.44 (d, 3H,  $J$  = 8.1 Hz; Ar-H), 7.99 (t, 3H,  $J$  = 7.5 Hz; Ar-H), 7.82 (t, 3H,  $J$  = 7.6 Hz; Ar-H), 3.89 (q, 12H,  $J$  = 7.2 Hz;  $\text{CH}_2$ ), 1.44 (t, 18H,  $J$  = 7.2 Hz;  $\text{CH}_3$ ).

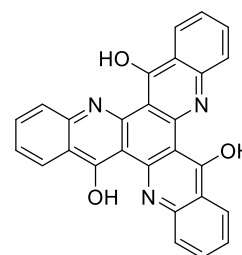


**TAN-N-2iPr: 6,12,18-Tris(*N,N*-diisopropyl)-5,11,17-triazatrinaphthylene (method B)**

1,3,5-tris((2-(*N,N*-diisopropyl)carbamoyl)phenylamino)benzene 1.56 g (2.13 mmol,

1.0 eq.) was dissolved in 30 mL of chloroform, 1.40 g (12.77 mmol, 6.0 eq.) lutidine was added in the solution at room temperature, 1.84 g (6.38 mmol, 3 eq.) trifluoromethanesulfonic anhydride was added to the solution. The reaction finished in 30 min. The reaction mixture was then poured into water and extracted into dichloromethane, the organic phase was concentrated under reduced pressure. The residue was purified by column chromatography over silica gel with pentane : ethyl acetate (4:1) as eluent to lead to 0.5 g of a light yellow solid (35%).

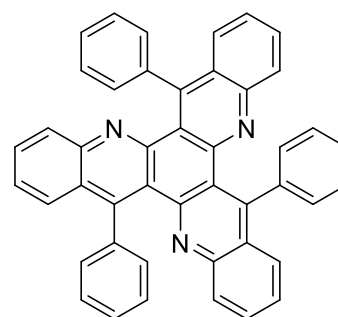
$^1\text{H NMR}$  (300 MHz,  $\text{CDCl}_3$ ): 8.31 (d, 3H,  $J = 8.4$  Hz; Ar-H), 7.96 (d, 3H,  $J = 8.3$  Hz; Ar-H), 7.69 (t, 3H,  $J = 7.6$  Hz; Ar-H), 7.38 (t, 3H,  $J = 7.6$  Hz; Ar-H), 4.54 (m, 6H; CH), 1.49 (d, 36H,  $J = 6.3$  Hz;  $\text{CH}_3$ ).



#### **TAN-3OH: 6,12,18-trihydroxy-5,11,17-triazatrinaphthylene**

The final decomposed compound was TAN-3OH, obtained by filtration of the decomposed solution. Due to the low solubility of TAN-3OH in solvent, -TOF mass spectroscopy was performed and 428.2 was found on the spectrum while calculated molecular weight for  $[\text{C}_{27}\text{H}_{14}\text{N}_3\text{O}_3]^+$  is 428.44.

## **2.2 Synthesis of Triazastarphene Substituted by $\text{C}_{\text{sp}2}$ and $\text{C}_{\text{sp}}$**



#### **TAN-Ph: 6,12,18-triphenyl-5,11,17-triazatrinaphthylene**

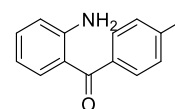
0.94 g (3.00 mmol, 1.0 eq.) of 1,3,5-tribromobenzene, 1.95 g (9.85 mmol, 3.3 eq.) of 2-aminobenzophenone, 2.48 g (17.92 mmol, 6.0 eq.) of potassium carbonate, 0.027 g (0.03 mmol, 0.01 eq.) of  $\text{Pd}_2(\text{dba})_3$  and 0.048 g (0.09 mmol, 0.03 eq.) of BrettPhos were added into a dry round-bottom flask. Then, 30 mL of *t*-butanol were added into

the flask. The mixture was stirred at reflux for 72 hours under nitrogen. After cooling to room temperature, the reaction mixture was filtered and the filtrate was concentrated under reduced pressure. The residue was purified by column chromatography over silica gel using pentane : dichloromethane (4:1) as eluent to yield 1.20 g of a light yellow solid (66%).

$^1\text{H}$  NMR (300 MHz,  $\text{CDCl}_3$ ):  $\delta$  = 7.58 (m, 15H; Ar-H), 7.36 (m, 9H; Ar-H), 7.16 (d, 3H,  $J$  = 7.9 Hz; Ar-H).

$^{13}\text{C}$  NMR (151 MHz,  $\text{CDCl}_3$ )  $\delta$  = 150.0, 148.7, 146.5, 142.5, 130.1, 129.8, 129.5, 128.4, 128.0, 127.6, 126.9, 126.7, 123.3.

ESI+ HRMS ( $m/z$ ): calculated for  $[\text{C}_{45}\text{H}_{28}\text{N}_3]^+$ : 610.2277, found: 610.2272.

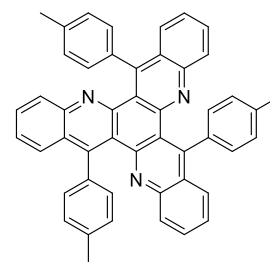


### 2-amino-4'-methylbenzophenone:

3.02 g (17.65 mmol, 4.4 eq.) of 4-Bromotoluene were dissolved in 20 mL of freshly distilled THF and cooled down to  $-78\text{ }^\circ\text{C}$ , then 16.2 mL (19.41 mmol, 4.8 eq.) of 1.2M n-BuLi in pentane was added to the solution drop by drop. The mixture was stirred at  $-78\text{ }^\circ\text{C}$  for 2 hours. 0.55 g (4.01 mmol, 1.0 eq.) of 2-aminobenzoic acid dissolved in 20 mL of THF was added to the mixture drop by drop. The mixture was stirred overnight and was allowed to return to room temperature. After reaction, 10 mL of water was slowly added to quench the excess n-BuLi, and then THF was removed under reduced pressure. 150 mL of water and 150 mL of dichloromethane were added to the residue. Aqueous phase was extracted three times with dichloromethane. The organic phases were collected and organic solvent was removed under reduced pressure. The residue was then purified by column chromatography over silica gel with dichloromethane as eluent to give 0.31 g of a yellow solid (36%).

$^1\text{H}$  NMR (300 MHz,  $\text{CD}_2\text{Cl}_2$ ):  $\delta$  = 7.58 (d, 2H,  $J$  = 8.1 Hz; Ar-H), 7.48 (dd, 1H,  $J$  = 8.0, 1.6 Hz; Ar-H), 7.32 (m, 3H; Ar-H), 6.79 (dd, 1H,  $J$  = 9.6, 1.0 Hz; Ar-H), 6.64 (ddd, 1H,  $J$  = 8.1, 7.1, 1.1 Hz; Ar-H), 6.03 (s, 2H; NH), 2.47 (s, 3H;  $\text{CH}_3$ ).

$^1\text{H}$  NMR corresponds with published data.<sup>[335]</sup>



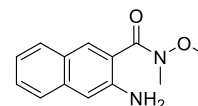
### TAN-MePh: 6,12,18-tri-*p*-tolyl-5,11,17-triazatrinaphthylene

0.13 g (0.41 mmol, 1.0 eq.) of 1,3,5-tribromobenzene, 0.31 g (1.47 mmol, 3.3 eq.) of 2-amino-4'-methylbenzophenone, 0.36 g (2.61 mmol, 6.0 eq.) of potassium carbonate, 0.004 g (0.004 mmol, 0.01 eq.) of Pd<sub>2</sub>(dba)<sub>3</sub> and 0.007 g (0.013 mmol, 0.03 eq.) of BrettPhos were added into a dry round-bottom flask. 20 mL *t*-butanol were added into the flask. The mixture was stirred at reflux for 72 hours under nitrogen. After cooling to room temperature, the reaction mixture was filtered and the filtrate was concentrated under reduced pressure. The residue was then purified by column chromatography over silica gel with pentane : dichloromethane (7:3) as eluent to give 0.21 g of a light yellow solid (74%).

<sup>1</sup>H NMR (300 MHz, CD<sub>2</sub>Cl<sub>2</sub>): δ = 7.61 (ddd, 3H, *J* = 8.5, 1.4, 0.6 Hz; Ar-H), 7.56 (ddd, 3H, *J* = 8.3, 5.7, 1.4 Hz; Ar-H), 7.37 (m, 9H; Ar-H), 7.22 (d, 6H, *J* = 8.0 Hz; Ar-H), 7.17 (ddd, 3H, *J* = 8.4, 1.3, 0.6 Hz; Ar-H), 2.56 (s, 9H; CH<sub>3</sub>).

<sup>13</sup>C NMR (75 MHz, CD<sub>2</sub>Cl<sub>2</sub>): δ = 150.1, 148.8, 146.6, 139.2, 136.3, 130.0, 129.6, 129.4, 128.9, 128.1, 127.6, 126.7, 123.5, 21.6.

ESI+ HRMS (m/z): calculated for [C<sub>48</sub>H<sub>34</sub>N<sub>3</sub>]<sup>+</sup>: 652.27472, found: 652.27374.

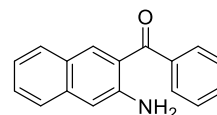


### 2-amino-*N*-methoxy-*N*-methyl-3-naphthamide

1.00 g (5.34 mmol, 1.0 eq.) of 3-amino-2-naphthoic acid was dissolved in 50 mL dichloromethane and cooled down to 0 °C. 1.72 g (6.41 mmol, 1.2 eq.) of diphenyl chlorophosphate was added drop wise and stirred for 10 min. Then, 1.30 g (12.82 mmol, 2.4 eq.) of triethylamine was added and the mixture was stirred for 10 min following by addition of 0.62 g (6.41 mmol, 1.2 eq.) of *N,O*-dimethylhydroxylamine hydrochloride. After overnight stirring and return to room temperature, the reaction mixture was poured into water and extracted with dichloromethane, then the organic phase was collected and organic solvent was removed under reduced pressure. The residue was finally purified by column chromatography over silica gel with dichloromethane : ethyl acetate (1:1) as eluent to give 0.98 g of a brown oil (80%).

<sup>1</sup>H NMR (300 MHz, CDCl<sub>3</sub>): δ = 7.86 (s, 1H; Ar-H), 7.69 (dd, 1H, *J* = 8.2, 0.6 Hz; Ar-H), 7.57 (d, 1H, *J* = 8.3 Hz; Ar-H), 7.40 (ddd, 1H, *J* = 8.2, 6.8, 1.3 Hz; Ar-H), 7.23 (m, 1H; Ar-H), 7.03 (s, 1H; Ar-H), 4.68 (s, 2H; NH), 2.90 (s, 3H; CH<sub>3</sub>), 2.82 (s, 3H; CH<sub>3</sub>).





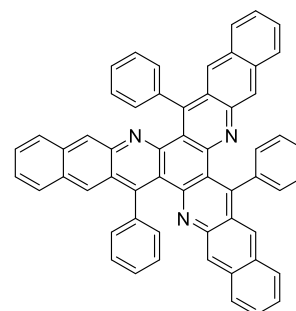
### 2-amino-3-benzoylnaphthalene

1.30 g (5.91 mmol, 1.0 eq.) of 2-amino-*N*-methoxy-*N*-methyl-3-naphthamide was dissolved in 30 mL of freshly distilled THF and cooled to 0 °C. Then, 8.8 mL (17.7 mmol, 3 eq.) of 2 mol/L phenylmagnesium chloride solution was dropwise added to the solution. The mixture was stirred at 0°C for 5 hours, then carefully quenched with 5 mL of water. After THF evaporation under reduced pressure, the residue was dissolved in dichloromethane and washed with water. Then the organic phase was collected and organic solvent was removed under reduced pressure. The residue was then purified by column chromatography over silica gel using dichloromethane as eluent to give 1.00 g of an orange powder (68%).

$^1\text{H}$  NMR (300 MHz,  $\text{CDCl}_3$ ):  $\delta$  = 7.98 (s, 1H; Ar-H), 7.80 (m, 2H; Ar-H), 7.53 (m, 6H; Ar-H), 7.19 (ddd, 1H,  $J$  = 8.1, 6.7, 1.2 Hz; Ar-H), 7.03 (s, 1H; Ar-H), 5.42 (s, 2H; NH).

$^{13}\text{C}$  NMR (75 MHz,  $\text{CDCl}_3$ ):  $\delta$  = 199.1, 146.1, 139.5, 137.1, 136.1, 132.1, 130.0, 129.3, 129.1, 128.3, 125.8, 125.3, 122.8, 110.5.

ESI+ HRMS ( $m/z$ ): calculated for  $[\text{C}_{17}\text{H}_{13}\text{NONa}]^+$ : 270.0889, found: 270.0899.



### TAA-Ph: 7,15,23-triphenyl-6,14,22-triazatrianrylene

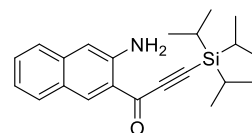
0.096 g (0.30 mmol, 1.0 eq.) of 1,3,5-tribromobenzene, 0.25 g (1.01 mmol, 3.3 eq.) of 2-amino-3-benzoylnaphthalene, 0.25 g (1.83 mmol, 6.0 eq.) of potassium carbonate, 0.003 g (0.0031 mmol, 0.01 eq.) of  $\text{Pd}_2(\text{dba})_3$  and 0.005 g (0.0092 mmol, 0.03 eq.) of BrettPhos were added into a dry round-bottom flask. Then, 20 mL *t*-butanol was added into the flask. The mixture was stirred at reflux for 72 hours under nitrogen. After cooling to room temperature, the reaction mixture was filtered and the filtrate was concentrated under reduced pressure. The residue was purified by column chromatography over silica gel using pentane : dichloromethane (7:3) as eluent to yield 0.20 g of a light yellow solid (87%).

$^1\text{H}$  NMR (300 MHz,  $\text{CDCl}_3$ ):  $\delta$  = 8.18 (s, 3H; Ar-H), 7.94 (d, 3H,  $J$  = 8.1 Hz; Ar-H), 7.84 (d, 3H,  $J$  = 8.1 Hz; Ar-H), 7.75 (s, 3H; Ar-H), 7.68 (m, 9H; Ar-H), 7.45 (m, 12H;

Ar-H).

$^{13}\text{C}$  NMR (151 MHz,  $\text{CDCl}_3$ ):  $\delta = 150.4, 149.2, 142.6, 141.5, 134.3, 132.1, 129.6, 129.0, 128.3, 128.2, 127.5, 127.0, 126.8, 126.6, 125.9, 122.5$ .

FD+ HRMS (m/z): calculated for  $[\text{C}_{57}\text{H}_{33}\text{N}_3]^+$ : 759.26745, found: 759.26958.



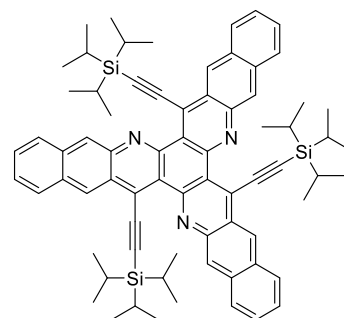
### 1-(3-(2-aminonaphthalenyl)-3-(triisopropylsilyl)-2-propyn-1-one

0.66 g (3.60 mmol, 3.0 eq.) of triisopropylsilylacetylene was dissolved in 20 mL of freshly distilled THF and cooled down to  $-78\text{ }^\circ\text{C}$ . Then, 2.25 mL (3.60 mmol, 3.0 eq.) of 1.6M n-BuLi solution was added to the solution drop by drop. After stirring  $-78\text{ }^\circ\text{C}$  during 2 hours, 0.28 g (1.20 mmol, 1.0 eq.) of 2-amino-N-methoxy-N-methyl-3-naphthamide dissolved in 20 mL of THF was added to the mixture drop by drop. Then, the mixture was stirred and was allowed to rise to room temperature overnight. After reaction, 10 mL of water was slowly added to quench the excess of organolithium compounds, and then THF was removed under reduced pressure. 150 mL of water and 150 mL of dichloromethane were added to the residue. The aqueous phase was extracted three times with dichloromethane. The combined solution was concentrated under reduced pressure. The residue was purified by column chromatography over silica gel with dichloromethane as eluent to give 0.31 g of an orange solid (65%).

$^1\text{H}$  NMR (300 MHz,  $\text{CDCl}_3$ ):  $\delta = 8.87$  (s, 1H; Ar-H), 7.69 (d, 1H,  $J = 8.3$  Hz; Ar-H), 7.52 (d, 1H,  $J = 8.3$  Hz; Ar-H), 7.42 (m, 1H; Ar-H), 7.20 (ddd, 1H,  $J = 8.1, 6.7, 1.2$  Hz; Ar-H), 6.92 (s, 1H; Ar-H), 5.82 (s, 2H; NH), 1.22 (m, 21H;  $\text{CH}_3\text{CHCH}_3$ ).

$^{13}\text{C}$  NMR (75 MHz,  $\text{CDCl}_3$ ):  $\delta = 179.7, 146.3, 138.2, 138.0, 129.9, 129.7, 126.0, 125.3, 122.8, 122.3, 110.1, 103.5, 97.4, 18.8, 11.3$ .

ESI+ HRMS (m/z): calculated for  $[\text{C}_{22}\text{H}_{30}\text{NOSi}]^+$ : 352.2091, found: 352.2097.



### TAA-Tips: 7,15,23-tri(triisopropylsilylethynyl)-6,14,22-triazatriantrylene

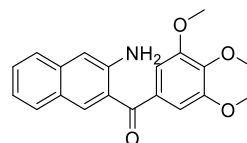
0.081 g (0.26 mmol, 1.0 eq.) of 1,3,5-tribromobenzene, 0.30 g (0.85 mmol, 3.3 eq.) of

1-(3-(2-aminonaphthalenyl)-3-(triisopropylsilyl)-2-propyn-1-yl)-1-ethyne, 0.21 g (1.50 mmol, 6.0 eq.) of potassium carbonate, 0.002 g (0.0026 mmol, 0.01 eq.) of Pd<sub>2</sub>(dba)<sub>3</sub> and 0.004 g (0.0078 mmol, 0.03 eq.) of BrettPhos were added into a dry round-bottom flask. Then, 20 mL *t*-butanol was added into the flask. The mixture was stirred at reflux for 72 hours under nitrogen. After cooling to room temperature, the reaction mixture was filtered and the filtrate was dried under reduced pressure. The residue was purified by column chromatography over silica gel with pentane : dichloromethane (4:1) as eluent to give 0.20 g of a light yellow solid (74%).

<sup>1</sup>H NMR (300 MHz, CDCl<sub>3</sub>): δ = 9.49 (s, 3H; Ar-H), 9.01 (s, 3H; Ar-H), 8.11 (m, 6H; Ar-H), 7.60 (m, 6H; Ar-H), 1.50 (m, 9H; CH), 1.36 (d, 54H, *J* = 6.8 Hz; CH<sub>3</sub>).

<sup>13</sup>C NMR (151 MHz, CDCl<sub>3</sub>): δ = 149.6, 143.0, 134.8, 133.0, 129.2, 128.3, 127.8, 127.4, 127.3, 126.8, 125.1, 104.8, 19.2, 12.0.

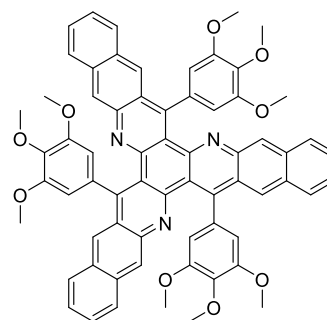
ESI+ HRMS (*m/z*): calculated for [C<sub>72</sub>H<sub>82</sub>N<sub>3</sub>Si<sub>3</sub>]<sup>+</sup>: 1072.5811, found: 1072.5802.



### 2-amino-3-(3,4,5-trimethoxy)benzoylnaphthalene

3.86 g (15.63 mmol, 3.0 eq.) of 5-bromo-1,2,3-trimethoxybenzene was dissolved in 25 mL of freshly distilled THF and cooled down to -78 °C. Then, 6.25 mL (15.63 mmol, 3.0 eq.) of 2.5 M *n*-BuLi solution was added drop by drop and the mixture was stirred at -78 °C for 2 hours. After addition of 1.20 g (5.21 mmol, 1.0 eq.) of 2-amino-*N*-methoxy-*N*-methyl-3-naphthamide dissolved in 20 mL of THF drop by drop, the mixture was stirred and was allowed to rise to -10 °C in 3 hours. After reaction, 10 mL of water was carefully added to quench the excess lithium compound and the resulting mixture was concentrated under reduced pressure. Then, 200 mL of water and 200 mL of dichloromethane were added and aqueous phase was extracted three times with dichloromethane. The combined solution was concentrated under reduced pressure. The residue was purified by column chromatography over silica gel with dichloromethane : ethyl acetate (9:1) as eluent to give 1.60 g of a yellow solid (90%).

<sup>1</sup>H NMR (300 MHz, CDCl<sub>3</sub>): δ = 7.97 (s, 1H; Ar-H), 7.60 (d, 1H, *J* = 8.2 Hz; Ar-H), 7.50 (d, 1H, *J* = 7.9 Hz; Ar-H), 7.38 (ddd, 1H, *J* = 9.7, 5.5, 2.1 Hz; Ar-H), 7.15 (ddd, 1H, *J* = 8.1, 6.8, 1.2 Hz; Ar-H), 7.02 (s, 2H; Ar-H), 6.99 (s, 1H; Ar-H), 5.39 (s, 2H; NH), 3.93 (s, 3H; CH<sub>3</sub>), 3.81 (s, 6H; CH<sub>3</sub>).



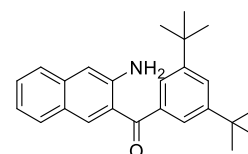
**TAA-OMePh: 7,15,23-tri(3,4,5-trimethoxyphenyl)-6,14,22-triazatrianrylene**

0.34 g (1.08 mmol, 1.0 eq.) of 1,3,5-tribromobenzene, 1.20 g (3.56 mmol, 3.3 eq.) of 2-amino-3-(3,4,5-trimethoxy)benzoylnaphthalene, 0.90 g (6.50 mmol, 6.0 eq.) of potassium carbonate, 0.010 g (0.011 mmol, 0.01 eq.) of Pd<sub>2</sub>(dba)<sub>3</sub> and 0.018 g (0.032 mmol, 0.03 eq.) of BrettPhos were added into a dry round-bottom flask. Then, 20 mL *t*-butanol was added into the flask. The mixture was stirred at reflux for 72 hours under nitrogen. After cooling to room temperature, the reaction mixture was filtered and the filtrate was concentrated under reduced pressure. The residue was purified by column chromatography over silica gel with dichloromethane : ethyl acetate (19:1) as eluent to give 0.40 g of a yellow solid (36%).

<sup>1</sup>H NMR (300 MHz, CDCl<sub>3</sub>): δ = 8.37 (s, 3H; Ar-H), 8.00 (s, 3H; Ar-H), 7.95 (d, 6H, *J* = 7.8 Hz; Ar-H), 7.49 (m, 6H; Ar-H), 7.15 (ddd, 1H, *J* = 8.1, 6.8, 1.2 Hz; Ar-H), 6.73 (s, 6H; Ar-H), 4.25 (s, 9H; CH<sub>3</sub>), 3.82 (s, 18H; CH<sub>3</sub>).

<sup>13</sup>C NMR (75 MHz, CDCl<sub>3</sub>): δ = 171.2, 153.8, 150.6, 148.4, 143.1, 137.5, 137.3, 134.4, 132.2, 129.2, 128.1, 127.6, 127.2, 127.0, 126.6, 126.1, 122.7, 107.0, 104.7, 61.6, 60.5, 56.5, 21.1, 14.3.

ESI+ HRMS (m/z): calculated for [C<sub>66</sub>H<sub>52</sub>O<sub>9</sub>N<sub>3</sub>]<sup>+</sup>: 1030.36981, found: 1030.36641.

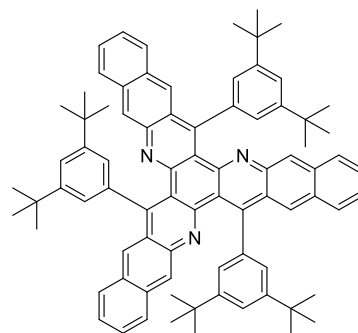


**2-amino-3-(3,5-di-*tert*-butyl)benzoylnaphthalene**

3.51 g (13.03 mmol, 3.0 eq.) of 1-bromo-3,5-di-*tert*-butylbenzene was dissolved in 25 mL of freshly distilled THF and cooled down to -78 °C. Then, 5.21 mL (13.03 mmol, 3.0 eq.) of 2.5 M *n*-BuLi solution was added drop by drop, and the mixture was stirred at -78 °C for 2 hours. 1.00 g (4.34 mmol, 1.0 eq.) of 2-amino-*N*-methoxy-*N*-methyl-3-naphthamide dissolved in 20 mL of THF was added to the mixture drop by drop. The mixture was stirred and was allowed to rise to -10 °C in 3 hours. After reaction, 10 mL of water was slowly added to quench the excess of lithium reagent, and then THF was removed under reduced pressure. 200 mL of water

and 200 mL of dichloromethane were added and aqueous phase was extracted three times with dichloromethane. The combined solution was concentrated under reduced pressure. The residue was purified by column chromatography over silica gel with dichloromethane : ethyl acetate (9:1) as eluent to give 0.4 g of a yellow solid (26%).

$^1\text{H}$  NMR (300 MHz,  $\text{CDCl}_3$ ):  $\delta$  = 8.05 (s, 1H; Ar-H), 7.70 (m, 1H; Ar-H), 7.67 (d, 2H,  $J$  = 1.8 Hz; Ar-H), 7.60 (dd, 2H,  $J$  = 11.1, 8.3 Hz; Ar-H), 7.44 (ddd, 1H,  $J$  = 8.3, 6.8, 1.2 Hz; Ar-H), 7.19 (ddd, 1H,  $J$  = 8.1, 6.8, 1.2 Hz; Ar-H), 7.05 (s, 1H; Ar-H), 5.56 (s, 2H; NH), 1.39 (s, 18H;  $\text{CH}_3$ ).



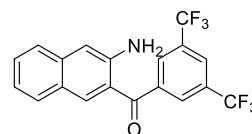
**TAA-tBuPh: 7,15,23-tri(3,5-di-tert-butylphenyl)-6,14,22-triazatriantrylene**

0.11 g (0.35 mmol, 1.0 eq.) of 1,3,5-tribromobenzene, 0.41 g (1.15 mmol, 3.3 eq.) of (2-amino-3-(3,5-di-tert-butyl)benzoyl)naphthalene, 0.29 g (2.10 mmol, 6.0 eq.) of potassium carbonate, 0.0032 g (0.0035 mmol, 0.01 eq.) of  $\text{Pd}_2(\text{dba})_3$  and 0.0056 g (0.011 mmol, 0.03 eq.) of BrettPhos were added into a dry round-bottom flask. Then, 20 mL of *t*-butanol was added into the flask. The mixture was stirred at reflux for 72 hours under nitrogen. After cooling to room temperature, the reaction mixture was filtered and the filtrate was concentrated under reduced pressure. The residue was purified by column chromatography over silica gel with dichloromethane : ethyl acetate (19:1) as eluent to give 0.20 g of a yellow solid (53%).

$^1\text{H}$  NMR (300 MHz,  $\text{CDCl}_3$ ):  $\delta$  = 8.37 (s, 3H; Ar-H), 7.88 (t, 6H,  $J$  = 8.0 Hz; Ar-H), 7.74 (dd, 6H,  $J$  = 4.7, 3.0 Hz; Ar-H), 7.45 (ddd, 6H,  $J$  = 19.0, 10.8, 6.2 Hz; Ar-H), 7.32 (d, 6H,  $J$  = 1.7 Hz; Ar-H), 1.38 (s, 54H;  $\text{CH}_3$ ).

$^{13}\text{C}$  NMR (75 MHz,  $\text{CDCl}_3$ ):  $\delta$  = 150.9, 134.2, 132.1, 129.2, 128.0, 127.6, 126.7, 125.7, 124.1, 120.5, 35.1, 31.8.

ESI+ HRMS ( $m/z$ ): calculated for  $[\text{C}_{81}\text{H}_{82}\text{N}_3]^+$ : 1096.65033, found: 1096.64698.

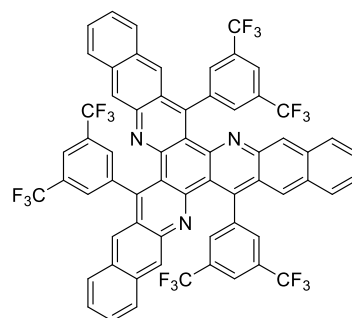


### 2-amino-3-(3,5-bis(trifluoromethyl))benzoylnaphthalene

3.82 g (13.03 mmol, 3.0 eq.) of 1-bromo-3,5-bis(trifluoromethyl)benzene was dissolved in 25 mL of freshly distilled THF and cooled down to  $-78\text{ }^{\circ}\text{C}$ . Then, 5.21 mL (13.03 mmol, 3.0 eq.) of 2.5 M n-BuLi solution was added drop by drop and the mixture was stirred at  $-78\text{ }^{\circ}\text{C}$  for 2 hours. After addition drop by drop of 1.00 g (4.34 mmol, 1.0 eq.) of 2-amino-N-methoxy-N-methyl-3-naphthamide dissolved in 20 mL of THF, the mixture was stirred and was allowed to rise to  $-10\text{ }^{\circ}\text{C}$  in 3 hours. After reaction, 10 mL of water was carefully added to quench the excess lithium compound, and then THF was removed under reduced pressure. 200 mL of water and 200 mL of dichloromethane were added and aqueous phase was extracted three times with dichloromethane. The combined solution was concentrated under reduced pressure and the residue was purified by column chromatography over silica gel with dichloromethane : ethyl acetate (9:1) as eluent to give 0.6 g of a yellow solid (36%).

$^1\text{H}$  NMR (300 MHz,  $\text{CDCl}_3$ ):  $\delta$  = 8.20 (s, 2H; Ar-H), 8.10 (s, 1H; Ar-H), 7.85 (s, 1H; Ar-H), 7.60 (m, 2H; Ar-H), 7.47 (t, 1H,  $J$  = 7.6 Hz; Ar-H), 7.22 (t, 1H,  $J$  = 7.5 Hz; Ar-H), 7.14 (s, 1H; Ar-H), 5.68 (s, 2H; NH).

$^{13}\text{C}$  NMR (75 MHz,  $\text{CDCl}_3$ ):  $\delta$  = 195.8, 141.4, 137.6, 136.2, 132.3, 131.9, 130.0, 129.7, 129.5, 125.6, 123.6, 111.6.



### TAA- $\text{CF}_3\text{Ph}$ : 7,15,23-tri(3,5-di-trifluoromethylphenyl)-6,14,22-triazatrianrylene

0.20 g (0.63 mmol, 1.0 eq.) of 1,3,5-tribromobenzene, 0.80 g (2.09 mmol, 3.3 eq.) of 2-amino-3-(3,5-bis(trifluoromethyl))benzoylnaphthalene, 0.53 g (3.81 mmol, 6.0 eq.) of potassium carbonate, 0.0058 g (0.0063 mmol, 0.01 eq.) of  $\text{Pd}_2(\text{dba})_3$  and 0.010 g (0.019 mmol, 0.03 eq.) of BrettPhos were added into a dry round-bottom flask. Then, 20 mL of *t*-butanol was added into the flask. The mixture was stirred at reflux for 72 hours under nitrogen. After cooling to room temperature, the reaction mixture was filtered and the filtrate was dried under reduced pressure. The residue was finally

purified by column chromatography over silica gel using dichloromethane : ethyl acetate (19:1) as eluent to give 0.32 g of a yellow solid (42%).

$^1\text{H}$  NMR (300 MHz,  $\text{CDCl}_3$ ):  $\delta$  = 8.28 (s, 3H; Ar-H), 8.01 (s, 6H; Ar-H), 7.92 (m, 9H; Ar-H), 7.68 (s, 3H; Ar-H), 7.53 (dddd, 6H,  $J$  = 9.5, 7.9, 6.6, 1.1 Hz; Ar-H).

$^{13}\text{C}$  NMR (75 MHz,  $\text{CDCl}_3$ ):  $\delta$  = 149.6, 145.2, 144.0, 142.4, 134.5, 132.4, 131.9, 131.4, 129.9, 128.7, 127.4, 127.1, 126.8, 126.5, 125.8, 122.7, 120.7.

ESI+ HRMS (m/z): calculated for  $[\text{C}_{63}\text{H}_{28}\text{N}_3\text{F}_{18}]^+$ : 1168.19903, found: 1168.19605.

### 3. Device Fabrication

#### 3.1 Thin film OFETs Fabricated by Spin-Coating with Triazastarphene Substituted by NH (Chapter 2)

Highly n-doped Si wafers coated with a 200 nm thick  $\text{SiO}_2$  layer ( $\text{SiO}_2/\text{Si}$ ) were used as substrates. The substrates were washed sequentially with acetone, ethanol and isopropanol in an ultrasonic bath. Then UV/ $\text{O}_3$  treatment was applied for 15 min to increase the surface energy of the substrates. PVT dielectric layer was spin-coated (2000 rpm, 30 s) and dried in vacuum oven at 80 °C for 2 hours. Organic semiconducting layer was spin-coated (2000 rpm, 30 s) in the glove box from chlorobenzene solution. Then an annealing treatment was applied for 20 minutes with temperature varied from 80 to 180 °C. Finally, 10 nm  $\text{MoO}_3$  and 60 nm silver layers were thermally deposited using patterned electrode mask. Electrical properties were determined using a Keithley 4200-SCS.

#### 3.2 Perovskite Solar Cells (PSCs) with Triazastarphene Substituted by NH as Hole Transport Material (Chapter 2)

FTO glass substrates (Nippon sheet glass) were sequentially cleaned with the detergent solution, acetone, and ethanol. And then by spray pyrolysis deposition, a compact  $\text{TiO}_2$  layer was coated on the cleaned FTO substrate heated at 450 °C. A precursor solution is diluting titanium diisopropoxide (Sigma-Aldrich) in ethanol (0.6 mL; 10 mL). Mesoporous  $\text{TiO}_2$  films were prepared using a diluted  $\text{TiO}_2$  paste (Dyesol 30 NR-D) solution. Films were spin-coated at 2,000 rpm for 10 s, and sintered on a hot plate at 500 °C for 30 min. After cooling to room temperature, films were treated with 0.1 M Lithium bistrifluoromethanesulfonimide solution (Li-TFSI, Aldrich) in acetonitrile by spin-coating at 3,000 rpm for 10 s, and finally baked again at 500 °C for 30 min. The lead excess  $(\text{FAPbI}_3)_{0.85}(\text{MAPbBr}_3)_{0.15}$  precursor solution was prepared by mixing FAI (1.1 M),  $\text{PbI}_2$  (1.15 M), MABr (0.2 M) and  $\text{PbBr}_2$  (0.2 M)

in a mixed solvent of DMF:DMSO = 4:1 (volume ratio). Another solution of CsPbI<sub>3</sub> was also prepared as 1.15 M in DMF:DMSO (same volume ratio). For triple cations mixed perovskite solution, (FAPbI<sub>3</sub>)<sub>0.85</sub>(MAPbBr<sub>3</sub>)<sub>0.15</sub> and CsPbI<sub>3</sub> solutions were mixed as 10 vol% ratio. The perovskite precursor solution was spin coated at 2000 rpm for 10 s, followed by 6000 rpm for 30 s. Trifluorotoluene (110 μl) was dropped on the spinning substrate at the 20 s in the second step. The films were annealed at 100 °C for 90 min in the glove box. The hole-transporting materials were applied from different solution in chlorobenzene. Tert-butylpyridine (Tbp), Tris(2-(1H-pyrazol-1-yl)-4-tert-butylpyridine)cobalt(III) (FK209) and Tris(bis(trifluoromethylsulfon-yl)imide) (Li-TFSI) were added as additives. Equimolar amounts of additives were added for all hole-transporters: 330 mol% *tert*-butylpyridine, 50 mol% Li-TFSI from a 1.8M stock solution in acetonitrile and 3 mol% tris(2-(1H-pyrazol-1-yl)-4-*tert*-butylpyridine)cobalt(III) tri[hexafluorophosphate] (FK209) from a 0.25M stock solution in acetonitrile. Finally, 70 nm of Au was deposited by thermal evaporation as the back electrode.

### 3.3 Thin Film OFETs Prepared by Dip-coating with Triazastarphene

#### Substituted by C<sub>sp2</sub> and C<sub>sp</sub> (Chapter 3)

Highly n-doped Si wafers coated with a 200 nm thick SiO<sub>2</sub> layer (SiO<sub>2</sub>/Si) were used as substrates. The substrates were washed sequentially with acetone, ethanol and isopropanol in an ultrasonic bath. Then UV/O<sub>3</sub> treatment was applied for 15 min to increase the surface energy of the substrates. PVT dielectric layer was spin-coated (2000 rpm, 30 s) and dried in vacuum oven at 80 °C for 2 hours. For top-contact device, organic semiconducting layer was dip-coated with lifting speed of 2 mm/min from THF solution. Then 60 nm of gold was thermal deposited using patterned electrode mask. For bottom-contact device, electrode was deposited before dip-coating. Electrical properties were measured using Keithley 4200-SCS.

### 3.4 Single Crystal OFETs with Triazastarphene Substituted by C<sub>sp2</sub> and C<sub>sp</sub> (Chapter 3)

Highly n-doped Si wafers coated with a 200 nm thick SiO<sub>2</sub> layer (SiO<sub>2</sub>/Si) were used as substrates. The substrates were washed sequentially with acetone, ethanol and isopropanol in an ultrasonic bath. Then UV/O<sub>3</sub> treatment was applied for 15 min to increase the surface energy of the substrates. PVT dielectric layer was spin-coated (2000 rpm, 30 s) and dried in vacuum oven at 80 °C for 2 hours. Then 60 nm of gold



was thermal deposited using patterned electrode mask. Single crystal was placed on the substrate and went through the length of the OFET channel. Methanol lamination was applied to increase the crystal and electrode contact. Electrical properties were measured using Keithley 4200-SCS.

## 4. Crystallographic Data

**Table 1.** Crystallographic parameters for TAN-N-Pent, TAN-N-Ph, TAN-N-4MePh, TAN-N-2,6MePh, TAN-N-3,5MePh, TAN-N-2,4,6MePh and TAA-N-Pent.

	<b>TAN-N-Pent</b>	<b>TAN-N-Ph</b>	<b>TAN-N-4MePh</b>	<b>TAN-N-2,6MePh</b>
<b>Chemical formula</b>	C <sub>84</sub> H <sub>96</sub> N <sub>12</sub>	C <sub>45</sub> H <sub>30</sub> N <sub>6</sub>	C <sub>48</sub> H <sub>36</sub> N <sub>6</sub>	C <sub>51</sub> H <sub>42</sub> N <sub>6</sub>
<b>Formula weight</b>	1273.72	654.75	696.83	738.90
<b>Crystal system</b>	Orthorhombic	Triclinic	Monoclinic	Triclinic
<b>Space group</b>	P n a 21	P -1	P 21/c	P -1
<b>a / Å</b>	25.2687(7)	11.8008(3)	20.3130(12)	12.0696(4)
<b>b / Å</b>	7.2210(2)	12.0247(3)	18.5732(12)	12.4128(4)
<b>c / Å</b>	36.8720(10)	12.6868(3)	9.7332(6)	14.7236(5)
<b>α / °</b>	90	104.4160(10)	90	83.0350(10)
<b>β / °</b>	90	101.2010(10)	99.115(2)	74.5390(10)
<b>γ / °</b>	90	103.2270(10)	90	88.0490(10)
<b>V / Å<sup>3</sup></b>	6727.9(3)	1635.97(7)	3625.7(4)	2110.34(12)
<b>Z</b>	4	2	4	2
<b>D<sub>calc</sub> / mg·m<sup>-3</sup></b>	1.257	1.329	1.277	1.163
<b>Temperature / K</b>	120	120	120	120
<b>No. of reflections measured</b>	49538	69836	108947	41017
<b>No. of independent reflections</b>	11413	5735	6886	6573
<b>Residuals: R</b>	0.0501	0.0388	0.0483	0.0529
<b>Residuals: wR<sup>2</sup></b>	0.1357	0.1072	0.1141	0.1406
<b>Goodness of fit indicator</b>	1.003	1.014	1.004	1.003

Experiment Part

	TAN-N-3,5MePh	TAN-N-2,4,6MePh	TAA-N-Pent
<b>Chemical formula</b>	C <sub>53</sub> H <sub>44</sub> C <sub>16</sub> N <sub>6</sub>	C <sub>54</sub> H <sub>48</sub> N <sub>6</sub>	C <sub>54</sub> H <sub>54</sub> N <sub>6</sub>
<b>Formula weight</b>	977.64	780.98	787.03
<b>Crystal system</b>	Triclinic	Triclinic	Triclinic
<b>Space group</b>	P -1	P -1	P -1
<b>a / Å</b>	10.8447(6)	16.9797(4)	10.3963(5)
<b>b / Å</b>	14.0178(7)	17.5177(4)	11.0575(6)
<b>c / Å</b>	17.9561(9)	18.7234(4)	19.5279(10)
<b>α / °</b>	111.675(2)	63.0140(10)	103.998(2)
<b>β / °</b>	93.971(2)	63.9220(10)	102.593(2)
<b>γ / °</b>	107.870(2)	66.0700(10)	93.541(2)
<b>V / Å<sup>3</sup></b>	2362.3(2)	4307.19(18)	2110.21(19)
<b>Z</b>	2	4	2
<b>D<sub>calc</sub> / mg·m<sup>-3</sup></b>	1.374	1.204	1.239
<b>Temperature / K</b>	120	120	120
<b>No. of reflections measured</b>	57722	201100	41011
<b>No. of independent reflections</b>	9684	15403	7399
<b>Residuals: R</b>	0.0545	0.0456	0.0445
<b>Residuals: wR<sup>2</sup></b>	0.1388	0.1153	0.1155
<b>Goodness of fit indicator</b>	1.007	1.022	1.007

**Table 2.** Crystallographic parameters for TAN-Ph, TAN-MePh, TAA-Ph, TAA-Tips, TAA-OMe-Ph and TAA-tBuPh.

	TAN-Ph	TAN-MePh	TAA-Ph
<b>Chemical formula</b>	C <sub>45</sub> H <sub>27</sub> N <sub>3</sub>	C <sub>48</sub> H <sub>33</sub> N <sub>3</sub>	C <sub>38</sub> H <sub>22</sub> N <sub>2</sub>
<b>Formula weight</b>	609.69	651.77	506.57
<b>Crystal system</b>	Triclinic	Triclinic	Trigonal
<b>Space group</b>	P -1	P -1	R 3 :H
<b>a / Å</b>	11.4220(5)	11.2751(10)	26.890(2)
<b>b / Å</b>	11.8638(6)	12.3505(11)	26.890(2)
<b>c / Å</b>	13.6400(7)	13.4070(12)	9.3703(8)
<b>α / °</b>	115.445(2)	99.461(3)	90
<b>β / °</b>	98.835(2)	92.650(3)	90
<b>γ / °</b>	107.484(2)	108.041(3)	120

Experiment Part

<b>V / Å<sup>3</sup></b>	1503.75(13)	1741.6(3)	5867.6(10)
<b>Z</b>	2	2	9
<b>D<sub>calc</sub> /mg·m<sup>-3</sup></b>	1.347	1.243	1.290
<b>Temperature / K</b>	120	120	120
<b>No. of reflections measured</b>	46762	44512	11458
<b>No. of independent reflections</b>	5703	8436	5457
<b>Residuals: R</b>	0.1159	0.0486	0.0559
<b>Residuals: wR<sup>2</sup></b>	0.1065	0.1159	0.0995
<b>Goodness of fit indicator</b>	1.009	1.026	1.006

	<b>TAA-Tips</b>	<b>TAA-OMePh</b>	<b>TAA-tBuPh</b>
<b>Chemical formula</b>	C <sub>73</sub> H <sub>83</sub> Cl <sub>2</sub> N <sub>3</sub> Si <sub>3</sub>	C <sub>66</sub> H <sub>51</sub> N <sub>3</sub> O <sub>9</sub>	C <sub>81</sub> H <sub>81</sub> N <sub>3</sub>
<b>Formula weight</b>	1157.59	1030.09	1096.48
<b>Crystal system</b>	Monoclinic	Triclinic	Triclinic
<b>Space group</b>	P 21/n	P -1	P -1
<b>a / Å</b>	18.2212(10)	11.2358(6)	14.2405(16)
<b>b / Å</b>	10.4445(5)	15.7124(9)	17.0268(18)
<b>c / Å</b>	33.2572(19)	16.9610(10)	17.130(2)
<b>α / °</b>	90	68.562(2)	118.098(3)
<b>β / °</b>	91.409(2)	84.545(2)	99.825(4)
<b>γ / °</b>	90	75.900(2)	99.093(3)
<b>V / Å<sup>3</sup></b>	6327.3(6)	2703.1(3)	3471.8(7)
<b>Z</b>	4	2	2
<b>D<sub>calc</sub> /mg·m<sup>-3</sup></b>	1.215	1.266	1.049
<b>Temperature / K</b>	120	120	120
<b>No. of reflections measured</b>	98701	89514	
<b>No. of independent reflections</b>	13996	12760	
<b>Residuals: R</b>	0.0649	0.0496	0.0942
<b>Residuals: wR<sup>2</sup></b>	0.1747	0.1164	0.2703
<b>Goodness of fit indicator</b>	1.055	1.009	1.022

**Table 3.** Crystallographic parameters for TAN-Pent-BF<sub>2</sub> and TAA-Pent-BF<sub>2</sub>.

	<b>TAN-Pent- BF<sub>2</sub></b>	<b>TAA-Pent-BF<sub>2</sub></b>
<b>Chemical formula</b>	C <sub>42</sub> H <sub>45</sub> B <sub>3</sub> F <sub>6</sub> N <sub>6</sub>	C <sub>55</sub> H <sub>53</sub> B <sub>3</sub> F <sub>6</sub> N <sub>6</sub>
<b>Formula weight</b>	780.27	1015.36
<b>Crystal system</b>	Triclinic	Orthorhombic
<b>Space group</b>	P -1	P 21 21 21
<b><i>a</i> / Å</b>	11.2452(13)	13.7095(5)
<b><i>b</i> / Å</b>	13.8457(17)	16.1314(4)
<b><i>c</i> / Å</b>	14.2301(18)	21.9916(8)
<b><i>α</i> / °</b>	117.346(3)	90
<b><i>β</i> / °</b>	91.726(4)	90
<b><i>γ</i> / °</b>	100.686(4)	90
<b><i>V</i> / Å<sup>3</sup></b>	1916.9(4)	4863.5(3)
<b><i>Z</i></b>	2	4
<b><i>D</i><sub>calc</sub> / mg·m<sup>-3</sup></b>	1.352	1.387
<b>Temperature / K</b>	120	120
<b>No. of reflections measured</b>	53972	20862
<b>No. of independent reflections</b>	11011	8855
<b>Residuals: <i>R</i></b>	0.0503	0.0426
<b>Residuals: <i>wR</i><sup>2</sup></b>	0.1202	0.1103
<b>Goodness of fit indicator</b>	1.002	1.010



## References

- [1] “Conductors, Insulators, Semiconductors - Fundamentals Semiconductor Technology from A to Z,” can be found under <https://www.halbleiter.org/en/fundamentals/conductors-insulators-semiconductors/>, **2019**.
- [2] “History of semiconductors : Hitachi High-Technologies GLOBAL,” can be found under <https://www.hitachi-hightech.com/global/products/device/semiconductor/history.html>, **2019**.
- [3] H. Kallmann, M. Pope, *J. Chem. Phys.* **1960**, *32*, 300–301.
- [4] H. Kallmann, M. Pope, *Nature* **1960**, *186*, 31.
- [5] H. Shirakawa, E. J. Louis, A. G. MacDiarmid, C. K. Chiang, A. J. Heeger, *J. Chem. Soc. Chem. Commun.* **1977**, *0*, 578–580.
- [6] D. Braga, G. Horowitz, *Adv. Mater.* **2009**, *21*, 1473–1486.
- [7] O. D. Jurchescu, M. Popinciuc, B. J. van Wees, T. T. M. Palstra, *Adv. Mater.* **2007**, *19*, 688–692.
- [8] A. C. Arias, J. D. MacKenzie, I. McCulloch, J. Rivnay, A. Salleo, *Chem. Rev.* **2010**, *110*, 3–24.
- [9] A. Tsumura, H. Koezuka, T. Ando, *Appl. Phys. Lett.* **1986**, *49*, 1210–1212.
- [10] M. Chu, J.-X. Fan, S. Yang, D. Liu, C. F. Ng, H. Dong, A.-M. Ren, Q. Miao, *Adv. Mater.* **2018**, *30*, 1803467.
- [11] Z. Bao, J. Locklin, J. Locklin, *Organic Field-Effect Transistors*, CRC Press, **2018**.
- [12] W.-Y. Sit, S. H. Cheung, C. Y. H. Chan, K. K. Tsung, S. W. Tsang, S. K. So, *Adv. Electron. Mater.* **2016**, *2*, 1500273.
- [13] C. R. Newman, C. D. Frisbie, D. A. da Silva Filho, J.-L. Brédas, P. C. Ewbank, K. R. Mann, *Chem. Mater.* **2004**, *16*, 4436–4451.
- [14] D. Choi, P.-H. Chu, M. McBride, E. Reichmanis, *Chem. Mater.* **2015**, *27*, 4167–4168.
- [15] M. M. Ling, Z. Bao, *Chem. Mater.* **2004**, *16*, 4824–4840.
- [16] Z. A. Lamport, R. Li, C. Wang, W. Mitchell, D. Sparrowe, D.-M. Smilgies, C. Day, V. Coropceanu, O. D. Jurchescu, *J. Mater. Chem. C* **2017**, *5*, 10313–10319.
- [17] H. Li, J.-L. Brédas, *J. Phys. Chem. Lett.* **2018**, *9*, 6550–6555.
- [18] D. M. Chapin, C. S. Fuller, G. L. Pearson, *Lett. Ed.* **1954**, 676–677.
- [19] M. A. Green, Y. Hishikawa, E. D. Dunlop, D. H. Levi, J. Hohl-Ebinger, A. W. Y. Ho-Baillie, *Prog. Photovolt. Res. Appl.* **2018**, *26*, 427–436.
- [20] D. Kearns, M. Calvin, *Lett. Ed.* **1958**, 950–951.
- [21] M. Jørgensen, K. Norrman, S. A. Gevorgyan, T. Tromholt, B. Andreasen, F. C. Krebs, *Adv. Mater.* **2012**, *24*, 580–612.
- [22] W. Zhao, S. Li, H. Yao, S. Zhang, Y. Zhang, B. Yang, J. Hou, *J. Am. Chem. Soc.* **2017**, *139*, 7148–7151.
- [23] U. Opara Krašovec, M. Bokalič, M. Topič, *Sol. Energy Mater. Sol. Cells* **2013**, *117*, 67–72.
- [24] S. Mathew, A. Yella, P. Gao, R. Humphry-Baker, B. F. E. Curchod, N. Ashari-Astani, I. Tavernelli, U. Rothlisberger, M. K. Nazeeruddin, M. Grätzel, *Nat. Chem.* **2014**, *6*, 242–247.
- [25] K. Kakiage, Y. Aoyama, T. Yano, K. Oya, J. Fujisawa, M. Hanaya, *Chem. Commun.* **2015**, *51*, 15894–15897.
- [26] M. M. Lee, J. Teuscher, T. Miyasaka, T. N. Murakami, H. J. Snaith, *Science* **2012**, *338*, 643–

- 647.
- [27] "Photovoltaic Research | NREL," can be found under <https://www.nrel.gov/pv/index.html>, **2019**.
- [28] C. Rodríguez-Seco, L. Cabau, A. Vidal-Ferran, E. Palomares, *Acc. Chem. Res.* **2018**, *51*, 869–880.
- [29] X. Xu, K. Feng, Z. Bi, W. Ma, G. Zhang, Q. Peng, *Adv. Mater.* **2019**, *31*, 1901872.
- [30] B. C. Thompson, J. M. J. Fréchet, *Angew. Chem. Int. Ed.* **2018**, 58–77.
- [31] J. Zhang, Y. Li, H. Hu, G. Zhang, H. Ade, H. Yan, *Chem. Mater.* **2019**, DOI 10.1021/acs.chemmater.9b00980.
- [32] M. Chen, D. Liu, W. Li, R. Gurney, D. Li, J. Cai, E. L. K. Spooner, R. C. Kilbride, J. D. McGettrick, T. M. Watson, Z. Li, R. A. L. Jones, D. G. Lidzey, T. Wang, *ACS Appl. Mater. Interfaces* **2019**, DOI 10.1021/acsami.9b07317.
- [33] D. S. Baranov, O. L. Krivenko, M. S. Kazantsev, D. A. Nevostruev, E. S. Kobeleva, V. A. Zinoviev, A. A. Dmitriev, N. P. Gritsan, L. V. Kulik, *Synth. Met.* **2019**, *255*, 116097.
- [34] C. Sekine, Y. Tsubata, T. Yamada, M. Kitano, S. Doi, *Sci. Technol. Adv. Mater.* **2014**, *15*, 034203.
- [35] M. A. Baldo, D. F. O'Brien, Y. You, A. Shoustikov, S. Sibley, M. E. Thompson, S. R. Forrest, *Nature* **1998**, *395*, 151.
- [36] H. Uoyama, K. Goushi, K. Shizu, H. Nomura, C. Adachi, *Nature* **2012**, *492*, 234–238.
- [37] J.-H. Kwon, R. Pode, *Org. Light Emit. Diode - Mater. Process Devices* **2011**, DOI 10.5772/18521.
- [38] W. Heisenberg, *Z. Für Phys.* **1927**, *43*, 172–198.
- [39] R. S. Mulliken, *Science* **1967**, *157*, 13–24.
- [40] *Wikipedia Aatomic Orbital* **2019**.
- [41] Linus. Pauling, *J. Am. Chem. Soc.* **1931**, *53*, 1367–1400.
- [42] J. D. Dunitz, A. Gavezzotti, *Chem. Soc. Rev.* **2009**, *38*, 2622.
- [43] V. Coropceanu, J. Cornil, D. A. da Silva Filho, Y. Olivier, R. Silbey, J.-L. Brédas, *Chem. Rev.* **2007**, *107*, 926–952.
- [44] X. Zhao, T. Liu, X. Hou, Z. Liu, W. Shi, T. J. S. Dennis, *J. Mater. Chem. C* **2018**, *6*, 5489–5496.
- [45] T. Brixner, J. Stenger, H. M. Vaswani, M. Cho, R. E. Blankenship, G. R. Fleming, *Nature* **2005**, *434*, 625–628.
- [46] Z. Shuai, L. Wang, C. Song, *Theory of Charge Transport in Carbon Electronic Materials*, Springer Science & Business Media, **2012**.
- [47] V. Balzani, A. Juris, M. Venturi, S. Campagna, S. Serroni, *Chem. Rev.* **1996**, *96*, 759–834.
- [48] C. A. Hunter, J. K. M. Sanders, *J. Am. Chem. Soc.* **1990**, *112*, 5525–5534.
- [49] L. Li, Q. Tang, H. Li, X. Yang, W. Hu, Y. Song, Z. Shuai, W. Xu, Y. Liu, D. Zhu, *Adv. Mater.* **2007**, *19*, 2613–2617.
- [50] H. Dong, X. Fu, J. Liu, Z. Wang, W. Hu, *Adv. Mater.* **2013**, *25*, 6158–6183.
- [51] J. E. Anthony, D. L. Eaton, S. R. Parkin, *Org. Lett.* **2002**, *4*, 15–18.
- [52] M. Yamagishi, J. Takeya, Y. Tominari, Y. Nakazawa, T. Kuroda, S. Ikehata, M. Uno, T. Nishikawa, T. Kawase, *Appl. Phys. Lett.* **2007**, *90*, 182117.
- [53] K. Kudo, M. Yamashina, T. Moriizumi, *Jpn. J. Appl. Phys.* **1984**, *23*, 130–130.
- [54] M. Madru, G. Guillaud, M. A. Sadoun, M. Maitrot, C. Clarisse, M. L. Contellec, J.-J. André, J. Simon, *Chem. Phys. Lett.* **1987**, *142*, 103–105.

- [55] J. T. E. Quinn, J. Zhu, X. Li, J. Wang, Y. Li, *J. Mater. Chem. C* **2017**, *5*, 8654–8681.
- [56] A. N. Aleshin, J. Y. Lee, S. W. Chu, J. S. Kim, Y. W. Park, *Appl. Phys. Lett.* **2004**, *84*, 5383–5385.
- [57] X. Zhang, G. Yuan, Q. Li, B. Wang, X. Zhang, R. Zhang, J. C. Chang, C. Lee, S. Lee, *Chem. Mater.* **2008**, *20*, 6945–6950.
- [58] C. Wang, Y. Liu, Z. Ji, E. Wang, R. Li, H. Jiang, Q. Tang, H. Li, W. Hu, *Chem. Mater.* **2009**, *21*, 2840–2845.
- [59] H. Klauk, U. Zschieschang, R. T. Weitz, H. Meng, F. Sun, G. Nunes, D. E. Keys, C. R. Fincher, Z. Xiang, *Adv. Mater.* **2007**, *19*, 3882–3887.
- [60] L. Jiang, W. Hu, Z. Wei, W. Xu, H. Meng, *Adv. Mater.* **2009**, *21*, 3649–3653.
- [61] H. Meng, F. Sun, M. B. Goldfinger, F. Gao, D. J. Londono, W. J. Marshal, G. S. Blackman, K. D. Dobbs, D. E. Keys, *J. Am. Chem. Soc.* **2006**, *128*, 9304–9305.
- [62] M. Chen, L. Yan, Y. Zhao, I. Murtaza, H. Meng, W. Huang, *J. Mater. Chem. C* **2018**, *6*, 7416–7444.
- [63] J. Liu, H. Zhang, H. Dong, L. Meng, L. Jiang, L. Jiang, Y. Wang, J. Yu, Y. Sun, W. Hu, A. J. Heeger, *Nat. Commun.* **2015**, *6*, 10032.
- [64] L. Yan, Y. Zhao, H. Yu, Z. Hu, Y. He, A. Li, O. Goto, C. Yan, T. Chen, R. Chen, Y.-L. Loo, D. F. Perepichka, H. Meng, W. Huang, *J. Mater. Chem. C* **2016**, *4*, 3517–3522.
- [65] A. Li, L. Yan, C. He, Y. Zhu, D. Zhang, I. Murtaza, H. Meng, O. Goto, *J. Mater. Chem. C* **2017**, *5*, 370–375.
- [66] A. Li, L. Yan, M. Liu, I. Murtaza, C. He, D. Zhang, Y. He, H. Meng, *J. Mater. Chem. C* **2017**, *5*, 5304–5309.
- [67] M. E. Hajlaoui, F. Garnier, L. Hassine, F. Kouki, H. Bouchriha, *Synth. Met.* **2002**, *129*, 215–220.
- [68] L. A. Morrison, D. Stanfield, M. Jenkins, A. A. Baronov, D. L. Patrick, J. M. Leger, *Org. Electron.* **2016**, *33*, 269–273.
- [69] C. Reese, W.-J. Chung, M. Ling, M. Roberts, Z. Bao, *Appl. Phys. Lett.* **2006**, *89*, 202108.
- [70] H. Moon, R. Zeis, E.-J. Borkent, C. Besnard, A. J. Lovinger, T. Siegrist, C. Kloc, Z. Bao, *J. Am. Chem. Soc.* **2004**, *126*, 15322–15323.
- [71] X. Chi, D. Li, H. Zhang, Y. Chen, V. Garcia, C. Garcia, T. Siegrist, *Org. Electron.* **2008**, *9*, 234–240.
- [72] M. Yamagishi, J. Takeya, Y. Tominari, Y. Nakazawa, T. Kuroda, S. Ikehata, M. Uno, T. Nishikawa, T. Kawase, *Appl. Phys. Lett.* **2007**, *90*, 182117.
- [73] V. C. Sundar, J. Zaumseil, V. Podzorov, E. Menard, R. L. Willett, T. Someya, M. E. Gershenson, J. A. Rogers, *Science* **2004**, *303*, 1644–1646.
- [74] D. A. da Silva Filho, E.-G. Kim, J.-L. Brédas, *Adv. Mater.* **2005**, *17*, 1072–1076.
- [75] V. Y. Butko, X. Chi, D. V. Lang, A. P. Ramirez, *Appl. Phys. Lett.* **2003**, *83*, 4773–4775.
- [76] L. B. Roberson, J. Kowalik, L. M. Tolbert, C. Kloc, R. Zeis, X. Chi, R. Fleming, C. Wilkins, *J. Am. Chem. Soc.* **2005**, *127*, 3069–3075.
- [77] C. Goldmann, S. Haas, C. Krellner, K. P. Pernstich, D. J. Gundlach, B. Batlogg, *J. Appl. Phys.* **2004**, *96*, 2080–2086.
- [78] O. D. Jurchescu, J. Baas, T. T. M. Palstra, *Appl. Phys. Lett.* **2004**, *84*, 3061–3063.
- [79] M. Wang, J. Li, G. Zhao, Q. Wu, Y. Huang, W. Hu, X. Gao, H. Li, D. Zhu, *Adv. Mater.* **2013**, *25*, 2229–2233.



- [80] J. E. Anthony, J. S. Brooks, D. L. Eaton, S. R. Parkin, *J. Am. Chem. Soc.* **2001**, *123*, 9482–9483.
- [81] J. E. Anthony, D. L. Eaton, S. R. Parkin, *Org. Lett.* **2002**, *4*, 15–18.
- [82] C. D. Sheraw, T. N. Jackson, D. L. Eaton, J. E. Anthony, *Adv. Mater.* **2003**, *15*, 2009–2011.
- [83] D. H. Kim, D. Y. Lee, H. S. Lee, W. H. Lee, Y. H. Kim, J. I. Han, K. Cho, *Adv. Mater.* **2007**, *19*, 678–682.
- [84] S. K. Park, T. N. Jackson, J. E. Anthony, D. A. Mourey, *Appl. Phys. Lett.* **2007**, *91*, 063514.
- [85] S. Wang, S. Zhou, Y. Tong, Z. Song, H. Wang, Q. Tang, X. Zhao, Y. Liu, *Adv. Mater. Interfaces* **2019**, *6*, 1801984.
- [86] J. Dong, P. Yu, S. A. Arabi, J. Wang, J. He, C. Jiang, *Nanotechnology* **2016**, *27*, 275202.
- [87] M. L. Tang, T. Okamoto, Z. Bao, *J. Am. Chem. Soc.* **2006**, *128*, 16002–16003.
- [88] M. L. Tang, S. C. B. Mannsfeld, Y.-S. Sun, H. A. Becerril, Z. Bao, *J. Am. Chem. Soc.* **2009**, *131*, 882–883.
- [89] C. Du, Y. Guo, Y. Liu, W. Qiu, H. Zhang, X. Gao, Y. Liu, T. Qi, K. Lu, G. Yu, *Chem. Mater.* **2008**, *20*, 4188–4190.
- [90] M. L. Tang, A. D. Reichardt, T. Siegrist, S. C. B. Mannsfeld, Z. Bao, *Chem. Mater.* **2008**, *20*, 4669–4676.
- [91] K. Takimiya, H. Ebata, K. Sakamoto, T. Izawa, T. Otsubo, Y. Kunugi, *J. Am. Chem. Soc.* **2006**, *128*, 12604–12605.
- [92] T. Yamamoto, K. Takimiya, *J. Am. Chem. Soc.* **2007**, *129*, 2224–2225.
- [93] S. Haas, Y. Takahashi, K. Takimiya, T. Hasegawa, *Appl. Phys. Lett.* **2009**, *95*, 022111.
- [94] K. Niimi, S. Shinamura, I. Osaka, E. Miyazaki, K. Takimiya, *J. Am. Chem. Soc.* **2011**, *133*, 8732–8739.
- [95] M. M. Payne, S. R. Parkin, J. E. Anthony, C.-C. Kuo, T. N. Jackson, *J. Am. Chem. Soc.* **2005**, *127*, 4986–4987.
- [96] S. Subramanian, S. K. Park, S. R. Parkin, V. Podzorov, T. N. Jackson, J. E. Anthony, *J. Am. Chem. Soc.* **2008**, *130*, 2706–2707.
- [97] R. K. Hallani, K. J. Thorley, Y. Mei, S. R. Parkin, O. D. Jurchescu, J. E. Anthony, *Adv. Funct. Mater.* **2016**, *26*, 2341–2348.
- [98] J. H. Gao, R. J. Li, L. Q. Li, Q. Meng, H. Jiang, H. X. Li, W. P. Hu, *Adv. Mater.* **2007**, *19*, 3008–3011.
- [99] R. Li, H. Dong, X. Zhan, Y. He, H. Li, W. Hu, *J. Mater. Chem.* **2010**, *20*, 6014–6018.
- [100] T. Okamoto, K. Kudoh, A. Wakamiya, S. Yamaguchi, *Org. Lett.* **2005**, *7*, 5301–5304.
- [101] K. Yamada, T. Okamoto, K. Kudoh, A. Wakamiya, S. Yamaguchi, J. Takeya, *Appl. Phys. Lett.* **2007**, *90*, 072102.
- [102] K. Xiao, Y. Liu, T. Qi, W. Zhang, F. Wang, J. Gao, W. Qiu, Y. Ma, G. Cui, S. Chen, X. Zhan, G. Yu, J. Qin, W. Hu, D. Zhu, *J. Am. Chem. Soc.* **2005**, *127*, 13281–13286.
- [103] H. Jiang, X. Yang, Z. Cui, Y. Liu, H. Li, W. Hu, Y. Liu, D. Zhu, *Appl. Phys. Lett.* **2007**, *91*, 123505.
- [104] M. Leufgen, O. Rost, C. Gould, G. Schmidt, J. Geurts, L. W. Molenkamp, N. S. Oxtoby, M. Mas-Torrent, N. Crivillers, J. Veciana, C. Rovira, *Org. Electron.* **2008**, *9*, 1101–1106.
- [105] T. Yamada, R. Kumai, Y. Takahashi, T. Hasegawa, *J. Mater. Chem.* **2010**, *20*, 5810–5812.
- [106] Y. Takahashi, T. Hasegawa, S. Horiuchi, R. Kumai, Y. Tokura, G. Saito, *Chem. Mater.* **2007**, *19*, 6382–6384.
- [107] M. Mas-Torrent, P. Hadley, S. T. Bromley, X. Ribas, J. Tarrés, M. Mas, E. Molins, J. Veciana, C.

- Rovira, *J. Am. Chem. Soc.* **2004**, *126*, 8546–8553.
- [108] Naraso, J. Nishida, S. Ando, J. Yamaguchi, K. Itaka, H. Koinuma, H. Tada, S. Tokito, Y. Yamashita, *J. Am. Chem. Soc.* **2005**, *127*, 10142–10143.
- [109] Z. Bao, A. J. Lovinger, A. Dodabalapur, *Appl. Phys. Lett.* **1996**, *69*, 3066–3068.
- [110] R. Zeis, T. Siegrist, Ch. Kloc, *Appl. Phys. Lett.* **2005**, *86*, 022103.
- [111] L. Li, Q. Tang, H. Li, X. Yang, W. Hu, Y. Song, Z. Shuai, W. Xu, Y. Liu, D. Zhu, *Adv. Mater.* **2007**, *19*, 2613–2617.
- [112] H. Jiang, P. Hu, J. Ye, R. Ganguly, Y. Li, Y. Long, D. Fichou, W. Hu, C. Kloc, *Angew. Chem.* **2018**, *130*, 10269–10274.
- [113] G. Guillaud, M. Al Sadoun, M. Maitrot, J. Simon, M. Bouvet, *Chem. Phys. Lett.* **1990**, *167*, 503–506.
- [114] M. L. Tang, J. H. Oh, A. D. Reichardt, Z. Bao, *J. Am. Chem. Soc.* **2009**, *131*, 3733–3740.
- [115] D. M. de Leeuw, M. M. J. Simenon, A. R. Brown, R. E. F. Einerhand, *Synth. Met.* **1997**, *87*, 53–59.
- [116] A. Facchetti, M.-H. Yoon, C. L. Stern, G. R. Hutchison, M. A. Ratner, T. J. Marks, *J. Am. Chem. Soc.* **2004**, *126*, 13480–13501.
- [117] J. G. Laquindanum, H. E. Katz, A. Dodabalapur, A. J. Lovinger, *J. Am. Chem. Soc.* **1996**, *118*, 11331–11332.
- [118] D. Shukla, S. F. Nelson, D. C. Freeman, M. Rajeswaran, W. G. Ahearn, D. M. Meyer, J. T. Carey, *Chem. Mater.* **2008**, *20*, 7486–7491.
- [119] J. H. Oh, S.-L. Suraru, W.-Y. Lee, M. Könemann, H. W. Höffken, C. Röger, R. Schmidt, Y. Chung, W.-C. Chen, F. Würthner, Z. Bao, *Adv. Funct. Mater.* **2010**, *20*, 2148–2156.
- [120] M. Stolte, M. Gsänger, R. Hofmockel, S.-L. Suraru, F. Würthner, *Phys. Chem. Chem. Phys.* **2012**, *14*, 14181–14185.
- [121] T. He, M. Stolte, F. Würthner, *Adv. Mater.* **2013**, *25*, 6951–6955.
- [122] F. Zhang, Y. Hu, T. Schuettfort, C. Di, X. Gao, C. R. McNeill, L. Thomsen, S. C. B. Mannsfeld, W. Yuan, H. Sirringhaus, D. Zhu, *J. Am. Chem. Soc.* **2013**, *135*, 2338–2349.
- [123] G. Horowitz, F. Kouki, P. Spearman, D. Fichou, C. Noguez, X. Pan, F. Garnier, *Adv. Mater.* **1996**, *8*, 242–245.
- [124] R. J. Chesterfield, J. C. McKeen, C. R. Newman, P. C. Ewbank, D. A. da Silva Filho, J.-L. Brédas, L. L. Miller, K. R. Mann, C. D. Frisbie, *J. Phys. Chem. B* **2004**, *108*, 19281–19292.
- [125] J.-D. Oh, H.-S. Seo, D.-K. Kim, E.-S. Shin, J.-H. Choi, *Org. Electron.* **2012**, *13*, 2192–2200.
- [126] R. Schmidt, J. H. Oh, Y.-S. Sun, M. Deppisch, A.-M. Krause, K. Radacki, H. Braunschweig, M. Könemann, P. Erk, Z. Bao, F. Würthner, *J. Am. Chem. Soc.* **2009**, *131*, 6215–6228.
- [127] J. Soeda, T. Uemura, Y. Mizuno, A. Nakao, Y. Nakazawa, A. Facchetti, J. Takeya, *Adv. Mater.* **2011**, *23*, 3681–3685.
- [128] A. S. Molinari, H. Alves, Z. Chen, A. Facchetti, A. F. Morpurgo, *J. Am. Chem. Soc.* **2009**, *131*, 2462–2463.
- [129] Z. Bao, A. J. Lovinger, J. Brown, *J. Am. Chem. Soc.* **1998**, *120*, 207–208.
- [130] Q. Tang, Y. Tong, H. Li, W. Hu, *Appl. Phys. Lett.* **2008**, *92*, 083309.
- [131] X. Shao, S. Wang, X. Li, Z. Su, Y. Chen, Y. Xiao, *Dyes Pigments* **2016**, *132*, 378–386.
- [132] M. Ichikawa, T. Kato, T. Uchino, T. Tsuzuki, M. Inoue, H.-G. Jeon, T. Koyama, Y. Taniguchi, *Org. Electron.* **2010**, *11*, 1549–1554.
- [133] M.-H. Yoon, C. Kim, A. Facchetti, T. J. Marks, *J. Am. Chem. Soc.* **2006**, *128*, 12851–12869.

- [134] M. Minarul Islam, S. Pola, Y.-T. Tao, *Chem. Commun.* **2011**, 47, 6356–6358.
- [135] Z. Liang, Q. Tang, J. Xu, Q. Miao, *Adv. Mater.* **2011**, 23, 1535–1539.
- [136] Z. Liang, Q. Tang, R. Mao, D. Liu, J. Xu, Q. Miao, *Adv. Mater.* **2011**, 23, 5514–5518.
- [137] X. Xu, Y. Yao, B. Shan, X. Gu, D. Liu, J. Liu, J. Xu, N. Zhao, W. Hu, Q. Miao, *Adv. Mater.* **2016**, 28, 5276–5283.
- [138] G. Xue, J. Wu, C. Fan, S. Liu, Z. Huang, Y. Liu, B. Shan, H. L. Xin, Q. Miao, H. Chen, H. Li, *Mater. Horiz.* **2016**, 3, 119–123.
- [139] Y. Nicolas, F. Castet, M. Devynck, P. Tardy, L. Hirsch, C. Labrugère, H. Allouchi, T. Toupance, *Org. Electron.* **2012**, 13, 1392–1400.
- [140] G. Gruntz, H. Lee, L. Hirsch, F. Castet, T. Toupance, A. L. Briseno, Y. Nicolas, *Adv. Electron. Mater.* **2015**, 1, 1500072.
- [141] J.-H. Dou, Y.-Q. Zheng, Z.-F. Yao, T. Lei, X. Shen, X.-Y. Luo, Z.-A. Yu, S.-D. Zhang, G. Han, Z. Wang, Y. Yi, J.-Y. Wang, J. Pei, *Adv. Mater.* **2015**, 27, 8051–8055.
- [142] H. W. Kroto, J. R. Heath, S. C. O'Brien, R. F. Curl, R. E. Smalley, *Nature* **1985**, 318, 162.
- [143] R. C. Haddon, A. S. Perel, R. C. Morris, T. T. M. Palstra, A. F. Hebard, R. M. Fleming, *Appl. Phys. Lett.* **1995**, 67, 121–123.
- [144] H. Li, B. C.-K. Tee, J. J. Cha, Y. Cui, J. W. Chung, S. Y. Lee, Z. Bao, *J. Am. Chem. Soc.* **2012**, 134, 2760–2765.
- [145] K.-Y. Wu, T.-Y. Wu, S.-T. Chang, C.-S. Hsu, C.-L. Wang, *Adv. Mater.* **2015**, 27, 4371–4376.
- [146] A. A. Popov, S. Yang, L. Dunsch, *Chem. Rev.* **2013**, 113, 5989–6113.
- [147] M. L. Tang, A. D. Reichardt, N. Miyaki, R. M. Stoltenberg, Z. Bao, *J. Am. Chem. Soc.* **2008**, 130, 6064–6065.
- [148] H. Nakanotani, M. Saito, H. Nakamura, C. Adachi, *Appl. Phys. Lett.* **2009**, 95, 033308.
- [149] L. Tan, Y. Guo, Y. Yang, G. Zhang, D. Zhang, G. Yu, W. Xu, Y. Liu, *Chem. Sci.* **2012**, 3, 2530–2541.
- [150] K. A. McGarry, W. Xie, C. Sutton, C. Risko, Y. Wu, V. G. Young, J.-L. Brédas, C. D. Frisbie, C. J. Douglas, *Chem. Mater.* **2013**, 25, 2254–2263.
- [151] W. Xie, P. L. Prabhumirashi, Y. Nakayama, K. A. McGarry, M. L. Geier, Y. Urugami, K. Mase, C. J. Douglas, H. Ishii, M. C. Hersam, C. D. Frisbie, *ACS Nano* **2013**, 7, 10245–10256.
- [152] X. Zhu, Y. Zhang, X. Ren, J. Yao, S. Guo, L. Zhang, D. Wang, G. Wang, X. Zhang, R. Li, W. Hu, *Small* **0**, 1902187.
- [153] P. R. Warren, J. F. M. Hardigree, A. E. Lauritzen, J. Nelson, M. Riede, *AIP Adv.* **2019**, 9, 035202.
- [154] J. C. Ribierre, L. Zhao, S. Furukawa, T. Kikitsu, D. Inoue, A. Muranaka, K. Takaishi, T. Muto, S. Matsumoto, D. Hashizume, M. Uchiyama, P. André, C. Adachi, T. Aoyama, *Chem. Commun.* **2015**, 51, 5836–5839.
- [155] P. J. Skabara, J.-B. Arlin, Y. H. Geerts, *Adv. Mater.* **2013**, 25, 1948–1954.
- [156] S. Sergeev, W. Pisula, Y. Henri Geerts, *Chem. Soc. Rev.* **2007**, 36, 1902–1929.
- [157] T. Wöhrlé, I. Wurzbach, J. Kirres, A. Kostidou, N. Kapernaum, J. Litterscheidt, J. C. Haenle, P. Staffeld, A. Baro, F. Giesselmann, S. Laschat, *Chem. Rev.* **2016**, 116, 1139–1241.
- [158] J. E. Anthony, *Chem. Rev.* **2006**, 106, 5028–5048.
- [159] W. Wu, Y. Liu, D. Zhu, *Chem. Soc. Rev.* **2010**, 39, 1489–1502.
- [160] K. I. Bolotin, K. J. Sikes, Z. Jiang, M. Klima, G. Fudenberg, J. Hone, P. Kim, H. L. Stormer, *Solid State Commun.* **2008**, 146, 351–355.

- [161] D. Adam, P. Schuhmacher, J. Simmerer, L. Häussling, K. Siemensmeyer, K. H. Etzbachi, H. Ringsdorf, D. Haarer, *Nature* **1994**, *371*, 141.
- [162] K. Lin, B. Xie, Z. Wang, R. Xie, Y. Huang, C. Duan, F. Huang, Y. Cao, *Org. Electron.* **2018**, *52*, 42–50.
- [163] Y. M. Sun, K. Xiao, Y. Q. Liu, J. L. Wang, J. Pei, G. Yu, D. B. Zhu, *Adv. Funct. Mater.* **2005**, *15*, 818–822.
- [164] R. Juárez, M. M. Oliva, M. Ramos, J. L. Segura, C. Alemán, F. Rodríguez-Ropero, D. Curcó, F. Montilla, V. Coropceanu, J. L. Brédas, Y. Qi, A. Kahn, M. C. Ruiz Delgado, J. Casado, J. T. López Navarrete, *Chem. - Eur. J.* **2011**, *17*, 10312–10322.
- [165] M. Lehmann, G. Kestemont, R. G. Aspe, C. Buess-Herman, M. H. J. Koch, M. G. Debije, J. Piris, M. P. de Haas, J. M. Warman, M. D. Watson, V. Lemaire, J. Cornil, Y. H. Geerts, R. Gearba, D. A. Ivanov, *Chem. - Eur. J.* **2005**, *11*, 3349–3362.
- [166] M. Oukachmih, P. Destruel, I. Seguy, G. Ablart, P. Jolinat, S. Archambeau, M. Mabilia, S. Fouet, H. Bock, *Sol. Energy Mater. Sol. Cells* **2005**, *85*, 535–543.
- [167] A. M. van de Craats, J. M. Warman, A. Fechtenkötter, J. D. Brand, M. A. Harbison, K. Müllen, *Adv. Mater.* **1999**, *11*, 1469–1472.
- [168] L. Li, S. Zhao, B. Li, L. Xu, C. Li, J. Shi, H. Wang, *Org. Lett.* **2018**, DOI 10.1021/acs.orglett.8b00482.
- [169] S. A. Ponomarenko, S. Kirchmeyer, A. Elschner, B.-H. Huisman, A. Karbach, D. Drechsler, *Adv. Funct. Mater.* **2003**, *13*, 591–596.
- [170] A. Mishra, C.-Q. Ma, P. Bäuerle, *Chem. Rev.* **2009**, *109*, 1141–1276.
- [171] S. F. Acquah, A. V. Penkova, D. A. Markelov, A. S. Semisalova, B. E. Leonhardt, J. M. Magi, *ECS J. Solid State Sci. Technol.* **2017**, *6*, M3155–M3162.
- [172] P. A. Heiney, J. E. Fischer, A. R. McGhie, W. J. Romanow, A. M. Denenstein, J. P. McCauley Jr., A. B. Smith, D. E. Cox, *Phys. Rev. Lett.* **1991**, *66*, 2911–2914.
- [173] Y. Shirota, *J. Mater. Chem.* **2005**, *15*, 75–93.
- [174] H. Ohishi, M. Tanaka, H. Kageyama, Y. Shirota, *Chem. Lett.* **2004**, *33*, 1266–1267.
- [175] A. Cravino, S. Roquet, O. Alévêque, P. Leriche, P. Frère, J. Roncali, *Chem. Mater.* **2006**, *18*, 2584–2590.
- [176] M. Saliba, T. Matsui, K. Domanski, J.-Y. Seo, A. Ummadisingu, S. M. Zakeeruddin, J.-P. Correa-Baena, W. R. Tress, A. Abate, A. Hagfeldt, M. Grätzel, *Science* **2016**, *354*, 206–209.
- [177] M. Zhang, G. Wang, D. Zhao, C. Huang, H. Cao, M. Chen, *Chem. Sci.* **2017**, *8*, 7807–7814.
- [178] C. Yin, J. Lu, Y. Xu, Y. Yun, K. Wang, J. Li, L. Jiang, J. Sun, A. D. Scully, F. Huang, J. Zhong, J. Wang, Y.-B. Cheng, T. Qin, W. Huang, *Adv. Energy Mater.* **2018**, *8*, 1800538.
- [179] C. Wu, T.-L. Liu, W.-Y. Hung, Y.-T. Lin, K.-T. Wong, R.-T. Chen, Y.-M. Chen, Y.-Y. Chien, *J. Am. Chem. Soc.* **2003**, *125*, 3710–3711.
- [180] H. Li, Y.-J. Hwang, B. A. E. Courtright, F. N. Eberle, S. Subramaniam, S. A. Jenekhe, *Adv. Mater.* **2015**, *27*, 3266–3272.
- [181] H. Li, T. Earmme, G. Ren, A. Saeki, S. Yoshikawa, N. M. Murari, S. Subramaniam, M. J. Crane, S. Seki, S. A. Jenekhe, *J. Am. Chem. Soc.* **2014**, *136*, 14589–14597.
- [182] I. Aujard, J.-P. Baltaze, J.-B. Baudin, E. Cogné, F. Ferrage, L. Jullien, É. Perez, V. Prévost, L. M. Qian, O. Ruel, *J. Am. Chem. Soc.* **2001**, *123*, 8177–8188.
- [183] L. M. Wilson, A. C. Griffin, *J. Mater. Chem.* **1993**, *3*, 991–994.
- [184] X.-M. Liu, C. He, J. Huang, *Tetrahedron Lett.* **2004**, *45*, 6173–6177.

## Reference

---

- [185] P. Ganesan, X. Yang, J. Loos, T. J. Savenije, R. D. Abellon, H. Zuilhof, E. J. R. Sudhölter, *J. Am. Chem. Soc.* **2005**, *127*, 14530–14531.
- [186] J. Roncali, C. Thobie-Gautier, H. Brisset, J.-F. Favart, A. Guy, *J. Electroanal. Chem.* **1995**, *381*, 257–260.
- [187] S. Roquet, R. de Bettignies, P. Leriche, A. Cravino, J. Roncali, *J. Mater. Chem.* **2006**, *16*, 3040.
- [188] B. Fraboni, C. Femoni, I. Mencarelli, L. Setti, R. Di Pietro, A. Cavallini, A. Fraleoni-Morgera, *Adv. Mater.* **2009**, *21*, 1835–1839.
- [189] D. Meng, H. Fu, C. Xiao, X. Meng, T. Winands, W. Ma, W. Wei, B. Fan, L. Huo, N. L. Doltsinis, Y. Li, Y. Sun, Z. Wang, *J. Am. Chem. Soc.* **2016**, *138*, 10184–10190.
- [190] L. Jiang, J. Gao, E. Wang, H. Li, Z. Wang, W. Hu, L. Jiang, *Adv. Mater.* **2008**, *20*, 2735–2740.
- [191] F. K.-C. Leung, F. Ishiwari, T. Kajitani, Y. Shoji, T. Hikima, M. Takata, A. Saeki, S. Seki, Y. M. A. Yamada, T. Fukushima, *J. Am. Chem. Soc.* **2016**, *138*, 11727–11733.
- [192] N. Seiki, Y. Shoji, T. Kajitani, F. Ishiwari, A. Kosaka, T. Hikima, M. Takata, T. Someya, T. Fukushima, *Science* **2015**, *348*, 1122–1126.
- [193] F. Yang, S. Cheng, X. Zhang, X. Ren, R. Li, H. Dong, W. Hu, *Adv. Mater.* **2018**, *30*, 1702415.
- [194] K. Takimiya, M. Nakano, H. Sugino, I. Osaka, *Synth. Met.* **2016**, *217*, 68–78.
- [195] R. T. Weitz, K. Amsharov, U. Zschieschang, M. Burghard, M. Jansen, M. Kelsch, B. Rhamati, P. A. van Aken, K. Kern, H. Klauk, *Chem. Mater.* **2009**, *21*, 4949–4954.
- [196] R. J. Kline, D. M. DeLongchamp, D. A. Fischer, E. K. Lin, M. Heeney, I. McCulloch, M. F. Toney, *Appl. Phys. Lett.* **2007**, *90*, 062117.
- [197] K. C. Dickey, J. E. Anthony, Y.-L. Loo, *Adv. Mater.* **2006**, *18*, 1721–1726.
- [198] H. N. Tsao, D. Cho, J. W. Andreasen, A. Rouhanipour, D. W. Breiby, W. Pisula, K. Müllen, *Adv. Mater.* **2009**, *21*, 209–212.
- [199] A. Zen, J. Pflaum, S. Hirschmann, W. Zhuang, F. Jaiser, U. Asawapirom, J. P. Rabe, U. Scherf, D. Neher, *Adv. Funct. Mater.* **2004**, *14*, 757–764.
- [200] J. E. Anthony, J. S. Brooks, D. L. Eaton, S. R. Parkin, *J. Am. Chem. Soc.* **2001**, *123*, 9482–9483.
- [201] R. C. Haddon, X. Chi, M. E. Itkis, J. E. Anthony, D. L. Eaton, T. Siegrist, C. C. Mattheus, T. T. M. Palstra, *J. Phys. Chem. B* **2002**, *106*, 8288–8292.
- [202] C. W. Sele, B. K. C. Kjellander, B. Niesen, M. J. Thornton, J. B. P. H. van der Putten, K. Myny, H. J. Wondergem, A. Moser, R. Resel, A. J. J. M. van Breemen, N. van Aerle, P. Heremans, J. E. Anthony, G. H. Gelinck, *Adv. Mater.* **2009**, *21*, 4926–4931.
- [203] J. Wade, F. Steiner, D. Niedzialek, D. T. James, Y. Jung, D.-J. Yun, D. D. C. Bradley, J. Nelson, J.-S. Kim, *J. Mater. Chem. C* **2014**, *2*, 10110–10115.
- [204] L. Zhang, Y. Cao, N. S. Colella, Y. Liang, J.-L. Brédas, K. N. Houk, A. L. Briseno, *Acc. Chem. Res.* **2015**, *48*, 500–509.
- [205] T. Lei, Y. Zhou, C.-Y. Cheng, Y. Cao, Y. Peng, J. Bian, J. Pei, *Org. Lett.* **2011**, *13*, 2642–2645.
- [206] X. Xu, Y. Yao, B. Shan, X. Gu, D. Liu, J. Liu, J. Xu, N. Zhao, W. Hu, Q. Miao, *Adv. Mater.* **2016**, *28*, 5276–5283.
- [207] Y. Shu, G. E. Collis, C. J. Dunn, P. Kemppinen, K. N. Winzenberg, R. M. Williamson, A. Bilic, T. Birendra Singh, M. Bown, C. R. McNeill, L. Thomsen, *J. Mater. Chem. C* **2013**, *1*, 6299–6307.
- [208] J. L. Segura, R. Juárez, M. Ramos, C. Seoane, *Chem Soc Rev* **2015**, *44*, 6850–6885.
- [209] E. C. Rüdiger, M. Porz, M. Schaffroth, F. Rominger, U. H. F. Bunz, *Chem. - Eur. J.* **2014**, *20*,

- 12725–12728.
- [210] J. Li, S. Chen, P. Zhang, Z. Wang, G. Long, R. Ganguly, Y. Li, Q. Zhang, *Chem. - Asian J.* **2016**, *11*, 136–140.
- [211] B. Purushothaman, M. Bruzek, S. R. Parkin, A.-F. Miller, J. E. Anthony, *Angew. Chem. Int. Ed.* **2011**, *50*, 7013–7017.
- [212] M. M. Payne, S. A. Odom, S. R. Parkin, J. E. Anthony, *Org. Lett.* **2004**, *6*, 3325–3328.
- [213] P. T. Lynett, K. E. Maly, *Org. Lett.* **2009**, *11*, 3726–3729.
- [214] C. W. Ong, S.-C. Liao, T. H. Chang, H.-F. Hsu, *J. Org. Chem.* **2004**, *69*, 3181–3185.
- [215] B. Kohne, K. Praefcke, *Liebigs Ann. Chem.* **1985**, *1985*, 522–528.
- [216] N. Saettel, N. Katsonis, A. Marchenko, M.-P. Teulade-Fichou, D. Fichou, *J. Mater. Chem.* **2005**, *15*, 3175.
- [217] H. Bertrand, A. Granzhan, D. Monchaud, N. Saettel, R. Guillot, S. Clifford, A. Guédin, J.-L. Mergny, M.-P. Teulade-Fichou, *Chem. - Eur. J.* **2011**, *17*, 4529–4539.
- [218] H. Bertrand, R. Guillot, M.-P. Teulade-Fichou, D. Fichou, *Chem. - Eur. J.* **2013**, *19*, 14654–14664.
- [219] J. F. Araneda, W. E. Piers, B. Heyne, M. Parvez, R. McDonald, *Angew. Chem. Int. Ed.* **2011**, *50*, 12214–12217.
- [220] A. A. Taherpour, D. Kvaskoff, P. V. Bernhardt, C. Wentrup, *J. Phys. Org. Chem.* **2010**, n/a-n/a.
- [221] H. B. Maurice, R. Phillips, N. Karodia, *Afr. J. Pharm. Pharmacol.* **2009**, *3*, 602–610.
- [222] C. C. Price, V. Boekelheide, *J. Am. Chem. Soc.* **1946**, *68*, 1246–1250.
- [223] W. R. Wilson, R. F. Anderson, W. A. Denny, *J. Med. Chem.* **1989**, *32*, 23–30.
- [224] Q.-L. Luo, L. Lv, Y. Li, J.-P. Tan, W. Nan, Q. Hui, *Eur. J. Org. Chem.* **2011**, *2011*, 6916–6922.
- [225] C. M. Cardona, W. Li, A. E. Kaifer, D. Stockdale, G. C. Bazan, *Adv. Mater.* **2011**, *23*, 2367–2371.
- [226] N. G. Connelly, W. E. Geiger, *Chem. Rev.* **1996**, *96*, 877–910.
- [227] M. J. Frisch, G. W. Trucks, H. B. Schlegel, G. E. Scuseria, M. A. Robb, J. R. Cheeseman, G. Scalmani, V. Barone, B. Mennucci, G. A. Petersson, *Gaussian 09 Revis. 01 Gaussian Wallingford CT* **2009**.
- [228] M. L. Tang, Z. Bao, *Chem. Mater.* **2011**, *23*, 446–455.
- [229] S. Kazim, M. K. Nazeeruddin, M. Grätzel, S. Ahmad, *Angew. Chem. Int. Ed.* **2014**, *53*, 2812–2824.
- [230] J. Burschka, N. Pellet, S.-J. Moon, R. Humphry-Baker, P. Gao, M. K. Nazeeruddin, M. Grätzel, *Nature* **2013**, *499*, 316–319.
- [231] W. S. Yang, B.-W. Park, E. H. Jung, N. J. Jeon, Y. C. Kim, D. U. Lee, S. S. Shin, J. Seo, E. K. Kim, J. H. Noh, S. I. Seok, *Science* **2017**, *356*, 1376–1379.
- [232] M. A. Green, E. D. Dunlop, D. H. Levi, J. Hohl-Ebinger, M. Yoshita, A. W. Y. Ho-Baillie, *Prog. Photovolt. Res. Appl.* **2019**, *27*, 565–575.
- [233] C. S. Ponseca, T. J. Savenije, M. Abdellah, K. Zheng, A. Yartsev, T. Pascher, T. Harlang, P. Chabera, T. Pullerits, A. Stepanov, J.-P. Wolf, V. Sundström, *J. Am. Chem. Soc.* **2014**, *136*, 5189–5192.
- [234] S. D. Stranks, G. E. Eperon, G. Grancini, C. Menelaou, M. J. P. Alcocer, T. Leijtens, L. M. Herz, A. Petrozza, H. J. Snaith, *Science* **2013**, *342*, 341–344.
- [235] P. Gao, M. Grätzel, M. K. Nazeeruddin, *Energy Environ. Sci.* **2014**, *7*, 2448–2463.
- [236] A. Kojima, K. Teshima, Y. Shirai, T. Miyasaka, *J. Am. Chem. Soc.* **2009**, *131*, 6050–6051.

- [237] M. M. Lee, J. Teuscher, T. Miyasaka, T. N. Murakami, H. J. Snaith, *Science* **2012**, *338*, 643–647.
- [238] S. D. Stranks, H. J. Snaith, *Nat. Nanotechnol.* **2015**, *10*, 391–402.
- [239] H.-S. Kim, C.-R. Lee, J.-H. Im, K.-B. Lee, T. Moehl, A. Marchioro, S.-J. Moon, R. Humphry-Baker, J.-H. Yum, J. E. Moser, M. Grätzel, N.-G. Park, *Sci. Rep.* **2012**, *2*, 591.
- [240] M. Liu, M. B. Johnston, H. J. Snaith, *Nature* **2013**, *501*, 395–398.
- [241] K. Rakstys, A. Abate, M. I. Dar, P. Gao, V. Jankauskas, G. Jacopin, E. Kamarauskas, S. Kazim, S. Ahmad, M. Grätzel, M. K. Nazeeruddin, *J. Am. Chem. Soc.* **2015**, *137*, 16172–16178.
- [242] F. Zhang, C. Yi, P. Wei, X. Bi, J. Luo, G. Jacopin, S. Wang, X. Li, Y. Xiao, S. M. Zakeeruddin, M. Grätzel, *Adv. Energy Mater.* **2016**, *6*, 1600401.
- [243] Y.-K. Wang, Z.-C. Yuan, G.-Z. Shi, Y.-X. Li, Q. Li, F. Hui, B.-Q. Sun, Z.-Q. Jiang, L.-S. Liao, *Adv. Funct. Mater.* **2016**, *26*, 1375–1381.
- [244] S. Paek, P. Qin, Y. Lee, K. T. Cho, P. Gao, G. Grancini, E. Oveisi, P. Gratia, K. Rakstys, S. A. Al-Muhtaseb, C. Ludwig, J. Ko, M. K. Nazeeruddin, *Adv. Mater.* **2017**, *29*, n/a-n/a.
- [245] T. P. I. Saragi, T. Spehr, A. Siebert, T. Fuhrmann-Lieker, J. Salbeck, *Chem. Rev.* **2007**, *107*, 1011–1065.
- [246] M. L. Petrus, T. Bein, T. J. Dingemans, P. Docampo, *J. Mater. Chem. A* **2015**, *3*, 12159–12162.
- [247] P. Liu, B. Xu, Y. Hua, M. Cheng, K. Aitola, K. Sveinbjörnsson, J. Zhang, G. Boschloo, L. Sun, L. Kloo, *J. Power Sources* **2017**, *344*, 11–14.
- [248] A. Binek, M. L. Petrus, N. Huber, H. Bristow, Y. Hu, T. Bein, P. Docampo, *ACS Appl. Mater. Interfaces* **2016**, *8*, 12881–12886.
- [249] D. Li, J. Shi, Y. Xu, Y. Luo, H. Wu, Q. Meng, *Natl. Sci. Rev.* **2018**, *5*, 559–576.
- [250] S. Lv, L. Han, J. Xiao, L. Zhu, J. Shi, H. Wei, Y. Xu, J. Dong, X. Xu, D. Li, S. Wang, Y. Luo, Q. Meng, X. Li, *Chem. Commun.* **2014**, *50*, 6931–6934.
- [251] Q. Wang, Q. Dong, T. Li, A. Gruverman, J. Huang, *Adv. Mater.* **2016**, *28*, 6734–6739.
- [252] B. Xu, D. Bi, Y. Hua, P. Liu, M. Cheng, M. Grätzel, L. Kloo, A. Hagfeldt, L. Sun, *Energy Environ. Sci.* **2016**, *9*, 873–877.
- [253] C. Hoong Teh, R. Daik, E. Liang Lim, C. Chin Yap, M. Adib Ibrahim, N. Ahmad Ludin, K. Sopian, M. A. M. Teridi, *J. Mater. Chem. A* **2016**, *4*, 15788–15822.
- [254] F. Zhang, Z. Wang, H. Zhu, N. Pellet, J. Luo, C. Yi, X. Liu, H. Liu, S. Wang, X. Li, Y. Xiao, S. M. Zakeeruddin, D. Bi, M. Grätzel, *Nano Energy* **2017**, *41*, 469–475.
- [255] J. Zhang, B. Xu, L. Yang, C. Ruan, L. Wang, P. Liu, W. Zhang, N. Vlachopoulos, L. Kloo, G. Boschloo, L. Sun, A. Hagfeldt, E. M. J. Johansson, *Adv. Energy Mater.* **2018**, *8*, 1701209.
- [256] S. Lv, Y. Song, J. Xiao, L. Zhu, J. Shi, H. Wei, Y. Xu, J. Dong, X. Xu, S. Wang, Y. Xiao, Y. Luo, D. Li, X. Li, Q. Meng, *Electrochimica Acta* **2015**, *182*, 733–741.
- [257] B. Xu, D. Bi, Y. Hua, P. Liu, M. Cheng, M. Grätzel, L. Kloo, A. Hagfeldt, L. Sun, *Energy Environ. Sci.* **2016**, *9*, 873–877.
- [258] M. Cheng, B. Xu, C. Chen, X. Yang, F. Zhang, Q. Tan, Y. Hua, L. Kloo, L. Sun, *Adv. Energy Mater.* **2015**, *5*, 1401720.
- [259] B. Xu, J. Zhang, Y. Hua, P. Liu, L. Wang, C. Ruan, Y. Li, G. Boschloo, E. M. J. Johansson, L. Kloo, A. Hagfeldt, A. K.-Y. Jen, L. Sun, *Chem* **2017**, *2*, 676–687.
- [260] F. Zhang, C. Yi, P. Wei, X. Bi, J. Luo, G. Jacopin, S. Wang, X. Li, Y. Xiao, S. M. Zakeeruddin, M. Grätzel, *Adv. Energy Mater.* **2016**, *6*, 1600401.

- [261] X. Liu, X. Ding, Y. Ren, Y. Yang, Y. Ding, X. Liu, A. Alsaedi, T. Hayat, J. Yao, S. Dai, *J. Mater. Chem. C* **2018**, *6*, 12912–12918.
- [262] M. S. Kang, S. D. Sung, I. T. Choi, H. Kim, M. Hong, J. Kim, W. I. Lee, H. K. Kim, *ACS Appl. Mater. Interfaces* **2015**, *7*, 22213–22217.
- [263] K. Do, H. Choi, K. Lim, H. Jo, J. W. Cho, M. K. Nazeeruddin, J. Ko, *Chem. Commun.* **2014**, *50*, 10971–10974.
- [264] H. Zhang, J. Shi, X. Xu, L. Zhu, Y. Luo, D. Li, Q. Meng, *J. Mater. Chem. A* **2016**, *4*, 15383–15389.
- [265] Y. Wang, T.-S. Su, H.-Y. Tsai, T.-C. Wei, Y. Chi, *Sci. Rep.* **2017**, *7*, 7859.
- [266] A. Treibs, F.-H. Kreuzer, *Justus Liebig's Ann. Chem.* **1968**, *718*, 208–223.
- [267] N. Boens, V. Leen, W. Dehaen, *Chem. Soc. Rev.* **2012**, *41*, 1130–1172.
- [268] A. Loudet, K. Burgess, *Chem. Rev.* **2007**, *107*, 4891–4932.
- [269] F. Qiu, F. Zhang, R. Tang, Y. Fu, X. Wang, S. Han, X. Zhuang, X. Feng, *Org. Lett.* **2016**, *18*, 1398–1401.
- [270] M. A. Squillaci, F. Qiu, A. Aliprandi, F. Zhang, X. Feng, P. Samorì, *Adv. Mater.* **2016**, *28*, 5249–5254.
- [271] B. M. Bell, T. P. Clark, T. S. De Vries, Y. Lai, D. S. Laitar, T. J. Gallagher, J.-H. Jeon, K. L. Kearns, T. McIntire, S. Mukhopadhyay, H.-Y. Na, T. D. Paine, A. A. Rachford, *Dyes Pigments* **2017**, *141*, 83–92.
- [272] Y. Yang, X. Su, C. N. Carroll, I. Aprahamian, *Chem. Sci.* **2012**, *3*, 610–613.
- [273] M. Mamada, K. Inada, T. Komino, W. J. Potscavage, H. Nakanotani, C. Adachi, *ACS Cent. Sci.* **2017**, *3*, 769–777.
- [274] Y. Liu, C. Li, Z. Ren, S. Yan, M. R. Bryce, *Nat. Rev. Mater.* **2018**, *3*, 18020.
- [275] J. E. Kwon, S. Y. Park, *Adv. Mater.* **2011**, *23*, 3615–3642.
- [276] V. S. Padalkar, S. Seki, *Chem. Soc. Rev.* **2016**, *45*, 169–202.
- [277] L. Salem, *J. Chem. Phys.* **1962**, *37*, 2100–2113.
- [278] Ivo. Tjburg, Jacek. Jagiello, Alain. Vidal, Eugene. Papirer, *Langmuir* **1991**, *7*, 2243–2247.
- [279] M. O. Sinnokrot, E. F. Valeev, C. D. Sherrill, *J. Am. Chem. Soc.* **2002**, *124*, 10887–10893.
- [280] F. R. Ahmed, J. Trotter, *Acta Crystallogr.* **1963**, *16*, 503–508.
- [281] P. J. G. Saris, M. E. Thompson, *Org. Lett.* **2016**, *18*, 3960–3963.
- [282] M. Tonelli, G. Vettoretti, B. Tasso, F. Novelli, V. Boido, F. Sparatore, B. Busonera, A. Ouhtit, P. Farci, S. Blois, G. Giliberti, P. La Colla, *Antiviral Res.* **2011**, *91*, 133–141.
- [283] R. Kalirajan, V. Kulshrestha, S. Sankar, S. Jubie, *Eur. J. Med. Chem.* **2012**, *56*, 217–224.
- [284] A. R. Benoit, C. Schiaffo, C. E. Salomon, J. R. Goodell, H. Hiasa, D. M. Ferguson, *Bioorg. Med. Chem. Lett.* **2014**, *24*, 3014–3017.
- [285] C. Teixeira, N. Vale, B. Pérez, A. Gomes, J. R. B. Gomes, P. Gomes, *Chem. Rev.* **2014**, *114*, 11164–11220.
- [286] A. Kumar, N. Kumar, P. Roy, S. M. Sondhi, A. Sharma, *Med. Chem. Res.* **2015**, *24*, 3272–3282.
- [287] C. D. Geddes, *Dyes Pigments* **2000**, *45*, 243–251.
- [288] A. K. Cook, M. H. Emmert, M. S. Sanford, *Org. Lett.* **2013**, *15*, 5428–5431.
- [289] X.-J. Jiang, Y. Fu, L.-H. Xu, H.-L. Lu, S.-Q. Zang, M.-S. Tang, T. C. W. Mak, *Sens. Actuators B Chem.* **2014**, *202*, 388–394.
- [290] H. Karaca, İ. Şişman, E. Güzel, S. Sezer, F. Selimoğlu, B. Ergezen, M. Karaca, V. Eyüpoğlu, *J.*



- Coord. Chem.* **2018**, *71*, 1606–1622.
- [291] A. Bernthsen, *Zur Kenntniss der Amidine und Thiamide einbasischer organischer Säuren: Habilit. Schrift*, Neusser, **1878**.
- [292] A. Bernthsen, *Justus Liebigs Ann. Chem.* **1884**, *224*, 1–56.
- [293] F. D. Popp, *J. Org. Chem.* **1962**, *27*, 2658–2659.
- [294] D. C. Rogness, R. C. Larock, *J. Org. Chem.* **2010**, *75*, 2289–2295.
- [295] X. Pang, Z. Lou, M. Li, L. Wen, C. Chen, *Eur. J. Org. Chem.* **2015**, *2015*, 3361–3369.
- [296] D. Tselikhovsky, S. L. Buchwald, *J. Am. Chem. Soc.* **2010**, *132*, 14048–14051.
- [297] Z. Huang, Y. Yang, Q. Xiao, Y. Zhang, J. Wang, *Eur. J. Org. Chem.* **2012**, *2012*, 6586–6593.
- [298] H.-M. Guo, R.-Z. Mao, Q.-T. Wang, H.-Y. Niu, M.-S. Xie, G.-R. Qu, *Org. Lett.* **2013**, *15*, 5460–5463.
- [299] T.-J. Wang, W.-W. Chen, Y. Li, M.-H. Xu, *Org. Biomol. Chem.* **2015**, *13*, 6580–6586.
- [300] X. Chen, Y. Xie, C. Li, F. Xiao, G.-J. Deng, *Eur. J. Org. Chem.* **2017**, *2017*, 577–581.
- [301] Y. Lian, J. R. Hummel, R. G. Bergman, J. A. Ellman, *J. Am. Chem. Soc.* **2013**, *135*, 12548–12551.
- [302] W. Hu, Q. Zheng, S. Sun, J. Cheng, *Chem. Commun.* **2017**, *53*, 6263–6266.
- [303] C. Cheng, Y. Jiang, C.-F. Liu, J.-D. Zhang, W.-Y. Lai, W. Huang, *Chem. – Asian J.* **2016**, *11*, 3589–3597.
- [304] P. J. Stephens, P. N. Schatz, A. B. Ritchie, A. J. McCaffery, *J. Chem. Phys.* **1968**, *48*, 132–138.
- [305] J. R. Platt, *J. Chem. Phys.* **1949**, *17*, 484–495.
- [306] M. Taniguchi, J. S. Lindsey, *Photochem. Photobiol.* **2018**, *94*, 290–327.
- [307] N. G. Connelly, W. E. Geiger, *Chem. Rev.* **1996**, *96*, 877–910.
- [308] T. D. Anthopoulos, G. C. Anyfantis, G. C. Papavassiliou, D. M. de Leeuw, *Appl. Phys. Lett.* **2007**, *90*, 122105.
- [309] J. Tomasi, B. Mennucci, R. Cammi, *Chem. Rev.* **2005**, *105*, 2999–3094.
- [310] F. Neese, *Wiley Interdiscip. Rev. Comput. Mol. Sci.* **2012**, *2*, 73–78.
- [311] N. M. Brikci-Nigassa, G. Bentabed-Ababsa, W. Erb, F. Chevallier, L. Picot, L. Vitek, A. Fleury, V. Thiéry, M. Souab, T. Robert, S. Ruchaud, S. Bach, T. Roisnel, F. Mongin, *Tetrahedron* **2018**, *74*, 1785–1801.
- [312] G. Horowitz, F. Kouki, P. Spearman, D. Fichou, C. Nogues, X. Pan, F. Garnier, *Adv. Mater.* **1996**, *8*, 242–245.
- [313] H. Qian, F. Negri, C. Wang, Z. Wang, *J. Am. Chem. Soc.* **2008**, *130*, 17970–17976.
- [314] L. Schmidt-Mende, A. Fechtenkötter, K. Müllen, E. Moons, R. H. Friend, J. D. MacKenzie, *Science* **2001**, *293*, 1119–1122.
- [315] L. Zang, Y. Che, J. S. Moore, *Acc. Chem. Res.* **2008**, *41*, 1596–1608.
- [316] E. F. Valeev, V. Coropceanu, D. A. da Silva Filho, S. Salman, J.-L. Brédas, *J. Am. Chem. Soc.* **2006**, *128*, 9882–9886.
- [317] G. D’Avino, Y. Olivier, L. Muccioli, D. Beljonne, *J. Mater. Chem. C* **2016**, *4*, 3747–3756.
- [318] T. Liu, A. Troisi, *Adv. Mater.* **2013**, *25*, 1038–1041.
- [319] S. M. Gali, M. Matta, B. H. Lessard, F. Castet, L. Muccioli, *J. Phys. Chem. C* **2018**, *122*, 2554–2563.
- [320] V. Coropceanu, J. Cornil, D. A. da Silva Filho, Y. Olivier, R. Silbey, J.-L. Brédas, *Chem. Rev.* **2007**, *107*, 926–952.
- [321] S.-H. Wen, A. Li, J. Song, W.-Q. Deng, K.-L. Han, W. A. Goddard, *J. Phys. Chem. B* **2009**, *113*,

- 8813–8819.
- [322] J. H. Park, K. H. Lee, S. Mun, G. Ko, S. J. Heo, J. H. Kim, E. Kim, S. Im, *Org. Electron.* **2010**, *11*, 1688–1692.
- [323] M. Eslamian, F. Soltani-Kordshuli, *J. Coat. Technol. Res.* **2018**, *15*, 271–280.
- [324] R. Dheepika, S. Sonalin, P. Mohamed Imran, S. Nagarajan, *J. Mater. Chem. C* **2018**, *6*, 6916–6919.
- [325] Y. Fang, X. Wu, S. Lan, J. Zhong, D. Sun, H. Chen, T. Guo, *ACS Appl. Mater. Interfaces* **2018**, *10*, 30587–30595.
- [326] J. Lu, A. Dadvand, T. Chu, R. Movileanu, J.-M. Baribeau, J. Ding, Y. Tao, *Org. Electron.* **2018**, *63*, 267–275.
- [327] G. Giri, E. Verploegen, S. C. B. Mannsfeld, S. Atahan-Evrenk, D. H. Kim, S. Y. Lee, H. A. Becerril, A. Aspuru-Guzik, M. F. Toney, Z. Bao, *Nature* **2011**, *480*, 504–508.
- [328] C. Pitsalidis, A.-M. Pappa, S. Hunter, M. M. Payne, J. E. Anthony, T. D. Anthopoulos, S. Logothetidis, *ACS Appl. Mater. Interfaces* **2015**, *7*, 6496–6504.
- [329] Y. Su, X. Gao, J. Liu, R. Xing, Y. Han, *Phys. Chem. Chem. Phys.* **2013**, *15*, 14396–14404.
- [330] J. Jang, S. Nam, K. Im, J. Hur, S. N. Cha, J. Kim, H. B. Son, H. Suh, M. A. Loth, J. E. Anthony, J.-J. Park, C. E. Park, J. M. Kim, K. Kim, *Adv. Funct. Mater.* **2012**, *22*, 1005–1014.
- [331] S. Nam, J. Jang, John. E. Anthony, J.-J. Park, C. E. Park, K. Kim, *ACS Appl. Mater. Interfaces* **2013**, *5*, 2146–2154.
- [332] D. Grosso, *J. Mater. Chem.* **2011**, *21*, 17033–17038.
- [333] X. Zhang, H. Dong, W. Hu, *Adv. Mater.* **2018**, *30*, 1801048.
- [334] X. Zeng, D. Zhang, L. Duan, L. Wang, G. Dong, Y. Qiu, *Appl. Surf. Sci.* **2007**, *253*, 6047–6051.
- [335] L. D. Caspers, P. Finkbeiner, B. J. Nachtsheim, *Chem. – Eur. J.* **2017**, *23*, 2748–2752.



---

## Annexe

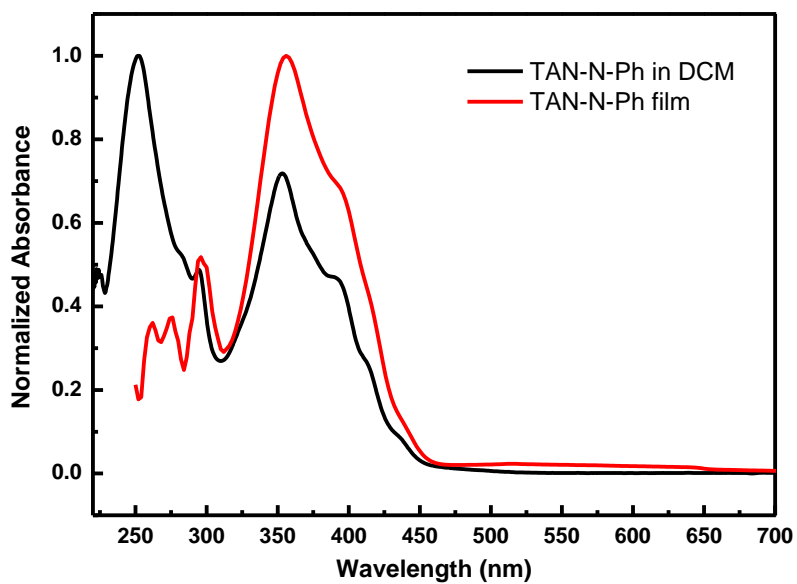


Figure A1. UV-visible spectra of TAN-N-Ph in DCM and film.

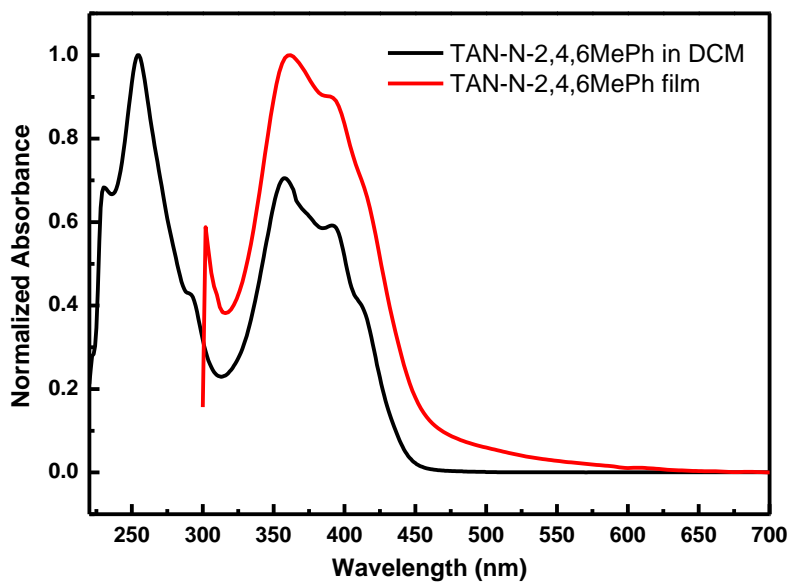


Figure A2. UV-visible spectra of TAN-N-2,4,6MePh in DCM and film.

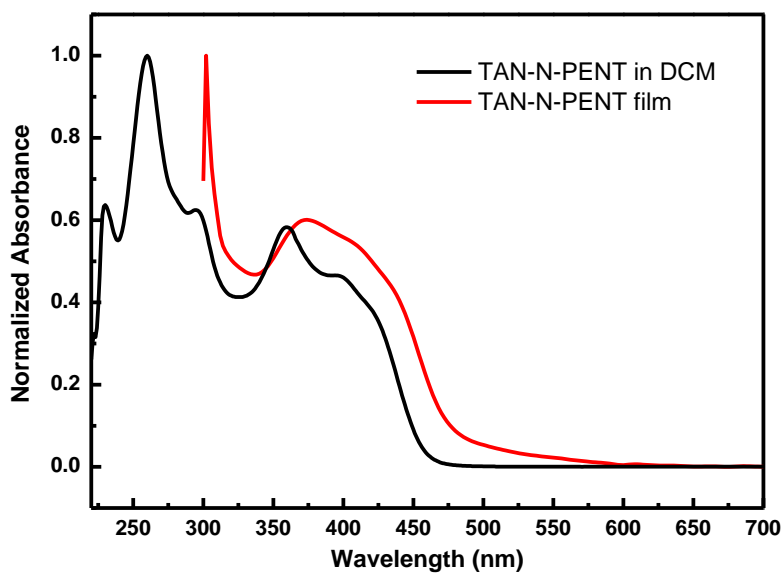


Figure A3. UV-visible spectra of TAN-N-Pent in DCM and film.

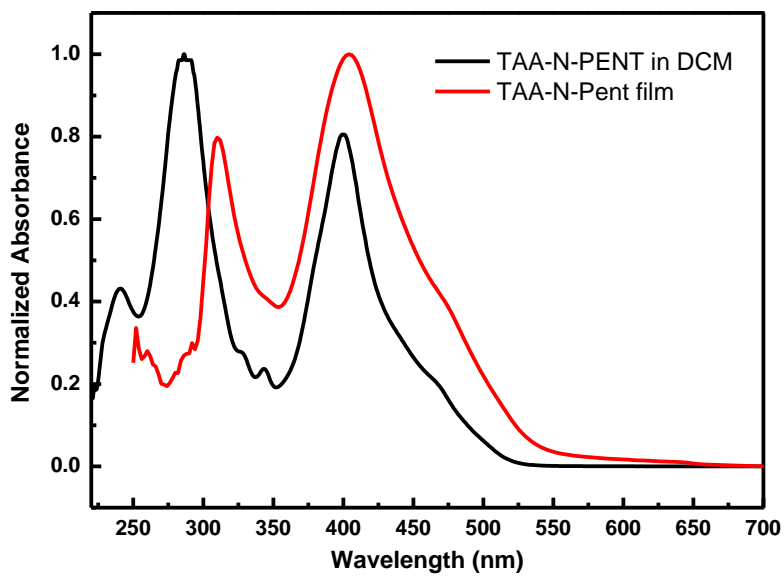


Figure A4. UV-visible spectra of TAA-N-Pent in DCM and film.

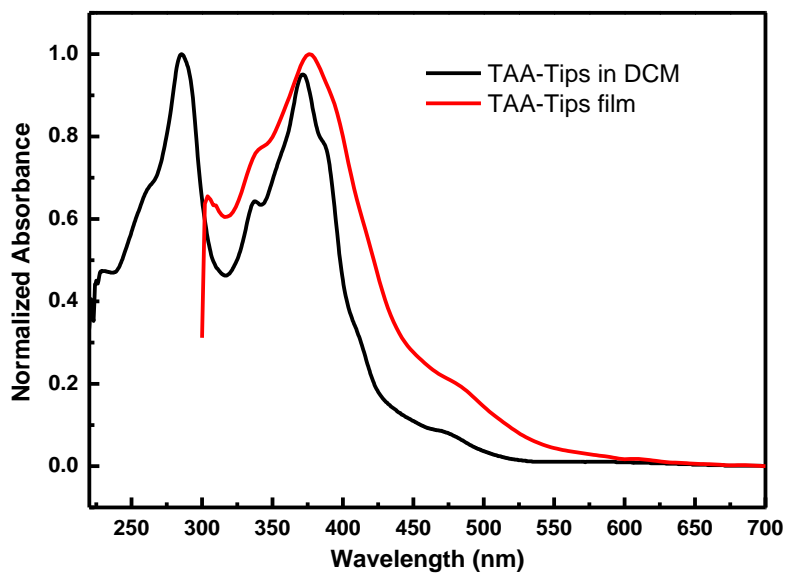


Figure A5. UV-visible spectra of TAA-Tips in DCM and film.